

Final Report

**Design and Application of
Electromechanical Actuators for Deep
Space Missions**

Submitted to:

NASA
Marshall Space Flight Center - EP64

Prepared by:

Tim A. Haskew, Assistant Professor
Department of Electrical Engineering

and

Dale E. Schinstock, Assistant Professor
Department of Mechanical Engineering

of

College of Engineering
The University of Alabama
Box 870286
Tuscaloosa, AL 35487-0286

Reporting Period:
8/16/92 - 12/15/95

BER Report No. 632-163

May 1996

Final Report

Design and Application of Electromechanical Actuators for Deep Space Missions

Submitted to:

NASA

Marshall Space Flight Center - EP64

Prepared by:

Tim A. Haskew, Assistant Professor
Department of Electrical Engineering

and

Dale E. Schinstock, Assistant Professor
Department of Mechanical Engineering

of

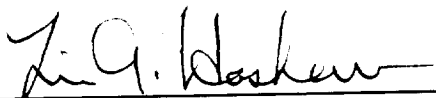
College of Engineering
The University of Alabama
Box 870286
Tuscaloosa, AL 35487-0286

Reporting Period:

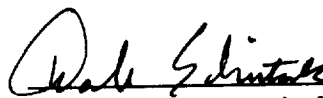
8/16/92 - 12/15/95

BER Report No. 632-163

May 1996



Tim A. Haskew, Ph.D.
Project Director, Co-Principal Investigator



Dale E. Schinstock, Ph.D.
Co-Principal Investigator

Preface

This document represents the completion of NASA Grant NAG8-240, "Design and Application of Electromechanical Actuators for Deep Space Mission." The investigators at The University of Alabama deeply appreciate the support of NASA personnel at Marshall Space Flight Center. Individuals that have been particularly helpful during the period of performance are Mr. Charles Cornelius, Mr. John R. Cowan, Ms. Rae Ann Weir, and Mr. John Sharkey.

We hope that you find our work useful, and intend to keep you apprised of all developments as we continue to work in the field of electromechanical actuation. The opportunity to work with all participants has been productive and rewarding.

TABLE OF CONTENTS

Preface	ii
Table of Contents	iii
I. Executive Summary.....	I.1
I.1. Accomplishments.....	I.1
I.2. Personnel	I.2
I.3. Technology Transfer	I.3
I.4. Future Efforts	I.4
II. The Electromechanical Actuation Test Facility	II.1
II.1. Mechanical Construction of the Test Stand	II.1
II.2. Present Mechanical Drive Train	II.3
II.3. Hydraulic Load System	II.4
II.4. Electrical Drive System	II.7
II.5. Instrumentation.....	II.7
III. Engine Startup Transient Load Tests.....	III.1
III.1. Description of the Experiment.....	III.1
III.2. Results of the Experiment.....	III.3
IV. Actuator Mechanical Model Development.....	IV.1
IV.1. Generation of Experimental Data Used in System Identification	IV.2
IV.2. Dynamic Model Identification	IV.4
IV.3. Parameter Estimation.....	IV.7
IV.4. Model Validation/Simulation Results	IV.12
IV.5. References	IV.17
V. Model Significance.....	V.1
V.1. Closed Loop Actuator-Load System.....	V.1
V.2. Effects of Engine Startup Transient Loads in the Closed Loop Actuator-Load System	V.5
V.3. References	V.9

VI.	Optimal Component Selection for Electromechanical Actuation	VI.1
VI.1.	Introduction.....	VI.1
VI.2.	Nomenclature.....	VI.1
VI.3.	System Definition and Analysis Description.....	VI.2
	VI.3.1. Actuator Model.....	VI.2
	VI.3.2. Load Models	VI.2
	VI.3.2.1. Passive	VI.3
	VI.3.2.2. Active.....	VI.3
	VI.3.3. Equivalent Circuit.....	VI.4
	VI.3.4. System Analysis	VI.6
VI.4.	Passive Load Analysis	VI.9
	VI.4.1. Passive Load Summary.....	VI.19
VI.5.	Active Load Analysis.....	VI.21
	VI.5.1. Active Load Summary	VI.28
VI.6.	Conclusion	VI.31
	VI.6.1. Future Development	VI.32
	VI.6.2. Single-Frequency Justification.....	VI.32
VII.	Health Monitoring and Fault Diagnosis	VII.1

Appendix A - Inertia Calculations

Appendix B - Health Monitoring of a Brushless Permanent Magnet Machine Using an Adaptive Kalman Filtering Approach

I. EXECUTIVE SUMMARY

This document is the final report submitted in completion of NASA Grant NAG8-240, "Design and Application of Electromechanical Actuators for Deep Space Missions." This is the sixth report issued during the period of performance from August 1992 through December 1995. Throughout the period of performance, our efforts have deviated significantly from the thrust in the original proposal. However, this grant was originally envisioned as a flexible vehicle for research and development associated with a dynamically changing program at Marshall focused on electromechanical actuation in the SSME TVC application.

Previous reports have contained documentation of various tasks and studies that were completed under this project. This report contains new information as well as an overview of the Electromechanical Actuation Test Facility. Completion of the test facility represents what we consider to be the major accomplishment of this project. The complete set of reports, a total of six including this report, forms a complete presentation of significant work funded on grant NAG8-240. This research project has been an extremely beneficial undertaking for The University of Alabama College of Engineering. The funding has allowed faculty in two departments to develop expertise in the growing field of electromechanical actuation. Additionally, the grant has enabled the development of a premier laboratory facility and the support of several graduate students. In fact, this project has funded one student through both the M.S. and Ph.D. degrees. Others have completed M.S. degrees alone through work associated with the project.

I.1. Accomplishments

During the 3.5 year period of performance, we have investigated many issues and have tried to answer several questions that were posed by NASA personnel. A bullet list of the major topics addressed, studies performed, and tasks completed is provided below. Note that the parenthetical dates reference reports in which information on the topic can be located.

- EMA Test Facility Development (2/93, 9/93, 2/94, 8/94, 3/95, 5/96)
- Roller Screw Modeling (2/93)
- Motor Selection (2/93, 2/94)
- Health Monitoring and Fault Diagnosis (2/93, 9/93, 2/94, 5/96)
- Analysis of Stiff-Arm Tests (9/93)
- Comparison of EMA and Hydraulic TVC Actuator Responses (9/93)
- Motor Drive Development (8/94, 3/95)
- Engine Startup Transients Load Tests (5/96)
- Actuator Model Development (5/96)
- Optimal Component Selection for EMAs (5/96)

Considering all results, findings, and accomplishments, the completion of the Electromechanical Actuation Test Facility (EMATF) is the most significant. The EMATF is an ideal facility for modeling and performance testing high-power electromechanical actuators under realistic loading conditions. Additionally, the facility is well suited for prototype development and system integration studies.

In this report, several new topics are presented. Results from engine startup transient load tests, performed in the EMATF, are presented. Also, experimental and theoretical work is combined to provide insight into actuator model development. The impact of actuator modeling on control system design is addressed. And finally, this report contains a preliminary study on methods for optimal selection of actuator components. This particular information was recently request by NASA personnel, and some interesting results are presented.

I.2. Personnel

Throughout the project, three faculty member have received support for efforts associated with this grant. Multiple M.S. students and one Ph.D. student have been supported by grant funds, and other students have been involved in research activities without grant funding. A list personnel information for the complete period of performance is provided in Table I.1.

Table I.1 - Personnel Information

Faculty			
Name	Department	Received Funding	
Tim A. Haskew	Electrical Engineering	Yes	
John Wander	Mechanical Engineering	Yes	
Dale E. Schinstock	Mechanical Engineering	Yes	
Jon G. Bredeson	Electrical Engineering	No	
Graduate/Undergraduate Students			
Name	Department	Degree Program	Funded
Sumit K. Bhattacharyya	EE	MS	Yes
Ramomohan Challa	CS	MS	No
Kris Cozart	ME	MS	Yes
Frank DeCord	ME	MS	Yes
David Tycyn Ewing	EE	MS	Yes
Stanley McCarter	EE	BS	No
Sean McGraw	EE	BS	No
Felix Naylor	EE	BS	No
Chris Nielsen	EE	BS	No
Stuart Payne	ME	MS	Yes
Thomas E. Salem	EE	MS/PhD	Yes
Yoon Gyeong Sung	ME	MS	No

I.3. Technology Transfer

Throughout performance of the project, emphasis was placed on publishing results in widely circulated technical journals and on presenting results at recognized conferences. Additionally, technology transfer was obtained through publication of theses and dissertations. The theses and dissertation listed below have been accepted and successfully defended while other M.S. theses are in preparation:

Salem, Thomas Eric, *Prime Mover Selection for Electromechanical Actuation in Thrust Vector Control Applications*, Master of Science Thesis, The University of Alabama, Department of Electrical Engineering, 1993.

Challa, Ramomohan, *Design of a Computer System to Test Roller Screw Actuators*, Master of Science Thesis, The University of Alabama, Department of Computer Science, 1994.

Salem, Thomas Eric, *Health Monitoring of a Brushless Permanent Magnet Machine Using an Adaptive Kalman Filtering Approach*, Doctor of Philosophy Dissertation, The University of Alabama, Department of Electrical Engineering, 1996.

In addition to theses and dissertations, the papers listed below have either been published or accepted for presentation and/or publication:

Haskew, Tim A., Dale E. Schinstock, Thomas E. Salem, and Jon G. Bredeson, "Brushless Machine Simulation and Monitoring," *Proceedings of the 31st Intersociety Energy Conversion Engineering Conference*, to appear, Washington, D.C., August 1996.

Schinstock, Dale E. and Tim A. Haskew, "Dynamic Load Testing of Roller Screw EMAs," *Proceedings of the 31st Intersociety Energy Conversion Engineering Conference*, to appear, Washington, D.C., August 1996.

Wander, J., V. Byrd, and J. Parker, "Initial Disturbance Accommodating Control System Analysis for Prototype Electromechanical Space Shuttle Steering Actuator," *Proceedings of the 1995 American Control Conference*, Seattle, Washington, June 1995.

Salem, Thomas and Tim A. Haskew, "Simulation of the Brushless DC Machine," *Proceedings of the Twenty-Seventh Southeastern Symposium on System Theory*, Starkville, Mississippi, pp. 18-22, March 1995.

Haskew, Tim A., "Health Monitoring and Other Selected Research Issues," *Proceedings of Prospector VI: Electric Actuation Workshop*, Park City, Utah, March 1994.

Other manuscripts are in progress for submission to refereed journals. The topics for planned submissions include:

- Real-Time Health Monitoring of Brushless Permanent Magnet Machines
- EMA Power Electronic Efficiencies with Various Control Strategies
- Optimal EMA Component Selection
- Dynamic Load Tests of EMAs
- EMA Model Developments

In addition to publication, technology transfer has been demonstrated through the involvement of the investigators in various conferences and on various professional society working groups and subcommittees. Specifically, Tim A. Haskew chaired the Key Research Issues working group sessions at *Prospector VI: Electric Actuation Workshop* and will chair an EMA session at the 1996 IECEC. He has also become active in related IEEE Power Engineering Society working groups and subcommittees focusing on motor monitoring and performance.

I.4. Future Efforts

While several studies have been completed during the period of performance, many issues remain open to further study. The authors intend to continue with a research focus on electromechanical actuation and provide further information on the open issues. It is expected that funded programs will be developed through governmental agencies and industrial entities that will continue to keep the EMATF up-to-date and well used.

In order to enhance our capabilities within the laboratory, the motor drive system will be upgraded using microprocessor controllers and field programmable gate array technology. This will allow a much simpler verification and study of control algorithms and electrical side fault impacts through software modification rather than hardware construction. Furthermore, a dedicated data acquisition and control computer will be provided for the electrical side of the facility.

Health monitoring efforts will be implemented in real-time using DSP technology, and health information based control architectures will be studied. Furthermore, much effort is planned in the areas of optimal component selection and actuator model development.

II. THE ELECTROMECHANICAL ACTUATION TEST FACILITY

The most significant accomplishment during this project was the completion of the Electromechanical Actuation Test Facility (EMATF). The EMATF provides an ideal setting for actuator prototyping, performance testing, modeling, and system integration studies. Hence, the laboratory is expected to be heavily used in the future. The most significant offering of the facility is the computer-controlled dynamic loading capability. When coupled with the instrumentation system, actuator testing and development can be performed under realistic loading conditions. The facility is housed within Department of Electrical Engineering facilities in the East Engineering Building. This report section contains an overview of the EMATF and its various subsystems. Detailed drawings, specifications, and electrical schematics are on file within the laboratory.

II.1. Mechanical Construction of the Test Stand

The general configuration of the test stand in the EMATF is shown in Figure II.1. This test stand was designed to produce large dynamic loads on a linear actuator, under force control or position control. It was also designed to be reconfigurable so that different actuators could easily be mounted in the stand for testing. The test stand will accept either rigidly mounted linear actuators, as shown in the figure, or self contained actuators with pivoting end connectors, like clevis mounts. Nominally, all components in the test stand were designed to withstand at least 100 kip in the extension of the hydraulic cylinder and 50 kip in the retraction of the hydraulic cylinder. The I-beam structure itself will withstand much larger loads, and was designed to be very stiff, and not contribute significantly to the dynamics of the loading and measurement systems.

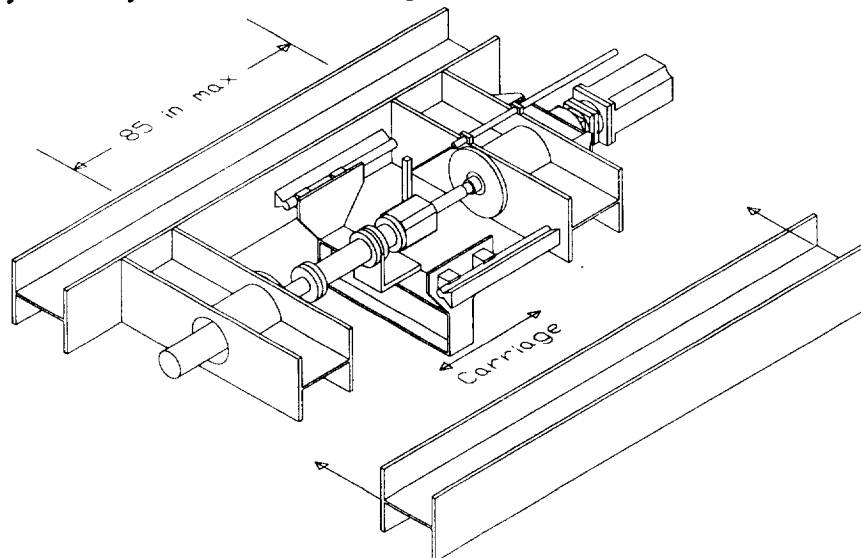


Fig. II.1 - EMA Test Stand with the Small Bore Cylinder

The two end beams of the structure can be moved up and down the length of the two side beams. The side beams are longer than shown in the figure, and allow a maximum span of 85 inches between the end beams. The hole patterns necessary to accept the mounting bolts for the end beams have been predrilled in the side beams along their length. Also, several load/extension pipes have been fabricated so that the length of the hydraulic cylinders can be adjusted. This allows different length actuators and cylinders to be placed in the stand with minimal effort required for reconfiguration. In Figure II.2, the stand is shown with a larger diameter cylinder mounted within the span between the two end beams.

The carriage within the test stand serves several purposes. It is useful in the alignment of rigidly mounted actuators and the load cylinders. Once the rails for the carriage are placed, the actuator and the cylinder may be aligned using the carriage as a reference. This allows the cylinders to be aligned very quickly when they are exchanged. The carriage can also be used to support one end of a self contained actuator. Another purpose for the carriage is in supporting instrumentation and side load actuators that must travel with the end of the actuator. The carriage has a friction slide, not shown in the figures, that allows motion in the transverse direction, along the beam of the carriage. This degree of freedom can be fixed with clamp bolts. The purposes of the carriage for the setup shown in the two figures, with a rigid mount actuator and no transverse loading, are to absorb the reaction torque of the nut resulting from axial loads and to provide transverse and vertical support to eliminate the chance of buckling over the long span of the drive train. The carriage rails may also be moved up and down the length of the side beams. The majority of the effort required in moving the rails is in their alignment after they are placed.

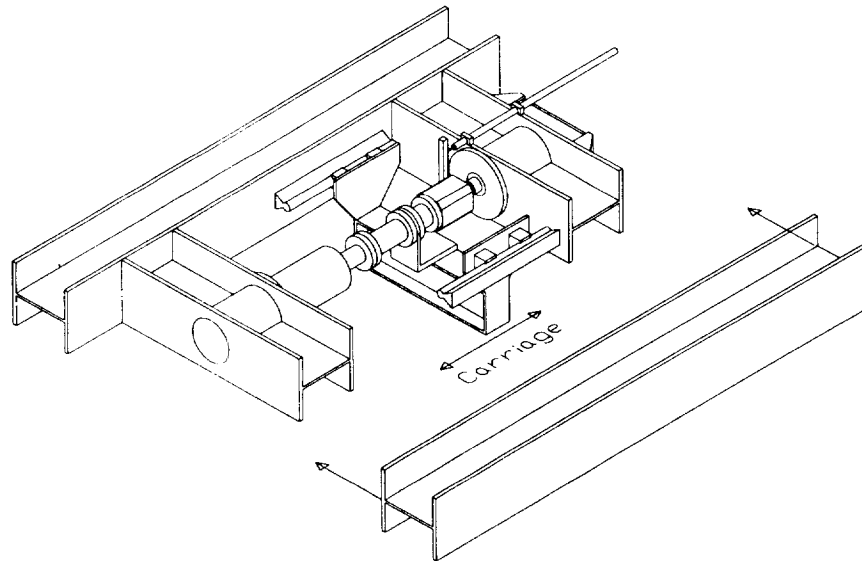


Fig. II.2 - EMA Test Stand with the Large Bore Cylinder

Not shown in the previous two figures is a transverse loading mechanism that may be used to produce side loads on the actuator. The mechanism is basically a spring that attaches to the carriage. It travels with the nut, pushing the side of it as it travels up and

down the screw. The force is adjusted by changing the compression of the spring, and is measured with a load cell.

II.2. Present Mechanical Drive Train

The present mechanical/hydraulic drive train in the EMA teststand is shown in Figure II.3. This figure shows the hydraulic loading system coupled to the electromechanical actuator. The axial load generated by hydraulic system is transformed to torsion in the roller nut. The axial load of the screw is transferred to the end beam of the teststand through the bearings on the roller screw. The load cell directly measures the force applied to the nut cage and nut, eliminating the dynamics of the loading system and test stand from the force measurement. Note in Figure II.1 that the carriage is attached to the drive train between the extension pipe and the load cell. Both the load cell and the extension pipe are hollow allowing the roller screw to extend through them. This is necessary for the load cell to be connected directly to the nut cage. The LVDT measures the displacement of the nut relative to the end beam.

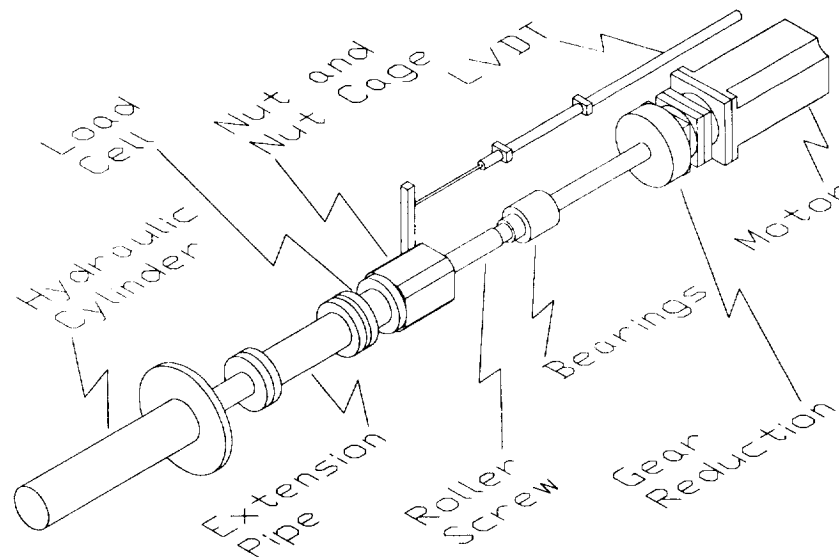


Fig. II.3 - Present Mechanical Drive Train

If it is assumed that the test stand structure is stiff, all of the energy of the measured axial load is either converted to mechanical energy in the EMA actuator system, dissipated in the EMA actuator system, or leaves the system through a torque applied to the motor. This is an important requirement for accurate dynamic analysis of the actuator system using the measured load.

The EMA actuator system includes the nut cage, the nut, the roller screw, the radial/thrust bearings, the gear reduction, and the motor. The particular roller screw and nut used are an SKF set with a non-preloaded nut, a 48 mm nominal diameter screw, and 20 mm lead. There are six radial/thrust ball bearings that are preloaded with three bearings absorbing compressive loads and three absorbing tensile loads. The gear reducer is a Micron planetary reducer with a 4 to 1 reduction. It was designed to mate directly to

the motor used in the system. The motor will be discussed in a subsequent section of the report.

II.3. Hydraulic Load System

A schematic drawing of the hydraulic load system is shown in Figure II.4. The key features of this hydraulic system are the high flow rate servo valve and the accumulator. These two components allow the system to generate large dynamic loads at high flow rates. Without the accumulator, the system becomes flow starved at relatively low velocities and force rates. This is due to the large cylinders used to generate the loads and the limited flow rates of fixed displacement pumps. The system also contains a high pressure filter along with the standard return line filter and reservoir strainer. A solenoid operated relief valve is used for safety purposes and no load pump start. Two different size cylinders are currently used in the system. Both of these cylinders are fairly large.

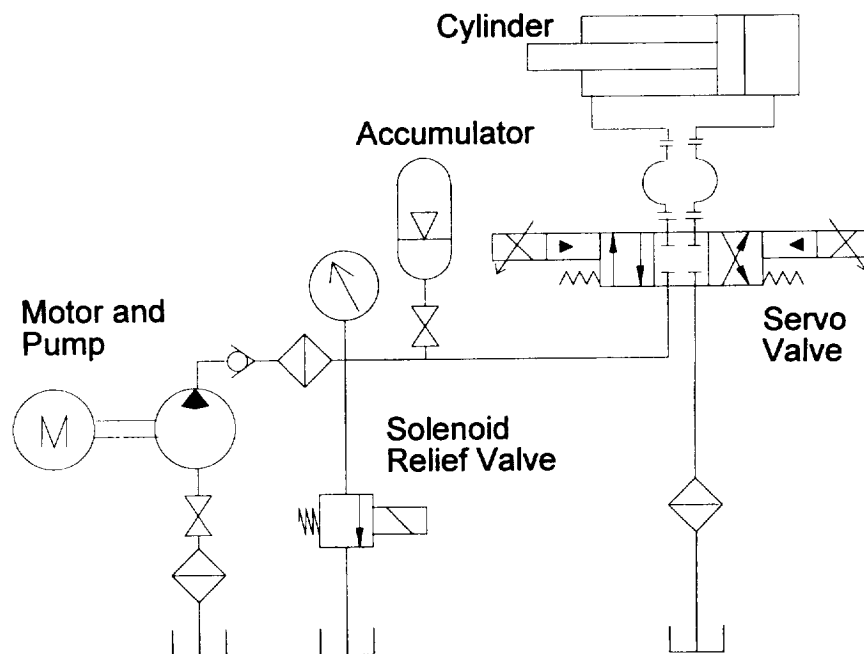


Fig. II.4 - Hydraulic System Schematic

Specifications for hydraulic load system are given below:

- Operating Pressure - Up to 3000 psi
- Prime Mover - 30 Hp, 1150 rpm AC induction motor
- Fixed Displacement Pump Flow Rate - 3.42 in³/rev, 17 gpm @ 1150 rpm
- Servo Valve - Two stage servo valve, $\Delta p = 72$ psi at 53 gpm, 40 Hz bandwidth at 5% displacement and 12 Hz bandwidth at 100% displacement
- Accumulator - 5 gallon gas charged accumulator, 1900 psi charge

- Large Cylinder - 7" bore, 3" rod, 4" stroke, max. force 115/94 kip (ext./retract), max. velocity w/o accumulator 1.7/2.1 in/s (ext./retract)
- Small Cylinder - 4" bore, 2.5" rod, 13" stroke, max. 38/23 kip (ext./retract), max. velocity w/o accumulator 5.2/8.5 in/s (ext./retract)

The hydraulic system may be used in either a position control mode or in a force control mode. The following two diagrams show the components involved in the position control loop and the force control loop respectively. The valve amplifier/controller implements an analog position controller for the spool of the main stage of the valve. A digital, load position control loop is implemented around the valve's spool position controller, using the computer. This is shown in Figure II.5. The position feedback used is usually from the long stroke LVDT, which is connected to the load at the location where position is to be controlled.

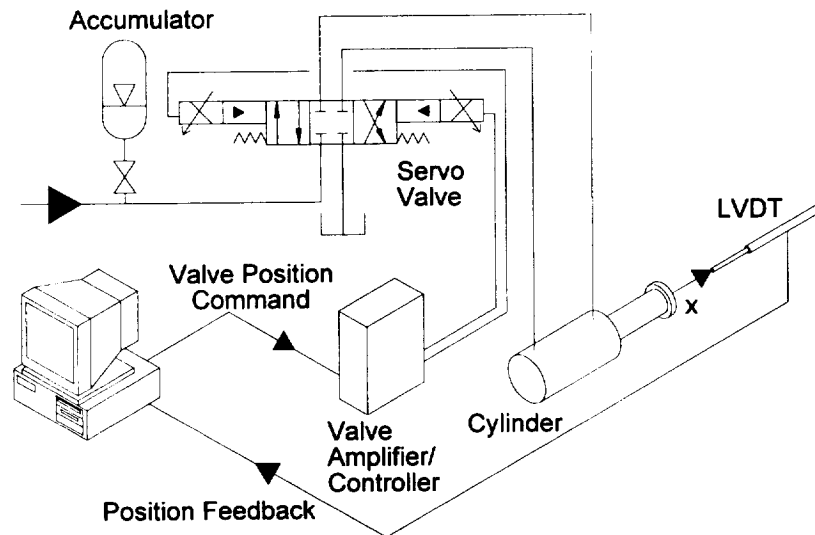


Fig. II.5 - Hydraulic Position Control Loop

The valve amplifier/controller can also be configured to implement an analog pressure control loop, around the spool position loop, using the feedback from a pressure transducer. To achieve an analog force controller the load cell output is fed back to the valve controller in place of a pressure transducer output, as illustrated in Figure II.6. The load cell is placed in the system so that it measures the force applied to the actuator being tested.

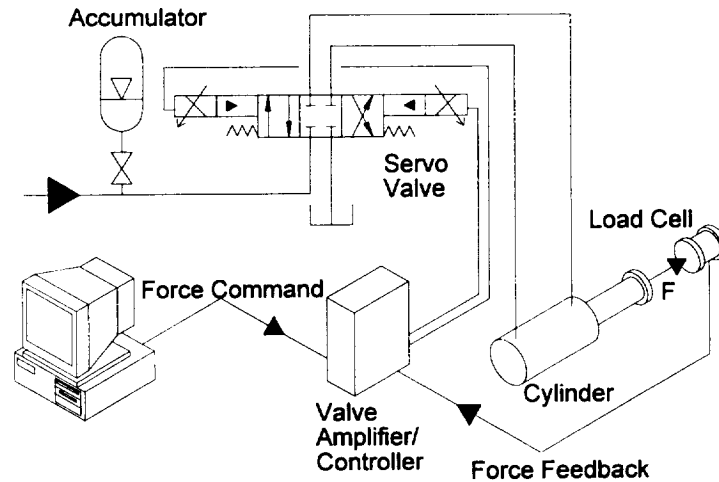


Fig. II.6 - Hydraulic Force Control Loop

The previous two figures do not show all of the instrumentation on the test stand. They show only that hardware involved in the hydraulic control loops. The accumulator is shown in these figures because it significantly affects the performance of the system.

As an example of what is achievable with the force control system and a stiff load, Figure II.7 is included. This figure was generated with the force control system and a stiff load. The load connected to the cylinder was a deadhead beam that was attached to the test stand using four 2 1/2 ft long sections of 3/4 in all thread inside of square tubing. This is a fairly stiff load. With this type of load it would be expected that a high frequency dynamic load could be generated. It should be pointed out that very little tuning of the control system was done before this load was generated. The purpose of the test to check out the system and to get a feel for what the how it performed.

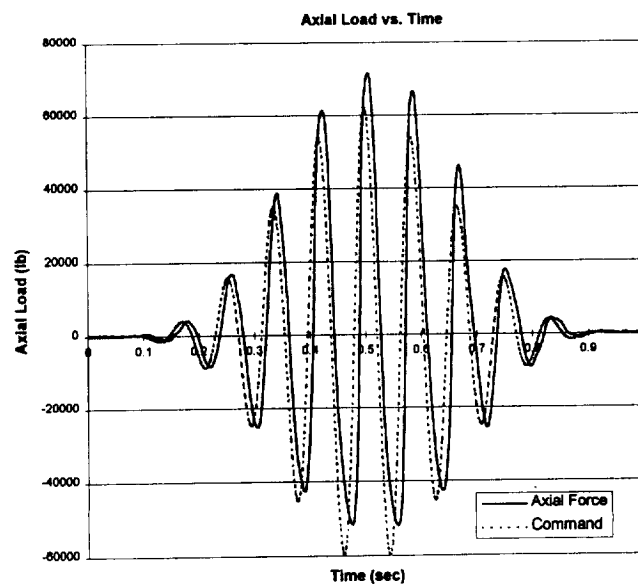


Fig. II.7 - 12 Hz, 62 kip, Deadhead Test

II.4. Electrical Drive System

The electrical drive system within the Electromechanical Actuation Test Facility is presently based on a six-pulse IGBT inverter operating without snubbers. The motor drive is modular in design. Hence, multiple inverters can be directly inserted into the drive assembly. The motor is equipped with a resolver, and the motor control unit has an onboard resolver-to-digital converter. Commutation logic is accomplished with discrete TTL components. The control loops are presently implemented in an analog fashion, but will be upgraded to microprocessor based loops. The control system is highly flexible in terms of reconfiguration and access to various quantities for measurement. A 400 A, 600 V IGBT inverter will soon be tested in the drive.

The motor on the test stand is a Kollmorgen Goldline B-802-B permanent magnet synchronous machine. Presently, the motor is being controlled as a brushless dc machine. The data on the motor is provided below:

- Output Power - 13.6 Hp (cont.)
- Speed - 2,750 RPM (max.)
- Stall Torque - 43.1 N-m (25°C, cont.), 40.7 N-m (40°C, cont.)
- Line Current - 32.4 A rms (cont.), 108.2 A rms (peak)
- Peak Torque - 129.2 N-m
- Line Voltage - 250 V dc (max.)
- Rotor Inertia - 0.00488 kg-m²
- Viscous Damping - 0.237 N-m/KRPM

Power sources within the facility are plentiful. The primary utility service is three-phase, 208 V, with an ampacity of 225 A. This source can be directly connected to an autotransformer and rectifier/filter, or it can be used to drive an MG set with a dc generator output. All power connections are easily accessible from a main power panel in the Electric Power and Machines Laboratory.

II.5. Instrumentation

The test stand and motor drive system are well instrumented. The instrumentation of the test stand includes the following:

- Axial Load Cell - +/- 100,000 lb force range, +/- 20,000 in-lb torque range
- Long Stroke LVDT - 16 in stroke
- Transverse Load Cell - 1500 lb range
- Transverse LVDT - 0.4 in stroke

The instrumentation incorporated into the on the motor drive includes the following:

- Current and voltage measurement on all phases of the motor and on dc bus
- 12-bit resolver to digital converter giving digital motor position and analog motor speed

The data acquisition system includes a 66 MHz 486 PC/AT computer, a 330 kHz, 12 bit, 16 channel A/D card and an external, sixteen channel, simultaneous sample and hold board. The sample rate of the A/D card specified is the rate at the A/D and therefore must be divided by the number of channels being sampled when calculating the sample rate for each channel. Also, this rate is that possible using block transfers of the data to the PC/AT memory without considering the CPU time required for tasks other than data acquisition. Therefore, the sample rate is reduced in the applications where the computer is also performing control tasks. The external sample and hold board is used to eliminate the channel to channel skew of the acquired data in applications with a high sampling rate.

III. ENGINE STARTUP TRANSIENT LOAD TESTS

This chapter of the report describes the dynamic load tests performed to qualify the effects of large dynamic loads, such as those experienced by the Space Shuttle Main Engine actuators, on the roller screw actuator. The loads that were applied to the roller screw during these tests are comparable to those measured in the NASA stiff arm, engine start and shutdown tests, TTB050 through TTB054. A maximum load of about 63.4 kips was applied to the roller screw during a series of dynamic load tests.

III.1. Description of the Experiment

Figure III.1 shows the configuration of the drive train for the dynamic load tests. For these tests the gear reduction and the motor were removed from the end of the roller screw. The end of the screw was fixed so that no rotation was allowed at the point where the motor attaches. This loading condition is more severe than one allowing large motion between the roller screw and nut. A well lubricated (greased) nut was used for testing. However, for the lubrication to work effectively, motion is required to draw the grease into the contact area. Since the end opposite the nut was fixed, only a small amount of relative rotation between the nut and screw was achieved. The relative rotation was the result of elastic deformation, wind up, of the screw along the length between the fixed end and the nut. This situation simulates a severe application of the roller screw. During the experiments the nut was located close to the bearings on the screw that absorb the thrust load. This nut location was chosen to eliminate concerns of screw buckling and/or of the excitation of low frequency modes in the hydraulic system.

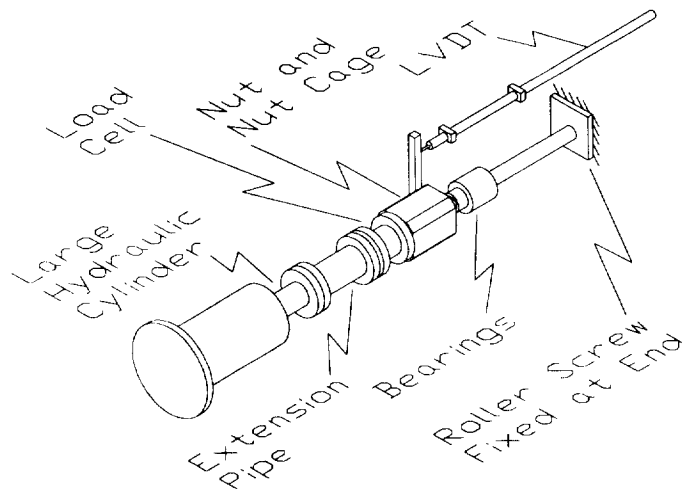


Fig. III.1 - Experimental Setup for The Dynamic Load Tests

The hydraulic system was used in a force control mode for these tests. Utilizing the load cell for force feedback, large, high frequency, dynamic load commands can be tracked. Since the load is stiff, as seen by the hydraulic system, the bandwidth of the closed loop force control system is high. With a stiff load, and therefore small motions, the hydraulic system has less of a tendency to saturate due to flow rate limits.

In building to the final, full amplitude test, several dynamic load tests were performed on the screw. Prior to, and after the completion of all of the tests, the screw was visually inspected for damage using a magnifying glass.

First the screw was loaded slowly to 65,000 lb in compression and then to 50,000 lb in tension to statically test the experimental apparatus. Then 5 tests with load time histories like the one shown in Figure III.2, except with a 20,000 lb peak load, were performed to evaluate the control system and test stand. After determining that the system was performing properly, the magnitude of the dynamic load was increased in the successive tests. The load was increased until the final test with a 63,400 lb measured peak load was reached. All of the dynamic load tests performed were similar to the one shown in Figure III.2. This is a modulated load with a 6 Hz fundamental frequency. The differences between each of the tests were in the magnitudes of the loads.

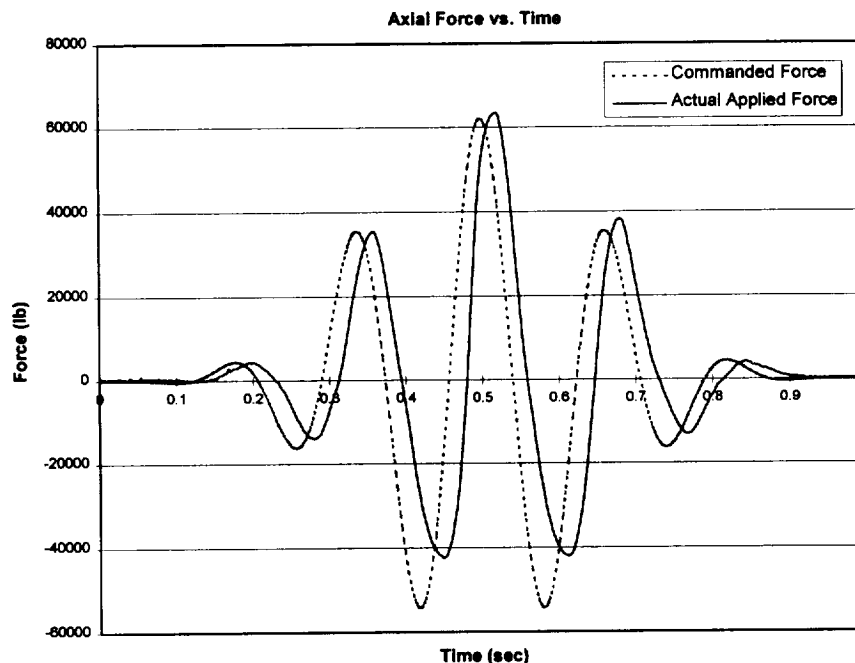


Fig. III.2 - Axial Force Applied During the 62 kip Dynamic Load Test

Table III.1 shows the succession of the dynamic load tests that were performed. It was not desirable to perform 8 dynamic load tests in building to the final test as shown in Table III.1. This was the result of a cautious approach to the completion of the experiment. The reason for multiple tests at 40, 50, and 60 kip is that it was originally hoped to perform the tests without involving the accumulator in the hydraulic circuit.

However, the test stand was not able to generate the commanded forces without the accumulator in the circuit.

Table III.1 - Tests With Greater Than 20 kip Commanded Load

<i>Commanded Peak Compressive Load (kip)</i>	<i>Measured Peak Compressive Load (kip)</i>	<i>Measured Peak Tensile Load (kip)</i>	<i>With/Without the Accumulator</i>
30	27.4	19.7	without
40	36.0	27.4	without
50	40.9	35.0	without
60	41.3	40.7	without
40	41.2	28.1	with
50	51.1	34.7	with
60	61.3	41.0	with
62	63.4	42.5	with

III.2. Results of the Experiment

After the tests were completed the testing apparatus was disassembled and an inspection of the screw was performed. Visual inspection revealed nine sets of spots like those shown in Figure III.3. Figure III.3 shows one set of spots corresponding to one planetary roller inside the roller nut. There are nine such planetary rollers inside the roller nut. The screw showed one set of spots for each roller. As would be expected, these spots were located in the wear bands on the faces of the screw threads. Each set includes spots on both faces of the screw thread, offset by a distance measured along the helix as shown in Figure III.3. This indicates that the spots were generated during both compression and tension of the screw.

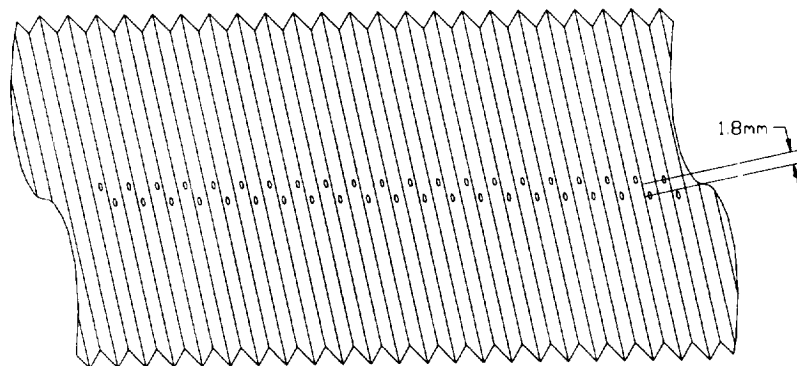


Fig. III.3 - Sketch of a Set of Spots Corresponding to One Planetary Roller

Each of the spots is very roughly circular, with some elongation along the face, and roughly 1 mm in height. A depth for the spots is not observable simply using a magnifying glass. They might be described as a growth in the width of the wear band in

the region where the rollers contacted the screw during the tests. Although, there is probably a small amount of material flow in these spots, they would not be considered a failure of the screw in practically any application. The result of these spots is probably a decreased screw life caused by premature flaking on the face of the screw threads.

Although these spots were not expected, they are certainly not surprising under the loading conditions. The particular roller screw and nut used are an SKF set with a non-preloaded nut, a 48 mm nominal diameter screw, and 20 mm lead. This screw-nut combination has a static load rating of 86,600 lb and a dynamic load rating (L_{10}) of 48,800 lb. The L_{10} rating is based on a 10 percent failure rate with one million revolutions of the screw at the rated load. This dynamic load rating is almost meaningless for the loading situation in this experiment. The applied loads were well within the static load rating of the screw-nut combination. With the number of number cycles completed in the tests it might have been expected to see no visual effects at all.

The displacement of the spots on opposing faces, and the shape of the spots, are well within what might be expected from a kinematics analysis of the contact points on the screw and a hertzian contact analysis for the contact area under the loads applied during testing. From strain calculations the displacement due to wind up was estimated to be about 2 degrees at a 60,000 pound axial load. The rotational stiffness of the nut mounting is rigid in comparison to that of the screw. Therefore our best estimate of the total angular displacement between the maximum rotation at full compressive load and full tensile load is about 3.5 to 4 degrees. This was crudely verified with a measurement during the tests. This is not of course an estimate of the travel of the rollers on the face of the screw thread. An estimate of requires a detailed kinematics calculation. Such a calculation was performed by persons at SKF using the information above, about the displacement due to wind up. The results were provided in a proprietary document. They supported the findings for the locations of the spots and the rough description of the shape of the spots.

What is not explained by the kinematics and hertzian contact analysis is the visibility of the spots. Only the shape and location of the spots is explained by this analysis. The visibility of spots might be explained by a break down in the lubrication and a corresponding increase in the friction in the contact area, causing a very high wear rate and a small amount of material flow. It was suggested by SKF that a dry lubrication might be better for this loading situation.

These tests answer the important question of whether the roller screw will withstand this type of loading. It will withstand this type of loading with minor damage that will perhaps decrease the life of the screw. There is still another important question that is left unanswered by this testing however. What will the actual forces exerted on the roller screw be during the engine start-up? This question is addressed in chapter V of this report.

IV. ACTUATOR MECHANICAL MODEL DEVELOPMENT

This chapter of the report describes the development of the mechanical model of the roller screw actuator in the test stand in the EMA Laboratory. Model development, or system identification, is a large problem to which there are many approaches. One approach to model development is to write the differential equations describing the system, assuming that the underlying physical principles are well understood, and then to calculate and/or measure the individual parameters in the differential equations of the model. Another approach is to try to fit ready made models, like transfer functions and auto-regressive models, to experimentally measured data. The first approach, if successful, results in a good understanding of the system and a model that applies to many situations. It however may not be possible since measurement and/or calculation of each physical parameter is often unrealistic. The second approach is the more efficient but does not result in an understanding of the system. The resulting estimated model may apply only to the data used in the model fit. The methods used here are a combination of these two approaches.

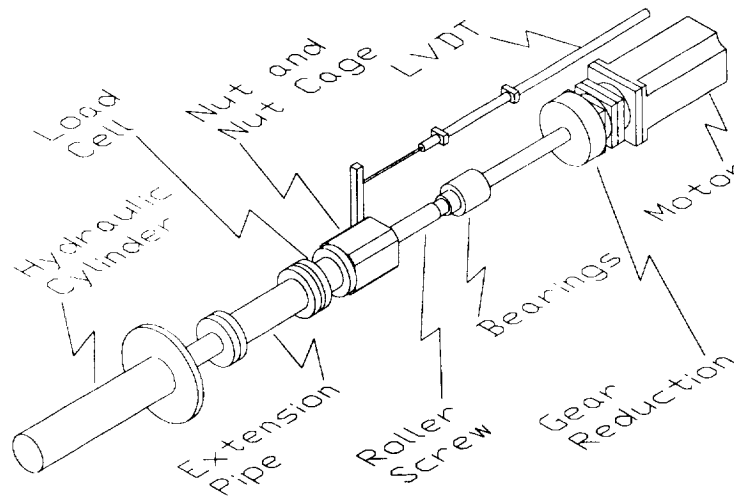


Fig. IV.1 - Actuator and Experimental Setup for Model Development

Figure IV.1 shows the actuator for which the model was developed and the experimental setup for the generation/collection of data. The mechanical system for which the models were developed includes all the components from the roller screw nut and cage back through the motor. For the mechanical model development there was no power applied to the motor. Forces were generated on the nut using the hydraulic system and measured with the load cell. The nuts translation up and down the screw was measured with the LVDT.

A brief description of the methods used to develop the actuator models is now given. First, a simple linear mathematical model was developed using common physical principles, and rough calculations were made to estimate as many of the parameters in the

model as possible using applicable physical principles and manufacturer's data. This model is a rigid body model with an effective mass and damping. The effective mass of the system was estimated with calculations. These calculations are shown in the Appendix A. The damping term could not be calculated and had to be developed experimentally. The behavior of the damping force, as a function of velocity was developed by measuring the force applied to the nut at several different steady state velocities. It was noticed in the experimental data that there were significant oscillations in the velocity response that could not be explained with the rigid body model and the applied force. Therefore it was deduced that a higher order model with at least two masses and one spring might be a better model. The parameters for two rigid body models, a linear model and a model with nonlinear damping, were estimated using least squares and experimental data. The parameters for the higher order model were found by trial and error. The trial and error method utilized comparison of simulated responses to measured responses.

IV.1. Generation of Experimental Data Used in System Identification

Many sets of experimental data were generated for model development. All of the data was generated using a position control loop in the hydraulic system. A position command profile was generated prior to a test and then commanded to the position control system, which used the LVDT as feedback and the cylinder for actuation. The forces exerted on the nut and the position of the nut were logged, and used in the system identification process.

In order to gain an understanding of the nature of the damping forces several constant velocity tests were run. The data for one of these tests is shown in Figure IV.2. Constant velocity tests were run for 0.1, 0.2, 0.3, 0.4, 0.5, -0.5, 0.6, 0.7, 0.8, 0.9, 1.0, -1.0, 1.5, 2.0, 2.5, 3.0, 3.5, 4.0, 5.0, and -5.0 in/s. Above a velocity of 5 in/s the flow of the hydraulic pump was insufficient to reach the commanded velocity.

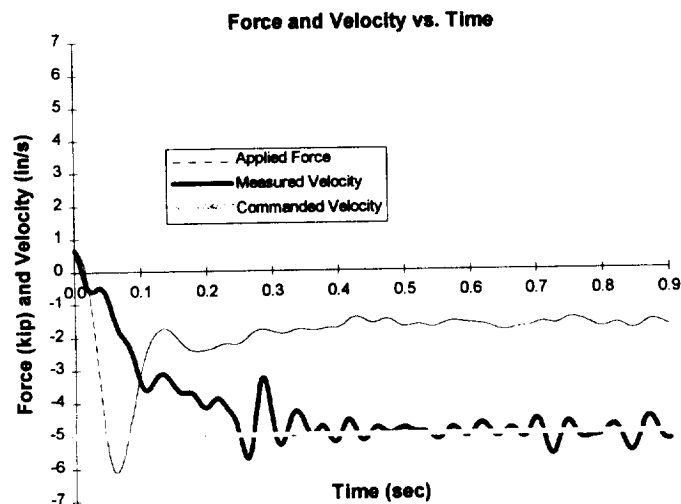


Fig. IV.2 - System Response to a -5 in/s Constant Velocity Command

The actual force data collected is noisier than that shown in Figure IV.2. Also, velocity is not measured directly with the LVDT. The data shown in Figures IV.2 through IV.5 are the results of filtering the raw position and force data, and then numerically differentiating the position data to obtain velocity. For the data in all of these figures, a 25 Hz, 12 pole, zero-phase filter was used on both the raw force and the raw position data. A 12 pole, zero-phase filter is obtained by using a 6 pole Butterworth filter. The data is passed through first in the forward direction and then again in the reverse direction, resulting in twice the attenuation and zero phase shift. The effects of the filtration process will be seen in figures in the next section of this report. To obtain velocity second order, central difference, numerical differentiation was utilized. Acceleration was also calculated, and used in parameter estimation. Acceleration was found using numerical differentiation of the velocity.

For least squares estimation of the parameters in the models, a more dynamic loading situation is desired than that obtained with a constant velocity command. Therefore several tests were run with square wave velocity profiles commanded to the position controller. The data from one, two, and three Hertz velocity commands are shown in Figures IV.3, IV.4, and IV.5 respectively.

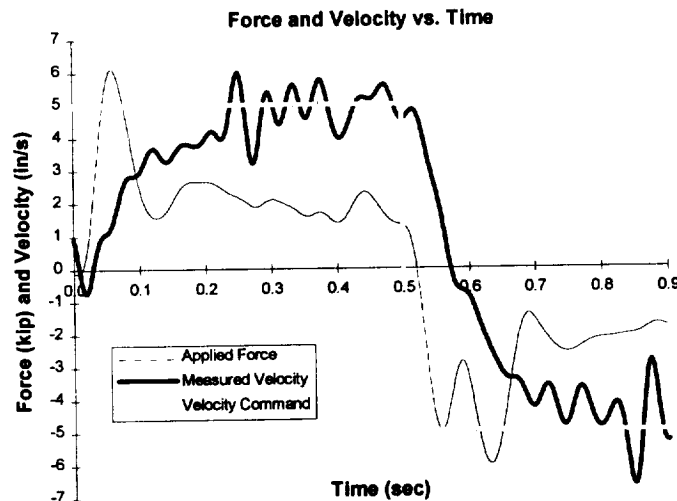


Fig. IV.3 - System Response to a 5 in/s, 1 Hz Square Wave, Velocity Command

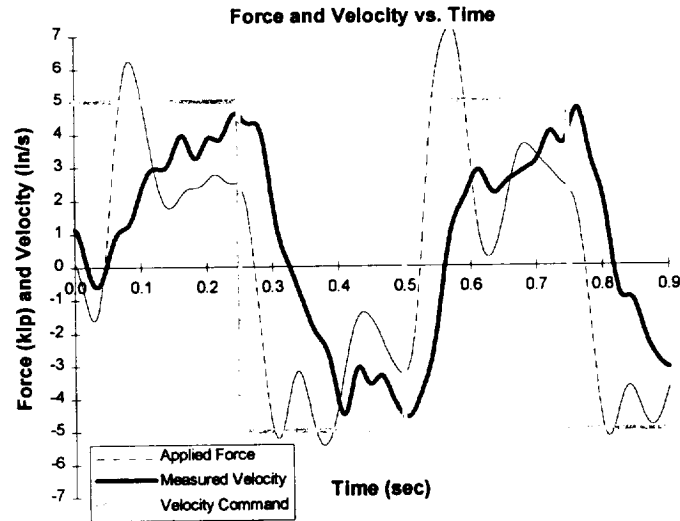


Fig. IV.4 - System Response to a 5 in/s, 2 Hz Square Wave, Velocity Command

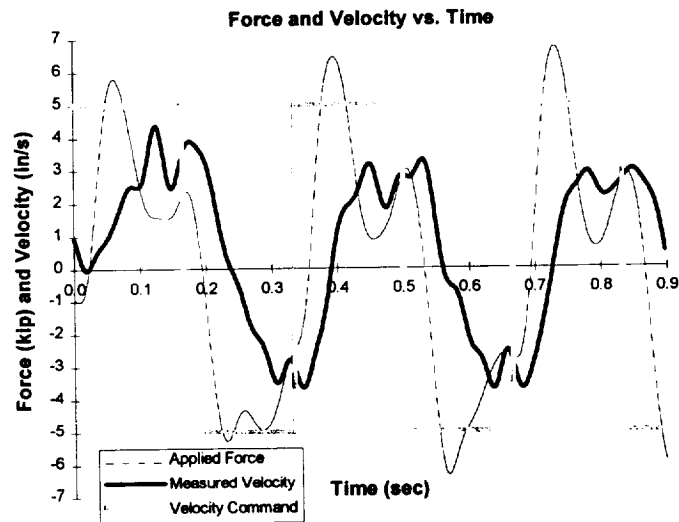


Fig. IV.5 - System Response to a 5 in/s, 3 Hz Square Wave, Velocity Command

IV.2. Dynamic Model Identification

As mentioned previously, in order to obtain an understanding of the behavior of the damping in the EMA system, many constant velocity tests were completed. The position plot in Figure IV.6 shows the raw and filtered position data corresponding to a negative 5 in/s velocity command. The data used to develop the friction model was taken from the end portions of the constant velocity tests, where the velocity has reached steady state.

The raw and filtered force data corresponding to the position data in Figure IV.6 is shown in Figure IV.7.

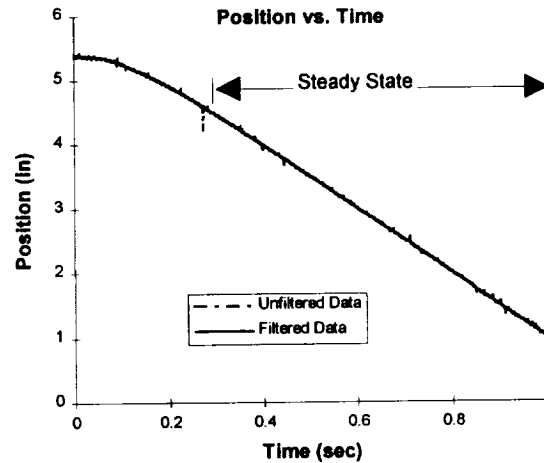


Fig. IV.6 - Position of the Roller Nut During a -5 in/s Velocity Move

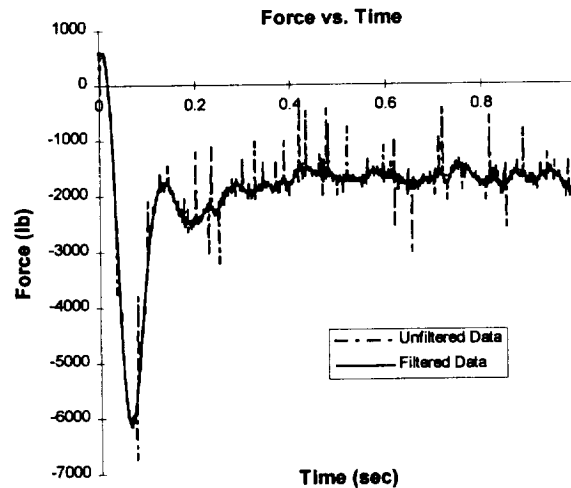


Fig. IV.7 - Force on the Roller Nut During a -5 in/s Velocity Move

The average force and velocity were found from the steady state data in each of the constant velocity tests. Then these steady state values were plotted against each other as shown in Figure IV.8. Several curve fits were experimented with in an attempt to find a mathematical expression for the relationship between the damping force and the velocity. It was found that a logarithmic function resulted in a fairly simple model with a good fit.

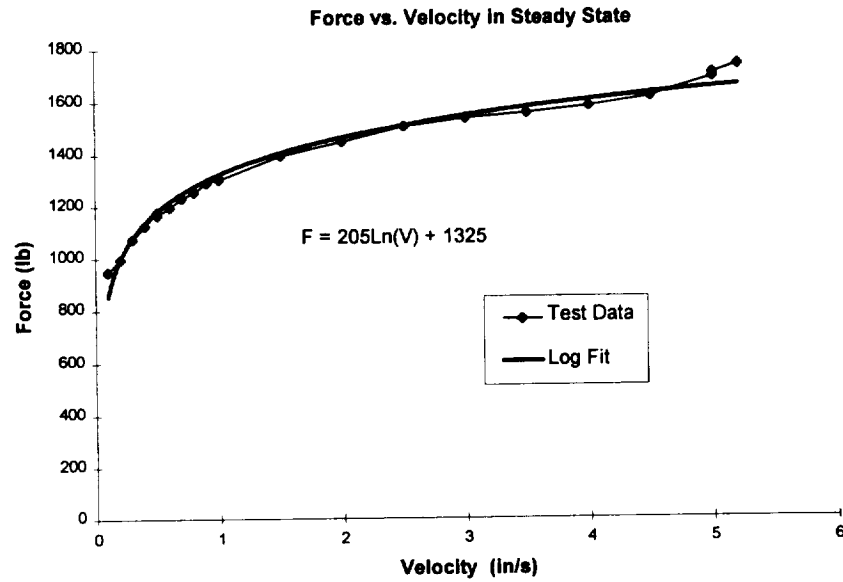


Fig. IV.8 - Force Applied to the Nut as a Function of Steady State Velocity

With an understanding of the damping force, an attempt at writing the differential equations that describe the system can be completed. The models that were used for the actuator are presented in Figure IV.9, equations (IV.1) and (IV.2), Figure IV.10 and equations (IV.3) and (IV.4).

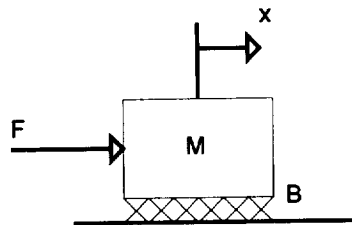


Fig. IV.9 - Rigid Body, 2nd Order Model

$$F = M \cdot \ddot{x} + B \cdot \dot{x} \dots\dots\dots(\text{IV.1})$$

$$F = M \cdot \ddot{x} + F_f \quad \text{where:} \quad F_f = \begin{cases} 0 & \text{for } \dot{x} < 0.001 \\ \text{sign}(\dot{x}) \cdot (b \cdot \ln(|\dot{x}|) + c) & \text{for } \dot{x} \geq 0.001 \end{cases} \dots\dots\dots(\text{IV.2})$$

$$\text{sign}(\dot{x}) = \begin{cases} 1 & \text{for } \dot{x} \geq 0 \\ -1 & \text{for } \dot{x} < 0 \end{cases}$$

Both a linear and a nonlinear rigid body model are presented above. Equation (IV.1) represents a typical linear model for the actuator and equation (IV.2) is basically the same model with a nonlinear damping force which is a logarithmic function of velocity. It is

important to note that this model is linear in the coefficients b and c . This is an important quality for a least squares model fit.

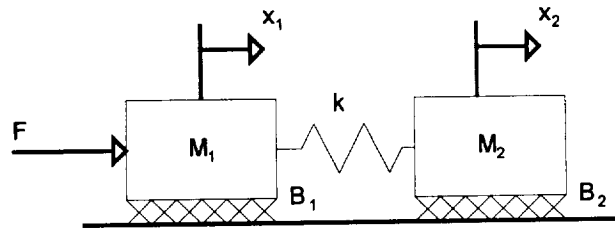


Fig. IV.10 - 4th Order Model

$$\begin{aligned} 1) \quad & F = M_1 \cdot \ddot{x}_1 + B_1 \cdot \dot{x}_1 + k \cdot (x_1 - x_2) \\ 2) \quad & 0 = M_2 \cdot \ddot{x}_2 + B_2 \cdot \dot{x}_2 + k \cdot (x_2 - x_1) \end{aligned} \quad \text{.....(IV.3)}$$

$$\begin{aligned} 1) \quad & F = M_1 \cdot \ddot{x}_1 + F_{fi} + k \cdot (x_1 - x_2) \\ 2) \quad & 0 = M_2 \cdot \ddot{x}_2 + F_{f2} + k \cdot (x_2 - x_1) \end{aligned} \quad \text{.....(IV.4)}$$

where:

$$F_{fi} = \begin{cases} 0 & \text{for } \dot{x}_i < 0.001 \\ \text{sign}(\dot{x}_i) \cdot (b_i \cdot \ln(|\dot{x}_i|) + c_i) & \text{for } \dot{x}_i \geq 0.001 \end{cases}$$

$$\text{sign}(\dot{x}_i) = \begin{cases} 1 & \text{for } \dot{x}_i \geq 0 \\ -1 & \text{for } \dot{x}_i < 0 \end{cases}$$

The models represented by equations (IV.3) and (IV.4) distribute the effective mass of the rigid body model between two locations separated by a spring. These models are important if the higher frequency oscillations in the velocity response of Figures IV.2 through IV.5 are to be accounted for. The spring in the model is due mainly to torsional wind-up of the roller screw. This means that the effective masses associated with M_1 would come from the nut, part of the inertia of the screw, and perhaps the bearings. The effective masses associated with M_2 would come from the gear reduction and motor. M_2 is by far the greater of the two effective masses.

IV.3. Parameter Estimation

Parameter estimation is a significant problem within the larger problem of system identification. After a parametric model has been identified, the problem of determining the coefficients for this model still remains. Parameter estimation is the determination, using experimental data, of the coefficients in the differential equation describing the system. For the EMA models described by equations (IV.1) and (IV.2), the results of parameter estimation are the coefficients M , B , b , and c .

There are many methods of performing parameter estimation. Some good texts that deal with parameter estimation methods are Ljung and Glad (1994), and Astrom and Wittenmark (1995), and Ljung (1987). Most of these methods utilize linear regression

models and least squares. Least squares is utilized in the system identification procedures described here. Least squares may be applied to any set of equations of the form:

$$\begin{aligned} Y_{(m \times 1)} &= \Phi_{(m \times n)} \cdot \theta_{(n \times 1)} \\ \text{where: } m &> n, \\ Y \text{ and } \Phi &\text{ are known,} \\ \theta &\text{ is to be determined} \end{aligned} \quad \text{.....(IV.5)}$$

For the parameter estimation problem, the vector Y and the matrix Φ in equation (IV.5) must be either measured variables or functions that can be calculated from the measured variables. The vector θ is the vector of parameters to be determined in the least squares sense. Φ is matrix formed using the regressors. Specifically, in the estimation problem, the regressors are those functions that are multiplied by the parameters in the differential equations. There are no restrictions in linear regression that the regressors be linear functions of the measured data, only that the equations are linear in the parameters to be determined.

Equation (IV.5) is the standard linear regression model that may be solved using the pseudo inverse matrix, Φ^* .

$$\Phi^* = (\Phi^T \Phi)^{-1} \Phi^T \quad \text{.....(IV.6)}$$

The least squares solution is found by multiplying the pseudo inverse by the known vector.

$$\hat{\theta} = \Phi^* Y \quad \text{.....(IV.7)}$$

If Φ is $m \times n$ and $m > n$, the pseudo-inverse solution for the parameters, $\hat{\theta}$, satisfies the following least squares condition:

$$\min_{\hat{\theta}} \|Y - \Phi \hat{\theta}\|^2 \quad \text{.....(IV.8)}$$

where $\|\cdot\|$ denotes the Euclidean norm.

The differential equations in model equations (IV.1) and (IV.2) are linear in the parameters. Therefore, a vector matrix equation in the form of equation (IV.5) may be found by writing the differential equation at the instants in time where the force and the derivatives of x are known from experimental measurement. For the linear model the elements of equation (IV.5) are:

$$\mathbf{Y} = \mathbf{F} = \begin{Bmatrix} F(1) \\ F(2) \\ \vdots \\ F(i) \\ \vdots \\ F(m) \end{Bmatrix} \quad \Phi = \begin{Bmatrix} \ddot{x}(1) & \dot{x}(1) \\ \ddot{x}(2) & \dot{x}(2) \\ \vdots & \vdots \\ \ddot{x}(i) & \dot{x}(i) \\ \vdots & \vdots \\ \ddot{x}(m) & \dot{x}(m) \end{Bmatrix} \quad \theta = \begin{Bmatrix} M \\ B \end{Bmatrix} \dots\dots\dots(\text{IV.9})$$

For the nonlinear model the elements of the equation (IV.5) are:

$$\mathbf{Y} = \mathbf{F} = \begin{Bmatrix} F(1) \\ F(2) \\ \vdots \\ F(i) \\ \vdots \\ F(m) \end{Bmatrix} \quad \Phi = \begin{Bmatrix} \ddot{x}(1) & \text{sign}(\dot{x}(1)) \cdot \ln(|\dot{x}(1)|) & \text{sign}(\dot{x}(1)) \\ \ddot{x}(2) & \text{sign}(\dot{x}(2)) \cdot \ln(|\dot{x}(2)|) & \text{sign}(\dot{x}(2)) \\ \vdots & \vdots & \vdots \\ \ddot{x}(i) & \text{sign}(\dot{x}(i)) \cdot \ln(|\dot{x}(i)|) & \text{sign}(\dot{x}(i)) \\ \vdots & \vdots & \vdots \\ \ddot{x}(m) & \text{sign}(\dot{x}(m)) \cdot \ln(|\dot{x}(m)|) & \text{sign}(\dot{x}(m)) \end{Bmatrix} \quad \theta = \begin{Bmatrix} M \\ b \\ c \end{Bmatrix} \dots\dots(\text{IV.10})$$

In equations (IV.9) and (IV.10) each row of \mathbf{F} and Φ correspond to one sample time at $t = t_i$, and m rows are formed for m samples used in the estimation calculation.

In equation (IV.8), it is seen that the least squares solution will minimize the 2-norm size for the vector of errors, $\mathbf{F} - \Phi\hat{\theta}$. In other words, the least squares solution for the model parameters, minimizes the size of the vector of errors between the measured force and the force calculated using the estimated parameters and the regressors (measured displacement, velocity, and acceleration).

The parameter estimation method described above is applicable to continuous time, linear and nonlinear differential models. The only restriction is that the model be linear in the parameters. There is a source of error in the method that is caused by the need to numerically calculate two derivatives of the position measurement, x , at each sample time. This calculation will amplify the high frequency content of x , which is often associated with noise. There are two possible solutions to this problem: 1) directly measure the acceleration with an accelerometer and the velocity with a velocity sensor, or 2) filter the position data before the derivative is calculated. The least desirable, but most cost effective method, method 2), was employed here.

The most common estimation methods use auto-regressive and/or discrete time models. While these methods are perhaps the simplest to use, their application is restrictive in the types of systems to which they apply. In the auto-regressive model the regressors are linear functions of the measured inputs and outputs of the system (Ljung and Glad, 1994, pg. 233). While the discrete time models are in general, not restricted to linear regressors, it is difficult to describe the nonlinearities in discrete time. Nonlinearities are usually best described in continuous time, and are not easily transformed to and from discrete time as are linear models such as transfer functions.

The basic process used in the parameter estimation is outlined below.

1. Excite the system with a dynamic input force, while recording the output of the position sensor, the LVDT, and the output of the force sensor, the load cell.
 - The force is generated using a velocity profile command, a position control loop, and the hydraulic system.
2. Post-process the recorded data.
 - First the position and force are calculated from the outputs of the sensors. Then this calculated position and force is filtered with a 12 pole filter with no phase shift. Finally, the first and second order derivatives of the position are calculated numerically to find velocity and acceleration.
3. Solve a set of equations, using the least squares method, to estimate the parameters.
 - In most cases a set of about 800 equations are formed using 800 samples, out of 1000 recorded, from a data set of one second duration, with a sample frequency of 1 kHz. Only 800 equations are formed to eliminate the data on either end of the set, which has undesirable end effects caused filtration and differentiation.
4. Attempt to validate the model.
 - This is done by comparing the estimated force to the measured force. The estimated force is calculated with the estimated parameters and the regressors.
 - It is also done by simulating the estimated model using the measured force from other data sets as the input to the model.

Many passes at the estimation procedure described above were performed using several different sets of data, several slight model variations, and several different cutoff frequencies for the filters. In each case the models were validated using the methods described in step 4 above. The following is a presentation of the results of one the best estimation passes, as determined by validation, and a discussion of the affects of variations.

The results of the parameter estimation for one pass of the procedure described above are presented in below in Table IV.1.

**Table IV.1 - Parameter Estimation Results using the 2 Hz
Square Wave Data Set with a 15 Hz Data Filter**

<i>2nd Order Linear Model</i>		<i>2nd Order Nonlinear Model</i>	
M	60 lb·s ² / in	M	58 lb·s ² / in
B	580 lb·s / in	b	502 lb
-----	-----	c	1354 lb

The data in Table IV.1 corresponds to a parameter estimation for the models in equations (IV.1) and (IV.2) using the raw data from Figure IV.4. The raw position and force that is shown filtered with a 25 Hz filter in Figure IV.4, were filtered with a 12 pole, 15 Hz, zero phase shift, low pass filter before differentiation and estimation. It was found, through

experimentation that, a 15 Hz filter would filter out the majority of the velocity oscillations that were assumed to be caused by the distribution of the parameters.

Figure IV.11 shows the estimated force found by calculating the right hand side of equations (IV.1) and (IV.2) using the estimated parameters and the acceleration and velocity used in parameter estimation. It also shows the measured force used in estimation. Neither the linear nor the nonlinear models are significantly better. The overall shape seems to be good in general. The excursions might be accounted for by using a higher order model and data from collocated sensors, which were not available in the setup for the testing performed.

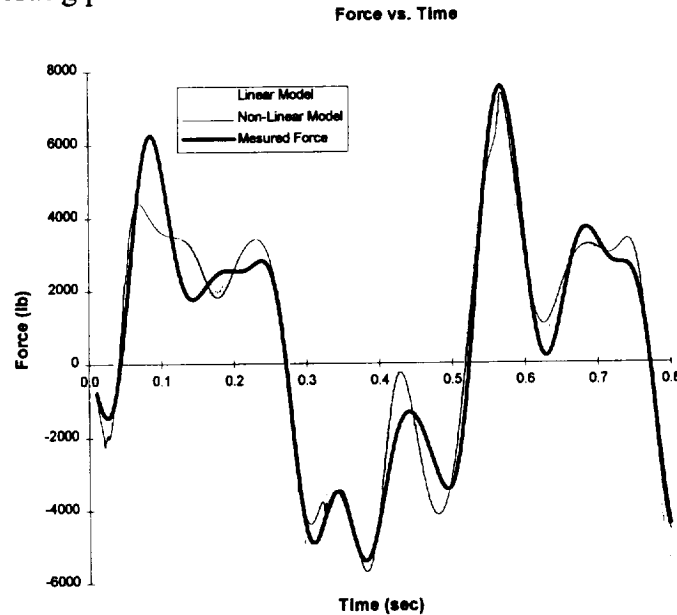


Fig. IV.11 - Estimated Force and Measured Force Comparison

If a data filter with a higher cutoff frequency is used then the velocity and acceleration have larger and higher frequency oscillations, giving rise to larger variations between the estimated force and the measured force. If a lower cutoff frequency is used then estimation results in a large mass value. This may be caused by attenuation of the rigid body acceleration which is found by calculating a second derivative of the position data. In general choosing the cutoff frequency for the data filter represents a trade off between filtering out the distributed parameter dynamics and the noise, and in the retention of information describing the rigid body motion of the system.

The models represented by equations (IV.1) and (IV.2) and the parameters in Table IV.1, result in fair simulation results as will be seen in the next section of this report. The masses found with estimation are somewhat different from that estimated with calculations in the Appendix A, $51 \text{ lb} \cdot \text{s}^2 / \text{in}$, but are reasonable values.

The model shown in Figure IV.10 is a higher order model for which the parameters could not be estimated with least squares. The reason for this is that the position variable, x_2 , was not measured in the data acquisition process. Therefore, the parameters for this model were estimated by trial and error. Initial guesses at the parameter values were obtained with rough inertia and rough spring constant calculations, and by distributing the

parameters of the rigid body model. The model was developed using simulations of the system with a force input from one of the data sets in Figures IV.2 through IV.5. The output of the model, the velocity of M_1 , was compared with the measured velocity of the nut. The parameters were then modified based on the differences between the simulated velocity and the measured velocity. The parameters resulting from this procedure are given in Table IV.2.

Table IV.2 - Trial and Error Parameter Estimation Results for the 4th Order Models

<i>4th Order Linear Model</i>		<i>4th Order Nonlinear Model</i>	
k	150,000 lb/in	k	150,000 lb/in
M_1	$6 \text{ lb} \cdot \text{s}^2 / \text{in}$	M_1	$6 \text{ lb} \cdot \text{s}^2 / \text{in}$
B_1	$180 \text{ lb} \cdot \text{s} / \text{in}$	b_1	100 lb
M_2	$66 \text{ lb} \cdot \text{s}^2 / \text{in}$	c_1	700 lb
B_2	$180 \text{ lb} \cdot \text{s} / \text{in}$	M_2	$66 \text{ lb} \cdot \text{s}^2 / \text{in}$
-----	-----	b_2	95 lb
-----	-----	c_2	667 lb

IV.4. Model Validation/Simulation Results

In order to validate the model parameters given in Table IV.1, simulations were performed using the measured forces from all of the data sets in Figures IV.2 through IV.5. The linear and the nonlinear model were simulated simultaneously with the same force input. The outputs of the models are compared to the measured velocity of the nut in Figures IV.12 through IV.15.

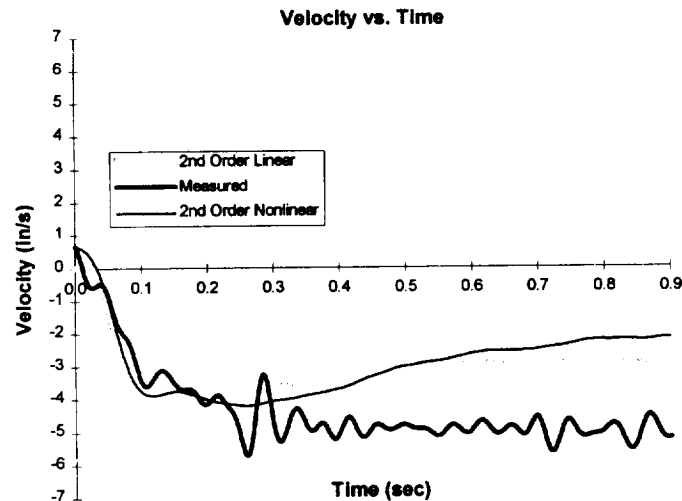


Fig. IV.12 - Simulated Velocity Using the Least Squares Models with the Force from the -5 in/s Constant Velocity Command

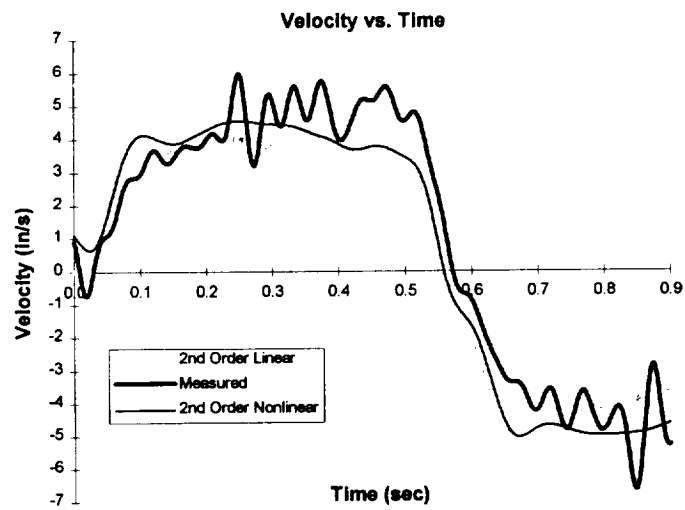


Fig. IV.13 - Simulated Velocity Using the Least Squares Models with the Force from the 5 in/s, 1 Hz Square Wave, Velocity Command

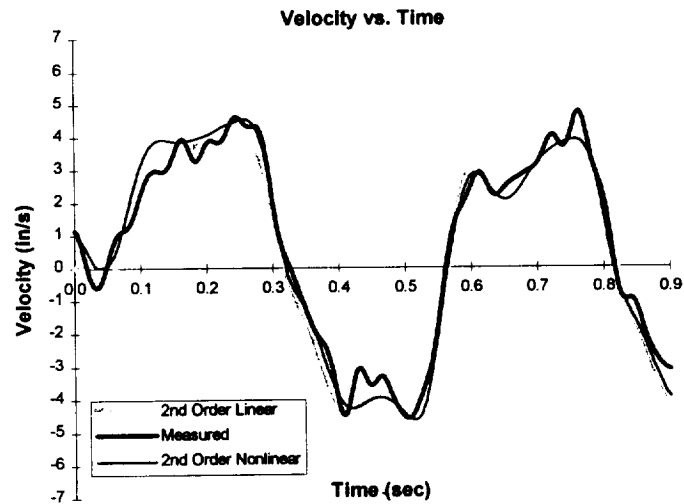


Fig. IV.14 - Simulated Velocity Using the Least Squares Models with the Force from the 5 in/s, 2 Hz Square Wave, Velocity Command

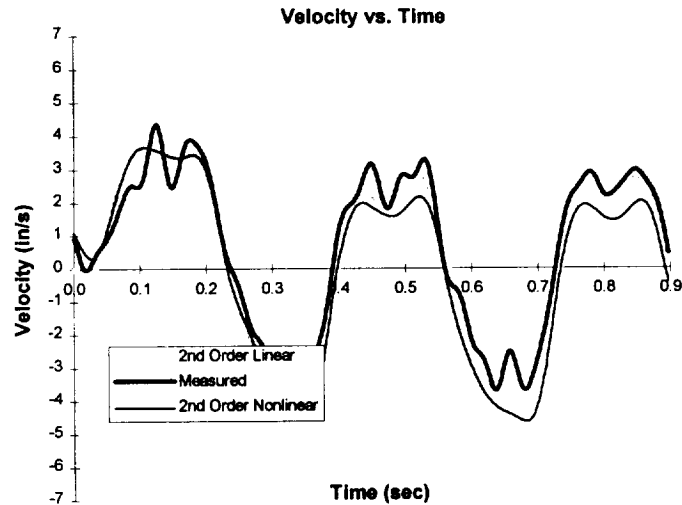


Fig. IV.15 - Simulated Velocity Using the Least Squares Models with the Force from the 5 in/s, 3 Hz Square Wave, Velocity Command

It is obvious from the previous figures that the best match between the measured and simulated velocities is for the 2 Hz square wave data. This is expected since the parameter estimation was performed using this data. One obvious problem with the models is the large error in the steady state velocity to the approximately constant force input. This is shown in Figure IV.12. A very good steady state response is obtained by estimating the parameters using the constant velocity data set. It is also possible to achieve a compromise between the steady state response and the dynamic response by estimating the parameters with a data set containing some of both.

From the previous four figures it is difficult to state that either the linear or the nonlinear model is a better match. Both models follow the rigid body trajectories fairly well. Neither, however, capture any of the higher frequency oscillations which are probably the effects of unmodeled disturbances and a system that might best be modeled with a higher order model.

To demonstrate that a higher order model might better capture the complete behavior of the EMA system, the 4th order trial and error model was estimated. This model was simulated using the same four input forces that were used in the simulation of the rigid body models. The results of these simulations are demonstrated in the following four figures.

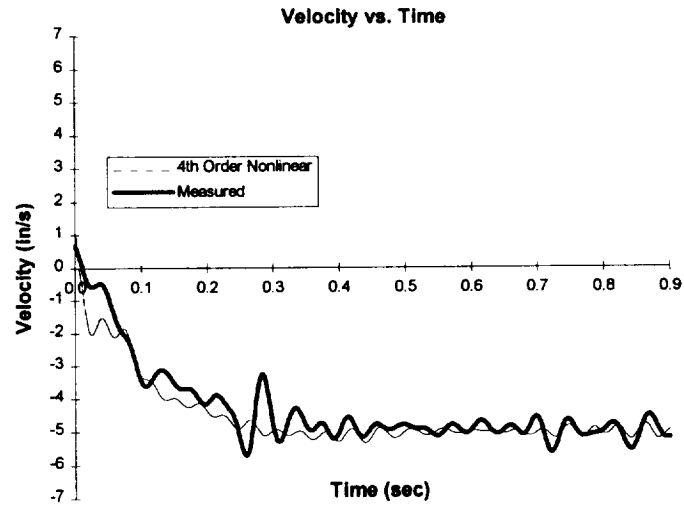


Fig. IV.16 - Simulated Velocity Using the Trial and Error Model with the Force from the -5 in/s Constant Velocity Command

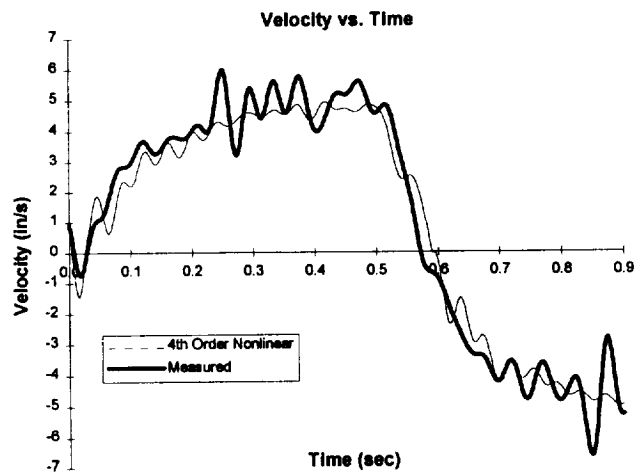


Fig. IV.17 - Simulated Velocity Using the Trial and Error Model with the Force from the 5 in/s, 1 Hz Square Wave, Velocity Command

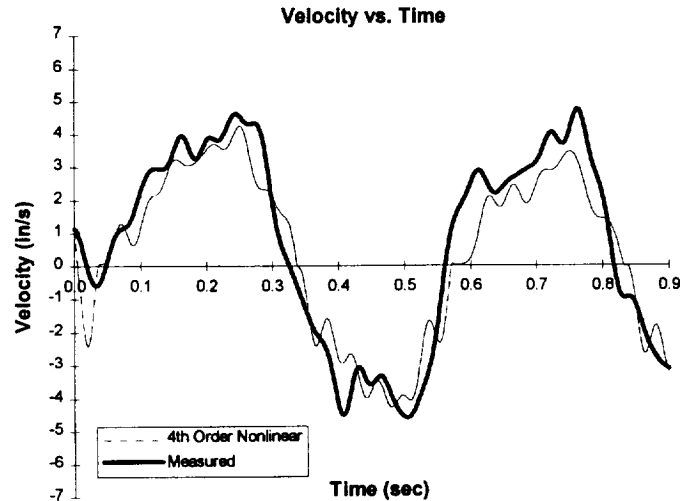


Fig. IV.18 - Simulated Velocity Using the Trial and Error Model with the Force from the 5 in/s, 2 Hz Square Wave, Velocity Command

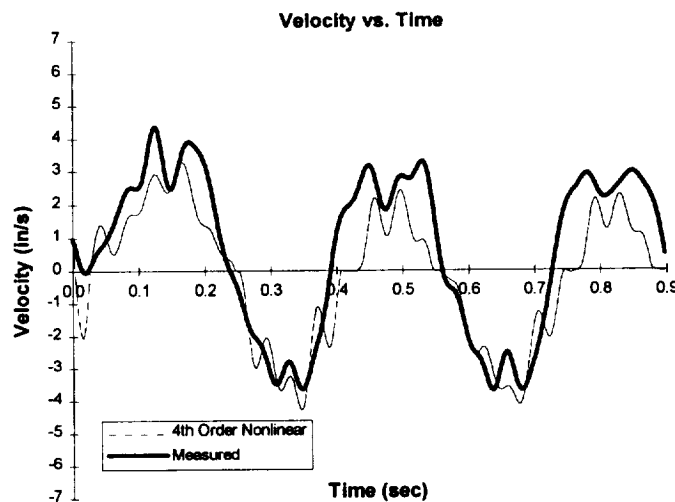


Fig. IV.19 - Simulated Velocity Using the Trial and Error Model with the Force from the 5 in/s, 3 Hz Square Wave, Velocity Command

As seen in the previous four figures the higher order model does capture some of the higher frequency oscillatory behavior. The simulated response and the measured response match very well for the constant velocity and the 1Hz data. This would be expected since the trial and error estimation process mainly involved these two data sets. In Figures IV.18 and IV.19 there is a distinct difference between the simulated response and the measured response in the regions where the velocity is near zero. A better match between the behavior of the real system and the system response should be obtainable using a least squares estimation rather than the trial and error method. This requires a measurement of the position of the motor along with the measurement of the position of the nut.

IV.5. References

Ljung, L. , Glad, T., *Modeling of Dynamic Systems*, ISBN 0-13-597097-0, Prentice-Hall, 1994.

Astrom, K.J., Wittenmark, B., *Adaptive Control, 2nd Edition*, ISBN 0-201-55866-1, Addison-Wesley, 1995.

Ljung, L. , Glad, T., *System Identification, Theory for the User*, ISBN 0-13-881640-9, Prentice-Hall, 1987.

V. MODEL SIGNIFICANCE

The significance of the estimated models is best demonstrated by considering the actuator in an application, and by considering the purpose of a model. In application there will be a significant load attached to the nut of the actuator and an actuation force, motor torque, will be applied at the motor side of the model. The load may experience large disturbance forces. The purpose of the actuator model is controller design and performance analysis of the actuator as it is used in an application.

V.1. Closed Loop Actuator-Load System

In the test setup used for system identification, the most significant mass, M_2 , is at the far end of the spring from the applied force. Therefore the effects of the spring are apparent in the test data. In application however, the motor will be used to develop the actuation forces. One might make the mistake of assuming that the spring constant is not important due to the size of the mass, M_1 . But the actuator will probably be driving a very significant load, like the Space Shuttle Main Engine (SSME) for example. Therefore, the forces applied at the nut will still be significant, and the effects of the spring in the higher order model may be profound.

For the purposes of this discussion the actuator is considered part of a closed loop control system with a large mass attached to the nut. Linear models are used for the actuator. An actuation force, the motor torque, is generated using a proportional-derivative controller. The dynamics of the motor controller are considered fast, and are ignored. The value for the load mass used, is that given for the equivalent mass of the SSME in Lominick (1973), $54.53 \text{ lb} \cdot \text{s}^2 / \text{in}$. Figures V.1 and V.2 show this system with a rigid body model for the actuator.

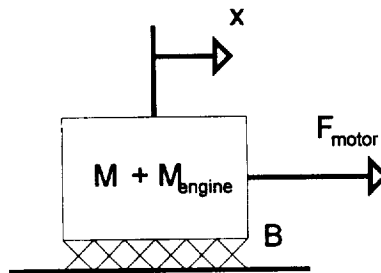


Fig. V.1 - Rigid Body Model of the Actuator and Load

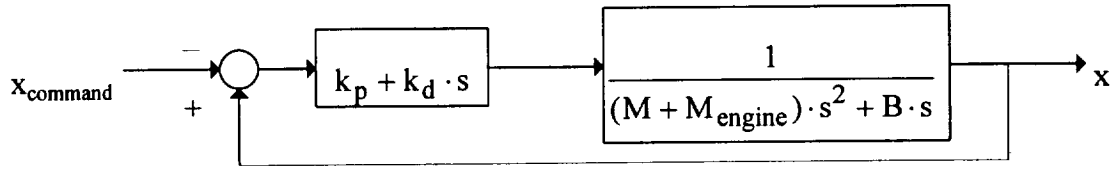


Fig. V.2 - Closed Loop Block Diagram with the Rigid Body Model

If the distributed mass model for the actuator is used, two very different models result, depending on whether the displacement used for the feedback is measured at the motor or at the end of the actuator. Figure V.3 shows the mechanical model for the distributed mass actuator and load. Figures V.4 and V.5 show the closed loop block diagrams for the two different closed loop systems.

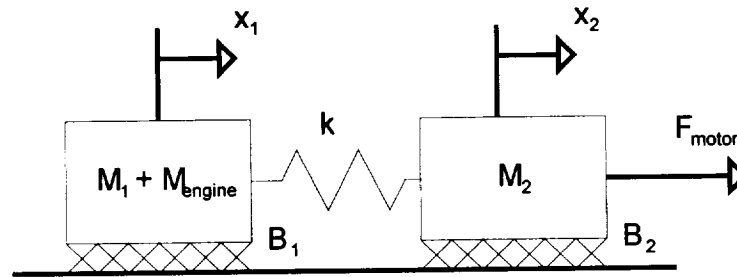


Fig. V.3 - Distributed Mass Model of the Actuator and Load

The following two polynomials are defined to simplify the representation of the actuator's transfer function:

$$\Delta(s) = M_t M_2 s^4 + (M_t B_2 + M_2 B_1) s^3 + (k(M_t + M_2) + B_1 B_2) s^2 + k(B_1 + B_2) s$$

$$A(s) = (M_t s^2 + B_1 s + k) \quad \text{.....(V.1)}$$

where: $M_t = M_1 + M_{\text{engine}}$

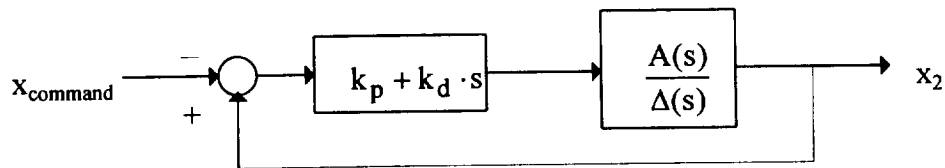


Fig. V.4 - Closed Loop Block Diagram with the Distributed Mass Model and Feedback of the Motor Position

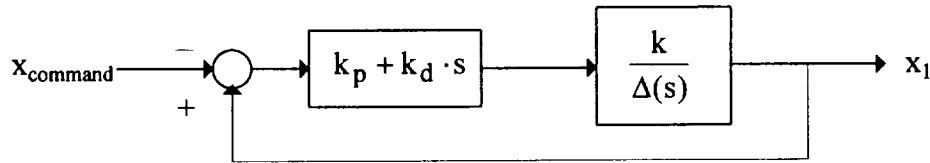


Fig. V.5 - Closed Loop Block Diagram with the Distributed Mass Model and Feedback of the End of Actuator Position

The closed loop system in Figure V.2 has one zero and two poles. Using the parameter values for the linear system from Table IV.1, the controller gains may be chosen using some design criteria. If the controller gains are chosen such that the two resulting poles have a 10 Hz bandwidth and a 0.707 damping ratio, the following system results:

Controller Gains: $K_p = 452000$, $K_d = 9595$

Closed Loop Zeros: $s = -47.1$

Closed Loop Poles: $s = -44.4 \pm 44.4i$

The 10 Hz bandwidth designed for is good only for "small signal" analysis. Some rough calculations are discussed here to determine how reasonable this design is in terms of the control authority needed. Suppose that a 10 Hz, sinusoidal, position profile with an amplitude, A , in inches, is to be generated. The maximum velocity due to this sinusoid is $A \cdot (2 \cdot \pi \cdot 10)$ in / s and the maximum acceleration is $A \cdot (2 \cdot \pi \cdot 10)^2$ in / s². The force required at the maximum velocity is $B \cdot \dot{x} = B \cdot A \cdot (2 \cdot \pi \cdot 10)$ lb. The force required at the maximum acceleration is $M \cdot \ddot{x} = M \cdot A \cdot (2 \cdot \pi \cdot 10)^2$ lb. Knowing the maximum torque of the motor (1150 in · lb) and the gear ratio between translation and rotation, the maximum value of the amplitude, A , can be found at which the motor will saturate. From the maximum velocity,

$$A_{\max} = \frac{1150 \text{ in} \cdot \text{lb}}{(0.03133 \text{ in} / \text{rad}) \cdot (580 \text{ lb} \cdot \text{s} / \text{in}) \cdot (2 \cdot \pi \cdot 10 \text{ rad} / \text{s})} = 1 \text{ in}.$$

From the maximum acceleration,

$$A_{\max} = \frac{1150 \text{ in} \cdot \text{lb}}{(0.03133 \text{ in} / \text{rad}) \cdot (114.5 \text{ lb} \cdot \text{s}^2 / \text{in}) \cdot ((2 \cdot \pi \cdot 10)^2 \text{ rad} / \text{s}^2)} = 0.08 \text{ in}.$$

The maximum amplitude is determined by the acceleration force. If the maximum torque allowed for the calculations above, is derated to the continuous torque of the motor then the amplitude will be about one third of this value. An amplitude of 0.08 inches may seem small, but at the motor this amplitude corresponds to about 145 degrees of rotation.

If the same controller gains found for the rigid body model are used for the distributed mass models then one system similar to the rigid body system results, and one very different system results. The closed loop system with position feedback from the motor has the following poles and zeros:

Closed Loop Zeros: $s = -47.1, -1.49 \pm 49.8i$

Closed Loop Poles: $s = -69.0 \pm 58.2i, -6.55 \pm 45.2i$

This system is similar to the rigid body model. Two of the poles are near those of the rigid body system. The other two poles are near the two complex zeros, which will somewhat cancel their effects. The similarity is best seen in the magnitude and phase plots for these two systems which are shown in Figure V.6. Although these two systems are similar, consideration of the spring constant is important, especially in the actual system where the spring constant changes with time as the nut travels along the screw.

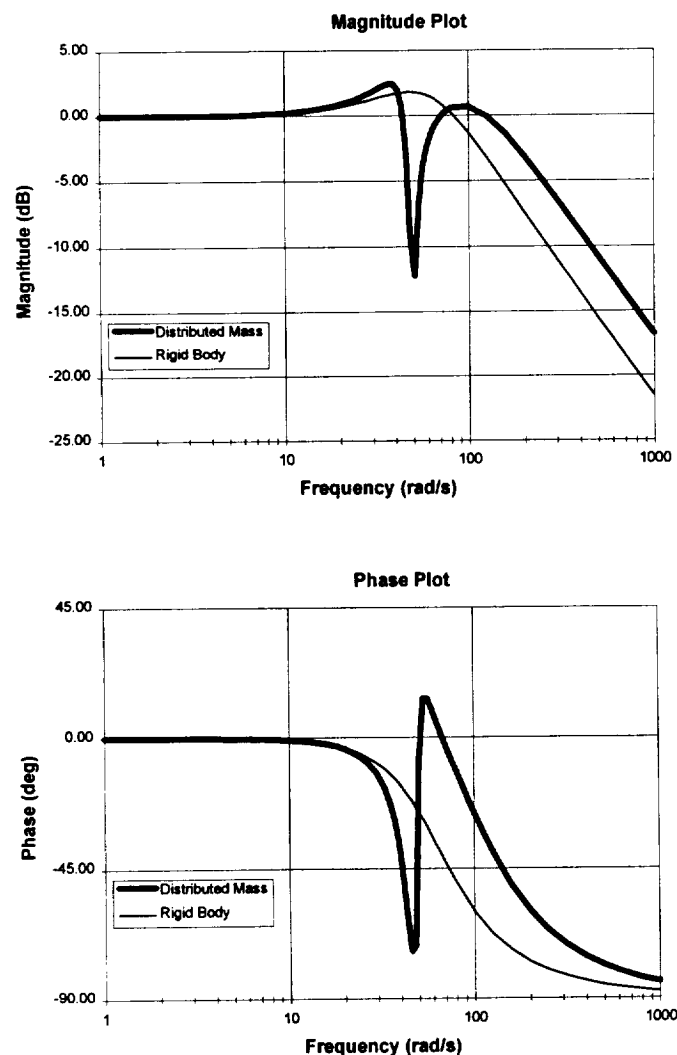


Fig. V.6 - Magnitude and Phase Plots for the Two Closed Loop Systems: the Rigid Body System and the Distributed Mass System with Motor Position Feedback

The last system that is discussed here is the one with the distributed mass model and position feedback from the end of the actuator. This closed loop system is shown in Figure V.5. If the same controller gains found for the rigid body model are used in this model a very different system results. The closed loop poles and zeros are:

Closed Loop Zeros: $s = -47.1$

Closed Loop Poles: $s = -36.3 \pm 31.8i, 33.5 \pm 78.6i$

There are two poles that are well into the right half plane. The root locus plots for this system show that the two purely imaginary poles created in the open loop system, by the addition of the spring, will move into the RHP for any proportional derivative gain set in the closed loop system. In the real system, the two open loop poles will be lightly damped, and there will be some range of gains for which this system is stable. Also, if the spring constant is increased, these two poles move away from the origin and have further to travel to get to the right half plane given the same damping ratio.

In general, as would be expected, the two open loop poles created by the addition of the spring to the model become less significant as the spring constant is raised. The farther they are from the origin the smaller their residues become. However, it has been shown here that the spring constant related to windup of the screw in this actuator, is low enough that it warrants careful consideration in controller design and in the performance analysis of the system. While it would be best to measure the position of the load directly, in terms of the accuracy of the control system, this is very dangerous in closed loop control with this type of actuator. Some type of dynamic compensation should be added to the controller if this type of feedback is to be used.

V.2. Effects of Engine Startup Transient Loads in the Closed Loop Actuator-Load System

This section of the report addresses the question of what forces might be expected on the screw of the actuator during engine start up and shut down. In order to address this a model of the engine and stiff arm system is compared to a closed loop engine and actuator system.

The loads that were applied to the roller screw during the dynamic load tests described in Chapter III are comparable to those measured in the NASA stiff arm, engine start and shutdown tests, TTB050 through TTB054. A stiff arm was used in place of the thrust vector control (TVC) actuator during these tests. A simple model for the stiff arm and engine system is shown below in Figure V.7. The forcing function is that exerted on the engine during start up and shut down, which is not explicitly known. The engine mass in this model is Lominick's equivalent engine mass. The spring constant for the stiff arm can be estimated from data in Laszar (1995). Using the data in this correspondence the lowest possible the spring constant was found to be about 175000 lb/in. The lowest value was chosen because the force on the spring in the model below will be smaller at high frequencies for lower spring constants.

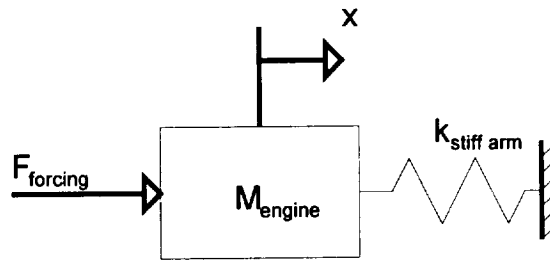


Fig. V.7 - System Model For the Stiff Arm Tests

The force on the stiff arm is the force exerted on the spring in Figure V.7. It is strictly a function of the forcing function on the engine for this model. The transfer function representing this relationship is given in Equation V.2 below. Using Lominick's equivalent engine mass and the spring constant of the stiff arm this transfer function can be evaluated. In Figure V.9 the magnitude ratio for this transfer function is plotted.

$$\frac{F_{\text{stiff arm}}(s)}{F_{\text{forcing}}(s)} = \frac{k_{\text{stiff arm}}}{M_{\text{engine}}s^2 + k_{\text{stiff arm}}} \dots\dots\dots (V.2)$$

Again, as for the closed loop controller discussion in the previous section of this chapter, the actuator is considered part of a closed loop system with the engine mass attached to the nut. The distributed mass, linear model with motor position feedback is used for the actuator. The parameters values for this model are given in Table IV.2. An actuation force, the motor torque, is generated using a proportional-derivative controller. The dynamics of the motor controller are considered fast, and are ignored. If the position command to the controller is constant then the model in Figure V.8 applies. With the constant command proportional control and derivative control are equivalent to a spring and a damper, respectively.

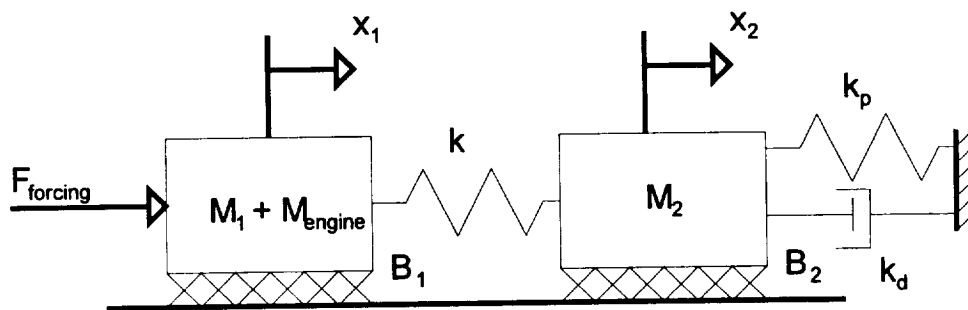


Fig. V.8 - Closed Loop Actuator Load System with a Constant Position Command, and a Proportional Derivative Controller Using Motor Position Feedback.

The force on the screw is the force exerted on the spring in Figure V.8. It is strictly a function of the forcing function on the engine for this model. The transfer function representing this relationship is given in Equation V.3 below.

$$\frac{F_{\text{screw}}(s)}{F_{\text{forcing}}(s)} = \frac{N(s)}{\Delta_2(s)}$$

where:

$$N(s) = k(M_2 s^2 + (B_2 + k_d)s + k_p) \quad \dots\dots\dots (V.3)$$

$$\Delta_2(s) = M_t M_2 s^4 + (M_t(B_2 + k_d) + M_2 B_1)s^3 + (M_t(k + k_p) + M_2 k + B_1(B_2 + k_d))s^2 + (B_1(k + k_p) + (B_2 + k_d)k)s + k k_p$$

$$M_t = M_1 + M_{\text{engine}}$$

The controller gains are again chosen, as in the previous section, using the rigid body model in Figure V.2 and the data for linear system in Table IV.1. If the controller gains are chosen such that the two resulting poles, in the rigid body system, have 1 Hz, 10 Hz, and 100 Hz bandwidths and a 0.707 damping ratio, then following three sets of controller gains result:

$$1 \text{ Hz Closed Loop Bandwidth: } K_p = 4520, \quad K_d = 438$$

$$10 \text{ Hz Closed Loop Bandwidth: } K_p = 452000, \quad K_d = 9595$$

$$100 \text{ Hz Closed Loop Bandwidth: } K_p = 45200000, \quad K_d = 101200$$

Using the controller gains above, the data for the distributed mass, linear actuator system in Table IV.2, and the Lominick's equivalent engine mass the transfer function in Equation V.3 can be evaluated. In Figure V.9, the magnitude ratios for this transfer function, with the three different sets of controller gains, are plotted along with the magnitude ratio of the stiff arm system.

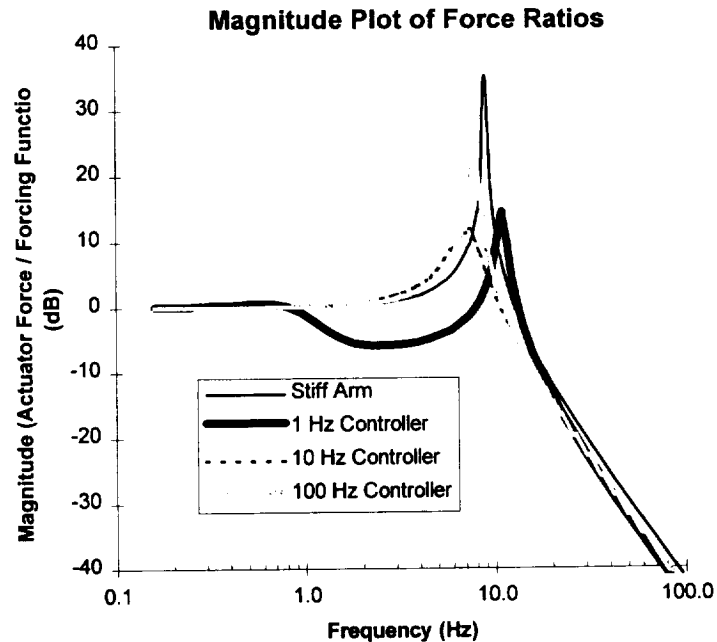


Fig. V.9 - Magnitude Ratios for the Stiff Arm System and Three Closed Loop Actuator Load Systems

The magnitude plots above demonstrate that the forces that can be expected on the actuator are very comparable to that measured by the stiff arm. The resonant peaks for all four systems are quite high. In reality these peaks will probably be limited somewhat due to unmodelled damping. The different controller gains did not affect these magnitude ratios as much as one might have expected. This is due to the large equivalent mass at the motor end of the actuator, representing a large impedance that is independent of the controller gains. The reason that the plots for the actuator systems are so similar to that for the stiff arm is that the spring constant of the screw is similar to that of the stiff arm. A low spring constant for the screw, while presenting difficulties in controller design, may be beneficial in terms of the reducing the transient loads exerted on the screw.

If a stiffer screw is used then more of the energy in the forcing function will be transferred to the screw. For a stiffer screw the magnitude plots for the actuator systems in Figure V.9 would have higher cutoff frequencies. In this case it would be difficult to predict the forces on the screw using the data from the stiff arm tests since the stiff arm may not have measured the higher frequency content of the forcing function. It should be noted here that the stiffness of the screw is actually a function of the location of the nut on the screw.

As a final note, the resonant frequency of the stiff arm model should be discussed. It is suspiciously close to the fundamental frequencies of the forces in the stiff arm data in the TTB tests. In fact, it falls almost exactly in the middle of the 6 to 10 Hz range in these tests. It therefore may be a poor assumption to say that the forcing function during engine start up and shut down has a more significant content at this frequency than at any other.

V.3. References

Lominick, J. L., "Design and Optimization of SSME TVC System," NASA correspondence from J. L. Lominick to Mr. Cornelius, October 17, 1973.

Laszar, "Engine Stiff Arm Modeling Information," NASA correspondence from Mr. Laszar to Ms. Weir, February 8, 1995.

VI. OPTIMAL COMPONENT SELECTION FOR ELECTROMECHANICAL ACTUATION

VI.1. Introduction

To achieve an optimal design for any electromechanical actuator, the individual components of the actuator must be properly selected with respect to one another. Here, the definition of optimality involves three basic issues:

- 1) power transfer to the load,
- 2) efficiency, and
- 3) torque requirements.

Clearly, with these three considerations, optimality is found by maximizing efficiency and power transfer to the load while minimizing torque requirements. This report chapter contains the appropriate analyses for component selection, based on component parameters. The analyses are based on a sinusoidal actuator velocity profile.

The ultimate objective for any actuator is to provide power to a load. Hence, maximum power transfer to the load is the primary optimization objective. Efficiency and torque requirement issues are secondary. Thus, guidelines for maximum power transfer are developed, and the impact of these guidelines on efficiency and torque requirements are explored.

VI.2. Nomenclature

n_m	number of motors	m_{noz}	nozzle assembly equivalent mass
b_m	motor viscous damping	k_{noz}	nozzle assembly spring constant
J_m	motor rotor moment of inertia	ω	angular frequency of excitation
T_{dev}	motor developed torque	$\dot{\theta}_m$	angular velocity of the motor rotor
N_g	gear ratio	$\dot{\theta}_s$	angular velocity of the screw shaft
b_g	gearhead viscous damping referred to the output side	v_{nut}	translational velocity of the nut
J_g	gearhead moment of inertia referred to the output side	P_h	screw pitch
b_s	screw shaft viscous damping	P_L	load power
J_s	screw shaft moment of inertia	η	efficiency
m_{nut}	nut mass		
b_{noz}	nozzle assembly viscous damping		

VI.3. System Definition and Analysis Description

Within this section, the system under analysis is defined. A system model is developed and converted to an equivalent electric circuit, and the analysis procedure employed to determine the criteria for an optimal design is presented.

VI.3.1. Actuator Model

The actuator under consideration for this study is simply illustrated in Figure VI.1. Note that the system is composed of an arbitrary number of motors, a gearhead, and a roller or ball screw. Each motor, the gearhead, and the screw shaft are rotational components and can each be modeled by a moment of inertia and a viscous damping coefficient. In addition, the motor contains a torque source, and the gearhead contains a velocity scaling dependent on the gear ratio. The nut is a translational system and modeled by an equivalent mass. Note that translational damping can be equivalently lumped with the viscous damping on the screw shaft. The scaling from rotary shaft motion to linear nut motion is defined by the screw lead.

The differential equation for motion of the motor rotor is presented in (VI.1). The gearhead motion is described by the differential equation provided in (VI.2). Screw shaft and nut motion are both governed by the differential equation presented in (VI.3).

$$n_m T_{dev} - n_m T_{m,out} = n_m J_m \frac{d\dot{\theta}_m}{dt} + n_m b_m \dot{\theta}_m \dots\dots\dots(VI.1)$$

$$\frac{1}{N_g} T_{m,out} = T_{g,out} + J_g \frac{d\dot{\theta}_s}{dt} + b_g \dot{\theta}_s \dots\dots\dots(VI.2)$$

$$T_{g,out} = P_h \left(F_{act} - F_{load} + m_{nut} \frac{dv_{nut}}{dt} \right) + J_s \frac{d\dot{\theta}_s}{dt} + b_s \dot{\theta}_s \dots\dots\dots(VI.3)$$

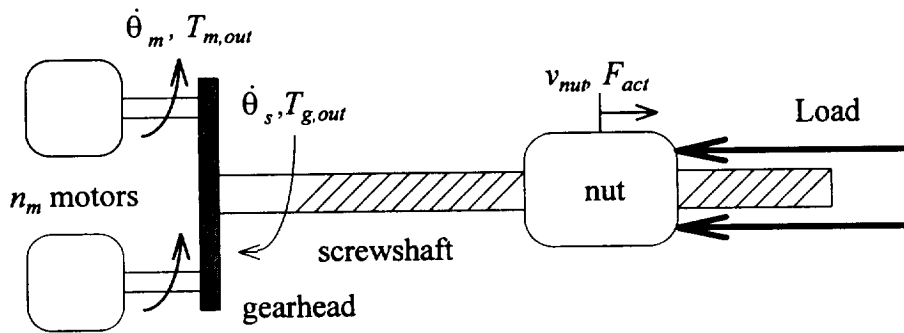


Fig. VI.1 - Actuator Schematic

VI.3.2. Load Models

Models for active and passive loads will be developed within this section. Consideration of both load types increases the general applicability of the design optimization methods presented herein.

VI.3.2.1. Passive

Passive loads are defined as those loads which impose no active force on the actuator. Hence, they are purely mass, spring, and damper systems as illustrated in Figure VI.2. The differential equation governing translational motion of the load is presented in (VI.4).

$$F_{act} = m_{noz} \frac{dv_{mut}}{dt} + b_{noz} v_{mut} + k_{noz} \int v_{mut} dt \dots\dots\dots(VI.4)$$

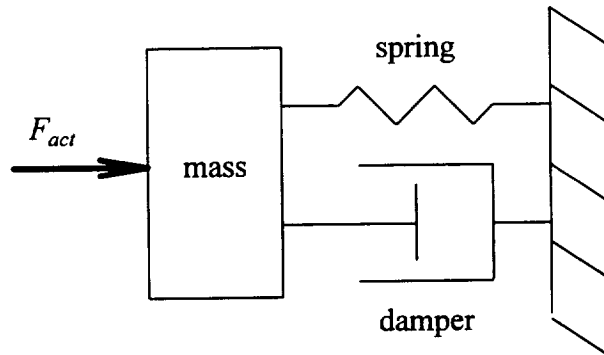


Fig. VI.2 - Passive Load Schematic

VI.3.2.2. Active

Active loads are loads which provide an active force on the actuator, as illustrated in Figure VI.3. This is the case in the thrust vector control application where acceleration and engine thrust must be borne by the actuator. In such a case, the load will contain an active force source in addition to a mass, spring constant, and damping coefficient. The mathematical model of this case is described by the differential equation in (VI.5).

$$F_{act} - F_{load} = m_{noz} \frac{dv_{mut}}{dt} + b_{noz} v_{mut} + k_{noz} \int v_{mut} dt \dots\dots\dots(VI.5)$$

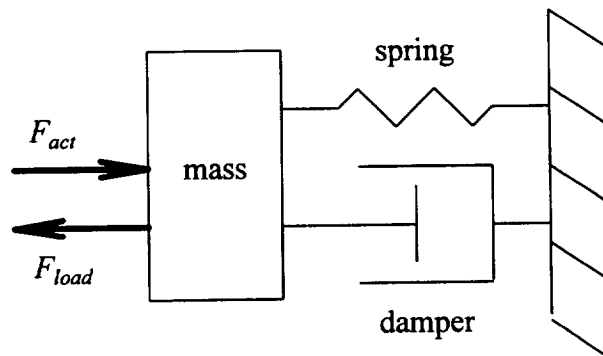


Fig. VI.3 - Active Load Schematic

VI.3.3. Equivalent Circuit

The load models above can be represented by an equivalent electrical circuit. In order to do so, we must define all analogous mechanical and electrical variables. We select voltage (v) to be analogous to torque (T) in the angular sense and force (F) in the translational sense. Also, we select current (i) to be analogous to angular velocity ($\dot{\theta}$) in rotary motion and linear velocity (v) in the translational sense. Analyzing the differential equations associated with inertia (J) and viscous damping (b), one finds that in light of our selected voltage and current analogies, inertia is analogous to inductance (L), and viscous damping is analogous to resistance (R). For translational motion, mass (m) is analogous to inductance, damping is analogous to resistance, and compliance (reciprocal of spring constant, k) is analogous to capacitance (C). The mechanical/electrical analogies are presented in Table VI.1, and the resulting equivalent circuit is provided in Figure VI.4 for passive and active loads.

Table VI.1 - Mechanical/Electrical Analogies

ROTATIONAL SYSTEMS		
<i>Fundamental Analogies</i>	$v \rightarrow T$	$i \rightarrow \dot{\theta}$
Mechanical Relationship	Electrical Relationship	Resulting Analogy
Inertia: $T = J \frac{d\dot{\theta}}{dt}$	Inductance: $v = L \frac{di}{dt}$	$L \rightarrow J$
Viscous Damping: $T = b\dot{\theta}$	Resistance: $v = Ri$	$R \rightarrow b$
TRANSLATIONAL SYSTEMS		
<i>Fundamental Analogies</i>	$v \rightarrow F$	$i \rightarrow v$
Mechanical Relationship	Electrical Relationship	Resulting Analogy
Mass: $F = m \frac{dv}{dt}$	Inductance: $v = L \frac{di}{dt}$	$L \rightarrow m$
Compliance: $F = k \int_0^t v d\tau$	Capacitance: $v = \frac{1}{C} \int_0^t i d\tau$	$C \rightarrow \frac{1}{k}$
Damping: $F = bv$	Resistance: $v = Ri$	$R \rightarrow b$

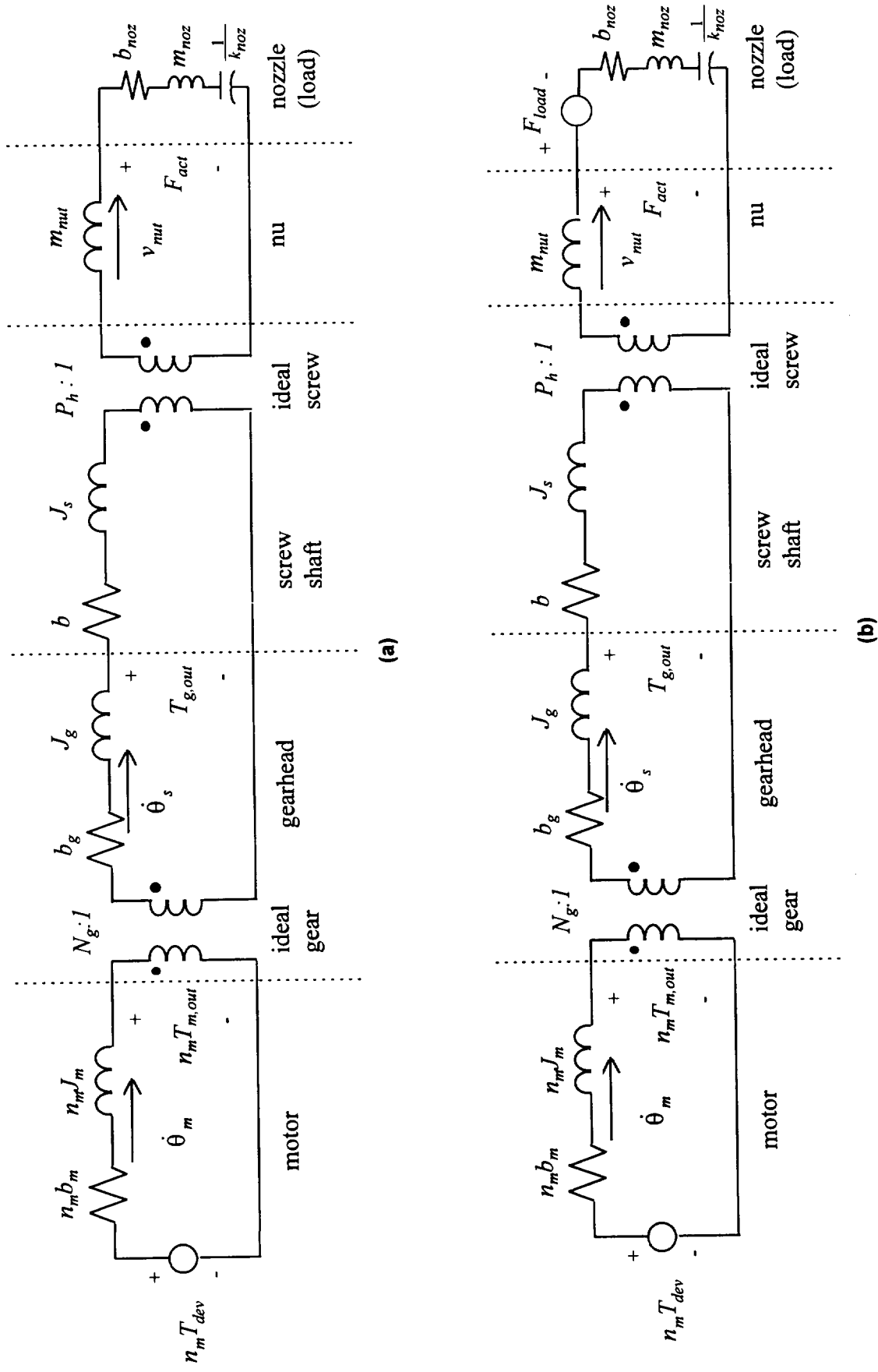


Fig. VI.4 - Actuator/Load Equivalent Circuits with (a) Passive Load and (b) Active Load

VI.3.4. System Analysis

Analysis of power transfer to the load, efficiency, and input torque in a dynamic sense would be highly dependent on the commanded motion profile. Hence, to obtain general results regarding component selection for optimal performance, a fixed motion profile must be considered. A sinusoidal velocity profile was adopted for this purpose. Clearly, most actuation applications will require a time varying velocity response that will contain both positive and negative excursions from null. The selection of a sinusoidal velocity allows consideration of this case and is amenable to multi-frequency analysis consistent with a Fourier series expansion of non-sinusoidal profiles. Furthermore, it may often be possible to determine a dominant frequency within an actuator's typical profile, thus optimizing about this frequency is reasonable.

The selection of a sinusoidal steady-state analysis allows the equivalent circuit to be represented in the frequency domain employing phasor methods. Such techniques neglect transients and focus on the sinusoidal steady-state solution to the differential equations defining the response of the network called the forced response. In the phasor domain, complex variables are indicated by overbars. The magnitude of the phasor is defined as the rms value of the sinusoid it represents, and the phase angle of the phasor is defined as the phase angle of the function of time referenced to the cosine. For our analysis, we define impedance as the ratio of the torque to velocity phasors in the rotational sense and the ratio of the force to velocity phasors in the translational sense. Impedance for the passive elements is derived from the defining differential equations. Table VI.2 defines the impedances required for analysis of the circuits in Figure VI.4.

Table VI.2 - Impedances of Passive Elements

ROTATIONAL ELEMENTS		
	Time Domain	Frequency Domain
Viscous Damping	$T = b\dot{\theta}$	$\bar{T} = b\bar{\dot{\theta}}$
Inertia	$T = J \frac{d\dot{\theta}}{dt}$	$\bar{T} = j\omega J\bar{\dot{\theta}}$
TRANSLATIONAL ELEMENTS		
	Time Domain	Frequency Domain
Damping	$F = bv$	$\bar{F} = b\bar{v}$
Mass	$F = m \frac{dv}{dt}$	$\bar{F} = j\omega m\bar{v}$
Compliance	$F = k \int_0^t v d\tau$	$\bar{F} = -j \frac{k}{\omega} \bar{v}$

The equivalent circuit for the system in the frequency domain is illustrated in Figure VI.5 for a passive load and Figure VI.6 for an active load. Note that both figures illustrate the reduction of the circuit to a single-loop circuit with all quantities referred to the equivalent motor.

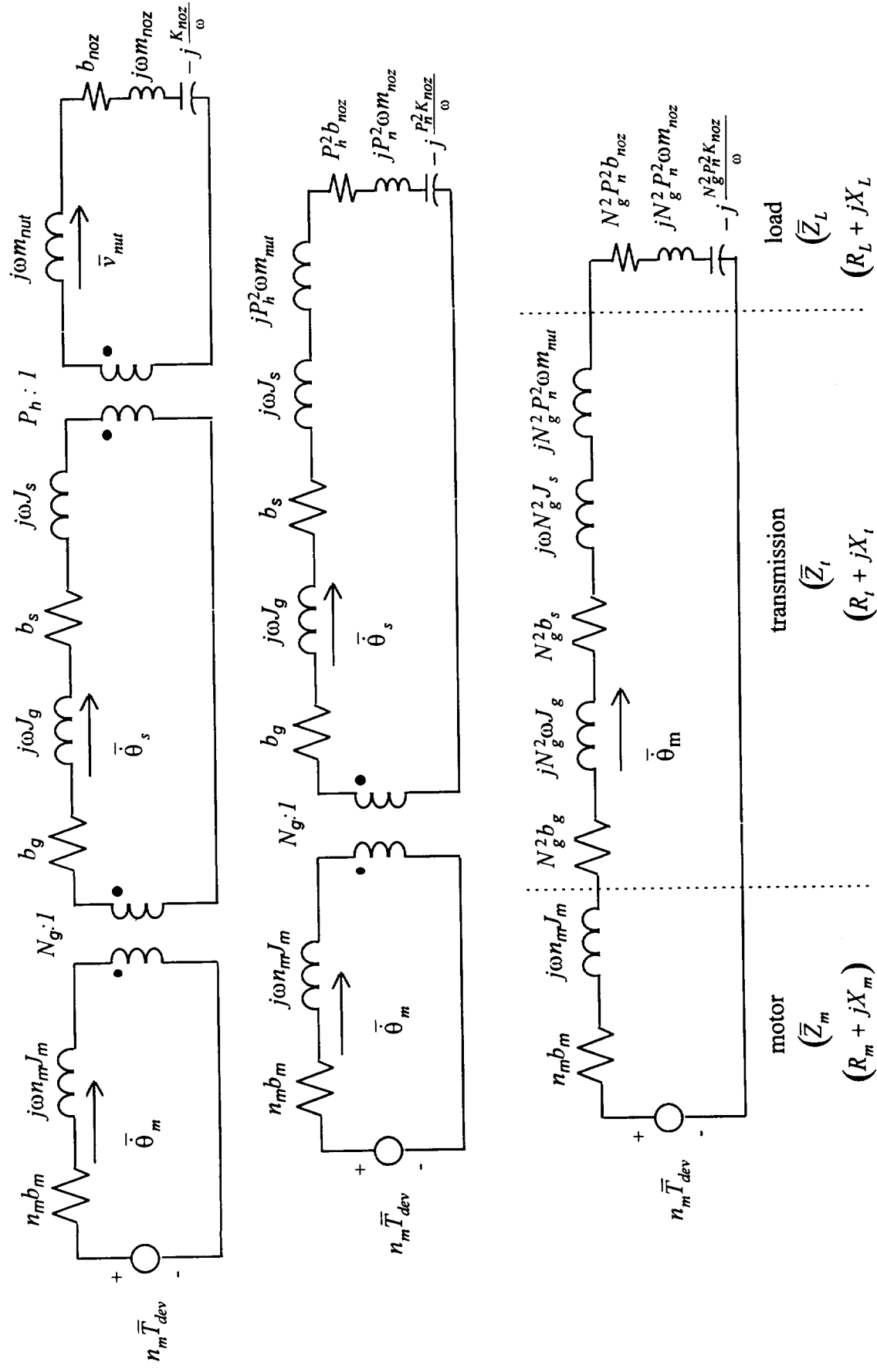


Fig. VI.5 - Passive Load Phasor Domain Equivalent Circuit

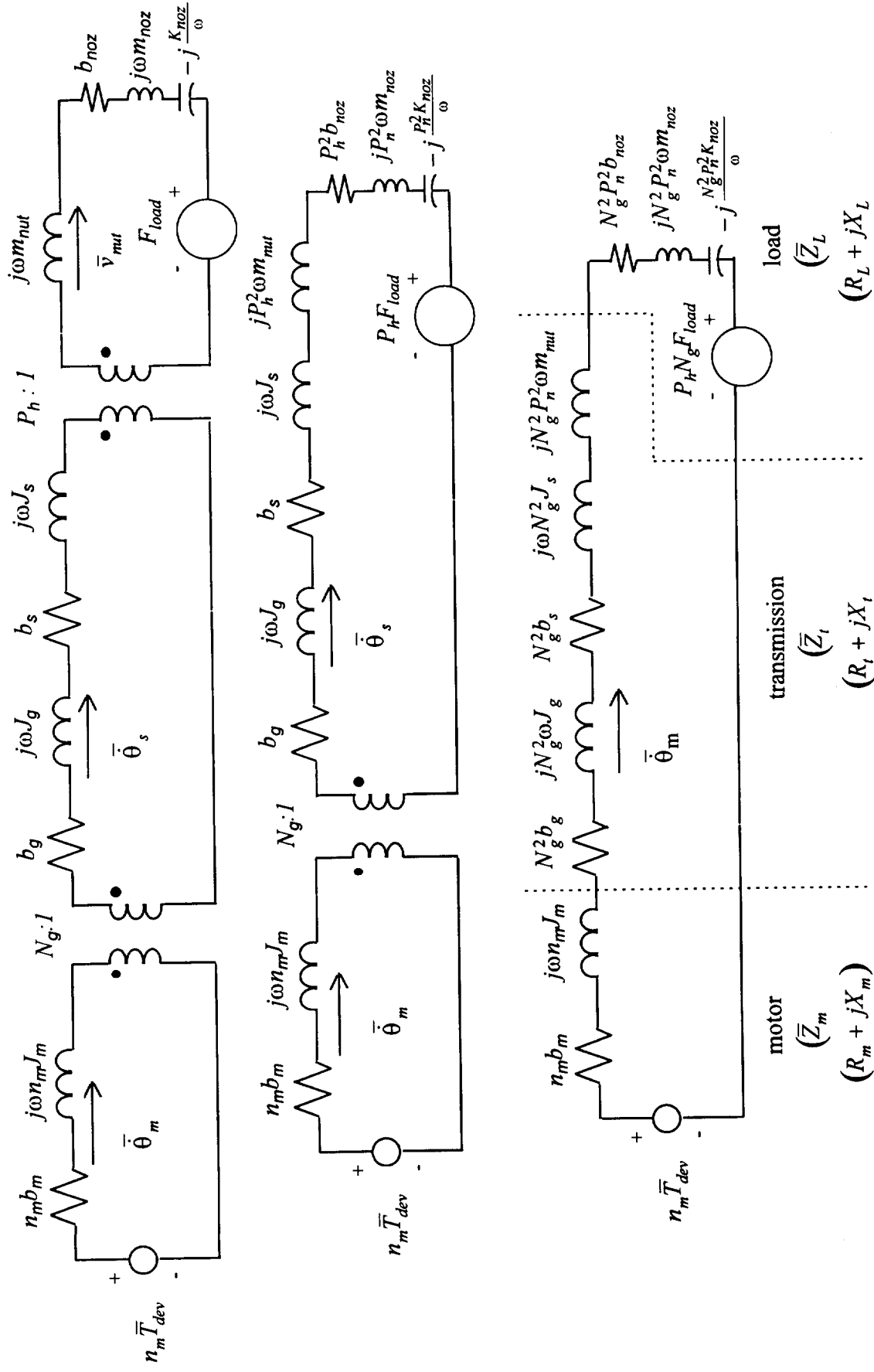


Fig. VI.6 - Active Load Phasor Domain Equivalent Circuit

While the forthcoming analysis will be generalized in terms of impedance values and forcing functions, actual data and frequency justification for the SSME TVC application will be presented later in this report.

VI.4. Passive Load Analysis

Within this report section, guidelines for optimal component selection and specification are developed for actuators to be utilized in applications with passive loads. In many applications with a source (motor) and passive load, an equivalent gearing can be selected to act as an impedance matching transformer to maximize power transfer to the load. The internal impedance of the gear mechanism can be referred to either side of the gear ratio and lumped either with the source impedance or the load impedance. However, in our case, two transformers employed and the source impedance is not necessarily fixed. Thus, as illustrated in Figure VI.5 (c), we refer all quantities to the equivalent motor shaft.

The general circuit for the passive load case is provided in Figure VI.7. Note that all variables are electrical equivalents (i.e. voltages and currents). The impedances are defined in rectangular and polar form in equations (VI.5) through (VI.7). The average power absorbed by the load will be the average power dissipated in load damping, as defined in (VI.8). Expressing the P_L in terms of defined parameters leads to (VI.9).

$$\bar{Z}_m = R_m + jX_m = Z_m \angle \gamma_m \dots\dots\dots(VI.5)$$

$$\bar{Z}_t = R_t + jX_t = Z_t \angle \gamma_t \dots\dots\dots(VI.6)$$

$$\bar{Z}_L = R_L + jX_L = Z_L \angle \gamma_L \dots\dots\dots(VI.7)$$

$$P_L = \text{Re} \left\{ \bar{V}_L \bar{I}^* \right\} \dots\dots\dots(VI.8)$$

$$P_L = \frac{V_L^2 \{Z_m \cos(-\gamma_m) + Z_t \cos(-\gamma_t) + Z_L \cos(-\gamma_L)\}}{\{Z_m \cos(-\gamma_m) + Z_t \cos(-\gamma_t) + Z_L \cos(-\gamma_L)\}^2 + \{Z_m \sin(-\gamma_m) + Z_t \sin(-\gamma_t) + Z_L \sin(-\gamma_L)\}^2} \dots\dots\dots(VI.9)$$

$$- \frac{V_L^2 \{Z_m \cos(\gamma_m) + Z_t \cos(\gamma_t)\}}{\{Z_m \cos(\gamma_m) + Z_t \cos(\gamma_t) + Z_L \cos(\gamma_L)\}^2 + \{Z_m \sin(\gamma_m) + Z_t \sin(\gamma_t) + Z_L \sin(\gamma_L)\}^2}$$

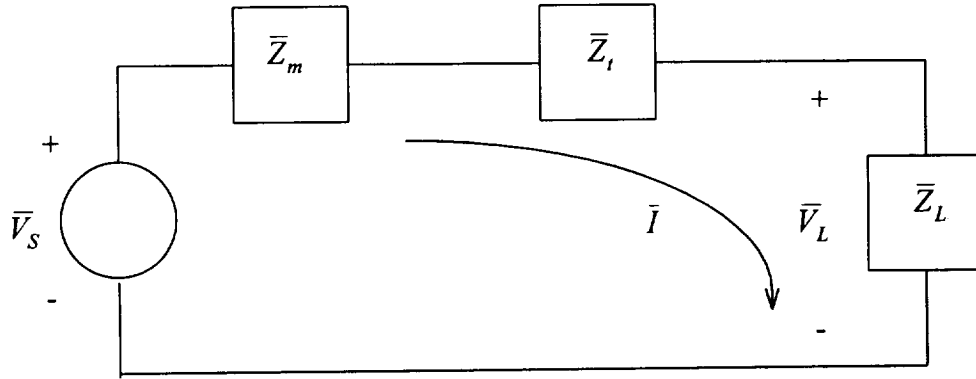


Fig. VI.7 - Simplified Equivalent Circuit with Passive Load

At first appearance, one might assume that the load power would be maximized when the total motor and transmission impedance were matched to the load impedance, as dictated by the Maximum Power Transfer Theorem, which is one of the most often misused theorems on a day to day basis. The Maximum Power Transfer Theorem states that if the source impedance is fixed, then maximum power transfer to the load will occur when the load impedance is equal to the conjugate of the source impedance. However, if the load impedance is fixed, then the theorem does not apply. Such a condition will be analyzed later.

We return to the load power expression in (VI.9) to begin our analysis. Consider the case where the input voltage phasor, motor impedance, and load impedance are fixed, but the magnitude and angle associated with the transmission impedance are allowed to vary. Realistically, the transmission will have negligible spring effects, and thus, the angle is bounded between 0 and 90 degrees. Figures VI.8 and VI.9 display the load power and efficiency, respectively. Both are plotted versus magnitude and angle for the transmission impedance. For the study, the values presented below were used:

$$\bar{V}_s = 100\angle 0^\circ V$$

$$\bar{Z}_m = 5\angle 80^\circ \Omega$$

$$\bar{Z}_L = 10\angle 80^\circ \Omega$$

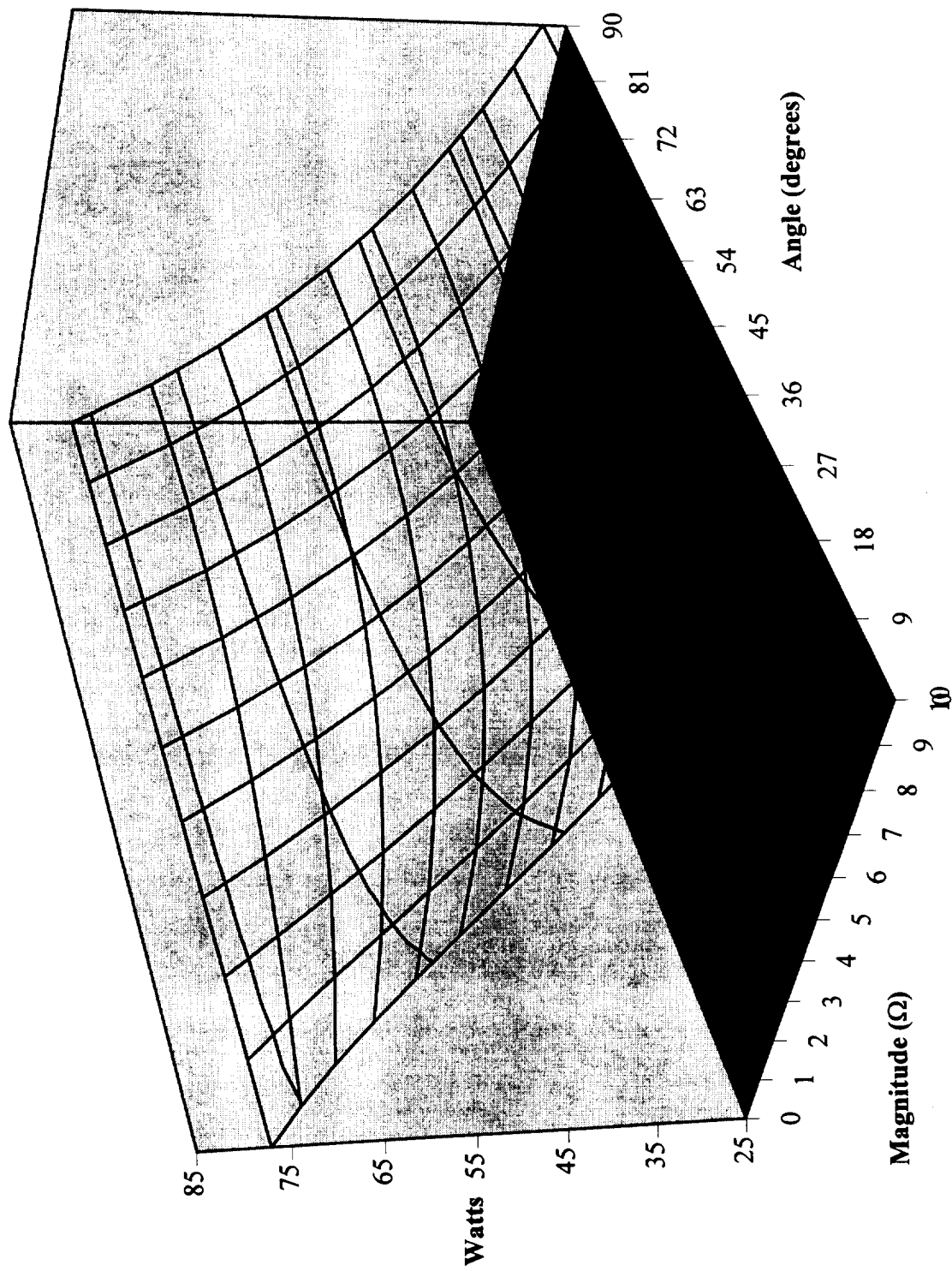


Fig. VI.8 - Load Power for Passive Load

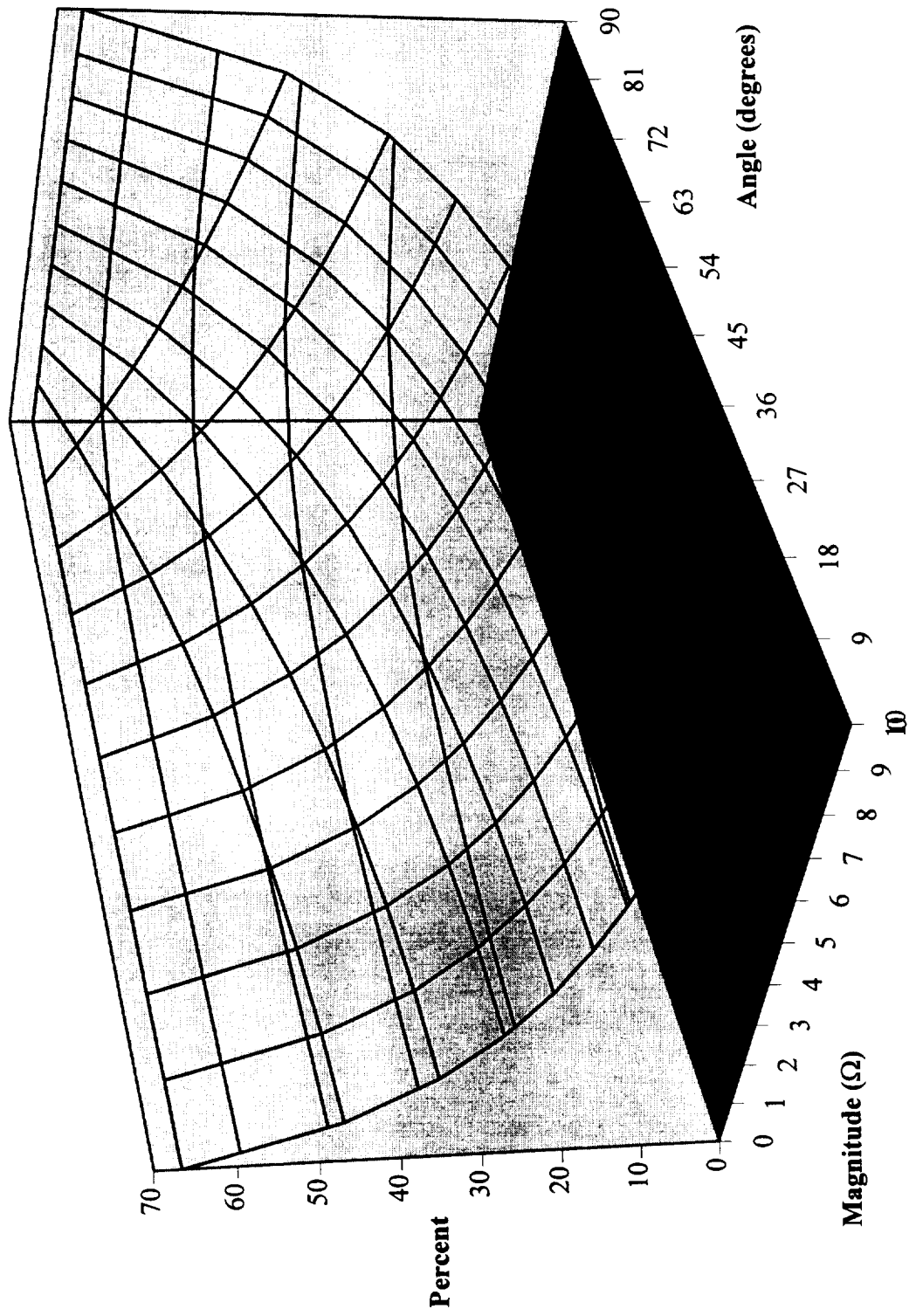


Fig. VI.9 - Efficiency for Passive Load Case Versus Magnitude and Angle

The transmission impedance was varied in magnitude and angle over the range specified in the figures. Note from the figures that maximum power transfer to the load is obtained when the transmission impedance magnitude and angle are minimum, and maximum efficiency can be obtained when the magnitude of the transmission impedance is as low as possible and the angle of the impedance is as close to 90 degrees as possible.

The analysis can also be performed varying the real and imaginary components of the transmission impedance. Figure VI.10 and VI.11 show load power and efficiency as functions of the real and imaginary components of the transmission impedance. Note that these figures indicate that minimizing the real part of the impedance maximizes efficiency while minimizing both the real and imaginary components maximizes power transfer to the load. Obviously, whether the analysis is performed in rectangular or polar coordinates does not affect the result. Both analyses lead to the conclusions that power transfer to the load is maximized when the series motor and load impedance has minimum magnitude and that efficiency is maximized when the real component of this impedance is minimum.

The non-linear nature of the efficiency and load power curves provided above prove useful for analysis. From Figure VI.8, we see that while load power continuously decreases with impedance magnitude, it has a global minimum with respect to angle. Hence, these conditions warrant investigation. In order to find the conditions for minimum power transfer to the load, the load power expression in (VI.9) was differentiated with respect to the transmission impedance angle. This derivative was equated to zero, and the relationship presented in (VI.10) was produced.

$$\gamma_t = \tan\left(\frac{X_m + X_t + X_L}{R_m + R_t + R_L}\right) = \tan\left(\frac{X_{eq}}{R_{eq}}\right) \dots\dots\dots(VI.10)$$

This equation indicates that the impedances of the motor and transmission, accounting for gear ratio and screw lead, should be selected such that the total equivalent system impedance magnitude is minimized. This, in turn, will maximize the current and hence, maximize the load power. In the complex plane, this is illustrated in Figure VI.12. The figure shows that when the angle of the transmission impedance is equal to the angle of the combined impedance of the motor and load, that the magnitude of the total impedance is a maximum. The circle indicates the locus of the total impedance and the feasible range is denoted.

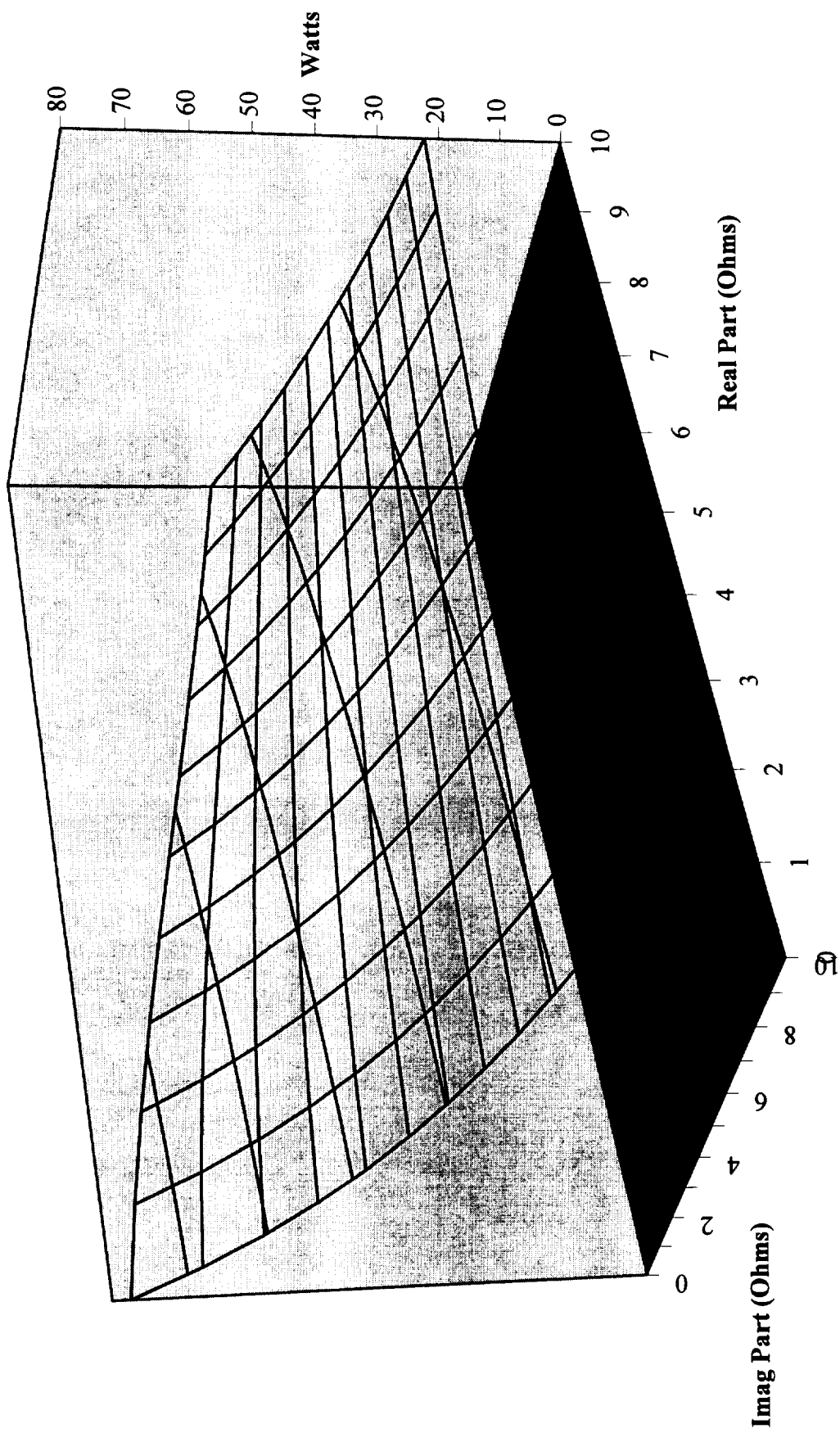


Fig. VI.10 - Load Power for Passive Load

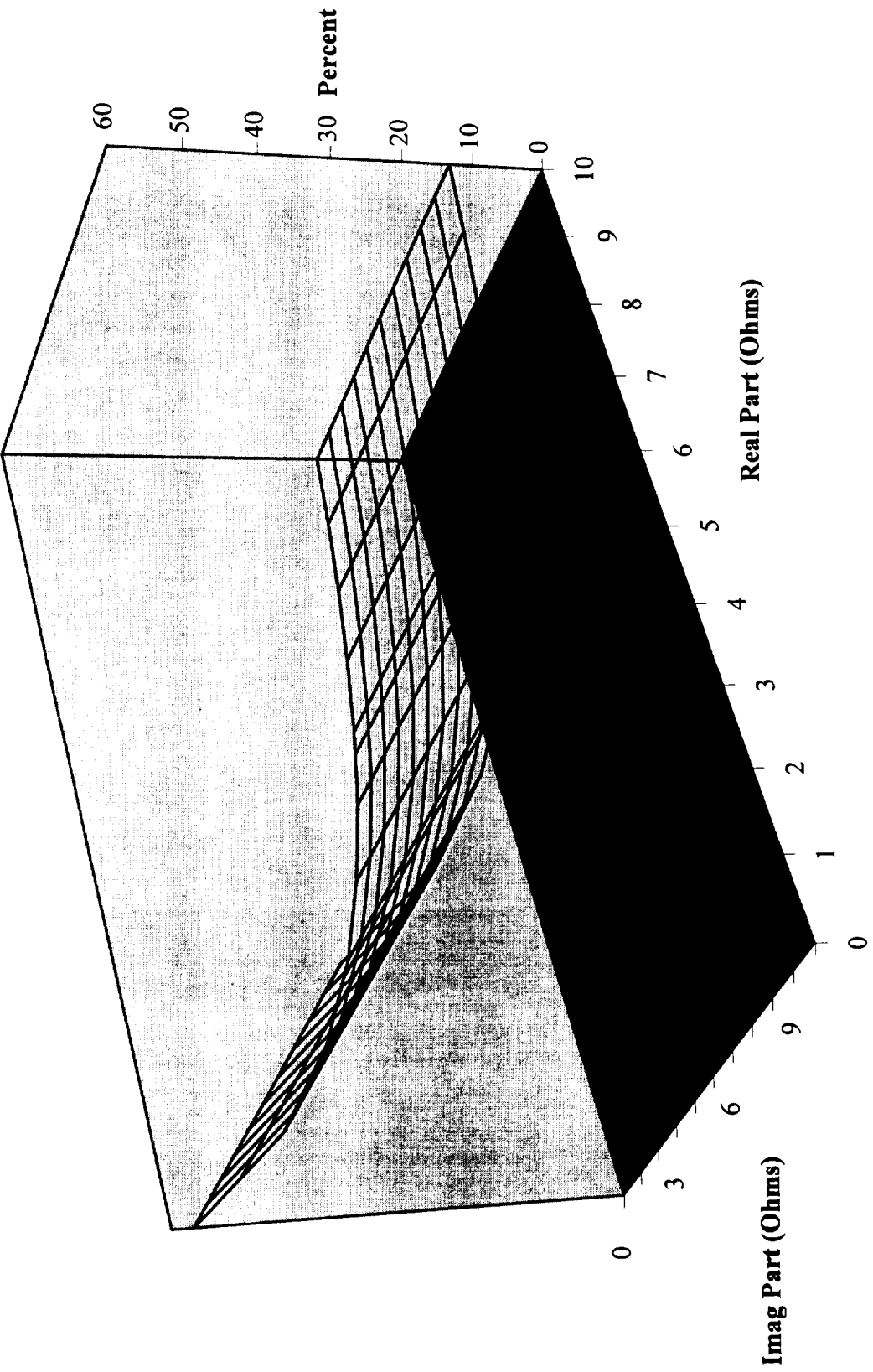


Fig. VI.11 - Efficiency for Passive Load Case Versus Real and Imaginary Impedance Components

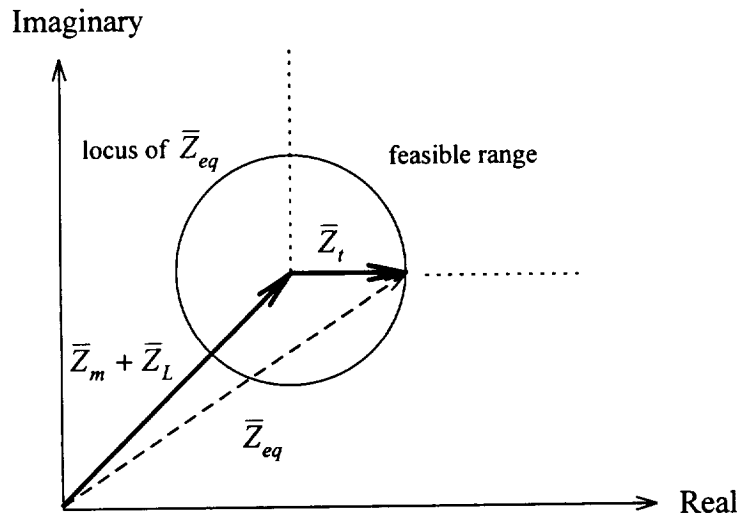


Fig. VI.12 - Total System Impedance

The foregoing has been based on the assumption that the gear ratio and screw lead were fixed. Let us combine the motor impedance with the transmission impedance and consider this to be an equivalent transmission impedance. Note from Figure VI.5 (c) that the load impedance is a function of $(N_g P_h)^2$. Thus, we can consider the load impedance as variable. Differentiating equation (VI.9) with respect to Z_L and equating the result to zero yields a maximum power transfer to the load under the conditions described in (VI.11).

$$|(\bar{Z}_m + \bar{Z}_t)| = Z_L \dots\dots\dots (VI.11)$$

N_g and P_h can be selected such that (VI.11) is true. This is equivalent to proper selection of an impedance matching transformer. The only difference is that the "transformer" is not ideal, and its effects must be considered, as was done in the previous work.

At this point, our analysis has produced three basic relationships for maximizing power transfer to the load and maximizing efficiency. We now turn to the issue of torque requirements. We assume that the load power has a fixed requirement, and then we vary the transmission impedance. The same impedance data that was previously employed is used again here. However, the load power is defined as:

$$P_L = 100 \text{ W}$$

Thus, the current is constrained to 4.8 A. Hence, we can calculate the input voltage, or torque equivalent, as a function of transmission impedance magnitude and angle. The results are presented in Figures VI.13 and VI.14. Note that torque requirements are minimized when the transmission impedance magnitude is minimized and when the angle approaches 90 degrees. Fortunately, this result is coincident, rather than in opposition to, our previous findings.

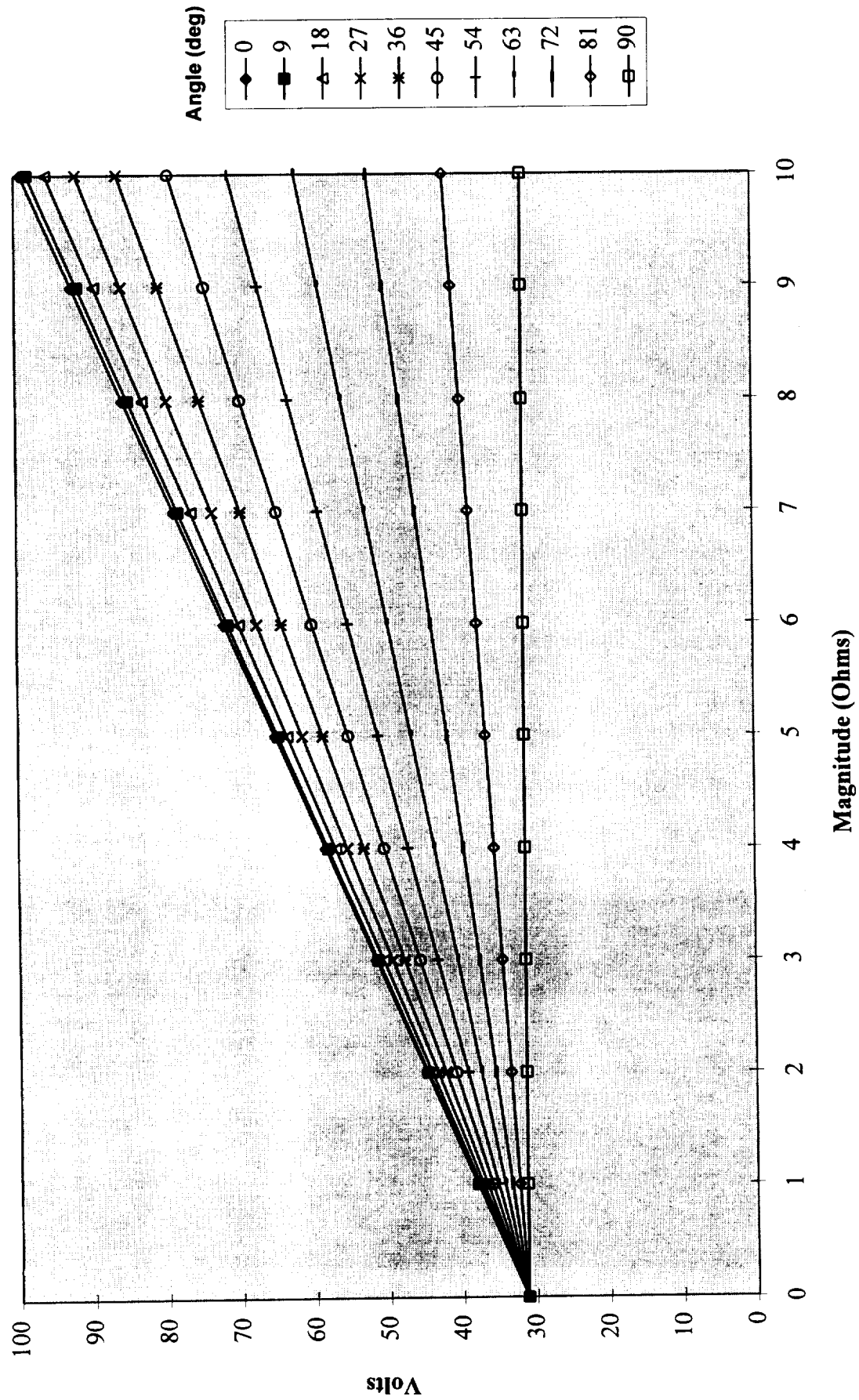


Fig. VI.13 - Input Voltage (torque) Versus Impedance Magnitude

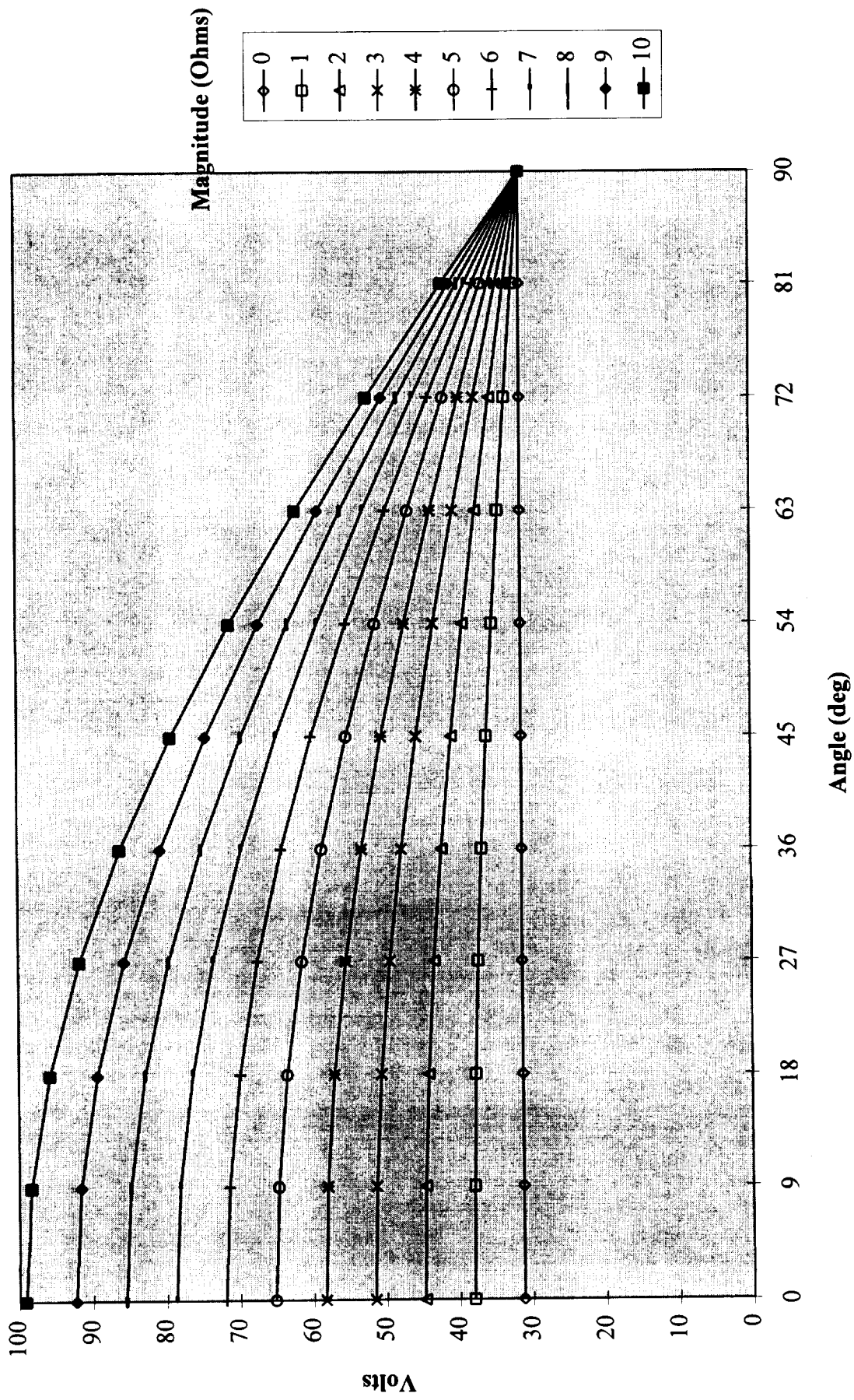


Fig. VI.14 - Input Voltage (torque) Versus Impedance Angle

VI.4.1. Passive Load Summary

Through the foregoing analyses, we have found several conditions for optimal component selection. All analyses were based on two fundamental assumptions:

- The actuator load was passive.
- The motion profile was defined by a fixed frequency sinusoidal velocity.

The analyses that were performed each had additional assumptions imposed. The various conclusions, assumptions, and impacts on power transfer to the load, efficiency, and torque requirements are summarized in Table VI.3. Under the effect column, the quantity is declared maximized, minimized, increased, or decreased. Increased implies that the quantity is not necessarily maximized, but merely increased. Decreased implies that the quantity is not minimized, but merely decreased.

While enforcing any one condition from Table VI.3 has a specific effect, not all will be possible in any given design application. Furthermore, implementation of multiple conditions may be identical. It must also be pointed out that enforcing the optimality conditions must be guided by some design weighting on the three issues: load power, efficiency, and torque requirements. The parameter selection process is not continuous. Hence, optimization is highly restricted. To illustrate this point, when a specific gear head is selected based on gear ratio, the gear damping and inertia become fixed. However, the table does provide some useful guidelines for actuator component selection.

Table VI.3 - Passive Load Actuator Optimization Conditions

Optimality Condition	Assumptions	Effect			Mechanical Implementation
		P_L	η	T_m	
(1) minimize: $ \bar{Z}_m + \bar{Z}_t $	<ul style="list-style-type: none"> Fixed gear ratio Fixed screw lead 	max	inc	min	<ul style="list-style-type: none"> Minimize motor damping and inertia Minimize screw damping and inertia Minimize gear damping and inertia
(2) $\tan\left(\frac{X_m + X_t}{R_m + R_t}\right) \rightarrow 90^\circ$	<ul style="list-style-type: none"> Fixed gear ratio Fixed screw lead 	inc	max	min	<ul style="list-style-type: none"> Maximize inertia to damping ratios of motor, gear, and screw
(3) minimize: $R_m + R_t$	<ul style="list-style-type: none"> Fixed gear ratio Fixed screw lead 	inc	max	min	<ul style="list-style-type: none"> Minimize motor damping Minimize screw damping Minimize gear damping
(4) $\gamma_t = \tan\left(\frac{X_{eq}}{R_{eq}}\right)$	<ul style="list-style-type: none"> Fixed gear ratio Fixed screw lead 	min	dec	max	<ul style="list-style-type: none"> Select gear and screw impedance such that the net impedance magnitude is minimized
(5) $ \bar{Z}_m + \bar{Z}_t = Z_L$	<ul style="list-style-type: none"> Fixed motor impedance Fixed transmission impedance 	max	-	-	<ul style="list-style-type: none"> Select gear ratio and screw lead such that the reflected load impedance is matched to the sum of the motor impedance, the reflected gear impedance, and the reflected screw impedance

VI.5. Active Load Analysis

In this report section, guidelines for the selection of actuator components are provided for the case when the actuator is to drive an active load. The general circuit for this situation is provided in Figure VI.15. Note that the circuit is presented as an equivalent electric circuit with voltages, currents, and impedances. The load contains a torque source modeled as a voltage source derived from a force function acting on the nut of the screw. This load source is selected as the phase reference at zero degrees. In this case, the load damping is a loss, but not a useful energy conversion. Hence, the power delivered to the load is the average power dissipated in the load forcing function. Expressed in terms of named circuit values, the load power is presented in (VI.12).

$$P_L = V_L \frac{[V_S Z_S \cos(\phi_S - \theta_S) + V_S Z_L \cos(\phi_S - \theta_L) - V_L Z_S \cos(\theta_S) - V_L Z_L \cos(\theta_L)]}{Z_S^2 + Z_L^2 + 2Z_S Z_L \cos(\theta_S - \theta_L)} \dots\dots\dots(VI.12)$$

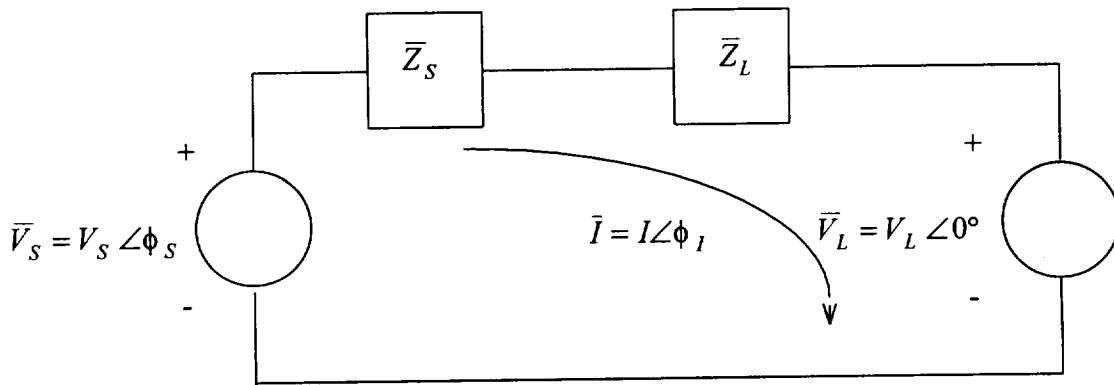


Fig. VI.15 - Simplified Equivalent Circuit with Active Load

Note that the source impedance includes both the equivalent motor and transmission impedance.

Component selection dictates the circuit values associated with the impedances and the magnitude of the load voltage. Thus, they form the focus for this study. The input source voltage and phase angle are controller dictated. For our purposes, then, we will consider power transfer to the load with variations in: $Z_S, \theta_S, Z_L, \theta_L$, and V_L . Note that all of these variables are dependent on gear ratio and screw lead according to Figure VI.6.

To determine the impact of load voltage, which can be varied by screw lead and gear ratio selection, on load power transfer, the load power expression in (VI.12) was differentiated with respect to load voltage. This derivative was equated to zero, and the result in (VI.13) was produced.

$$V_L = \frac{V_S}{2} \left\{ \cos(\phi_S) + \frac{X_{eq}}{R_{eq}} \sin(\phi_S) \right\} \dots\dots\dots (VI.13)$$

To illustrate the findings, the following parameters were assigned to the circuit in Figure VI.15:

$$\bar{V}_S = 100 \angle 30^\circ V$$

$$\bar{Z}_S = 2.5 \angle 65^\circ \Omega$$

$$\bar{Z}_L = 10 \angle 25^\circ \Omega$$

The load voltage magnitude was varied from 10 to 100 V. Using the above parameters, (VI.13) dictates that the load power should be maximum at a load voltage of 59.3 V. Figure VI.16 bears this to be true. Figure VI.17 illustrates the efficiency of the system versus load voltage magnitude. Note that the maximum efficiency does not occur at the same point as maximum power transfer.

For realistic equivalent circuit values (positive impedance angles and non-negative resistances), the load power can be shown to continuously decrease, in a non-linear fashion, with the magnitude of the source impedance and the load impedance. Hence, the conditions in (VI.14) and (VI.15) maximize the load power over the constrained region. Note that these conditions do not provide global or local minima.

$$Z_S \rightarrow 0 \dots\dots\dots (VI.14)$$

$$Z_L \rightarrow 0 \dots\dots\dots (VI.15)$$

Employing the same values for illustration as presented above, but fixing the load voltage magnitude at 75 V and varying the source impedance from 1 to 100 Ω , yields the load power and efficiency curves presented in Figures VI.18 and VI.19, respectively.

When either of the series impedance magnitudes are increased, the magnitude of the equivalent series impedance is increased. Thus, the current decreases. As a result, the load power decreases in a non-linear fashion. Though it would appear that the decrease would be proportional to the current decrease, the varying phase angle of the current also contributes. Also, the losses decrease as the current squared. The net result is an increase in efficiency with decreasing load power. This is illustrated in Figure VI.20.

Considering variations in the load and source impedance angles through analysis of the load power expression in (VI.12), it can be seen that maximum power transfer to the load occurs when the two impedance angles obey the relationship set forth in (VI.16).

$$\theta_S - \theta_L = \pm 180^\circ \dots\dots\dots (VI.16)$$

Clearly, this relationship illustrates the minimization of net series impedance magnitude and thus, maximum current. Hence, maximum load power and efficiency is obtained.

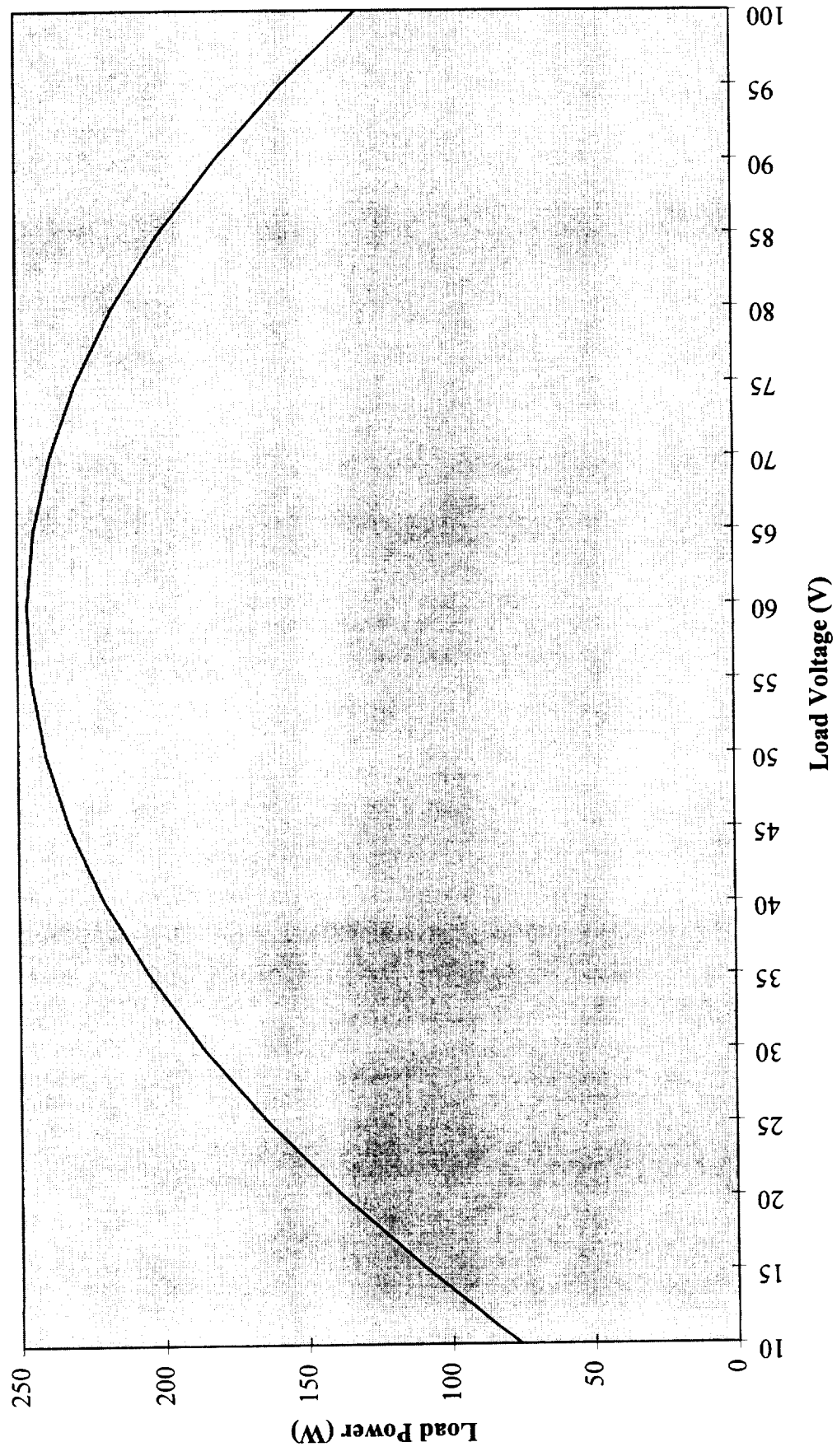


Fig. VI.16 - Load Power Versus Load Voltage

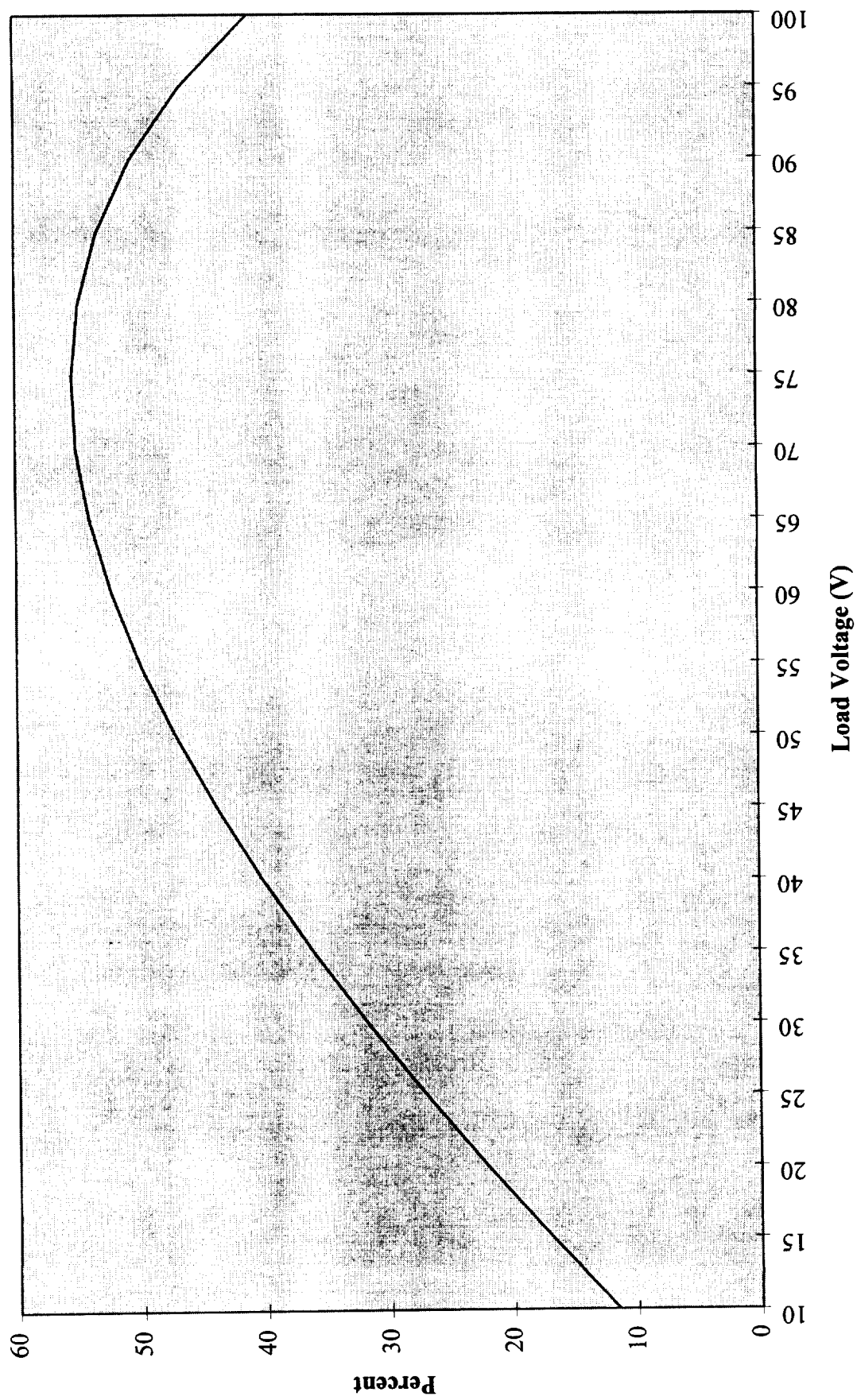


Fig. VI.17 - Efficiency Versus Load Voltage

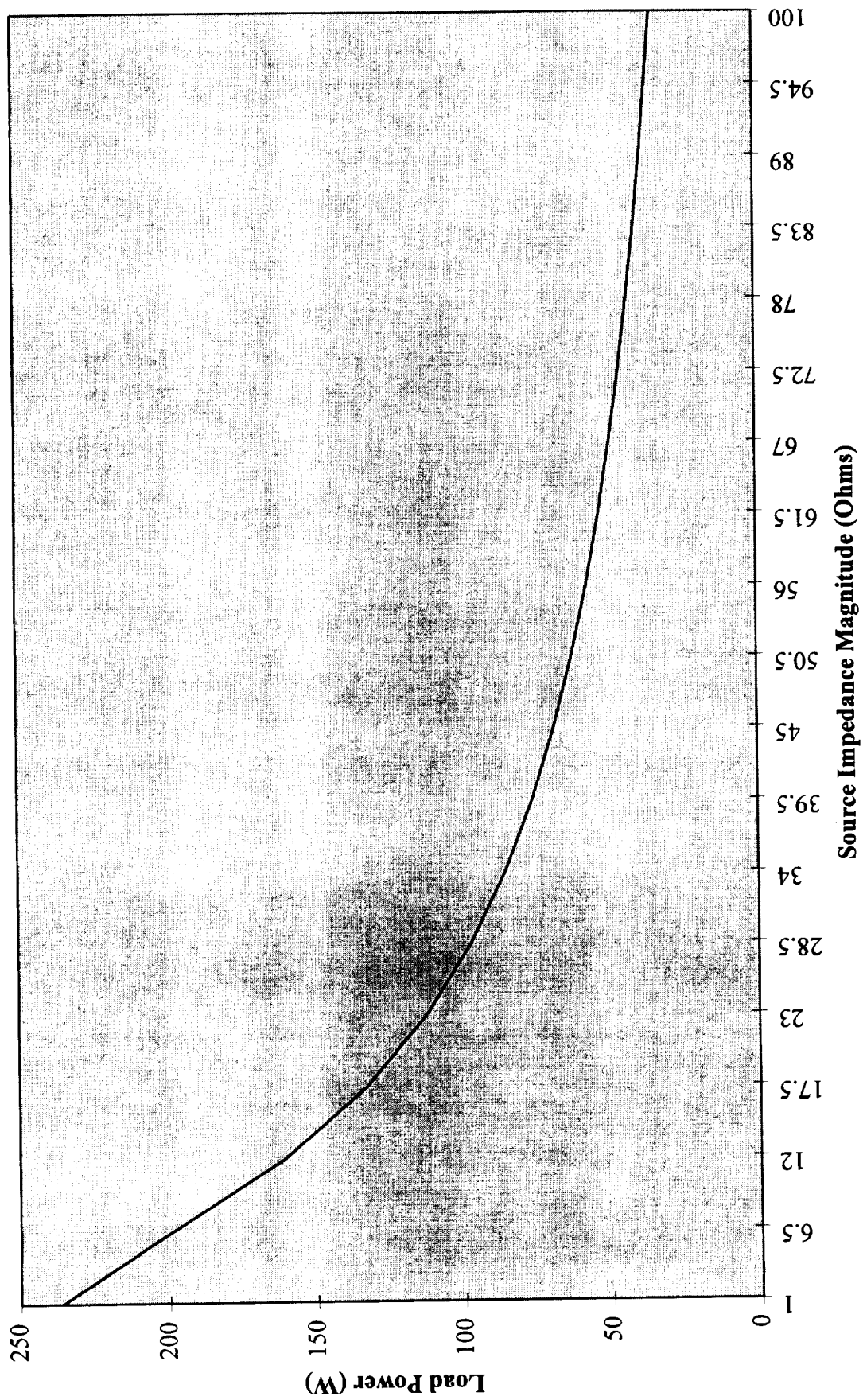


Fig. VI.18 - Load Power Versus Source Impedance Magnitude

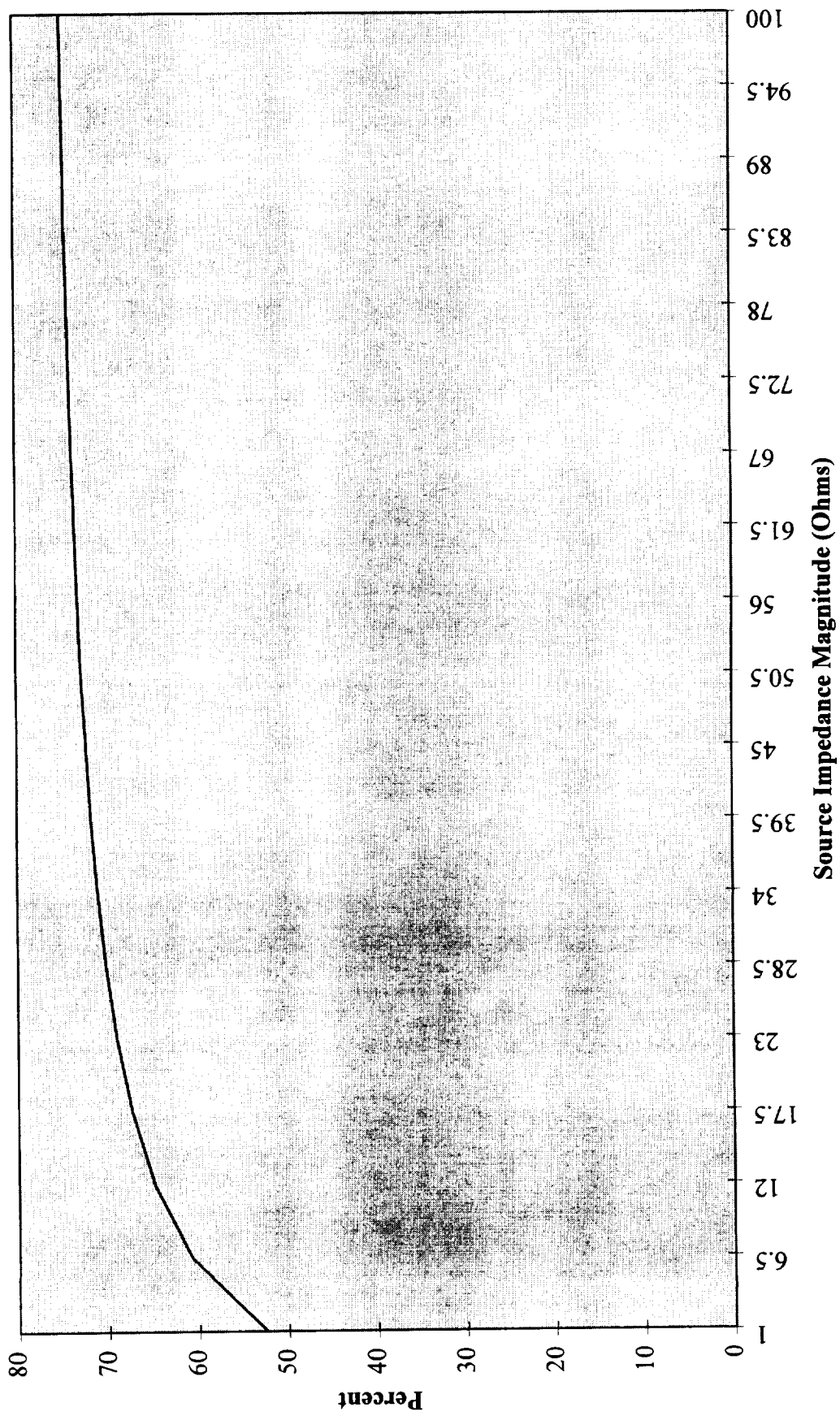


Fig. VI.19 - Efficiency Versus Source Impedance Magnitude

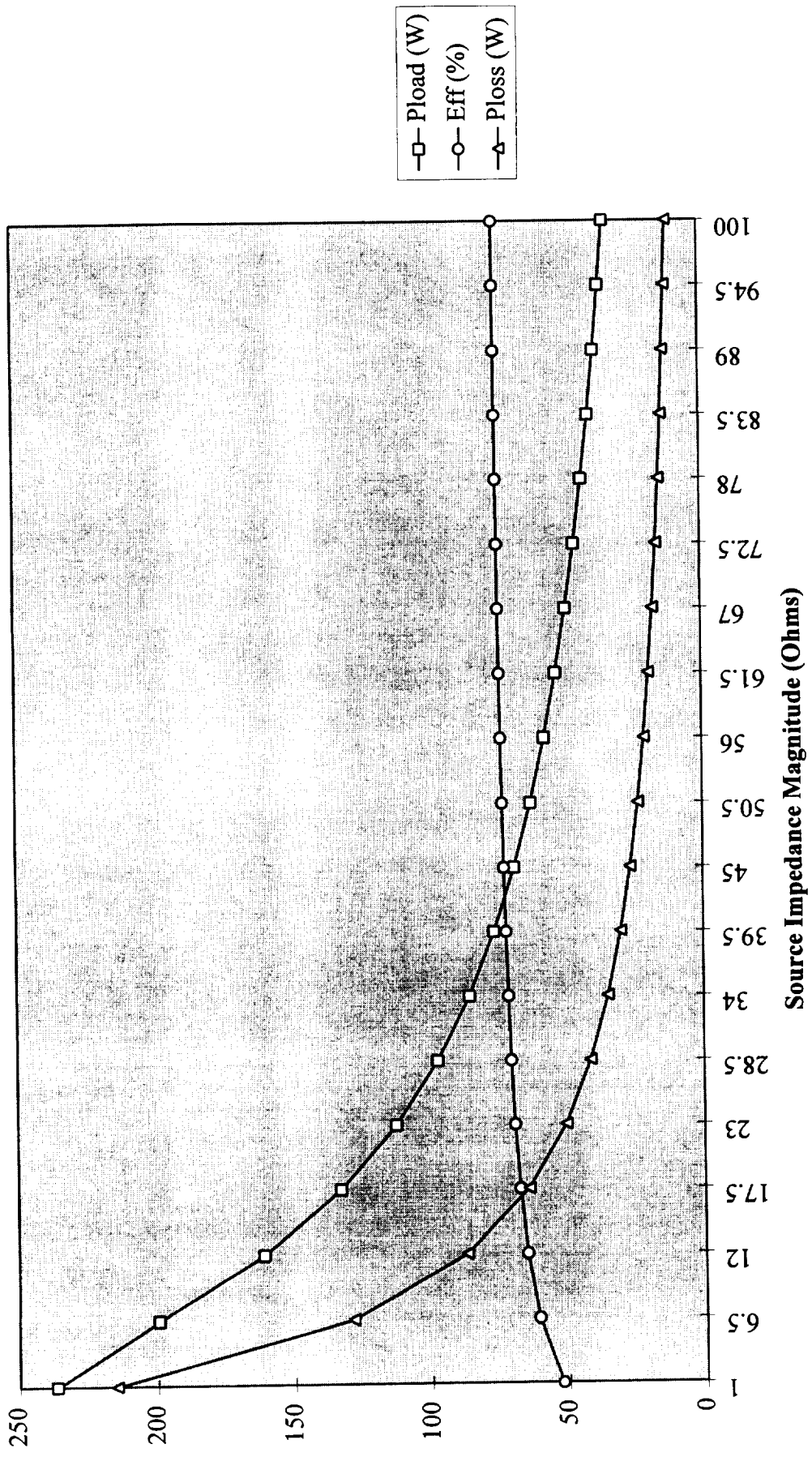


Fig. VI.20 - Illustration of Source Impedance Impact on Efficiency

This condition, however, is not realistic as it requires springs and negative damping. The condition expressed in (VI.17) is the best that is obtainable within the feasible range.

$$\theta_s - \theta_L = \pm 90^\circ \dots\dots\dots(VI.17)$$

This condition will also maximize efficiency over the feasible range.

Using the previously defined circuit values but varying the angle of the source impedance from 0 to 90 degrees produces the plots presented in Figures VI.21 and VI.22 for load power and efficiency, respectively.

To consider torque requirements, we return to the equivalent circuit of Figure VI.15. Assume a known load force and a desired sinusoidal velocity (current) profile. These known quantities define for both the load power and current phasor. Hence, the source voltage magnitude (torque) may be expressed as presented in (VI.18).

$$V_s = I |\bar{Z}_s + \bar{Z}_L| \dots\dots\dots(VI.18)$$

This expression indicates that minimizing the magnitude of the equivalent impedance, defined in (VI.19), will minimize the torque requirements.

$$|\bar{Z}_s + \bar{Z}_L| = Z_{eq} = \sqrt{Z_s^2 + Z_L^2 + 2Z_s Z_L \cos(\theta_s - \theta_L)} \dots\dots\dots(VI.19)$$

The minimum to this function is bounded by realistically obtainable values like non-negative damping and no springs. Hence, we see that (VI.14), (VI.15), and (VI.17) apply not only to aiding power transfer, but to reducing torque requirements as well.

VI.5.1. Active Load Summary

Through the foregoing analyses, we have found several conditions for optimal component selection. All analyses were based on two fundamental assumptions:

- The actuator load was active.
- The motion profile was defined by a fixed frequency sinusoidal velocity.

The analyses that were performed each had additional assumptions imposed. The various conclusions, assumptions, and impacts on power transfer to the load, efficiency, and torque requirements are summarized in Table VI.4. Under the effect column, the quantity is declared maximized, minimized, increased, or decreased. Increased implies that the quantity is not necessarily maximized, but merely increased. Decreased implies that the quantity is not minimized, but merely decreased.

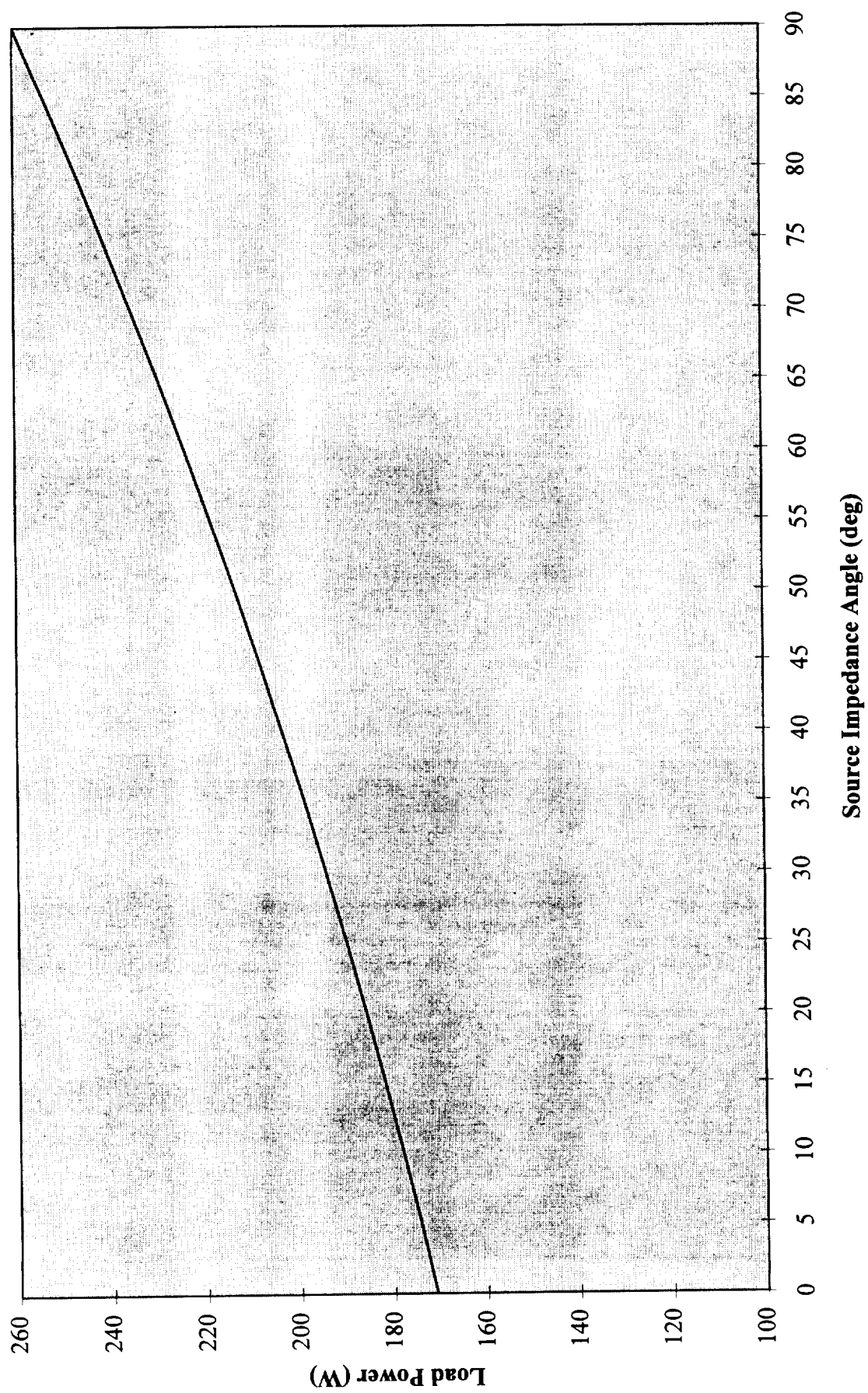


Fig. VI.21 - Load Power Versus Source Impedance Angle

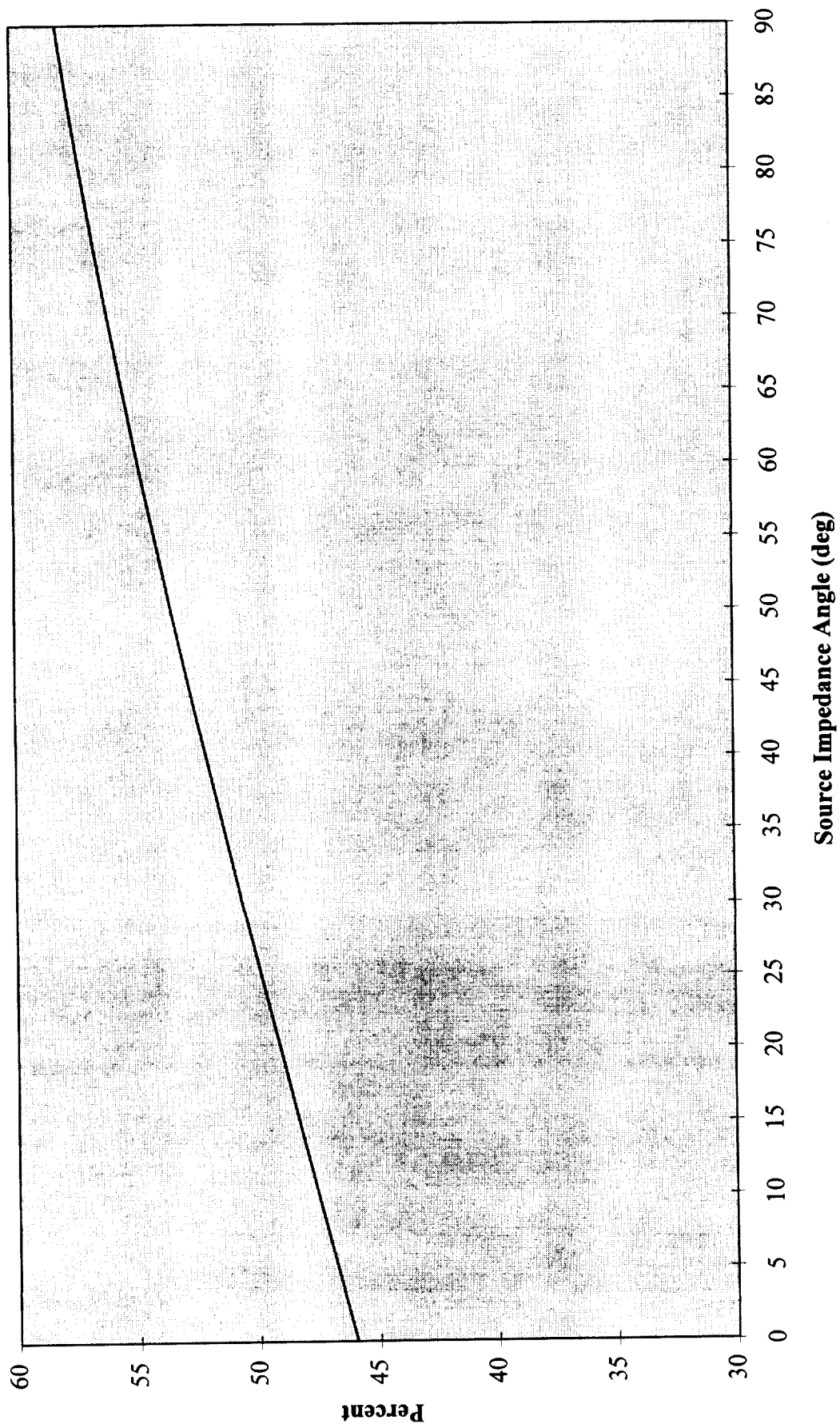


Fig. VI.22 - Efficiency Versus Source Impedance Angle

Table VI.4 - Active Load Actuator Optimization Conditions

Optimality Condition	Assumptions	Effect			Mechanical Implementation
		P_L	η	T_m	
(1) $V_L = \frac{V_s}{2} \left\{ \frac{\cos(\phi_s) + \frac{X_{eq}}{R_{eq}} \sin(\phi_s)}{R_{eq}} \right\}$	<ul style="list-style-type: none"> Fixed source/transmission impedance Fixed load impedance Fixed input torque phasor 	max	-	-	<ul style="list-style-type: none"> Choose gear ratio and screw lead to match load voltage Control source phase angle
(2) $Z_s \rightarrow 0$ $Z_L \rightarrow 0$	<ul style="list-style-type: none"> Fixed gear ratio Fixed screw lead Fixed input torque phasor Fixed load force 	inc	dec	dec	<ul style="list-style-type: none"> Minimize damping and inertia of motor, gearhead, and screw
(3) $\theta_s - \theta_L \rightarrow \pm 90^\circ$	<ul style="list-style-type: none"> Fixed gear ratio Fixed screw lead Fixed input torque phasor Fixed load force Fixed source and load impedance magnitudes 	inc	inc	dec	<ul style="list-style-type: none"> Select motor, gearhead, and screw impedance with respect to load impedance angle

Although the conditions set forth in Table VI.4 provide sound guidelines for component specification, strict enforcement will not be possible. Varying individual quantities will redefine others. Hence, these can only be applied in a very general sense. As with the passive load, selection of the most important optimality conditions must be driven by measures of importance placed upon load power, efficiency, and required torque.

VI.6. Conclusion

The previous sections have presented conditions for optimal component selection in the design of electromechanical actuators driving both passive and active loads. It is imperative to recognize that true optimality can only be defined when, for a given application, a designer specifies relative merit to power transfer, efficiency, and torque requirements. This enables a more clear definition of what optimality conditions are most critical.

Throughout this report section, variation in a single parameter was addressed with all other parameters and variables held constant. This limits the applicability of the findings. Variations in any single parameter will inherently produce a variation in other parameters. For example, the inertia of the gearhead can not be changed without a variation in the damping. As another example, selecting a new gear ratio will also result

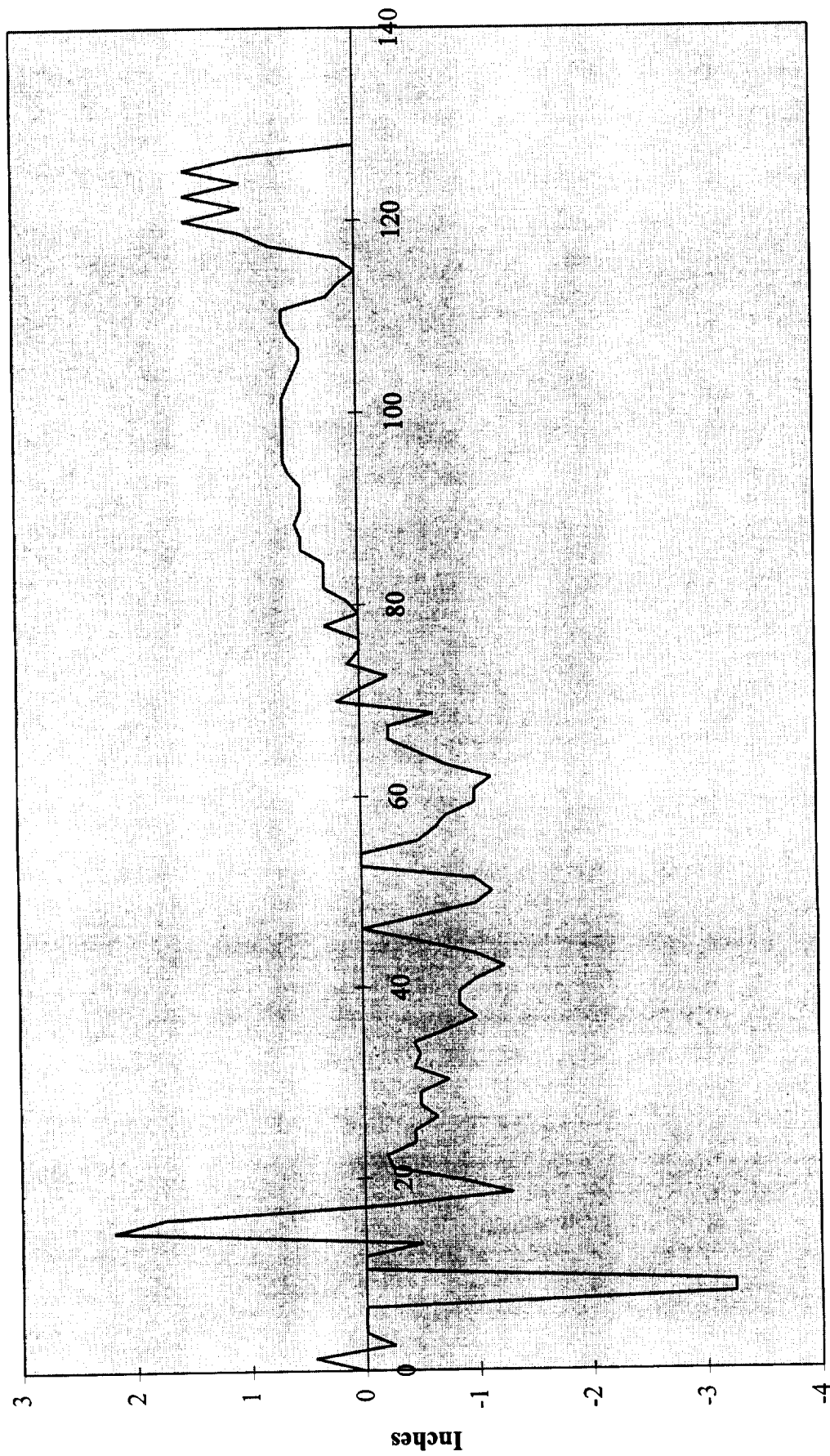
in a variation of the gearhead damping and inertia. All such parametric dependencies impact the three issues that define optimality.

VI.6.1. Future Development

To address the issue of a true, though constrained, optimal solution to the problem is the focus of future work by the authors. Only the active load case will be considered, and controller interactions will be included. While the presented work employed analytical expressions for load power, future efforts will include analysis of analytical expressions for efficiency and motor torque. Parametric dependencies upon one another will be addressed in a generalized manner such that optimal component selection can be performed based on data associated with commercially available products.

VI.6.2. Single-Frequency Justification

A major portion of this chapter's content has been based upon the single frequency assumption. The obvious question is whether or not such is reasonable. We turn to the SSME TVC application for consideration of this issue. A close approximation to an actual SSME nozzle position profile is presented in Figure VI.23. Figure VI.24 provides a plot of the nozzle velocity computed from the position data using a first-order backward finite-difference approximation. The software MATLAB was used to compute the harmonic content in the waveform. The frequency content in the power spectral density is presented in Figure VI.25. Note that an analysis could be performed about the maximum frequency component at 0.22 Hz. The response falls off about that point, but three distinct frequencies are dominant.



Time (s)

Fig. VI.23 - Actuator Position

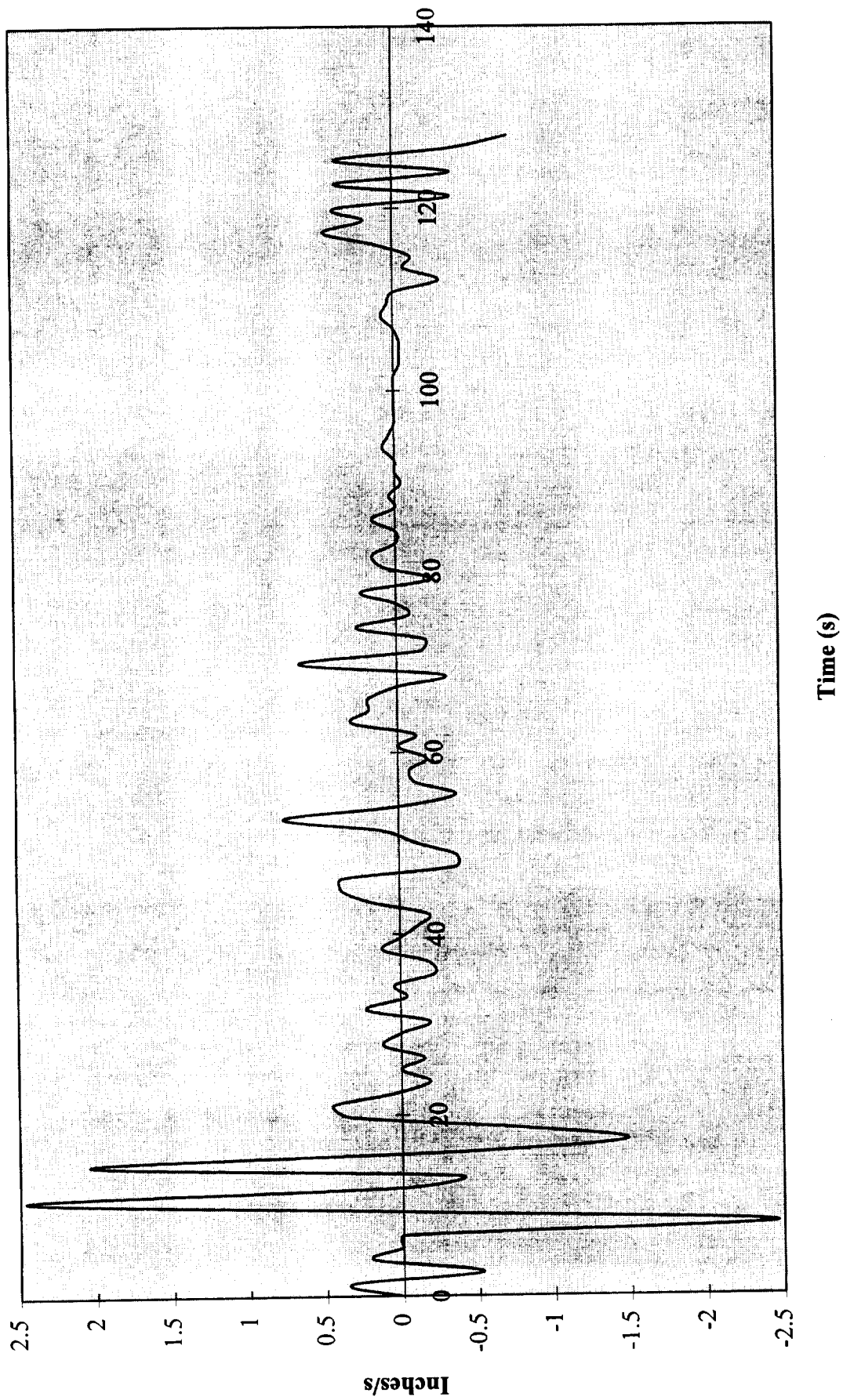


Fig. VI.24 - Actuator Velocity

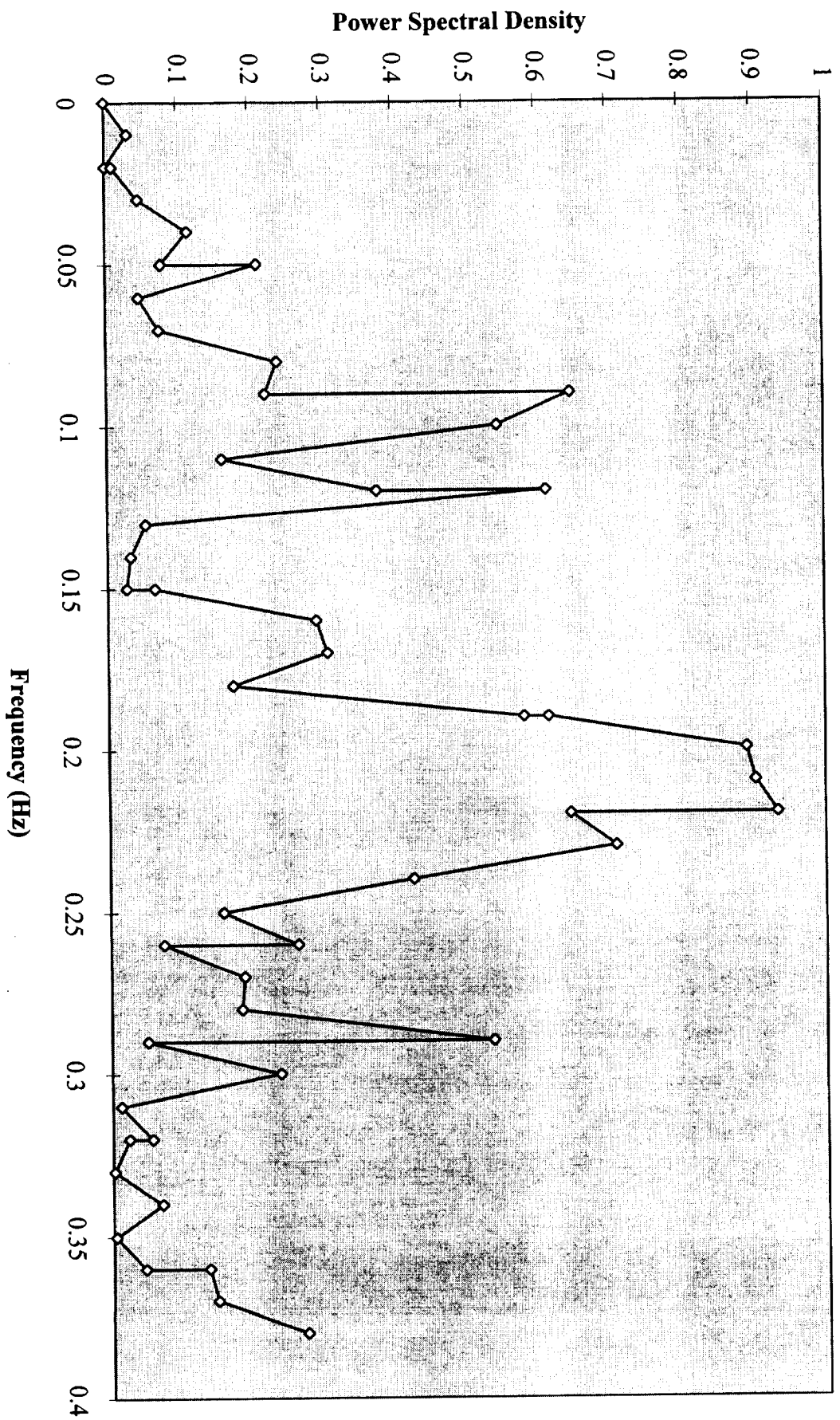


Fig. VI.25 - Frequency Content in Nozzle Velocity

VII. HEALTH MONITORING AND FAULT DIAGNOSIS

Throughout the performance of this grant, NASA representatives have expressed much interest in health monitoring and fault diagnosis (HMFD) of EMA systems. In light of this, we began investigating HMFD algorithms for such an application. Specifically, our focus was on the HMFD problem for electric machinery. Previous work had identified the brushless permanent magnet machine as the best candidate to be the prime mover in an EMA system for thrust vector control. Thus, our focus was narrowed to health monitoring and fault diagnosis specifically for the brushless permanent magnet motor.

The majority of our theoretical and experimental efforts on this topic were addressed in a recent Ph.D. dissertation written by one of the students funded on this grant. This dissertation is presently the most authoritative document we have produced on the topic, and it is presented in Appendix B.

The findings were that the adaptive Kalman filter approach to the HMFD application is feasible. Laboratory data, gathered in the Electromechanical Actuation Test Facility, is used for confirmation. Our future work will be aimed at developing a real-time implementation of the proposed system on digital signal processing hardware.

The development of a prototype system for HMFD will enable new research and development in the areas of adaptive and variable-structure control of EMA systems. Furthermore, such HMFD systems will enable reduced maintenance and higher reliability for EMA systems.

As Appendix B is a complete document, the topic is left at this point, and the reader is referred to the Appendix.

APPENDIX A

Inertia Calculations

Inertia Calculations

Conversion Factors

$$\text{Mass: } 1 = \frac{\text{lb} \cdot \text{s}^2 / \text{in}}{175.127 \text{ kg}} \quad \text{Moment of Inertia: } 1 = \frac{\text{lb} \cdot \text{s}^2 / \text{in}}{175.127 \text{ kg}} \cdot \frac{\text{in}^2}{25.4^2 \text{ mm}^2} = \frac{\text{lb} \cdot \text{s}^2 \cdot \text{in}}{112,985 \text{ kg} \cdot \text{mm}^2}$$

Table A.1 - Raw Inertia/Mass Data

Component	Inertia (kg · mm ²)	Mass (kg)	Inertia (lb · s ² · in)	Mass (lb · s ² / in)
Motor	4880		0.04319	
Gear	542.3		0.004800	
Screw	3182		0.02816	
Rollers	370.8		0.003282	
Nut Cage		18.16		0.1037
Nut		2.660		0.02398

Gear Ratio From Motor to Screw

$$N_{gr} = 1 / 4$$

Gear Ratio From Motor to Nut

$$N_{grscrew} = \frac{1}{4} \cdot \frac{20 \text{ mm}}{\text{rev}} \cdot \frac{\text{rev}}{2\pi \text{ rad}} = 0.7958 \text{ mm / rad}$$

---- OR ----

$$N_{grscrew} = \frac{1}{4} \cdot \frac{20 \text{ mm}}{\text{rev}} \cdot \frac{\text{rev}}{2\pi \text{ rad}} \cdot \frac{\text{in}}{25.4 \text{ mm}} = 0.03133 \text{ in / rad}$$

Table A.2 - Reflected Inertia at the Motor and Reflected Mass at the Nut

Component	Inertia (kg · mm ²)	Mass (kg)	Inertia (lb · s ² · in)	Mass (lb · s ² / in)
Motor	4880	7706	0.04319	44.00
Gear	542.3	856.3	0.004800	4.890
Screw	198.9	314.1	.001760	1.793
Rollers	23.18	36.60	0.0002051	0.2090
Nut Cage	11.50	18.16	0.0001018	0.1037
Nut	1.685	2.660	0.00002354	0.02398

Table A.3 - Total Reflected Inertia at the Motor and Total Reflected Mass at the Nut

Inertia (kg · mm ²)	Mass (kg)	Inertia (lb · s ² · in)	Mass (lb · s ² / in)
5658	8834	0.05008	51.02

APPENDIX B

Health Monitoring of a Brushless Permanent Magnet Machine Using an Adaptive Kalman Filtering Approach

**HEALTH MONITORING OF A
BRUSHLESS PERMANENT MAGNET MACHINE USING AN
ADAPTIVE KALMAN FILTERING APPROACH**

by

THOMAS ERIC SALEM

A DISSERTATION

Submitted in partial fulfillment of the requirements for
the degree of Doctor of Philosophy
in the Department of Electrical Engineering
in the Graduate School of
The University of Alabama

TUSCALOOSA, ALABAMA

1996

DEDICATION

This research work would not have been completed without the love, dedication, and support of my best friend. I am eternally thankful that she is also my wife. Therefore, this text is dedicated with love and honor to Karen.

ACKNOWLEDGMENTS

I am grateful for the financial support received from both the National Aeronautics and Space Administration, under grant NAG8-240, and the Department of Electrical Engineering. The encouragement and support to continue my graduate studies offered by Mr. John Duane and Dr. Kiran Vashi was greatly appreciated.

I am indebted to the faculty members who graciously served on my dissertation committee. Additionally, I am thankful for the assistance of Dr. John Wander, who participated on my thesis committee.

The support and encouragement of my committee chairperson, Dr. Tim A. Haskew, is deeply appreciated. In addition to providing wisdom and guidance for this research work, the personal relationship and respect received over the last five years has been especially satisfying. I look forward to future opportunities that would enable us to again work together.

For the numerous hours of philosophical discussion, I am indeed thankful for Dr. Harold Stern. Along with many helpful comments during the review process for this work, your wisdom and insight into the academic environment is a personal treasure. My best wishes for your continued success in education, and I look forward to our future endeavors.

Many thanks to my family members for their interest, commitment and support during the pursuit of this graduate work. Special thanks are offered to Mr. Jack Tymann

and his wife Lucille, who have been, and continue to be, gracious parents. I am very thankful for my parents and for everything that they have provided. Finally, I am truly grateful for the friendship and acceptance of Dr. Mark Brown and his wife Sharon, who have added fun and good times to the list of things that were accomplished during this past year.

CONTENTS

ACCEPTANCE	ii
DEDICATION	iii
ACKNOWLEDGEMENTS	iv
LIST OF TABLES	viii
LIST OF FIGURES	ix
1 INTRODUCTION	1
1.1 Dissertation Objective	3
1.2 Dissertation Overview	4
2 BACKGROUND AND SURVEY	5
2.1 Brushless Permanent Magnet Machine Technology	6
2.2 Health Monitoring Techniques	8
2.3 The Kalman Filter	12
3 MODEL DEVELOPMENT	14
3.1 The Brushless Permanent Magnet Machine Model	14
3.2 Machine Failure Mode Models	25
3.3 The Discrete Kalman Filter Equations	31
3.4 The Adaptive Kalman Filter Equations	36
4 SIMULATION AND EXPERIMENTAL RESULTS	50
4.1 Electromechanical Actuator Test Facility and Equipment	50

4.2	Machine Model Verification	53
4.2.1	Phase Resistance and Back Electromotive Force Constant ...	56
4.2.2	Self and Mutual Inductance	56
4.2.3	Viscous Damping Coefficient and System Inertia	60
4.2.4	Model Verification for Steady State Operation	67
4.2.5	Model Verification for Dynamic Operation	67
4.2.6	Model Verification for Failure Mode Operation	77
4.3	Discrete Kalman Filter Verification	88
4.3.1	Verification for Steady State Operation	92
4.3.2	Verification for Dynamic Operation	92
4.4	Adaptive Kalman Filter Verification	111
4.4.1	Flux Weakening Failure Mode	111
4.4.2	Open Circuit Failure Mode	113
4.4.3	Short Circuit Failure Mode	118
5	SUMMARY	120
5.1	Application Recommendation	120
5.2	Future Development Topics	121
	REFERENCES	125
	APPENDIX	129

LIST OF TABLES

3.1	Power electronic transistor status for motor operation	15
3.2	Power electronic transistor status and simplified motor drive model	17
4.1	Switch settings and resistance values for the laboratory resistor bank	55

LIST OF FIGURES

3.1	BPMM and power electronic motor drive electrical schematic	15
3.2	BPMM and simplified motor drive electrical schematic	17
3.3	Voltage waveforms of the simplified motor drive model	18
3.4	Electromechanical actuator system block diagram	22
3.5	Electrical schematic for the open circuit failure mode	27
3.6	Electrical schematic for the interphase short circuit failure mode	27
3.7	Electrical schematic for the intraphase short circuit failure mode	29
3.8	Block diagram of the discrete Kalman filter loop	32
3.9	Expanded block diagram of the discrete Kalman filter loop	35
3.10	Simple RL circuit diagram for evaluating linearized Kalman filter schemes	38
3.11	Simulated current with no parameter change	38
3.12	Simulated current with a small parameter change	39
3.13	Simulated current with a large parameter change	39
3.14	Linearized Kalman filter estimate with a small parameter change	41
3.15	Extended Kalman filter estimate with a small parameter change	41
3.16	Linearized Kalman filter estimate with a large parameter change	42
3.17	Extended Kalman filter estimate with a large parameter change	42
3.18	Block diagram of the adaptive Kalman filter loop	43
3.19	Block diagram of a parallel adaptive Kalman filter strategy	45

3.20	Expanded block diagram of the adaptive Kalman filter loop	47
4.1	Laboratory resistor bank	54
4.2	Experimental data for back EMF coefficient calculation	57
4.3	Current assuming a wye connected measurement of phase inductance	58
4.4	Current assuming a delta connected measurement of phase inductance	59
4.5	Current with mutual inductance set to 25% of self inductance	61
4.6	Current with mutual inductance set to 50% of self inductance	62
4.7	Current with mutual inductance set to 75% of self inductance	63
4.8	Test results used for evaluating the viscous damping coefficient	65
4.9	Test results used for evaluating the EMA system inertia	66
4.10	Steady state simulated and actual phase currents for a 75.0 volt bus	68
4.11	Steady state simulated and actual line voltages for a 75.0 volt bus	69
4.12	Steady state simulated and actual mechanical speeds for a 75.0 volt bus . . .	70
4.13	Steady state simulated and actual phase currents for a 150.0 volt bus	71
4.14	Steady state simulated and actual line voltages for a 150.0 volt bus	72
4.15	Steady state simulated and actual mechanical speeds for a 150.0 volt bus . .	73
4.16	Steady state simulated and actual phase currents for a 200.0 volt bus	74
4.17	Steady state simulated and actual line voltages for a 200.0 volt bus	75
4.18	Steady state simulated and actual mechanical speeds for a 200.0 volt bus . .	76
4.19	Simulated and actual phase currents for transient motor operation	78
4.20	Simulated and actual phase currents for transient motor operation (continued)	79
4.21	Simulated and actual line voltages for transient motor operation	80
4.22	Simulated and actual line voltages for transient motor operation (continued)	81

4.23	Simulated and actual mechanical speeds for transient motor operation	82
4.24	Simulated phase current for the flux weakening failure	83
4.25	Simulated mechanical speed for the flux weakening failure	84
4.26	Simulated phase currents for the open circuit failure	85
4.27	Actual phase currents for the open circuit failure	86
4.28	Simulated and actual mechanical speeds for the open circuit failure	87
4.29	Simulated phase currents for the short circuit failure	89
4.30	Actual phase currents for the short circuit failure	90
4.31	Simulated and actual mechanical speeds for the short circuit failure	91
4.32	Steady state noisy simulated and estimated phase currents for a 75.0 volt bus	93
4.33	Steady state noisy simulated and estimated mechanical speeds for a 75.0 volt bus	94
4.34	Steady state actual and estimated phase currents for a 75.0 volt bus	95
4.35	Steady state actual and estimated mechanical speeds for a 75.0 volt bus . . .	96
4.36	Steady state noisy simulated and estimated phase currents for a 150.0 volt bus	97
4.37	Steady state noisy simulated and estimated mechanical speeds for a 150.0 volt bus	98
4.38	Steady state actual and estimated phase currents for a 150.0 volt bus	99
4.39	Steady state actual and estimated mechanical speeds for a 150.0 volt bus . .	100
4.40	Steady state noisy simulated and estimated phase currents for a 200.0 volt bus	101
4.41	Steady state noisy simulated and estimated mechanical speeds for a 200.0 volt bus	102
4.42	Steady state actual and estimated phase currents for a 200.0 volt bus	103
4.43	Steady state actual and estimated mechanical speeds for a 200.0 volt bus . .	104

4.44	Noisy simulated and estimated phase currents for transient motor operation	105
4.45	Noisy simulated and estimated phase currents for transient motor operation (continued)	106
4.46	Noisy simulated and estimated mechanical speeds for transient motor operation	107
4.47	Actual and estimated phase currents for transient motor operation	108
4.48	Actual and estimated phase currents for transient motor operation (continued)	109
4.49	Actual and estimated mechanical speeds for transient motor operation	110
4.50	Simulated and estimated mechanical speeds for flux weakening failure . . .	112
4.51	Estimated fault resistance for the simulated open circuit failure	114
4.52	Estimated fault resistance for the simulated open circuit failure (continued)	115
4.53	Estimated fault resistance for the actual open circuit failure	116
4.54	Estimated fault resistance for the actual open circuit failure (continued) . . .	117
4.55	Estimated fault resistance for the simulated short circuit failure	119

CHAPTER 1

INTRODUCTION

As technology has continued to advance, so has man's ability to apply technology in innovative ways. Some of the leading advancements in technology application have arisen from the United State's space program. Guiding the development of research for the space program, the National Aeronautics and Space Administration (NASA) has actively sponsored work at The University of Alabama over the past few years. Under research grant NAG8-240, effort has progressed to examine the replacement of hydraulic actuator systems, used to position the space shuttle main engines, with electromechanical actuator (EMA) systems.

The task of positioning the shuttle main engines for thrust vector control (TVC) requires a high degree of reliability, a modest degree of accuracy in placement, and a high level of controllability. The EMA system under consideration for the TVC application consists of a roller or ball screw, gear box, redundant brushless permanent magnet machines, motor drive, and motor controller. Combined, these individual components transform electric power into linear motion. Each system component is being evaluated for compliance to the mission requirements.

Previous work led to the recommendation of utilizing a brushless permanent magnet machine (BPMM) as the prime mover for the EMA system in the TVC

application [1]. Current effort is proceeding to optimize the motor drive, controller, and to implement a health monitoring (HM) system. The concept of health monitoring entails observing specific machine measurements and deciding whether or not the motor is in a normal operating mode. Furthermore, if the measurements indicate that the machine is not functioning normally, the health monitoring system should detect the deviation and define which failure mode the motor has entered. For the brushless permanent magnet machine, four failure modes have been defined; flux weakening, bearing failure, armature open circuiting, and armature short circuiting [1]. The goal of the HM system is to discover the machine's transition out of a normal operating mode early enough and with enough accuracy to predict an impending fault. With this information, a control decision can be made to minimize load requirements of the motor or to even remove the motor from active service. Since the EMA has redundant prime movers, the loss of one motor from active service is not functionally debilitating.

Among various possible techniques for implementing a health monitoring system, the Kalman filter approach was selected primarily due to its flexibility and efficacious performance. Since the filter was first introduced in 1960 [2], numerous applications and innovations for the filter have been realized. The impact and utilization of the filter has been so great, that some have even stated that the Kalman filter represents the most widely applied and demonstrably useful result to emerge from the state variable approach of modern control theory [3]. The inherent beauty of the filter is that noisy measurements of a system are blended with a system model estimate to formulate the most likely status of operation for the system. Others have previously applied Kalman filtering techniques to power system fault detection scenarios with impressive performance results [4]. The filter has also been utilized for identification of specific machine parameters [5], and a similar

filtering approach utilizing state estimation techniques has been implemented for fault detection applications with induction motors [6].

By selectively choosing the system operational status from among several filters operating concurrently, an adaptive approach of the Kalman filter is realized. This adaptive approach not only filters the noisy measurements, but also enables the system to be modeled for various modes of operation, including the four fault modes. Thus, it is possible to perform the function of health monitoring by observing the transitions from a filter modeling normal operation to other filters modeling a progressive movement of the system into a particular fault mode.

1.1 Dissertation Objective

The principle purpose of this work is to verify the applicability of an adaptive Kalman filtering approach to the task of health monitoring a brushless permanent magnet machine. Enroute to this end, a detailed simulation for the permanent magnet machine has been developed. The simulation contains enough flexibility to describe various potential fault modes for the motor, and will form the basis for the system model used in the Kalman filter. A discrete Kalman filter has been realized for the motor, providing the feasibility for computer implementation and simulation. Finally, an adaptive Kalman filter has been formulated from combinations of various discrete filters. Simulation and laboratory experiments have been conducted with the adaptive filter strategy and substantiate this concept as a valid health monitoring technique. A literature survey of relevant topics has been conducted to gain insight into current techniques for accomplishing these tasks.

1.2 Dissertation Overview

The dissertation begins with a background and review of literature focused on permanent magnet machines, machine failure modes, health monitoring systems, and the Kalman filter. A theoretical discussion and presentation of the machine model, fault modes, discrete Kalman filter, and the adaptive Kalman filter is then presented in detail. Next, results from simulation studies and laboratory experiments are shown to verify the validity of this concept. Finally, a summary offers recommendations for the applicability of this approach with regard to real time processing, and also provides insight into future topics for research work in this area.

CHAPTER 2

BACKGROUND AND SURVEY

Arguably, the invention and advancement of the digital computer has singularly had the greatest impact on the promotion and application of technology in the twentieth century. The computer has spawned completely new patterns of thought and analysis on scientific and engineering problems. Furthermore, the processing capability that is available today has revolutionized solution techniques, making feasible what was only a decade ago impossible. One result of this process has been the utilization and refinement of state variable modeling techniques for various physical systems.

The brushless permanent magnet machine may be described as a state variable system, which can be expressed in discrete terms for digital simulation. Section one of this chapter details the development of brushless permanent magnet machine technology and outlines trends in the state variable approach for machine modeling. A discussion of potential motor fault scenarios is presented along with a brief overview of the impact to the machine for each fault. Next, strategies and techniques for health monitoring and fault prediction of state variable systems is presented. Selection criteria for the EMA motor health monitoring system is also reviewed. Finally, the Kalman filter, which relies upon the state variable system modeling approach, is introduced. In addition, recent literature is

presented which describes the implementation of an adaptive Kalman filtering approach as a health monitoring system for another application.

2.1 Brushless Permanent Magnet Machine Technology

Two types of brushless permanent magnet machines exist, the brushless dc motor (BDCM) and the permanent magnet synchronous motor (PMSM). Pillay and Krishnan [7] describe the different operating characteristics and control requirements for both motors. While quite similar in nature, the main difference between the machines is presented as the shape of the back electromotive force (EMF) waveform; which is sinusoidal for the PMSM and trapezoidal for the BDCM. The different EMF waveform shapes result from the arrangement of the stator windings and the shape of the permanent magnets, which can be either buried or surface mounted on the rotor [7]. The development of brushless permanent magnet machine technology has stemmed from the advancement of magnetic material composition. These newer materials allow for strong magnetic fields to be placed on the rotor, fields capable of producing substantial torque development. In addition, the expanding capabilities of high power electronic devices, which facilitate electronic commutation or switching for the stator, have revolutionized the implementation possibilities for the brushless technology.

Demerdash and Nehl [8] have developed a detailed dynamic model of the BDCM for use in an aerospace actuator application. Utilizing network graph theory techniques, a fourteenth-order state variable model for the motor and its associated drive components has been presented. A comparison of numeric simulation results and experimentally gathered machine data demonstrate a high correlation between the developed model and the actual system, even during transient phenomena. Rubaai and Yalamanchili [9] have presented a

computer modeling approach for design analysis of the brushless dc machine. Again, the simulation effort relies upon a state variable representation of the BDCM and allows the machine designer flexibility to vary specific motor parameters for optimization purposes. Consoli and Raciti [10] present a state variable approach to the analysis of the PMSM. The numeric simulation results are shown in comparison to experimentally gathered data to validate the state variable model.

In companion papers, Sudhoff and Krause [11, 12] present an average-value model for the brushless machine state variable equations by employing a few simplifying assumptions. The assertion is made that the BDCM is in fact a PMSM supplied with electrical energy from an inverter that regulates phase switching based upon rotor position [11]. Perhaps the most significant assertion is that the phase currents can be switched off instantaneously as dictated by the motor drive control strategy. This is a simplifying assumption of motor drive performance. However, the simulation and laboratory results indicate that only a small margin of error is introduced into the system model via this assumption.

Pillay and Krishnan [13] provide yet another description of brushless machine technology in state variable format. The scope of their work is to study the performance characteristics of the different motor drive and control strategies available for operating both the BDCM and PMSM. The simulation and experimental results indicate that the state variable machine model provides the capability for both transient and steady state operating phenomena to be accurately represented. The authors have extended their presentation and simulation of this study in companion papers [14, 15]. Again, both papers provide simulation and experimental results that substantiate the state variable approach for machine modeling.

One of the principle advantages contained in a state variable model description for a system is the accessibility of the system descriptive parameters for modification and change. This characteristic may be exploited to enable an accurate modeling of failure modes. Several modes of failure for brushless machine technology have previously been presented and discussed [1]. Therefore, the failure mode analysis for this research effort has been confined to four possible fault modes; bearing failure, flux weakening, armature phase open circuiting, and armature phase short circuiting.

Bearing failure can occur for numerous reasons, and is a complex disturbance to accurately model. Typically, system descriptive parameters like the viscous damping coefficient, system inertia, and load torque may be manipulated to model this failure [16]. If a brushless machine experiences excessively high temperatures for a substantial amount of time, the magnetic material of the rotor will begin to experience a degradation in flux capability. As a result, torque production will be decreased and the motor will begin to draw higher currents to maintain the load demand. Since the coefficient for the generated electromotive force is directly related to the flux capacity of the rotor, changing this descriptive system parameter is a reasonable strategy for modeling the flux weakening failure. Both the armature open circuit and short circuit failure modes involve changing the electrical phase parameters which are descriptive of the winding conductance. Again, a successful scheme for simulating the machine during these failure modes is to manipulate the system descriptive parameters (phase resistance, self, and mutual inductance), which are readily available within the state variable format.

2.2 Health Monitoring Techniques

Various schemes for machine fault detection are available today. The principle objective for the EMA machine health monitoring system is to detect and predict (in

real-time) an impending machine failure mode. Some detection techniques require expensive testing or diagnostic equipment and must be performed while the motor is out of service, or off line. Most often, these analysis procedures require a disturbance in system integrity, either through removing a machine component or by introducing a foreign substance into the machine system. Examples of these tests are particle analysis of the motor oil, designed to detect bearing wear, and radio frequency monitoring, which injects radio frequency signals into the stator to detect winding insulation wear based on changes in the measured signal patterns [16]. Other techniques, termed non-invasive, do not require the machine to be off line or otherwise out of service and do not compromise the system integrity. A few of the non-invasive approaches to machine health monitoring are the artificial neural network approach, spectral analysis of motor signals, and parameter estimation techniques [16].

The body of literature available today does not address the application of non-invasive health monitoring techniques to the brushless machine technology. However, significant information is available for understanding the implementation of these strategies for induction machines. Therefore, a survey of the literature available for the non-invasive techniques applied to induction motors has been conducted with the conjecture that the analysis technique could readily be used with the brushless machine technology and would obtain similar performance results or capabilities.

Chow, Sharpe, and Hung [16] present an artificial neural network (ANN) approach for fault detection of an induction machine. A study of two common machine faults, bearing wear and insulation failure resulting in a short circuit on the stator, has been conducted. The principle assertion for utilizing an ANN is that the nature of a fault mode for the motor is a highly nonlinear event. ANN techniques have been demonstrated to be

useful in situations dealing with nonlinear systems, and are demonstrated to be acceptable for fault detection.

Chow, Mangum, and Yee [17] have successfully shown that the artificial neural network approach for fault detection can be accomplished in real-time. Again, the two fault modes investigated were the bearing failure and stator short circuiting. A presentation is made for the learning scheme of the ANN and its performance in laboratory experimentation on fault detection.

Goode and Chow [18] extend the ANN concept by incorporating fuzzy logic techniques within the framework of an artificial neural network. This combination allows for an assessment of the general heuristic or qualitative information of the fault to be obtained. Once again, the bearing failure and stator short circuiting are studied, with successful results.

A second technique for fault detection in machines is the spectral analysis of current signals of the motor. Thomson [19] has utilized this scheme successfully for detecting the bearing wear and broken rotor bars for large three-phase induction motors. The basic premise for spectral analysis is that when a machine is experiencing fault conditions, characteristic spectral signatures contained in the current signals are observable.

Penman, Sedding, Lloyd, and Fink have recently suggested the use of spectral analysis of the axial leakage flux for detecting stator short circuit failure. In this approach, an axial leakage flux sensor is required to provide the data for spectral decomposition. One significant contribution to the fault analysis is the capability to predict the location of the short circuit. Results for laboratory experiments are presented to verify this technique. However, it should be noted that this scheme detects only one failure mode.

Farag, Bartheld, and Habetler [21] have combined the spectral analysis approach with a thermal model implemented on a microprocessor to provide on-line motor

protection. While this paper only proposes the technique in concept, significant detail and reference material has been provided to support the idea. An additional monitoring requirement for this scheme is the thermal sensor for the machine.

The utilization of system modeling techniques for fault detection via parameter estimation has also been explored. Cho, Lang, and Umans [6] employ a least-square-error estimator to predict various machine parameters. The analysis approach was shown to be sufficient for detecting broken rotor bars in an induction machine through stator phase resistance estimation. However, the authors describe a few limitations for this concept which may impact the widespread practical implementation of this technique.

Trutt, Cruz, Kohler, and Sottile [22] use a modeling approach toward machine fault detection to create a database of machine parameter deterioration trends. Again, the focus for this paper is on the induction motor, but the concept seems applicable to the brushless technology. Comparison of experimental observations with results from detailed modeling are presented to verify the capability of fault detection through trend analysis of motor parameters.

Of these three available non invasive monitoring techniques, only the parameter estimation approach enables a detailed quantification of the system behavior. While the other two schemes facilitate fault detection and prediction, they do not provide as much descriptive information of the system as desired for the EMA HM system. Furthermore, the ease of modeling the brushless permanent magnet machine as a state variable system readily facilitates the parameter estimation technique. Thus, the parameter estimation scheme was selected for implementation as the machine health monitoring system for this research application.

2.3 The Kalman Filter

Kalman's original work [2] spawned a plethora of research and development activity. Concurrently, the state variable approach for system modeling and analysis was being refined, with new applications for these techniques continually appearing in the literature. The impact of the digital computer upon the realm of engineering problem solution and formulation brought another wave of progress and advancement in this area.

The early work and development of state variable analysis and the Kalman filter has been historically chronicled by Kailath [23], which lists 390 references of which approximately 140 concern the Kalman filter. As the realization of the technical capability available within this analysis framework grew, numerous variations of the Kalman filter appeared. Magill [24] was the first to introduce the concept of a parallel Kalman filter structure, which has since become known as the adaptive Kalman filter (AKF). This architecture allows for nonlinear system behavior to be processed, and creates the opportunity for system hypothesis testing. Brown [25] expands Magill's work to facilitate the testing of system hypothesis, which is the foundation of the health monitoring system.

Another popular implementation scheme of Kalman filtering for nonlinear systems is the extended Kalman filter (EKF). Based on the strategy of linearization of the state estimate along a nominal system trajectory, the EKF has recently been utilized for estimating PMSM parameters [26]. While the authors present an intriguing scenario, several limitations exist for choosing the EKF as a health monitor. The principle objection, which will be elaborated in chapter 3, resides in the necessity of a small tolerance on the actual state deviation from the expected trajectory. Additionally, this application of the EKF is focused on processing data for the PMSM while operating in a normal mode

without the capability of handling failure modes. Nonetheless, the EKF has experienced widespread use in machine parameter estimation and control [27-29].

Within the framework of a health monitoring system, the AKF has been successfully implemented for various systems. Girgis has numerous articles (e.g., [4]) relating the application of Kalman filtering and adaptive Kalman filtering to power system condition monitoring. Chowdhury, Christenson, and Aravena [30] extend Girgis's work by developing a power system fault detector using hypothesis testing capabilities with successful results.

Companion papers by Maybeck, Hanlon, and Menke [31, 32] contain an implementation strategy of the AKF that most closely reflects the scheme which is used in this research work. Although the aircraft system discussed in the articles is not directly comparable to the brushless permanent magnet machine system, the technique of application and filter formulation contains valuable information. Furthermore, since the authors employ a state variable modeling approach for their system, the expectation of achieving similar performance results is reasonable.

Several research objectives were defined as a result of this background survey of technical literature related to the brushless permanent magnet machine, health monitoring systems, and the Kalman filter. Without question, developing an accurate state variable model for the brushless permanent magnet machine should be a realistic task. Furthermore, a descriptive implementation of the various failure modes for the machine within the state variable model should also be a realizable goal. Finally, given the successful implementation of the adaptive Kalman filter as an HM system for other applications, developing an AKF scheme for the BPMM HM system seems to be a worthwhile pursuit.

CHAPTER 3

MODEL DEVELOPMENT

This chapter presents the theoretical development of the various models employed throughout this research effort. The most fundamental modeling procedure describes the operation of the brushless permanent magnet machine, from both electrical and mechanical vantage points. Based upon the final state-space description of the machine, four distinct failure modes have been modeled. The discrete Kalman filter equations are shown utilizing the machine state-space model as the stochastic system or plant model. Additionally, a computer routine used extensively throughout the system simulation work for generating gaussian white noise is presented. Finally, the adaptive Kalman filtering approach for health monitoring of the machine is developed.

3.1 The Brushless Permanent Magnet Machine Model

Much modeling and simulation work has been focused on the emerging area of brushless permanent magnet machine technology [5, 7-15]. One commonly used electrical diagram for these machines is shown in Figure 3.1. Notice that the diagram contains both the machine and its associated power electronic drive. The transistors simply function as switches, and are themselves regulated by additional electronic equipment (not shown).

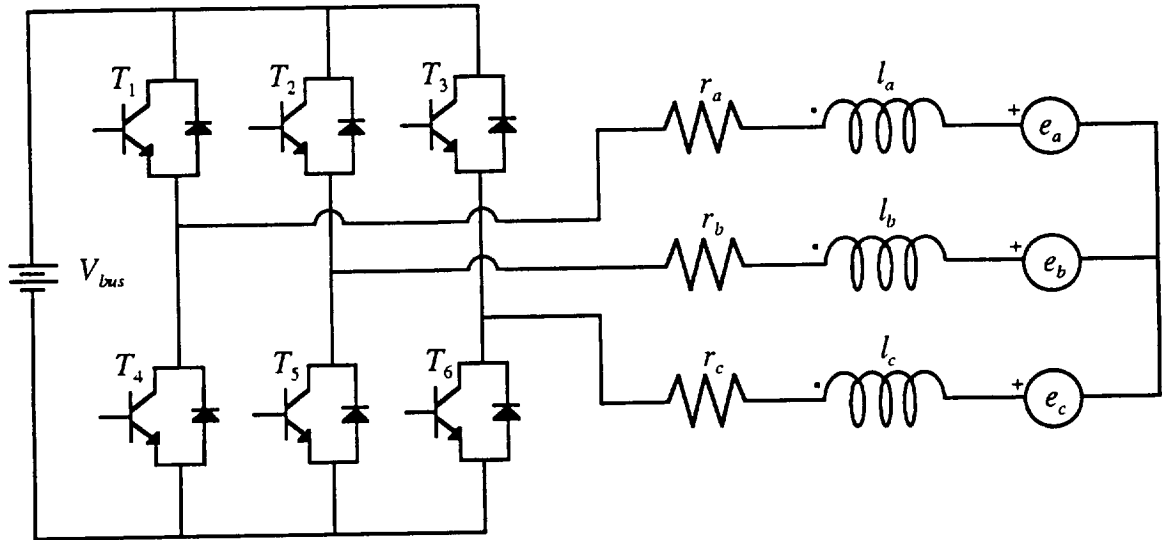


Figure 3.1 BPMM and power electronic motor drive electrical schematic

Region	Transistor Status						Angular Rotor Position
	1	2	3	4	5	6	
I	*	*	on	*	on	*	$330 < \theta_e \leq 30$
II	on	*	*	*	on	*	$30 < \theta_e \leq 90$
III	on	*	*	*	*	on	$90 < \theta_e \leq 150$
IV	*	on	*	*	*	on	$150 < \theta_e \leq 210$
V	*	on	*	on	*	*	$210 < \theta_e \leq 270$
VI	*	*	on	on	*	*	$270 < \theta_e \leq 330$

* denotes transistor off status

Table 3.1 Power electronic transistor status for motor operation

Typically, based upon knowledge of the angular rotor position obtained from Hall effect sensors or resolvers, the drive transistors are switched on or off to create the necessary rotating stator magnetic field for torque production and rotor motion. The switching sequence for the motor drive power electronic transistors is shown in Table 3.1, which defines six distinct switch operating regions for the machine.

Since the focal point of this research effort does not include monitoring the health of the motor drive, a simplified model for the switching action of the drive has been developed. Based upon modeling techniques for a three phase inverter [33], Figure 3.2 presents the machine with the simplified motor drive model. Notice that the six transistors have been functionally replaced with three switch resistors, each assuming one of two states. When a transistor is 'on' the switch resistance is low, and when a transistor is 'off' the switch resistance is high. The operation of the simplified motor drive is correlated with the actual drive as summarized in Table 3.2. Figure 3.3 shows the voltage waveforms for v_1 and v_2 versus rotor electrical angle position [33]. Thus, the switch resistors and the two voltage sources shown in Figure 3.2 are completely determined by angular rotor position.

Operation of the actual motor drive requires transistor switch commands based upon signals which describe the rotor electrical angle position. The laboratory BPMM was not equipped with Hall effect sensors, so data from a resolver chip was used to create pseudo Hall signals. Since these signals are binary and have a high signal to noise ratio, they are, practically speaking, immune to data corruption due to noise. Therefore, accurate knowledge of the rotor electrical angle position is readily available information that will be utilized throughout the remaining research effort as a control input for the machine model.

Regardless of the status of the switch resistors, Figure 3.2 can be analyzed electrically by using Kirchhoff's voltage law with an appropriate analysis technique.

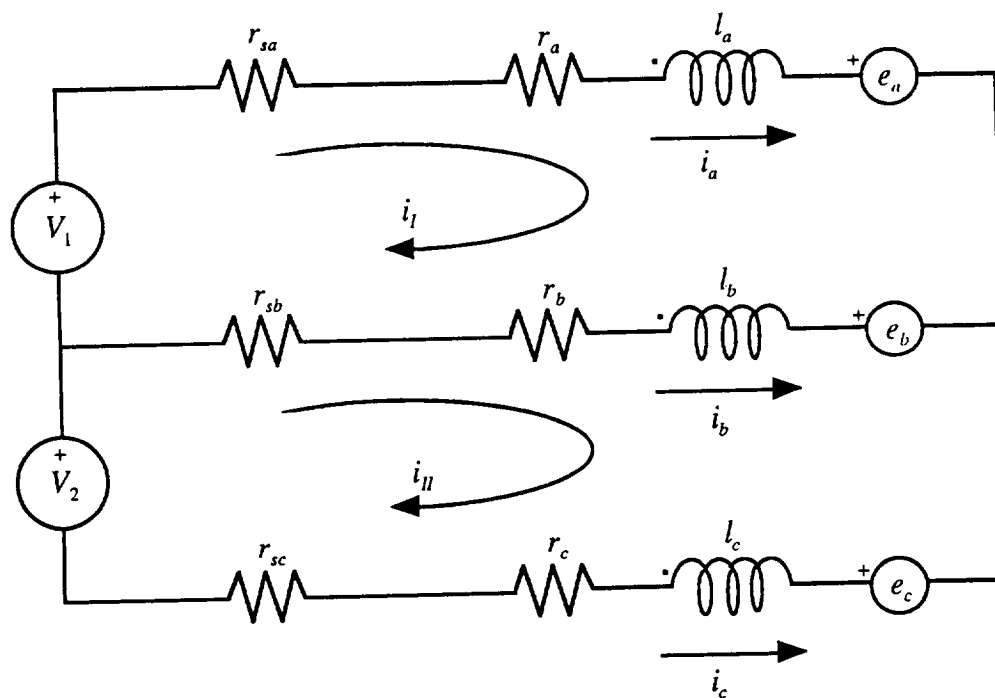


Figure 3.2 BPMM and simplified motor drive electrical schematic

Region	Transistor Status						Simplified Model			Angular Rotor Position
	1	2	3	4	5	6	r_{sa}	r_{sb}	r_{sc}	
I	*	*	on	*	on	*	high	low	low	$330 < \theta_e \leq 30$
II	on	*	*	*	on	*	low	low	high	$30 < \theta_e \leq 90$
III	on	*	*	*	*	on	low	high	low	$90 < \theta_e \leq 150$
IV	*	on	*	*	*	on	high	low	low	$150 < \theta_e \leq 210$
V	*	on	*	on	*	*	low	low	high	$210 < \theta_e \leq 270$
VI	*	*	on	on	*	*	low	high	low	$270 < \theta_e \leq 330$

* denotes transistor off status

Table 3.2 Power electronic transistor status and simplified motor drive model

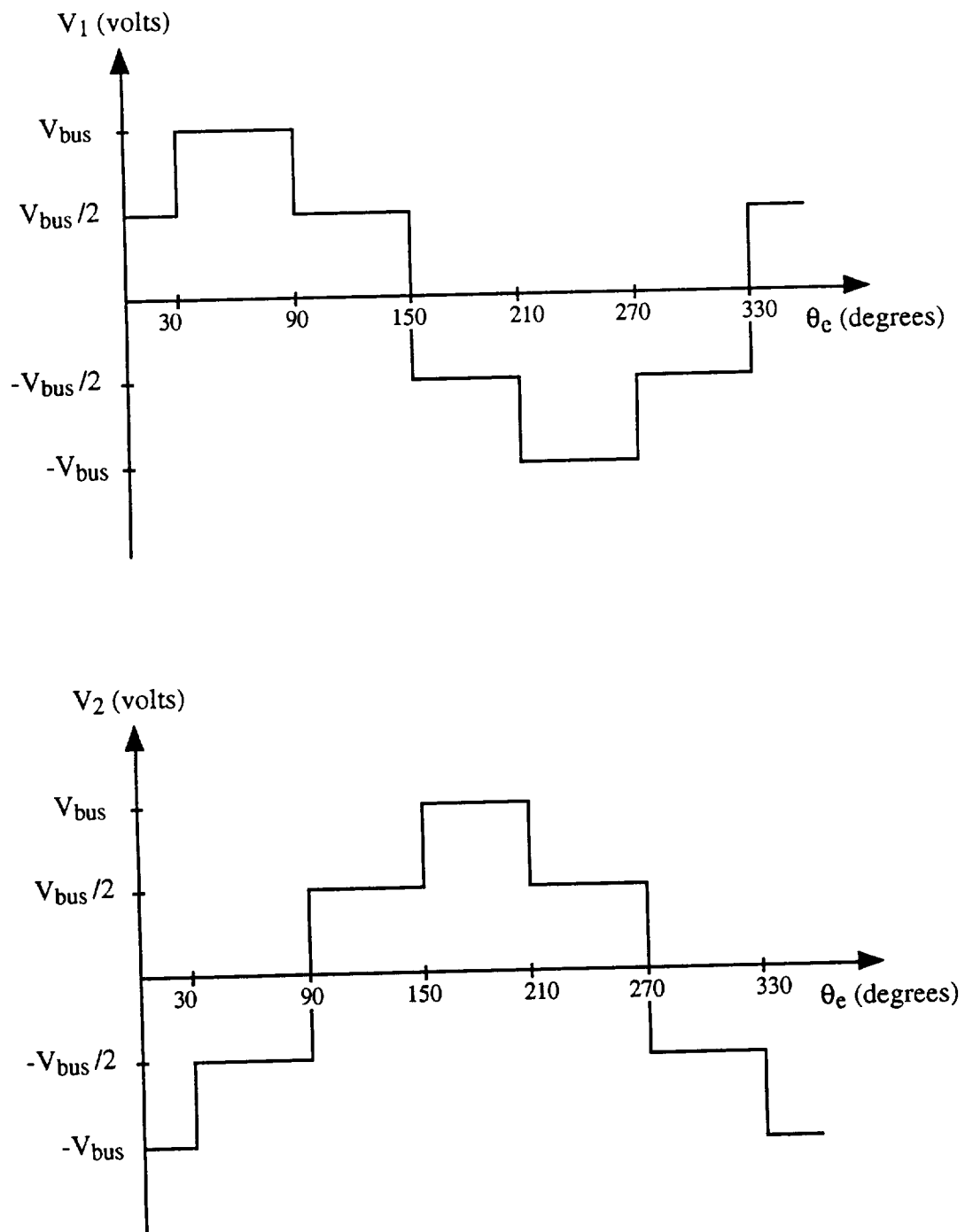


Figure 3.3 Voltage waveforms of the simplified motor drive model

Utilizing the inductor dot notation to define the mutual inductance between phase windings (m_{ab} , m_{ac} , m_{ba} , m_{bc} , m_{ca} , and m_{cb}), mesh analysis yields the following,

$$\begin{aligned} -v_1 + r_{sa}i_l + r_a i_l + l_a \frac{di_l}{dt} + m_{ab} \left(\frac{di_{II}}{dt} - \frac{di_l}{dt} \right) + m_{ac} \left(-\frac{di_{II}}{dt} \right) + e_a - e_b + \\ l_b \left(\frac{di_l}{dt} - \frac{di_{II}}{dt} \right) + m_{ba} \left(-\frac{di_l}{dt} \right) + m_{bc} \left(\frac{di_{II}}{dt} \right) + r_b (i_l - i_{II}) + r_{sb} (i_l - i_{II}) = 0 \end{aligned} \quad (3.1a),$$

$$\begin{aligned} -v_2 + r_{sb} (i_{II} - i_l) + r_b (i_{II} - i_l) + l_b \left(\frac{di_{II}}{dt} - \frac{di_l}{dt} \right) + m_{ba} \left(\frac{di_l}{dt} \right) + m_{bc} \left(-\frac{di_{II}}{dt} \right) + \\ e_b - e_c + l_c \left(\frac{di_{II}}{dt} \right) + m_{cb} \left(\frac{di_l}{dt} - \frac{di_{II}}{dt} \right) + m_{ca} \left(-\frac{di_l}{dt} \right) + r_c (i_{II}) + r_{sc} (i_{II}) = 0 \end{aligned} \quad (3.1b).$$

Assuming that the individual phase parameters (resistance, self, and mutual inductance) are equivalent, which would be the normal case for a 'healthy' machine, equations (3.1a) and (3.1b) may be simplified as,

$$(2l - 2m) \frac{di_l}{dt} + (m - l) \frac{di_{II}}{dt} = -(2r + r_{sa} + r_{sb})i_l + (r + r_{sb})i_{II} + v_1 - e_a + e_b \quad (3.2a),$$

$$(m - l) \frac{di_l}{dt} + (2l - 2m) \frac{di_{II}}{dt} = (r + r_{sb})i_l - (2r + r_{sb} + r_{sc})i_{II} + v_2 - e_b + e_c \quad (3.2b),$$

where,

$$r = r_a = r_b = r_c \quad (3.2c),$$

$$l = l_a = l_b = l_c \quad (3.2d),$$

$$m = m_{ab} = m_{ac} = m_{ba} = m_{bc} = m_{ca} = m_{cb} \quad (3.2e).$$

From referring to Figure 3.2, it is apparent that the individual phase currents for the machine are related to the mesh currents as,

$$i_a = i_I \quad (3.3a),$$

$$i_b = i_{II} - i_I \quad (3.3b),$$

$$i_c = -i_{II} \quad (3.3c).$$

Combining the equations of (3.2) and (3.3) results in the desired electrical network representation for the machine,

$$\begin{bmatrix} (2l-2m) & (l-m) \\ (m-l) & (2m-2l) \end{bmatrix} \begin{bmatrix} \frac{di_a}{dt} \\ \frac{di_c}{dt} \end{bmatrix} = \begin{bmatrix} -(2r+r_{sa}+r_{sb}) & -(r+r_{sb}) \\ (r+r_{sb}) & (2r+r_{sb}+r_{sc}) \end{bmatrix} \begin{bmatrix} i_a \\ i_c \end{bmatrix} + \begin{bmatrix} v_1 \\ v_2 \\ e_a \\ e_b \\ e_c \end{bmatrix} \quad (3.4).$$

The back electromotive force terms are specified by a deterministic machine parameter, the mechanical speed of the rotor, and the electrical angular position of the rotor as,

$$e_a = K_b \omega_{mech} (\sin(\theta_e)) \quad (3.5a),$$

$$e_b = K_b \omega_{mech} (\sin(\theta_e - 120^\circ)) \quad (3.5b),$$

$$e_c = K_b \omega_{mech} (\sin(\theta_e + 120^\circ)) \quad (3.5c).$$

The operation of the machine may also be presented in a mechanical sense by describing the relationship of the physical torque production of the machine as the sum of the load torque, inertia acceleration, and viscous damping, commonly done as [14],

$$\tau_{dev} = \tau_{load} + J \frac{d\omega_{mech}}{dt} + B\omega_{mech} \quad (3.6).$$

The developed torque for the motor is related to the converted electric power by,

$$\tau_{dev} = \frac{e_a i_a + e_b i_b + e_c i_c}{\omega_{mech}} \quad (3.7).$$

Thus, combining equation (3.6) with (3.7) and rearranging terms yields,

$$\frac{d\omega_{mech}}{dt} = \frac{1}{J} \left(\frac{e_a i_a + e_b i_b + e_c i_c}{\omega_{mech}} - \tau_{load} - B\omega_{mech} \right) \quad (3.8).$$

The actual motor used in the laboratory experiments for this research effort was coupled by a gear box to a roller screw as depicted in Figure 3.4. Therefore, along with describing the motion of the rotor, the mechanical operating parameters in (3.8) additionally include the dynamics of the screw, nut, and gear box. The inertia coefficient in (3.8) may be analytically determined as [1],

$$J = J_{motor} + (n_{gear})^2 J_{screw} + J_{gear} + (n_{gear} p_h)^2 m_{linear} \quad (3.9).$$

Equation (3.9) uses the gear reduction (n_{gear}), the screw lead (p_h), and the total mass associated with linear motion (m_{linear}) to express the system inertia within the machine frame of reference. The inertia coefficient may also be determined experimentally, as

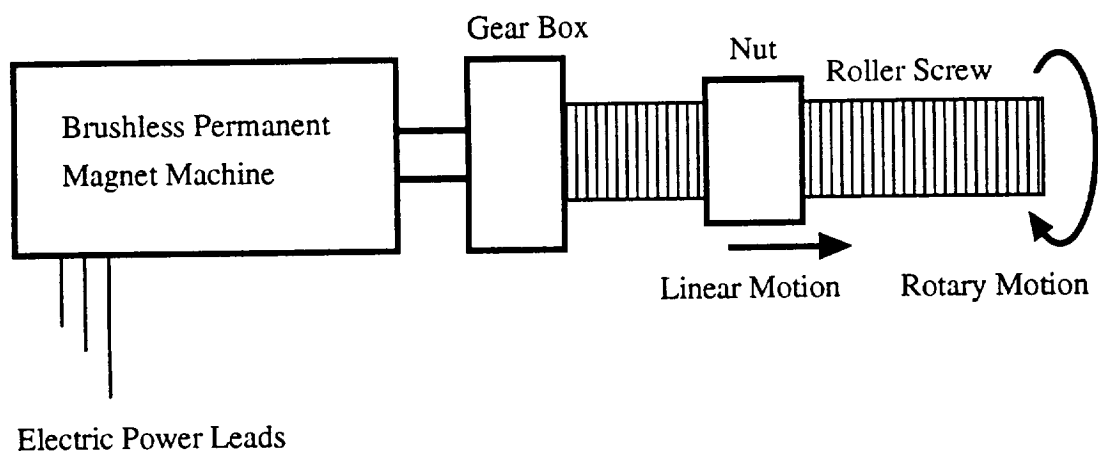


Figure 3.4 Electromechanical actuator system block diagram

presented in the next chapter. Additionally, from experimental data presented in Chapter Four, the viscous damping coefficient in equation (3.8) was found to be accurately modeled as a constant proportional to the mechanical speed. Thus, an accelerating torque may be defined as,

$$\tau_{acc} = \frac{e_a i_a + e_b i_b + e_c i_c}{\omega_{mech}} - \tau_{load} - c_{viscous} \quad (3.10).$$

Since the motor was a six-pole machine, three electrical revolutions occurred for each mechanical revolution of the rotor, thus,

$$\omega_e = 3\omega_{mech} \quad (3.11).$$

A complete set of equations describing the operation of the machine is obtained through merging equations (3.4), (3.5), (3.8), (3.10), (3.11), and Kirchhoff's current law,

$$\frac{d}{dt} \begin{bmatrix} i_a \\ i_c \\ \omega_e \\ \theta_e \end{bmatrix} = \begin{bmatrix} [L]^{-1}[R] & 0 & 0 \\ 0 & 0 & 0 \\ 0 & 0 & 1 \\ 0 & 0 & 0 \end{bmatrix} \begin{bmatrix} i_a \\ i_c \\ \omega_e \\ \theta_e \end{bmatrix} + \begin{bmatrix} [L]^{-1} \begin{bmatrix} 1 & 0 & -1 & 1 & 0 & 0 \\ 0 & 1 & 0 & -1 & 1 & 0 \\ 0 & 0 & 0 & 0 & 0 & 1/J \\ 0 & 0 & 0 & 0 & 0 & 0 \end{bmatrix} \begin{bmatrix} v_1 \\ v_2 \\ e_a \\ e_b \\ e_c \\ \tau_{acc} \end{bmatrix} \end{bmatrix}$$

$$i_a + i_b + i_c = 0 \quad (3.12).$$

The [L] and [R] matrices in (3.12) correspond to the inductance and resistance matrices described in (3.4). Restated in a traditional state-space format, this model is expressed as,

$$\dot{\underline{x}} = [A]\underline{x} + [B]\underline{u} \quad (3.13).$$

Along with the defined operation of the simplified motor drive contained in Table 3.2, the set of equations in (3.13) form the machine model that is used throughout the remaining work.

Since the machine simulation work will be accomplished with a digital computer, the set of differential equations in (3.13) are transformed into difference equations using a first order backward difference approximation technique as [34],

$$\frac{\underline{x}_{k+1} - \underline{x}_k}{\Delta t} = [A]\underline{x}_{k+1} + [B]\underline{u}_k \quad (3.14a),$$

$$\underline{x}_{k+1} = ([I] - \Delta t[A])^{-1} \underline{x}_k + ([I] - \Delta t[A])^{-1} \Delta t[B]\underline{u}_k \quad (3.14b),$$

which can be expressed as,

$$\underline{x}_{k+1} = [\phi_k]\underline{x}_k + [\theta_k][B]\underline{u}_k \quad (3.14c),$$

where,

$$[\phi_k] = ([I] - \Delta t[A])^{-1} \quad (3.14d),$$

and,

$$[\theta_k] = [\phi_k]\Delta t \quad (3.14e).$$

Equation (3.14c) expresses the state vector (\underline{x}) for the (k+1) time step as a combination of the previous state (\underline{x}_k) and control (\underline{u}_k) vectors. The relationship shown in (3.14c) forms a recursive state-space model suitable for computer implementation, requiring only an initial knowledge of the state and control vectors to commence simulation.

Notice that the control input vector containing the back EMF terms is based on the k^{th} time step, thus these inputs may be calculated using (3.5) with the known status of the state variables. Furthermore, the voltages within the control input vector are determined

according to Table 3.2 based on the known rotor electrical angular position. This same information additionally regulates the resistance value for each of the switch resistors. Thus, corresponding to the defined operating regions for the machine, six sets of $[\phi_k]$ and $[\theta_k]$ matrices in (3.14) are necessary for the simulation model. One of the tremendous results in this procedure is that non-linear operating performance of the brushless permanent magnet machine has been transformed into a model composed of six discrete linear state variable sets of equations.

3.2 Machine Failure Mode Models

Four distinct failure modes of the brushless permanent magnet machine are bearing failure, magnetic flux weakening, stator winding open circuiting, and stator winding short circuiting. The inherent beauty of the simulation model just developed is that all of the machine's mechanical and electrical operating parameters are available for manipulation and change. Thus, any possible machine fault that can be expressed in terms of these operating parameters is capable of being simulated.

Of the four fault types, bearing failure is clearly the most difficult to accurately model. Complete sections of textbooks are devoted to the study of bearing failure [35-37]. Perhaps quantifying the essence of this fault is so difficult because of the numerous ways that a bearing may fail. A few examples for bearing failure are the loss of bearing lubrication, particulate accumulation within the bearing, unusual bearing wear due to mechanical misalignment, and bearing performance degradation due to thermal constraints. Since the performance of the Kalman filter is heavily dependent upon the accuracy of the system model, the bearing fault mode has been excluded from this research effort. Future

study could endeavor to develop a reasonable system model for this fault which could be utilized by the Kalman filter.

Although the composition of magnetic materials has greatly advanced in recent years, the permanent magnets housed on the rotor of the machine are still susceptible to performance degradation due to magnetic flux weakening. Commonly resulting from operation in excessive temperatures, magnetic flux weakening decreases the capability of the machine to produce torque and reduces the generated back electromotive force. Hence, this fault may be implemented by altering the machine's back EMF constant used in (3.5) during simulation.

While the previous two fault modes were described by manipulating mechanical operating parameters, the remaining two fault simulations are accomplished by changing electrical operating parameters for the machine. When the windings of a stator phase experience deterioration leading to an eventual phase open circuiting, the associated phase resistance increases to infinity. Thus, phase winding open circuiting is modeled by transforming the appropriate electrical resistance parameter in (3.12) from a normal value to an infinite value. Figure 3.5 expands the BPMM electric diagram of Figure 3.2 to include a fault resistor, in this case on the 'A' phase of the motor. The fault resistor performs the necessary parameter transformation, and the model equations of (3.12) are adjusted to include this term. Set initially to zero, the ohmic value of the fault resistor is increased during the course of simulation to a sufficiently high resistance to be electrically considered infinite.

A stator winding short circuit failure may occur among two phase windings or between a single phase winding and electrical ground via the machine chassis. Figure 3.6 outlines the fault condition for two phase windings short circuiting together, in this case between the 'A' and 'B' phases. Notice that since this fault may occur at any point along the

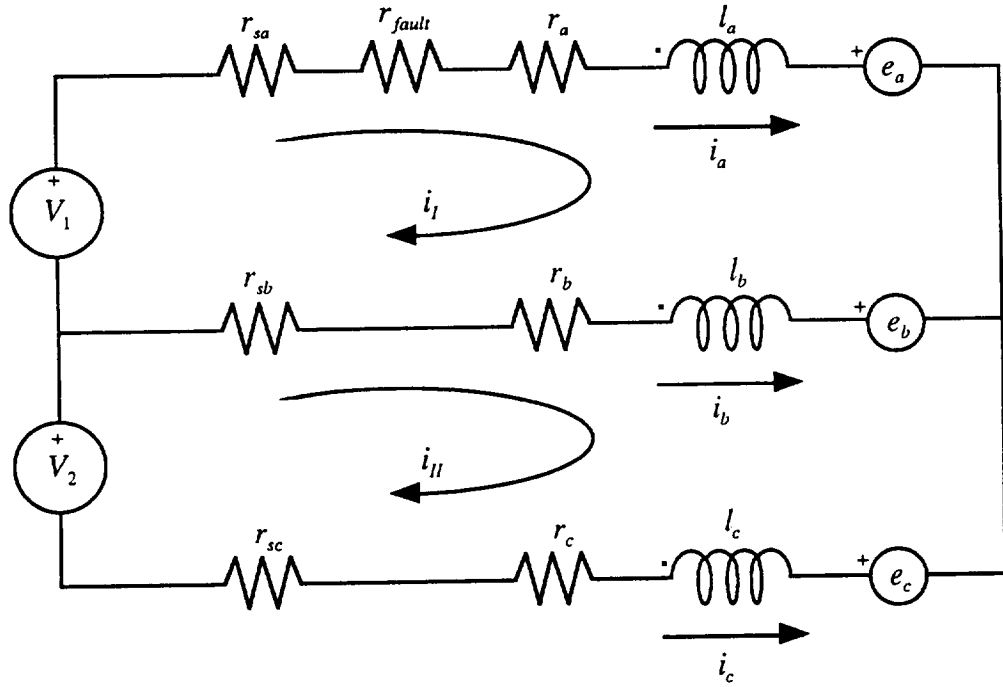


Figure 3.5 Electrical schematic for the open circuit failure mode

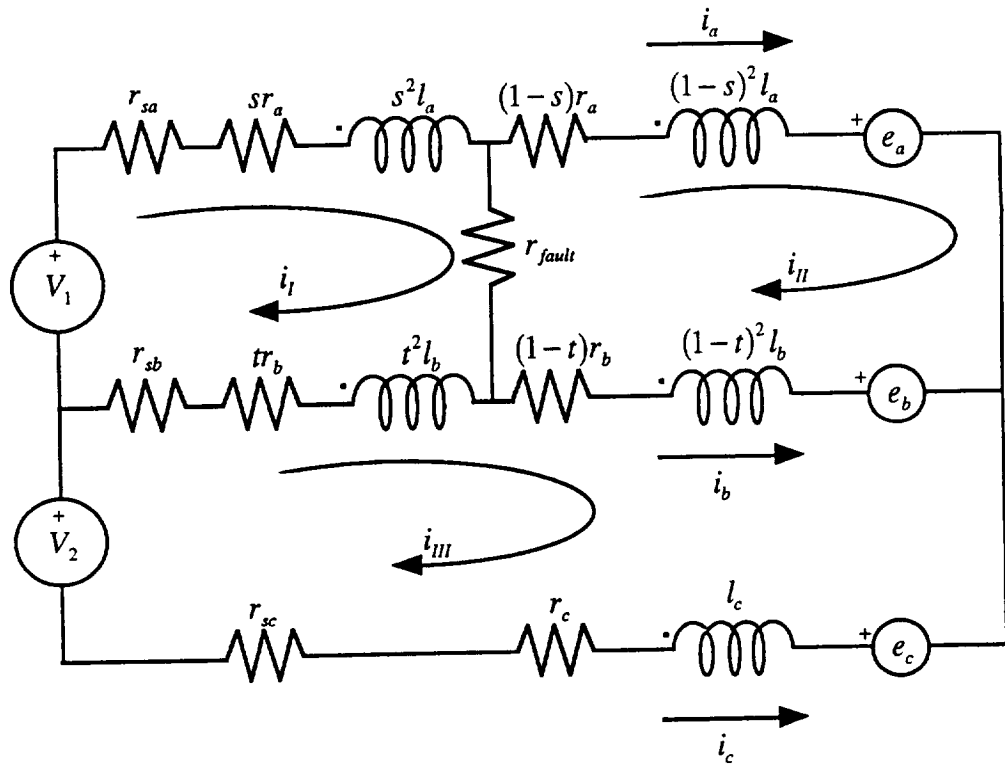


Figure 3.6 Electrical schematic for the interphase short circuit failure mode

windings, both affected phases have pre and post fault resistors and inductors in the diagram. The pre and post fault resistance values are linearly related by the percentage of winding turns at which the fault occurs, and sum to the original phase resistance. However, inductance is governed by the number of coil turns present in the winding [38]. Thus the self and mutual inductance values are assessed by calculating products of the percentage of winding turns. Thus, the equations in (3.4) are reevaluated based upon all of the parameter changes in the electric circuit diagram as,

$$[L] \frac{d}{dt} \begin{bmatrix} i_l \\ i_{ll} \\ i_{lll} \end{bmatrix} = [R] \begin{bmatrix} i_l \\ i_{ll} \\ i_{lll} \end{bmatrix} + \begin{bmatrix} -1 & 0 & 0 & 0 & 0 \\ 0 & 0 & 1 & -1 & 0 \\ 0 & -1 & 0 & 1 & -1 \end{bmatrix} \begin{bmatrix} v_1 \\ v_2 \\ e_a \\ e_b \\ e_c \end{bmatrix} \quad (3.15a),$$

and using (3.2c-3.2e),

$$[L] = \begin{bmatrix} 2s(t)m - (s^2 + t^2)l & (s^2 - 2st + t^2)m & t^2l - (s - st + t^2)m \\ (s^2 - 2st + t^2)m & 2(1-s)(1-t)m - (1-s)^2l - (1-t)^2l & (1-t)^2l + (s-1)(1-t)m \\ t^2l - (s - st + t^2)m & (1-t)^2l + (s-1)(1-t)m & (2t^2 - 2t + 2)(m-l) \end{bmatrix} \quad (3.15b),$$

$$[R] = \begin{bmatrix} (r_{sa} + r_{sb} + (s+t)r + r_{fault}) & -r_{fault} & -(r_{sb} + tr) \\ -r_{fault} & (r_{fault} + (2-s-t)r) & -(1-t)r \\ -(r_{sb} + tr) & -(1-t)r & (r_{sb} + r_{sc} + (2-t)r) \end{bmatrix} \quad (3.15c).$$

The values for s and t range between zero and one to represent the point at which the fault occurs.

Figure 3.7 depicts the scenario for a single phase winding short circuiting to electrical ground, in this case for phase 'A'. Once more, notice that since the fault condition

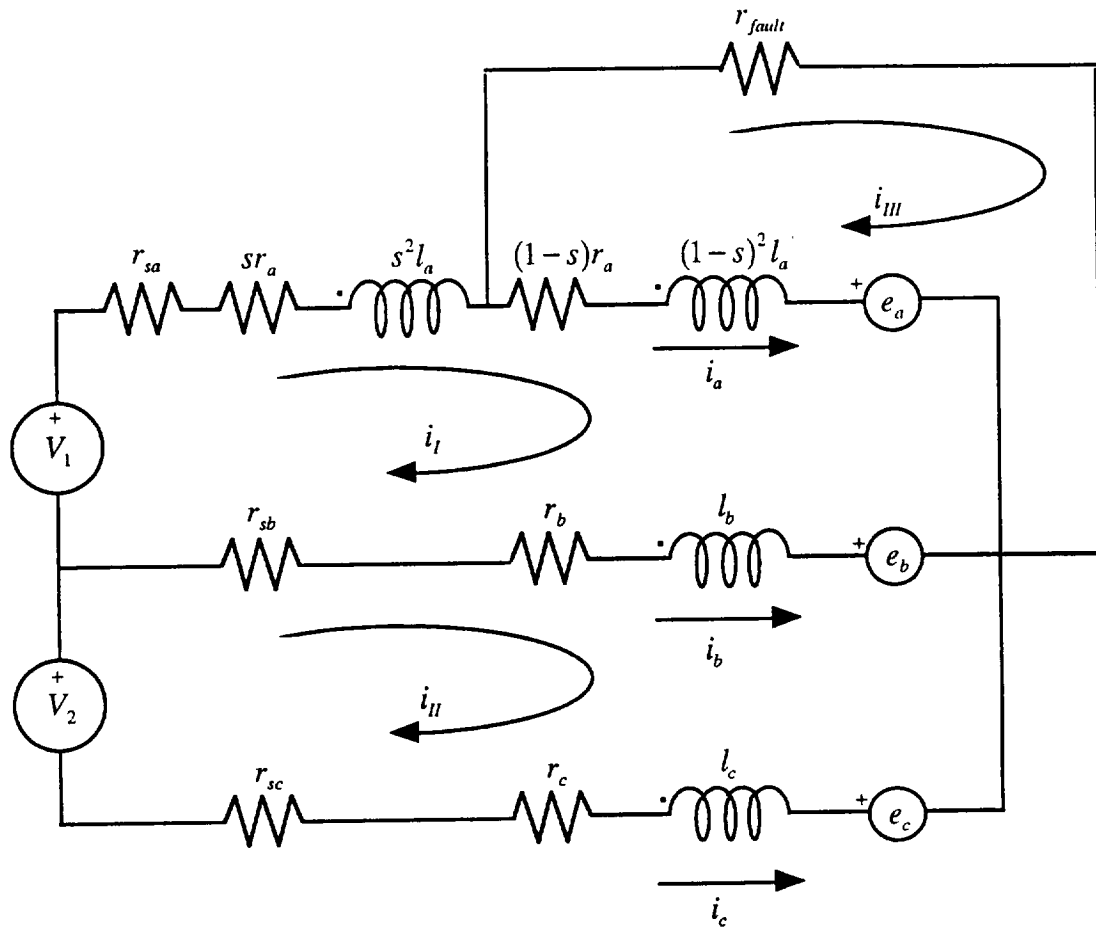


Figure 3.7 Electrical schematic for the intraphase short circuit failure mode

may occur at any point along the windings, the diagram includes both pre and post fault electric parameters. The faulted values for resistance and inductance are again calculated based upon knowledge of where the short occurred, and the equations in (3.4) are recalculated to reflect the parameter changes as,

$$[L] \frac{d}{dt} \begin{bmatrix} i_l \\ i_{ll} \\ i_{lll} \end{bmatrix} = [R] \begin{bmatrix} i_l \\ i_{ll} \\ i_{lll} \end{bmatrix} + \begin{bmatrix} -1 & 0 & 1 & -1 & 0 \\ 0 & -1 & 0 & 1 & -1 \\ 0 & 0 & -1 & 0 & 0 \end{bmatrix} \begin{bmatrix} v_1 \\ v_2 \\ e_a \\ e_b \\ e_c \end{bmatrix} \quad (3.16a),$$

again using (3.2c-3.2e),

$$[L] = \begin{bmatrix} 2(s^2 - s + 1)(m - l) & l - m & (1 - s)^2(l - m) \\ l - m & 2m - 2l & 0 \\ (1 - s)^2(l - m) & 0 & (1 - s)^2 l \end{bmatrix} \quad (3.16b),$$

$$[R] = \begin{bmatrix} (r_{sa} + r_{sb} + 2r) & -r_{sb} - r & (s - 1)r \\ -r_{sb} - r & (r_{sb} + r_{sc} + 2r) & 0 \\ (s - 1)r & 0 & r_{fault} + (1 - s)r \end{bmatrix} \quad (3.16c).$$

Once again, the value for s ranges between zero and one to represent the point at which the fault occurs.

3.3 The Discrete Kalman Filter Equations

Since the original presentation of his work in 1960 [2], R. E. Kalman's statistical processing technique for linear systems has been purported to be the most widely implemented and demonstrably utilized result from the state variable approach to modern control theory [3]. The technique, named in his honor as Kalman filtering, has been shown to yield statistically the optimal state estimate for a linear system [3]. Basically, three state variable estimation implementations for the filter exist; they are a system state variable predictor, a system state variable filter, and a system state variable smoother. The primary difference among the three estimation formats is contained in the time indexing for the state variable estimate. In other words, the predictor attempts to quantify the state values for future time, the filter formulation estimates state values occurring in present time, and the smoother implementation processes the state variable estimation for previous time. Regardless of which application is employed, Figure 3.8 presents a fundamental diagram conceptually depicting the processing operation of the filter loop.

To accomplish the goal of health monitoring for the brushless permanent magnet machine, the system state predictor format of the Kalman filter will be utilized. Since a digital computer will be utilized to implement the filter, the discrete Kalman filter will be presented within the context of the predictor structure for state variable estimation. The task of the filter will be to process, in discrete time steps, current noisy measurement data from the motor state variables to produce an optimal estimate for the future state of the machine. Ultimately, as will be presented in the next section, several filters will be operating concurrently to enable prediction of system failure.

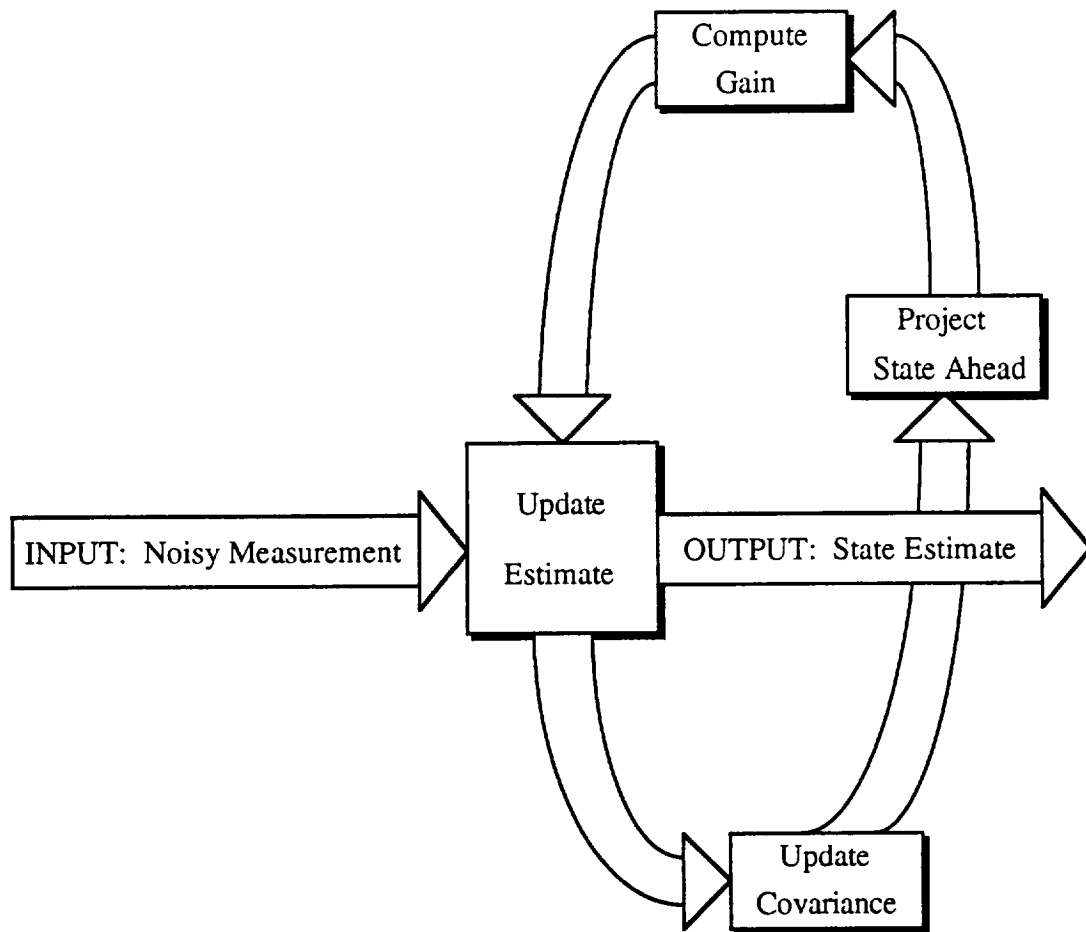


Figure 3.8 Block diagram of the discrete Kalman filter loop

The formulation of the predictor filter begins with describing the system in state variable format, a task already accomplished in section 3.1. The state variable model of equation (3.14) may be expanded to include a system noise vector (\underline{w}_k), a system measurement vector (\underline{z}_k), an observation matrix ($[H_k]$), and a measurement noise vector (\underline{v}_k) as,

$$\underline{x}_{k+1} = [\phi_k] \underline{x}_k + [\theta_k] [B] \underline{u}_k + \underline{w}_k \quad (3.17a),$$

$$\underline{z}_k = [H_k] \underline{x}_k + \underline{v}_k \quad (3.17b).$$

The measurement noise vector in (3.17b) accounts for data corruption occurring on the signals which measure state variables, while the system noise vector in (3.17a) describes the stochastic nature of the plant or system model. If the plant model is entirely deterministic, then the system noise vector may be considered as a quantification of the descriptive accuracy of the system model. Thus, for the BPMM application, the covariance structure of the system noise vector is functionally a measure of the confidence level for the plant model in equation (3.14).

The measurement vector in (3.17) is defined for the machine model as,

$$\underline{z}_k = \begin{bmatrix} i_a \\ i_b \\ i_c \\ \omega_{mech} \end{bmatrix} \quad (3.18).$$

The observation matrix in (3.17) which describes the ideal connection between the measurement and state vectors is,

$$[H_k] = \begin{bmatrix} 1 & 0 & 0 & 0 \\ 0 & 1 & 0 & 0 \\ -1 & -1 & 0 & 0 \\ 0 & 0 & 0.3142 & 0 \end{bmatrix} \quad (3.19).$$

Notice that the (4,3) entry of $[H_k]$ in (3.19) contains a conversion factor that changes the measured speed value from mechanical revolutions per minute to electrical radians per second. Furthermore, the noise vectors in (3.17) are assumed to be white sequences with zero cross correlation, thus the diagonal noise covariance matrices ($[Q_j]$ and $[R_j]$) may be described as [3],

$$E[\underline{w}_j \underline{w}_i^T] = \begin{cases} [Q_j], j = i \\ 0, j \neq i \end{cases} \quad (3.20a),$$

$$E[\underline{v}_j \underline{v}_i^T] = \begin{cases} [R_j], j = i \\ 0, j \neq i \end{cases} \quad (3.20b),$$

$$E[\underline{w}_j \underline{v}_i^T] = 0 \quad (3.20c).$$

Initiating the Kalman filter loop requires knowledge of the noise covariance in (3.20), knowledge of an a priori estimate for the state vector ($\hat{\underline{x}}_k^-$), and an understanding of the error covariance structure $[P_k]$ for the initial estimate. Once this information is obtained, the filter loop processes the system data according to Figure 3.9 along with the following equations [3],

$$[K_k] = [P_k^-][H_k^T]([H_k][P_k^-][H_k^T] + [R_k])^{-1} \quad (3.21),$$

$$\hat{\underline{x}}_k = \hat{\underline{x}}_k^- + [K_k](\underline{z}_k - [H_k]\hat{\underline{x}}_k^-) \quad (3.22),$$

$$[P_k] = ([I] - [K_k][H_k])[P_k^-] \quad (3.23),$$

$$\hat{\underline{x}}_{k+1}^- = [\phi_k]\hat{\underline{x}}_k + [\theta_k][B]\underline{u}_k \quad (3.24),$$

$$[P_{k+1}^-] = [\phi_k][P_k][\phi_k^T] + [Q_k] \quad (3.25).$$

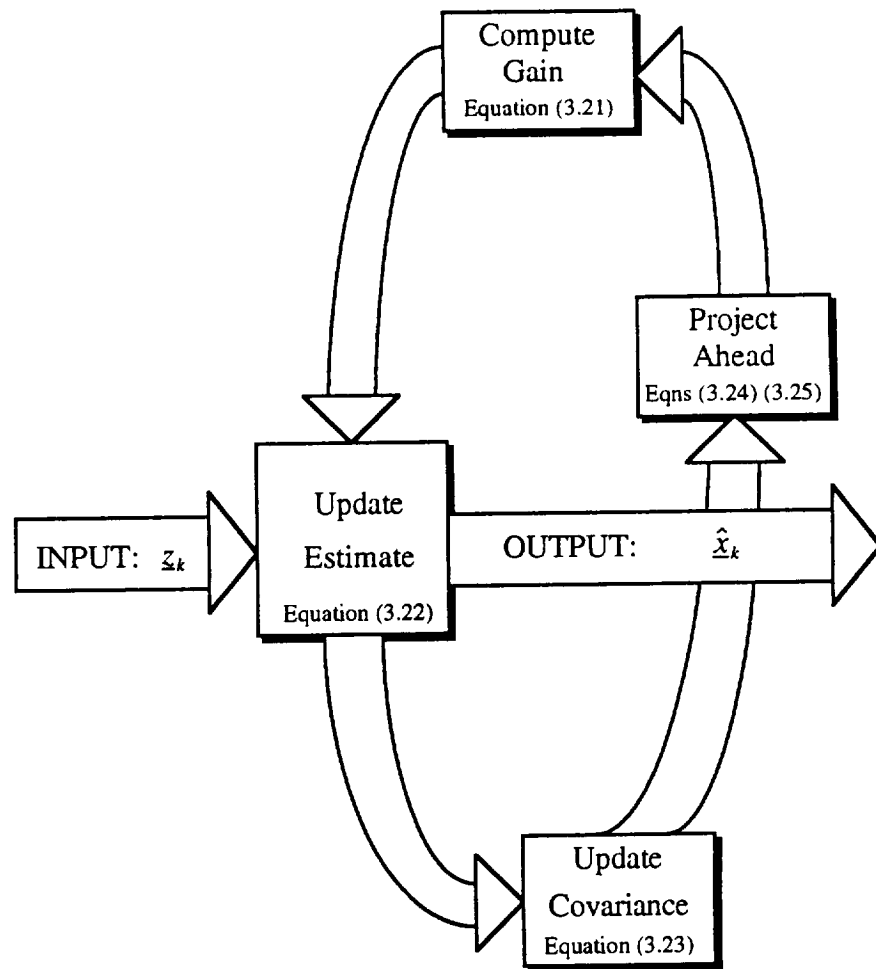


Figure 3.9 Expanded block diagram of the discrete Kalman filter loop

The $[K_k]$ matrix represents the Kalman gain and contains the optimal blending coefficients for adding the noisy measurement data to the current state vector estimate. The $[\phi_k]$ and $[\theta_k]$ matrices in (3.24) and (3.25) are the same matrices already developed in (3.14). Notice that the error covariance matrix for the state vector estimate, $[P_k]$ in equation (3.25), is not affected by the deterministic control input since it has no associated statistical uncertainty by definition. The equation set of (3.21 - 3.25) operating recursively as shown in Figure 3.9 forms the discrete Kalman filter.

Finally, implementation of the Kalman filter requires the presence of the noise sequences \underline{w}_k and \underline{v}_k . Thus, the capability for producing uncorrelated white noise sequences with gaussian distribution is necessary for the simulation studies of the Kalman filter. The basis for generating these random sequences stems from the work by Wichmann and Hill [39], which contains a random number generator conducive for computer implementation. The uniform distribution of this routine is transformed into a gaussian distribution via the central limit theorem [40]. Therefore, the variance of both noise sequences may be completely regulated within the simulation. These variances form the structure of the $[Q_k]$ and $[R_k]$ matrices found in equation (3.20).

3.4 The Adaptive Kalman Filter Equations

As previously mentioned, the principle goal for the health monitoring system of the brushless permanent magnet machine is to have the capability of predicting an impending motor failure. The failure modes of the motor have been described in section 3.3 as a deviation in either mechanical or electrical system parameters. Within the context of the Kalman filter, changes in the descriptive parameters may be thought of as a system

nonlinear behavior pattern. Thus, the health monitoring system is based upon a discrete Kalman filter variation capable of adequately addressing nonlinear system characteristics.

Three primary variations of the Kalman filter have been developed for nonlinear system applications; the linearized Kalman filter, the extended Kalman filter, and the adaptive Kalman filter. The linearized filter correlates the filter's performance along an unchanging nominal state space trajectory [3]. The structure of the extended Kalman filter is based upon a technique of linearization about a continually updated state space trajectory [3]. The adaptive Kalman filter processes nonlinear behavior through a set of Kalman filters with varying state models and selectively combines the estimated state space trajectories [3].

Essentially, the linearized and extended Kalman filters utilize the same strategy for adjusting the filter performance along a known or calculated state trajectory to successfully address the system nonlinear behavior. For systems having actual state trajectories with small deviation from the expected state trajectory, both techniques have found practical implementation with acceptable results [41]. However, the anticipated state trajectories for the BPMM system were expected to have significant perturbations off of nominal behavior (due to system failures), which was suspected to be problematic for the linearized Kalman filter technology. A simple approach was taken to verify this assertion by constructing both a linearized and an extended discrete Kalman filter for the circuit shown in Figure 3.10.

After the switch in Figure 3.10 is closed, current flows in the network as depicted in Figure 3.11. To simulate a fault condition, the resistance value in Figure 3.10 was increased at a particular time. Two different fault scenarios were constructed; one that was described by a small parameter change and another which was described by a large parameter deviation. Figures 3.12 and 3.13 depict the current flow in the circuit for a small

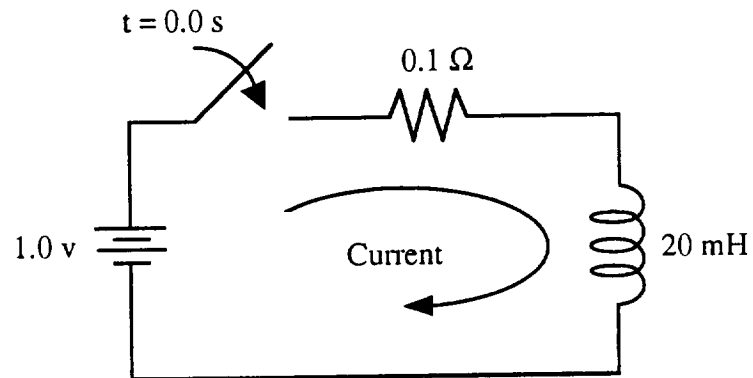


Figure 3.10 Simple RL circuit diagram for evaluating linearized Kalman filter schemes

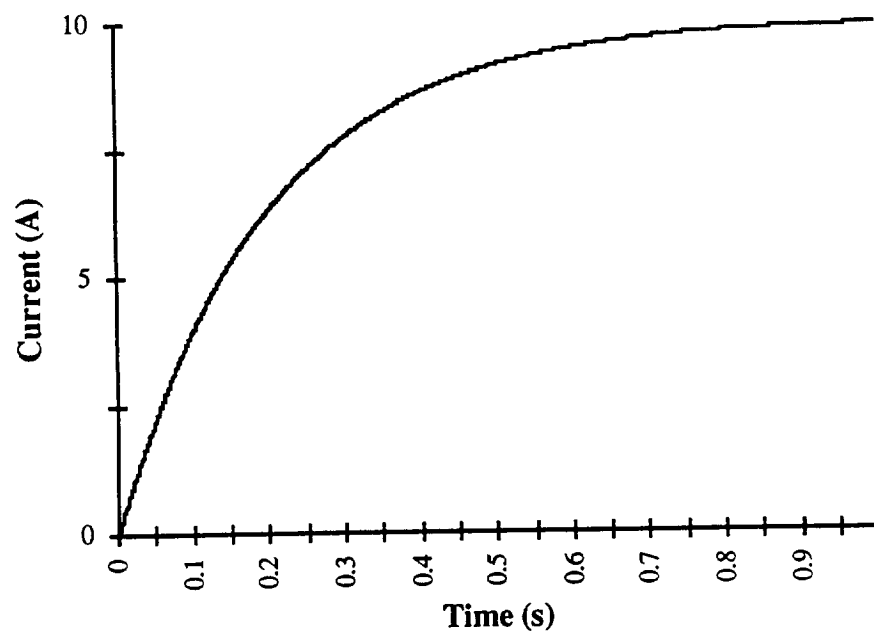


Figure 3.11 Simulated current with no parameter change

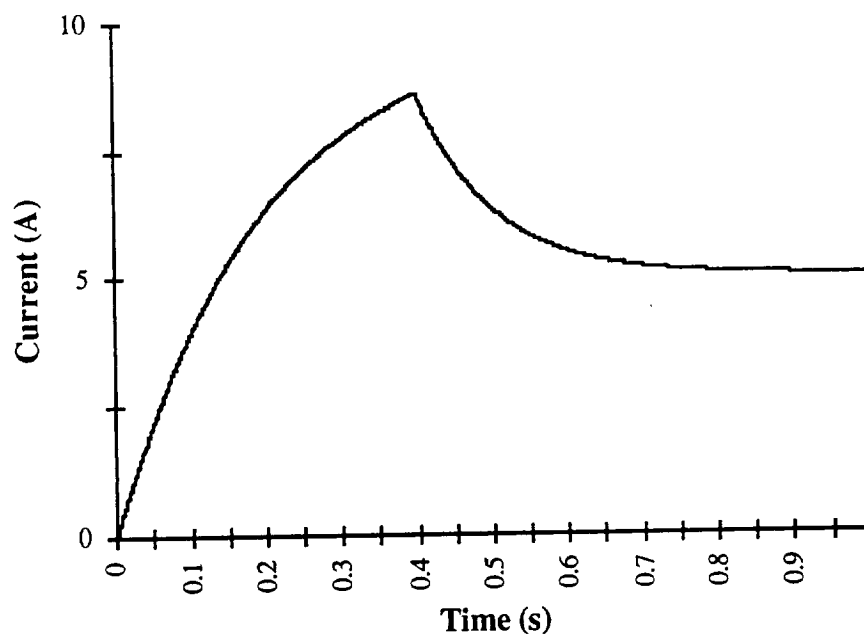


Figure 3.12 Simulated current with a small parameter change

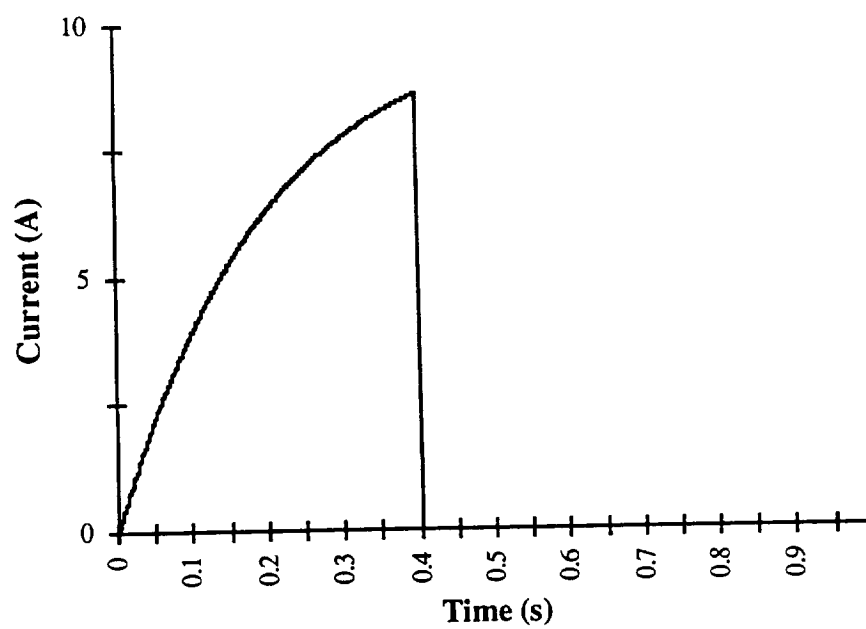


Figure 3.13 Simulated current with a large parameter change

increase in resistance (0.1Ω) and a large increase in resistance (100.0Ω) after 0.4 seconds.

The linearized and extended filters performed well when the circuit had no system parameter changes. Furthermore, both filters proved adequate when the circuit parameter deviation was small, as shown in Figure 3.14 and Figure 3.15 which only plot the filter's estimate for clarity. However, the filters had diminished performance when the circuit experienced a large parameter change. Notice that the linearized filter's estimate for the current, shown in Figure 3.16, has a significant steady state error after an increase in resistance. The extended filter's estimate for the current, shown in Figure 3.17, has a significant oscillation which eventually decays. From these results, it was determined to exclude the linearized and extended Kalman filter strategies from consideration as a health monitoring system. Thus, the adaptive Kalman filter was selected as the preferred approach for the HM application.

Various strategies for implementing an adaptive Kalman filter are possible. However, the conceptual foundation for constructing the filter is the same. Figure 3.18 depicts the general structure for the adaptive technique, which relies upon a parallel architecture of either discrete or continuous Kalman filters with varying system models. The diverse system models facilitate adjusting the descriptive system parameters to characterize the nonlinear behavior patterns. After each filter individually processes the system measurement, the updated state information from all filters is blended in a defined manner. The resulting estimate is propagated forward along with each filter's updated error covariance matrix. Thus, as the system progresses forward in time, the mathematics for each of the parallel Kalman filters must be calculated.

Developing an implementation strategy for the health monitoring application required addressing several issues. Since each machine failure mode may easily be described with a unique (or characteristic) set of state variable equations, the adaptive filter

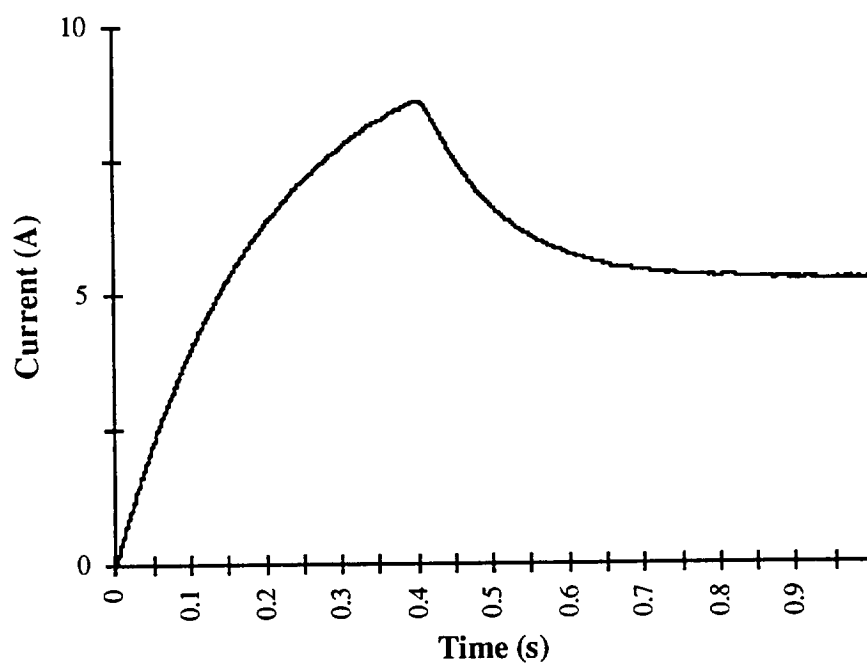


Figure 3.14 Linearized Kalman filter estimate with a small parameter change

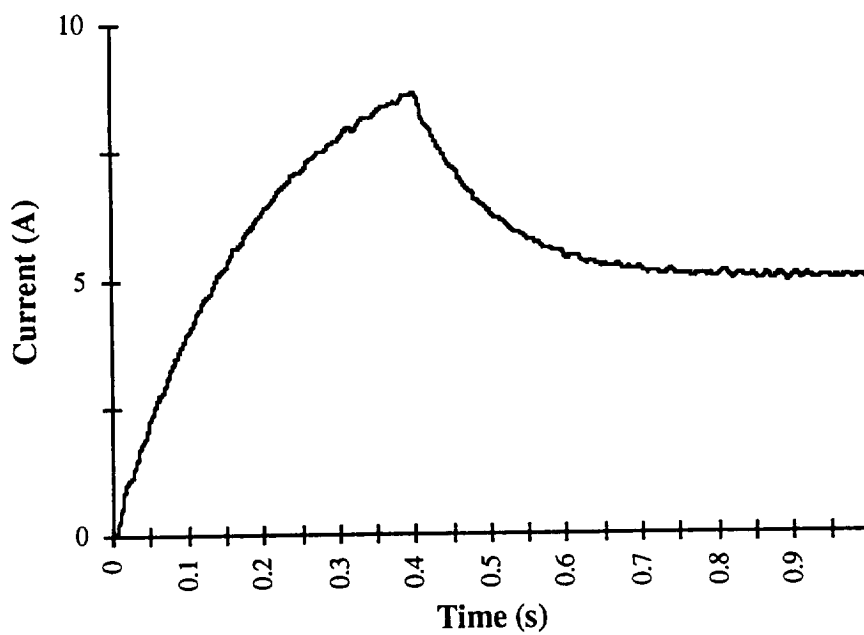


Figure 3.15 Extended Kalman filter estimate with a small parameter change

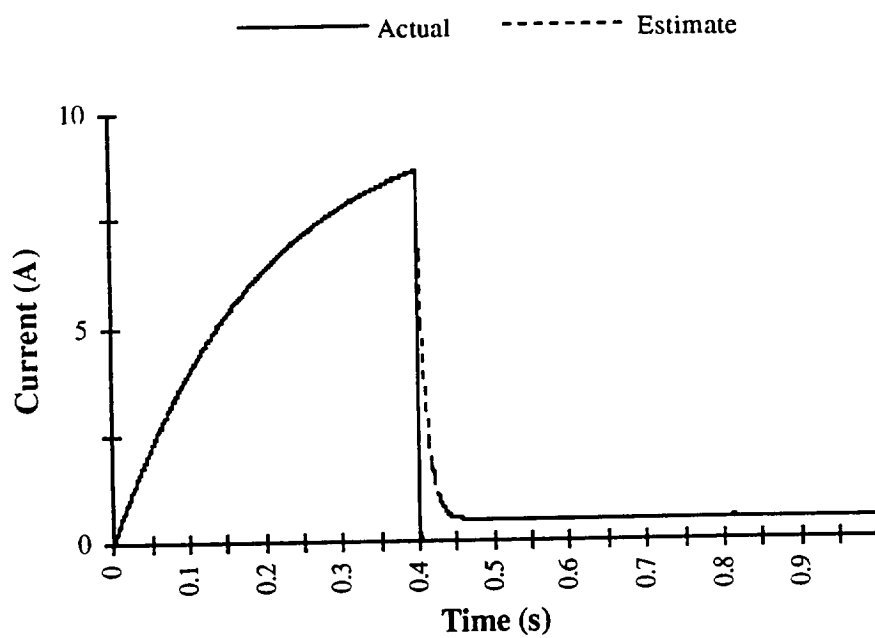


Figure 3.16 Linearized Kalman filter estimate with a large parameter change

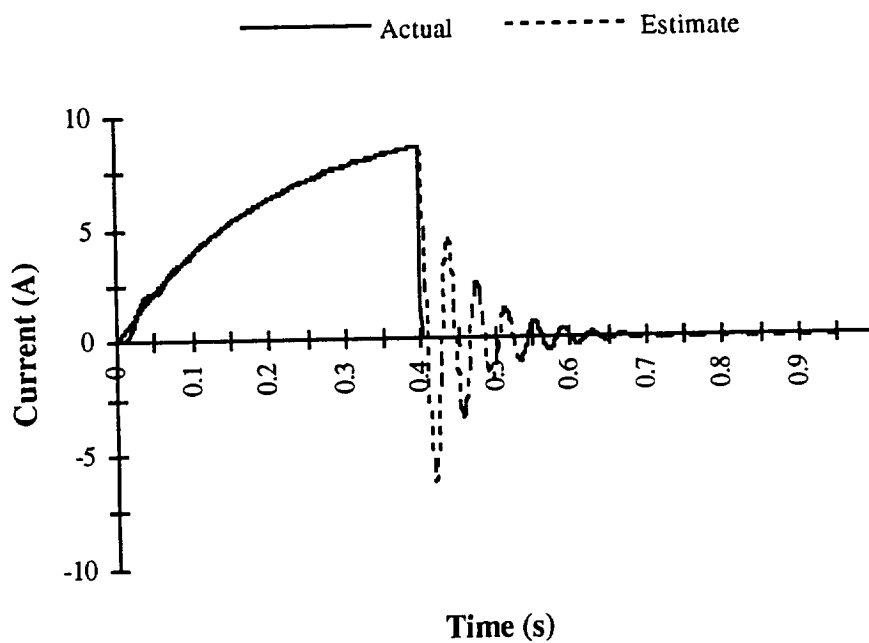


Figure 3.17 Extended Kalman filter estimate with a large parameter change

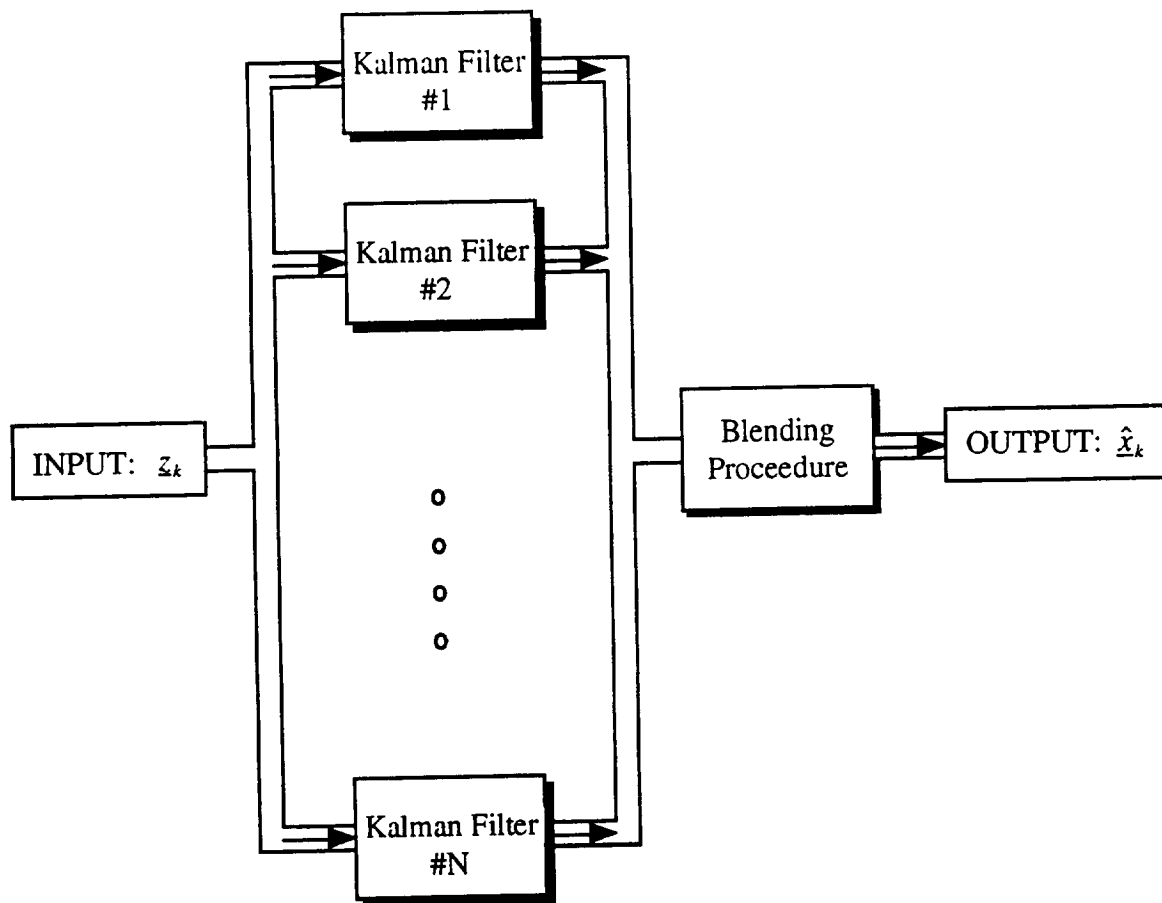
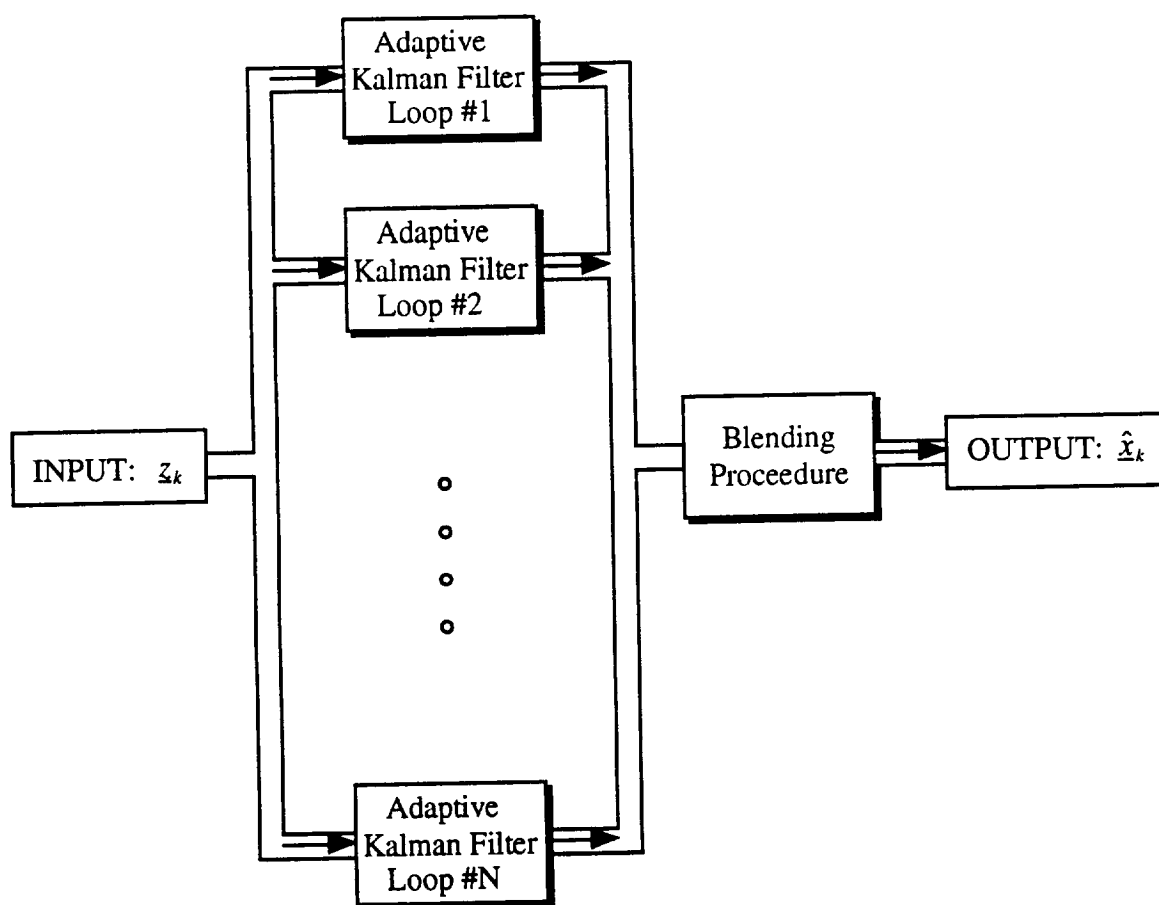


Figure 3.18 Block diagram of the adaptive Kalman filter loop

loop of Figure 3.18 may be individually applied to the specific machine failure modes. Conceptually, four sets of these loops operating concurrently (a three dimensional extension of Figure 3.18) would be required for the HM system. Figure 3.19 shows a generic block diagram for this three dimensional version of Figure 3.18. Since part of the HM system objective is to have real-time data processing capability, a minimum number of parallel filters was desired. Thus, a primary task was to decide on how many filters should be utilized within each adaptive loop and how each loop should accomplish the blending procedure.

To determine the minimum number of filters for the parallel structure, a quantification of computational burden was necessary. A typical method for assessing the computational burden of the Kalman filter is to tally the number of required floating point operations (FLOPs) to process the filter loop [42]. Without taking advantage of computational reduction or optimization strategies, a maximum FLOP count for the discrete filter, as constructed in section 3.3, was determined to be 1340 FLOPs per loop. The minimum acceptable time step for processing the discrete Kalman filter was evaluated to be 0.1 millisecond, see section 4.1 for details of this calculation. Therefore, for the HM application, operation of one discrete filter requires 13.4 million FLOPs per second.

A parallel architecture of five filters was initially selected for implementation, since the computational burden of 67.0 million FLOPs per second was close to the processing speed of the laboratory computer, see section 4.1 for equipment details. Additionally, choosing five filters appeared to facilitate a legitimate HM strategy by providing a reasonable number of transitional modes of machine operation. Obviously, the computational burden of four sets of adaptive filter loops operating concurrently (268 million FLOPs per second) would exceed the available processing capability. Therefore, an implementation scheme for detecting individual failure modes was chosen, with the



3.19 Block diagram of a parallel adaptive Kalman filter strategy

presumption that a parallel processing strategy could be developed in the future.

One other potential implementation strategy was defined and evaluated for the adaptive approach. Rather than selecting the bank of Kalman filters to depict an individual failure mode, the possibility exists to utilize the filter set to quantify an individual system descriptive parameter (i.e., resistance, inductance, viscous damping coefficient, etc.). Again, a parallel combination of filter loops would be required, as shown in Figure 3.19, to completely characterize the EMA system. As previously discussed, this type of parallel structure was determined to be beyond the available processing capability. Therefore, this concept was also abandoned for future development.

Different schemes for constructing the five filters were reviewed. As shown in Figure 3.20, an initial formulation for the adaptive filter loop enabled the system modeling of a normal mode, 25% of failure mode, 50% of failure mode, 75% of failure mode, and a complete failure mode. Conceptually, the HM objective would be realized through monitoring the selective transition of which filter more accurately described the system operation.

Before implementing this architecture, definition for the blending procedure was required. Again, the purpose of the blending procedure is to selectively combine and propagate the state estimate. With the intention of keeping the calculation as simple as possible, a weighted averaging scheme was developed. This scheme begins with a calculation of projection error for each Kalman filter as,

$$\epsilon^{(j)} = \left(\hat{z}_{k+1} - [H] \hat{x}_{k+1}^{(j)} \right)^2 [R] \quad (3.26),$$

with the (j) superscripts corresponding to the five Kalman filters (j=1,2,...,5). Notice that the calculation of error in (3.26) enables the inclusion of the statistical uncertainty for the state measurement ([R]).

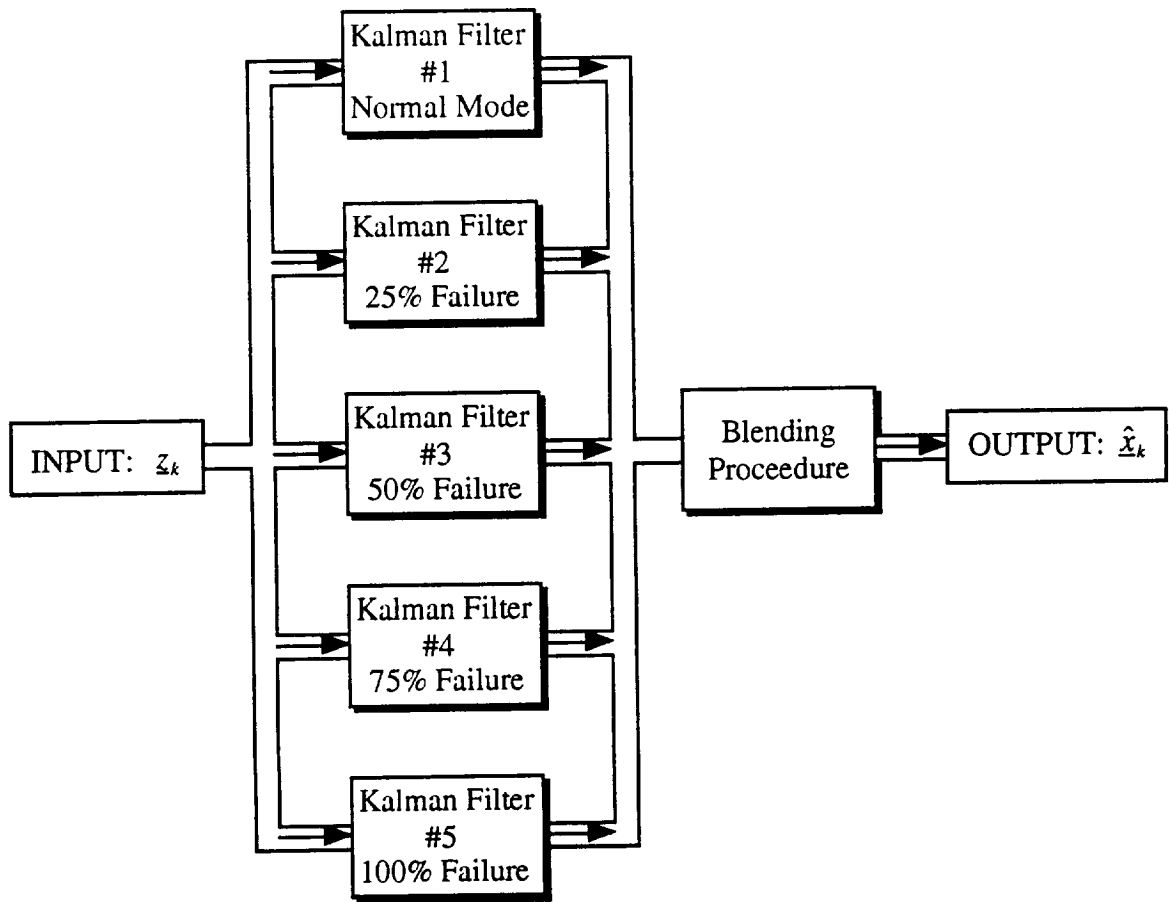


Figure 3.20 Expanded block diagram of the adaptive Kalman filter loop

Once the error for each filter has been determined, the two filters with the lowest error are chosen as the most probable state projections. These two errors are summed and a weighting factor for each filter is calculated as,

$$\Gamma_1 = 1 - \frac{\varepsilon_1}{\varepsilon_1 + \varepsilon_2} \quad (3.27a),$$

$$\Gamma_2 = 1 - \frac{\varepsilon_2}{\varepsilon_1 + \varepsilon_2} \quad (3.27b),$$

where the subscripts correspond to the two Kalman filters with the lowest projection error. If one of the weighting factors is greater than a defined tolerance, then the state projection from that filter is considered to be accurate and no estimate blending occurs. However, if both weighting factors are below this tolerance, then an evaluation is made to blend the state estimate as,

$$\hat{\underline{x}}_{k+1} = \Gamma_1 \left(\hat{\underline{x}}_{k+1}^{(1)} \right) + \Gamma_2 \left(\hat{\underline{x}}_{k+1}^{(2)} \right) \quad (3.28).$$

Furthermore, these weighting factors are utilized to calculate an estimated descriptive fault parameter.

For example, in the open circuit failure a fault resistance is included in the five Kalman filter system models. In this case, the normal mode filter has an extremely low fault resistance (no fault) and the other filters have progressively increasing values of fault resistance. An estimated fault resistance for this filter set would be calculated as,

$$R_{fault}^{est} = \Gamma_1 \left(R_{fault}^{(1)} \right) + \Gamma_2 \left(R_{fault}^{(2)} \right) \quad (3.29).$$

The goal of fault prediction would be realized through observing this estimated descriptive fault parameter and signaling a warning indication as the parameter exceeds a defined health limit. Since the BPMM faults are quantified through system parameter changes, an estimated descriptive fault parameter may be calculated for each failure mode.

CHAPTER 4

SIMULATION AND EXPERIMENTAL RESULTS

Both simulation and experimental results have been obtained from the electromechanical actuator system during numerous test procedures. After presenting a description of the laboratory test facility and equipment, the brushless permanent magnet machine model of section 3.1 is verified. Next, data is shown to substantiate the failure mode modeling of the machine. The applicability for using the Kalman filter technique with the BPMM operating in a normal mode is shown during several tests performed under various operating conditions. Finally, results are provided to verify the approach of using an adaptive Kalman filter as a health monitoring system for the machine.

4.1 Electromechanical Actuator Test Facility and Equipment

The Electromechanical Actuator Test Facility at The University of Alabama houses the EMA system and test equipment. As previously discussed, the EMA system consists of a roller screw, gear box, brushless permanent magnet machine, and motor drive. The EMA is mounted in a test frame designed and constructed at The University of Alabama for mechanically and electrically evaluating the performance of each element of the actuator

system. Therefore, the test frame is equipped with various control and instrumentation components necessary for conducting numerous experiments on the EMA.

Mechanically, the EMA system is comprised of a roller screw and a gear box. Translating rotational motion into linear movement, the laboratory EMA system uses an SKF Model SR48x20 R5 roller screw. The 48 millimeter (mm) diameter screw was equipped with a screw lead of 20 mm, was rated at a dynamic loading of 217.2 kiloNewtons (kN) (385.2 kN static loading), and contained no preload on the nut. The nut had a mass of 4.2 kilograms (kg) and an inertia of $6529 \text{ kg}(\text{mm})^2$ per meter. The screw shaft had a mass of 14.2 kg and an inertia of $4098 \text{ kg}(\text{mm})^2$ per meter. Coupling the motor to the screw, an AccuTrue Model #AT014-004-50 true planetary gear head manufactured by Micron with a 4 to 1 gear ratio was selected for the test system.

Electrically, the EMA system is comprised of a brushless permanent magnet machine and a motor drive. The BPMM chosen for this experimental application was a Kollmorgen Gold-Line model B-802-B-B3 brushless synchronous machine. The manufacturer has rated the machine's phase resistance at 0.1Ω , the phase inductance at 9.4 milliHenry, and the back EMF constant at 76.0 volt/kRPM. The power electronic motor drive used for operating the machine during the EMA experiments was designed and constructed at The University of Alabama. Based upon standard six-pulse power converter technology using insulated gate bipolar transistors (IGBT), the design and fabrication details for the motor drive are presented in [43].

The central resource for computer control and data observation in the EMA laboratory is a Gateway 2000 486-DX2 66 megahertz computer. The primary use of the computer system in this research effort was for data acquisition (DAQ) and analysis. Housed within the computer is a Computer Boards Inc., data acquisition card model #CIO-DAS16/330. Programming the DAQ system was accomplished through both the

manufacturer-supplied software library routines and the Microsoft Quick Basic programming language. Specific programs, contained in the Appendix, were developed for calibrating the system and for using the DAQ to obtain analog information on all sixteen channels. Additionally, a Computer Boards Inc., sample and hold card model #CIO-SSH16 was used with the data acquisition system to facilitate simultaneous data acquisition of all sixteen channels.

The received signals at the data acquisition board were sampled at a frequency of 10.0 kiloHertz (kHz). Frequency analysis performed on the various measured signal waveforms indicated that the most rapidly varying signal was the phase current signals, with a maximum frequency content of approximately 500.0 hertz. Thus, a sampling rate of 1.0 kHz was required on all signals to ensure compliance with the Nyquist sampling criteria [44]. Additionally, an evaluation was performed to determine the minimum time step necessary for motor simulation accuracy. Since the BPMM was rated at a maximum mechanical speed of 2750 RPM, the maximum electrical speed would be 864.0 radians per second. Because the motor simulation is regulated by the six rotor position regions, each having a range of 60 electrical degrees, the sampling frequency must be high enough to enable the accurate electrical description of rotor motion. For a sampling frequency of 1.0 kHz, which met or exceeded all of the calculated Nyquist sampling rates, motion of the rotor will traverse 49.5 electrical degrees. This obviously will yield inaccurate simulation performance, therefore the sampling frequency of 10.0 kHz was chosen as the basis for the data sampling frequency.

The data gathered for motor operation analysis included the following: dc bus voltage, the three line voltages, dc bus current, the three line currents, the three pseudo Hall effect signals (see section 3.1), mechanical rotor speed, and a few motor control signals. Since the laboratory tests were conducted at full duty cycle operation (no control action) of

the motor, the control signals were not pertinent for this research work. The currents were measured using Microswitch model #CSLA1CF linear output Hall effect sensors with a maximum current rating of 100 amperes. The voltage signals were obtained from voltage divider circuitry, while the rotor speed and pseudo Hall effect signals were derived from the resolver chip data. All of the measured waveforms reached the DAQ board at a signal range of ± 10.0 volts, and were converted within the DAQ programs to the appropriate signal unit values (amperes, revolutions per minute, etc.).

The armature open and short circuiting failure modes were experimentally implemented with the resistor bank shown schematically in Figure 4.1. Table 4.1 summarizes the resistance values obtained from the various switch settings on the resistor bank. The data in Table 4.1 was derived from utilizing Ohm's law by connecting a dc power supply to the resistor bank and measuring the applied voltage and current for each switch setting. The open circuit failure required the resistor bank to be connected in series with one of the motor phases and was implemented by progressively increasing the resistance of the resistor bank. The short circuit failure required the resistor bank to be connected in parallel with two phases of the motor and was implemented by progressively decreasing the resistance of the resistor bank.

4.2 Machine Model Verification

The first step towards validation of the brushless permanent magnet machine model was to verify the electrical and mechanical descriptive parameters of the machine. As will be discussed below, the individual phase resistance and back electromotive force constant were both experimentally verified, while the manufacturer's rating for the self and mutual inductance values were verified through simulation analysis. The mechanical

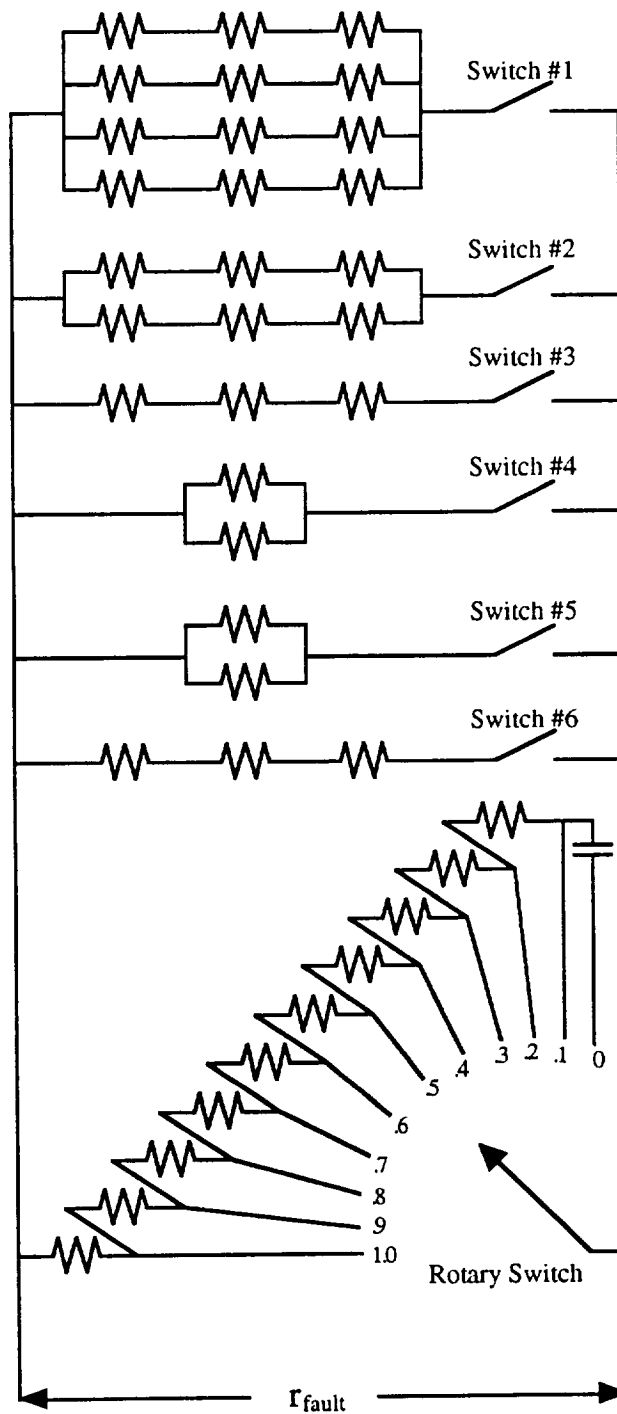


Figure 4.1 Laboratory resistor bank

Toggle Switch	Resistance (Ω)
# 1	125.0
# 2	61.3
# 3	61.3
# 4	24.0
# 5	12.0
# 6	6.0
Rotary Switch	Resistance (Ω)
0.1	1154.0
0.2	576.0
0.3	384.0
0.4	288.0
0.5	234.0
0.6	195.0
0.7	166.0
0.8	147.0
0.9	130.0
1.0	115.0

Table 4.1 Switch settings and resistance values for the laboratory resistor bank

parameters, the viscous damping coefficient and the system inertia, were both verified through experimentation.

4.2.1 Phase Resistance and Back Electromotive Force Constant

A digital Fluke multimeter was used to measure the phase to neutral resistance for all three electrical phases of the machine. The values obtained were consistent with the manufacturer's rating of 0.01 ohms. With the machine coupled to another laboratory motor, the BPMM was operated at various speeds as a generator with no electrical power connections. Again, using the digital Fluke multimeter, the phase to neutral voltages generated by the back EMF were measured. After converting the gathered data from volts (RMS) to volts (peak), the plot shown in Figure 4.2 was developed. The calculated value for the slope of the line shown in Figure 4.2 corresponds to the back EMF constant of the machine. After the appropriate conversions, the experimental value of 0.6573 volts (peak)/mechanical speed (rad/s) compared favorably with the rating provided by the manufacturer.

4.2.2 Self and Mutual Inductance

Results from steady-state simulation of the machine model were compared with experimentally gathered data of the machine to verify the self and mutual inductance values. The manufacturer's rated value for the phase inductance was converted to an individual phase self inductance quantity by evaluating the rating as either a wye connected measurement (divide rating by 2) or as a delta connected measurement (divide rating by 3) [45]. Assuming the wye connection for the measurement, Figure 4.3 shows the steady

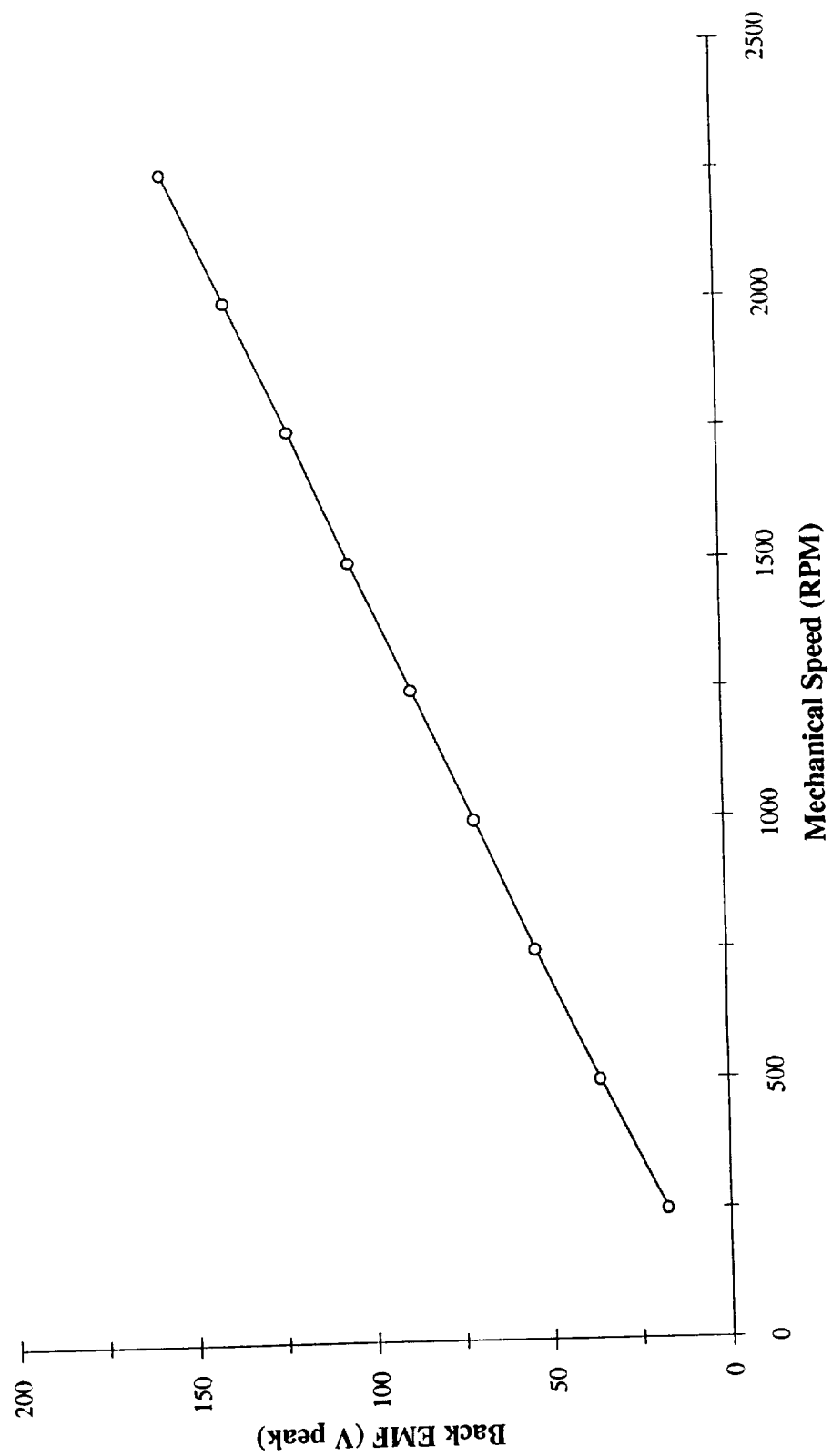


Figure 4.2 Experimental data for back EMF coefficient calculation

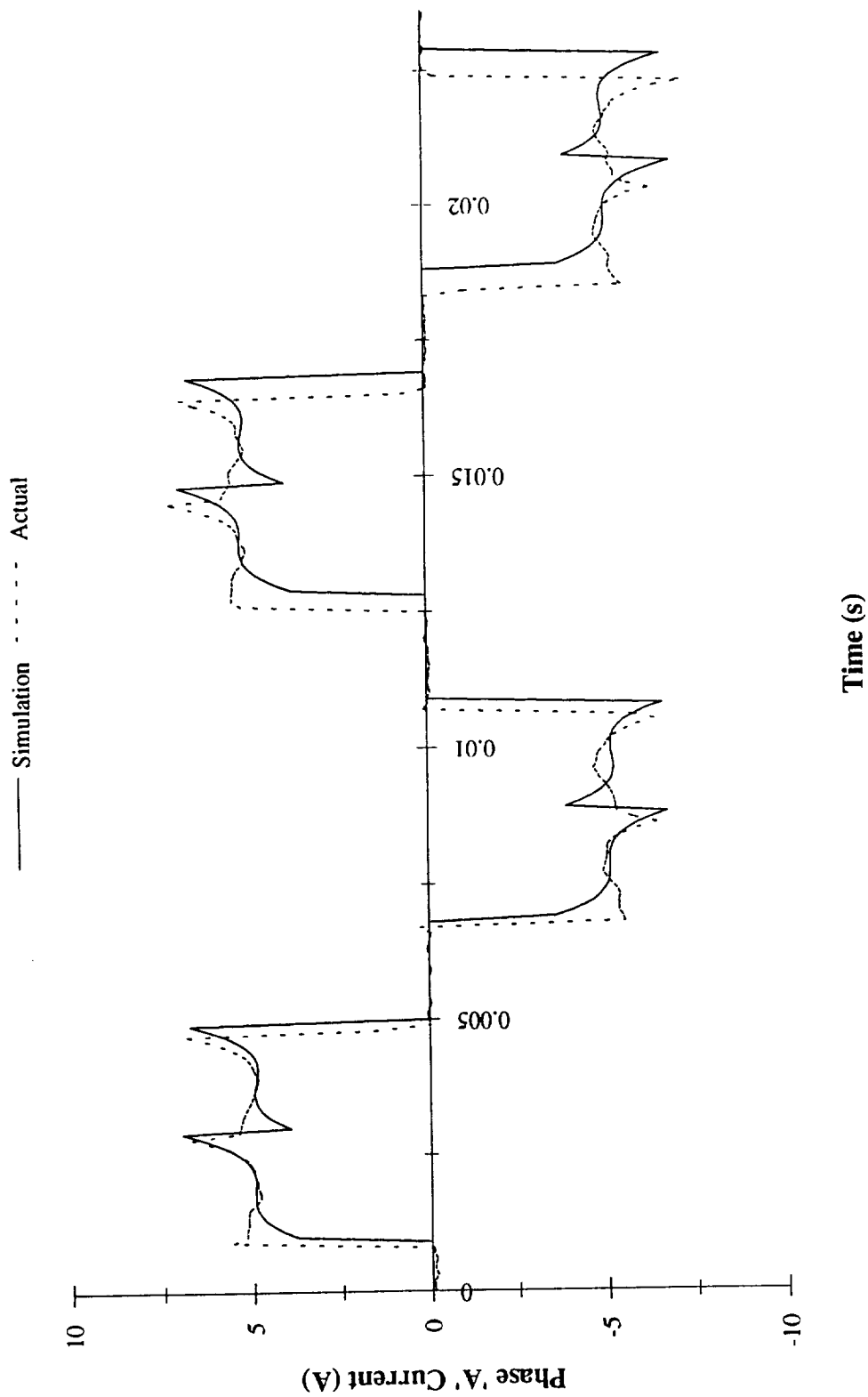


Figure 4.3 Current assuming a wye connected measurement of phase inductance

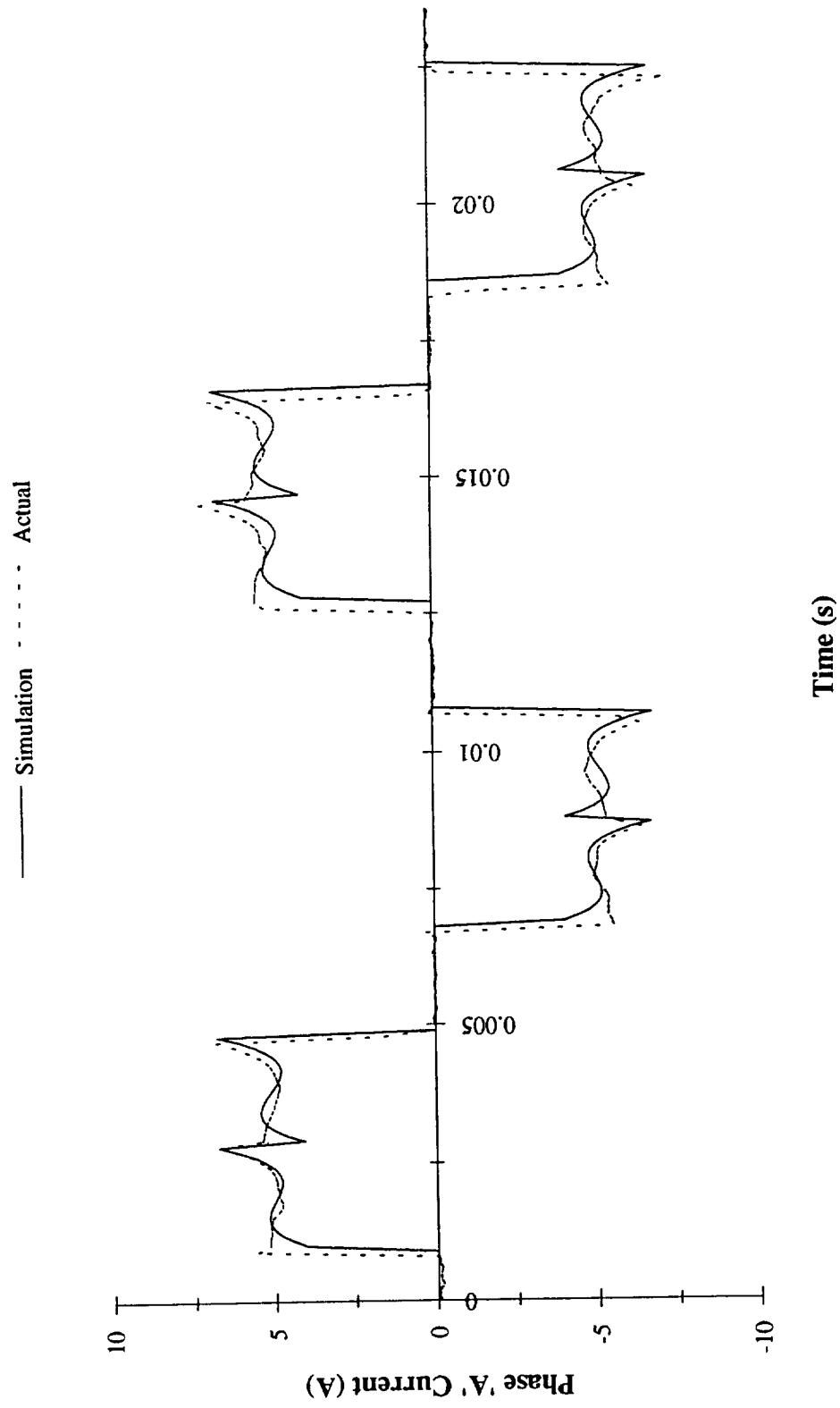


Figure 4.4 Current assuming a delta connected measurement of phase inductance

state simulation and experimental results for the 'A' phase current of the machine operating at a bus voltage of 200 volts. Assuming the delta connection, Figure 4.4 shows the steady-state simulation and experimental results for the 'A' phase current of the machine operating at the same bus voltage. Both simulation models used for generating the data in Figures 4.3 and 4.4 had the mutual inductance terms set to a value equal to 50% of the self inductance. From the phase shifting resulting from the difference in rotor speed between the simulation and actual current waveforms shown in Figures 4.3 and 4.4, it is apparent that the delta connected measurement value more accurately describes the machine. Thus, the individual phase self inductance parameter was established to be one-third of the rated value supplied by the manufacturer.

Finally, the mutual inductance term for the individual phases was calculated as a percentage of the self inductance value and verified through simulation. Three different test results are shown in Figures 4.5 to 4.7 with the mutual inductance terms set to 25%, 50% and 75% of the self inductance rating. All three figures show the simulated and measured phase 'A' currents of the BPMM operating at a bus voltage of 200 volts. Again, notice that the apparent phase shift for the waveforms shown in the figures is the result of a discrepancy in mechanical speed, which ranged from 1673.0 to 1720.0 RPM. From these results, it is apparent that the 50% of self inductance rating for the mutual term is the best descriptive fit for this parameter.

4.2.3 Viscous Damping Coefficient and System Inertia

Experimental results were obtained to verify the mechanical descriptive parameter for viscous damping. After coupling the machine to the roller screw via the gear box and locking the nut to the screw shaft, the system was operated in steady-state at various speeds

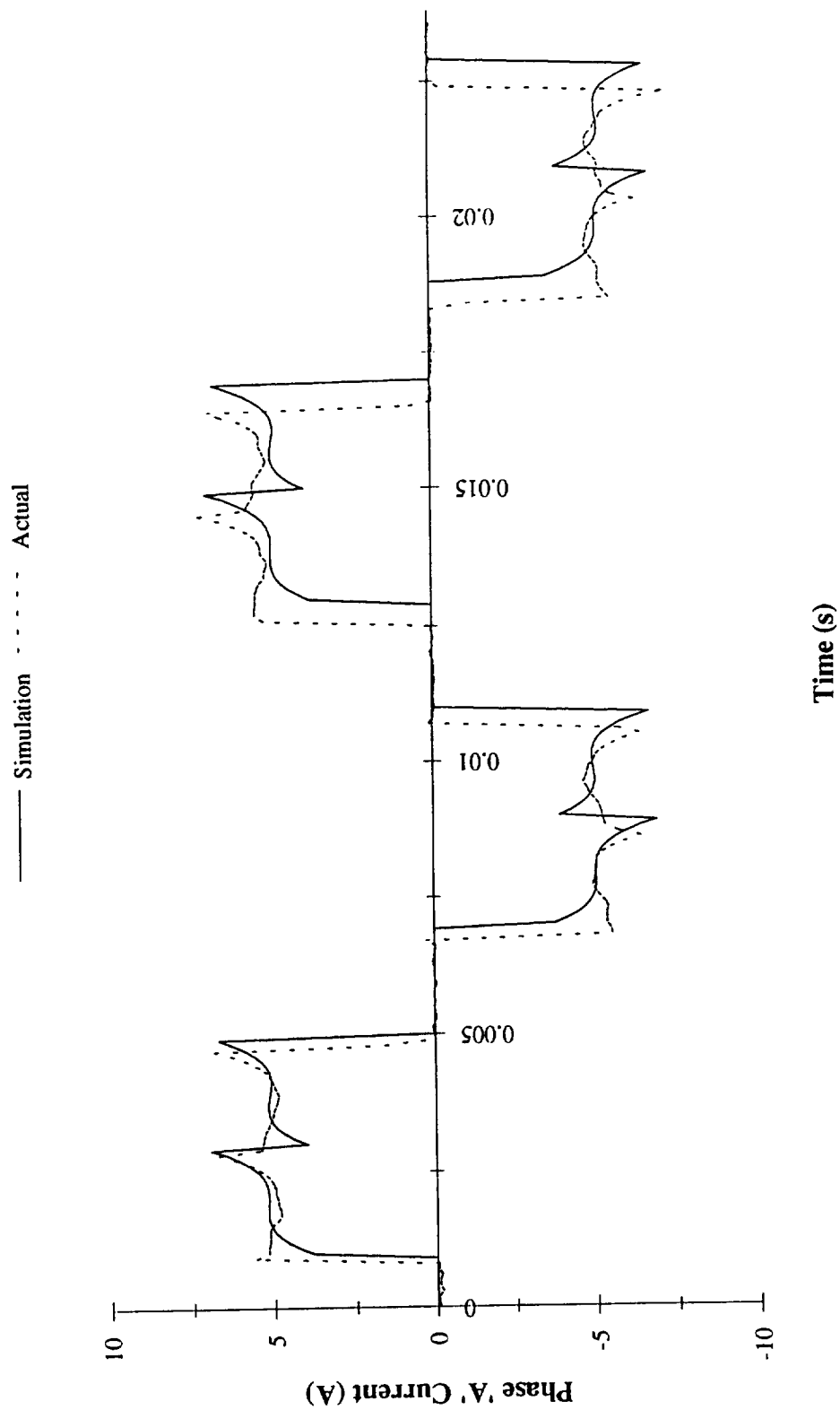


Figure 4.5 Current with mutual inductance set to 25% of self inductance

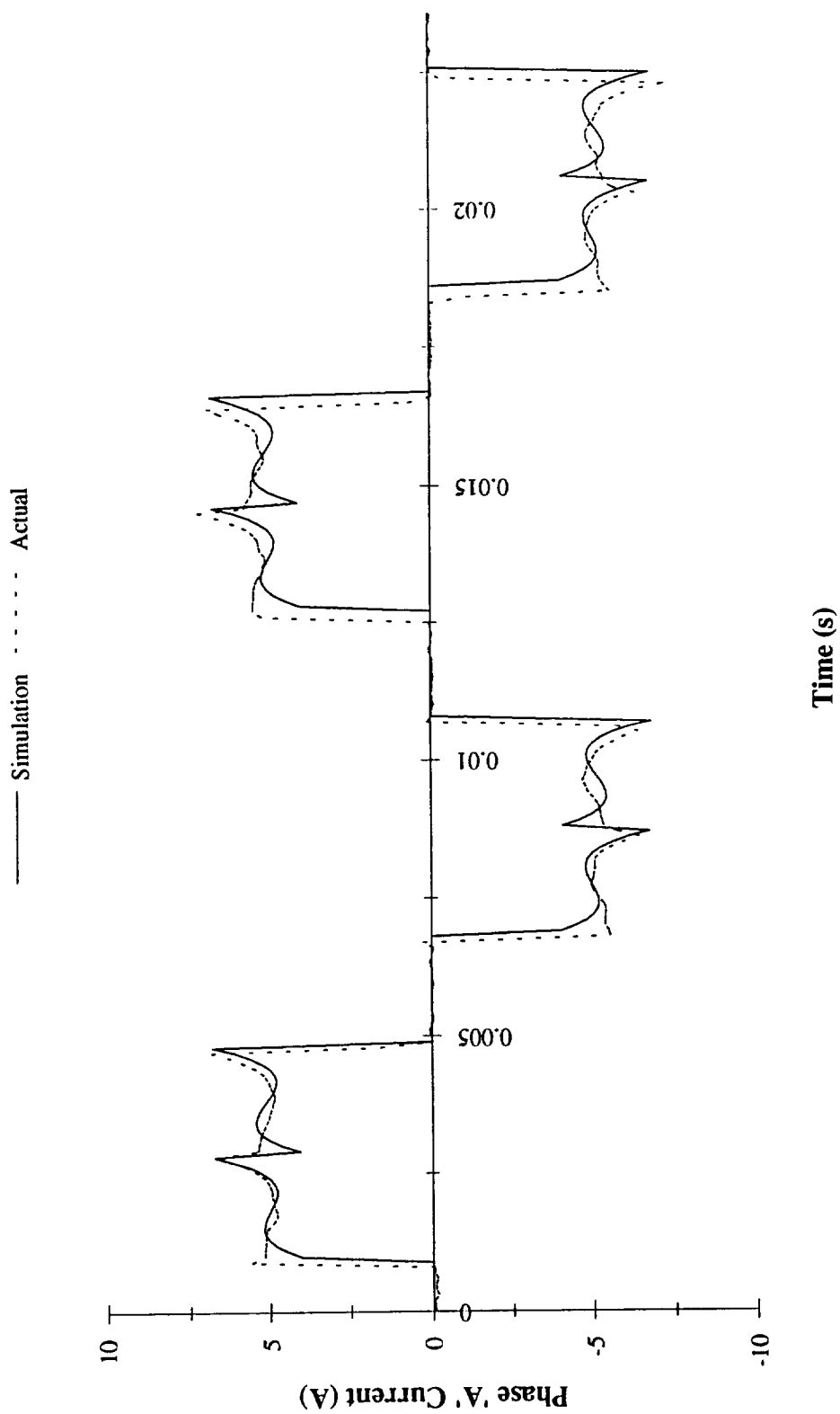


Figure 4.6 Current with mutual inductance set to 50% of self inductance

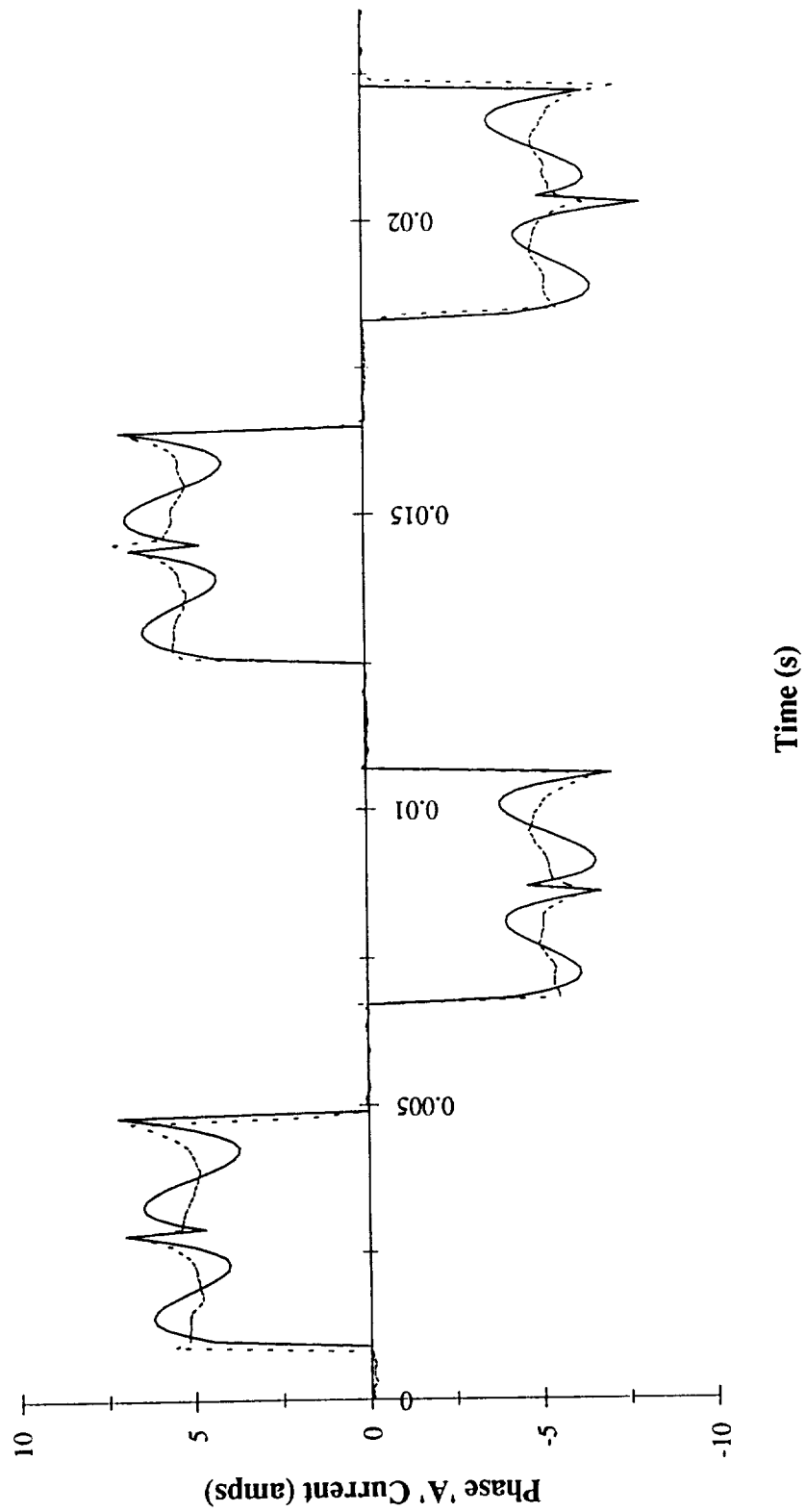


Figure 4.7 Current with mutual inductance set to 75% of self inductance

with no applied load torque. The mechanical equation of motion for the machine, as shown in (3.6) and (3.7), reduces during steady state operation at no load to,

$$\tau_{dev} = \frac{e_a i_a + e_b i_b + e_c i_c}{\omega_{mech}} = B \omega_{mech} \quad (4.1).$$

Figure 4.8 shows experimental results for various tests along with an approximation of the viscous term as a constant value that is proportional to the mechanical speed. From these results, it is apparent that equation (4.1) may be accurately approximated as,

$$\tau_{dev} = B \omega_{mech} = \left(\frac{5.5}{\omega_{mech}} \right) \omega_{mech} = c_{viscous} \quad (4.2),$$

for operating mechanical speeds greater than 75 rad/s (≈ 700 RPM).

Finally, the mechanical inertia coefficient for the EMA system was validated through experimentation. After the machine obtained steady-state operation, the three-phase power to the motor was disconnected and the system coasted to rest. Figure 4.9 shows the experimentally measured value for the mechanical speed of the motor during this test procedure along with an offset linear approximation for the decaying waveform. Once the supplied electric power was disconnected from the machine, the mechanical equation as derived in (3.6) became,

$$\tau_{dev} = 0 = c_{viscous} + J \frac{d\omega_{mech}}{dt} \quad (4.3).$$

Thus, the inertia coefficient of 0.0024 kgm^2 was obtained through dividing the constant

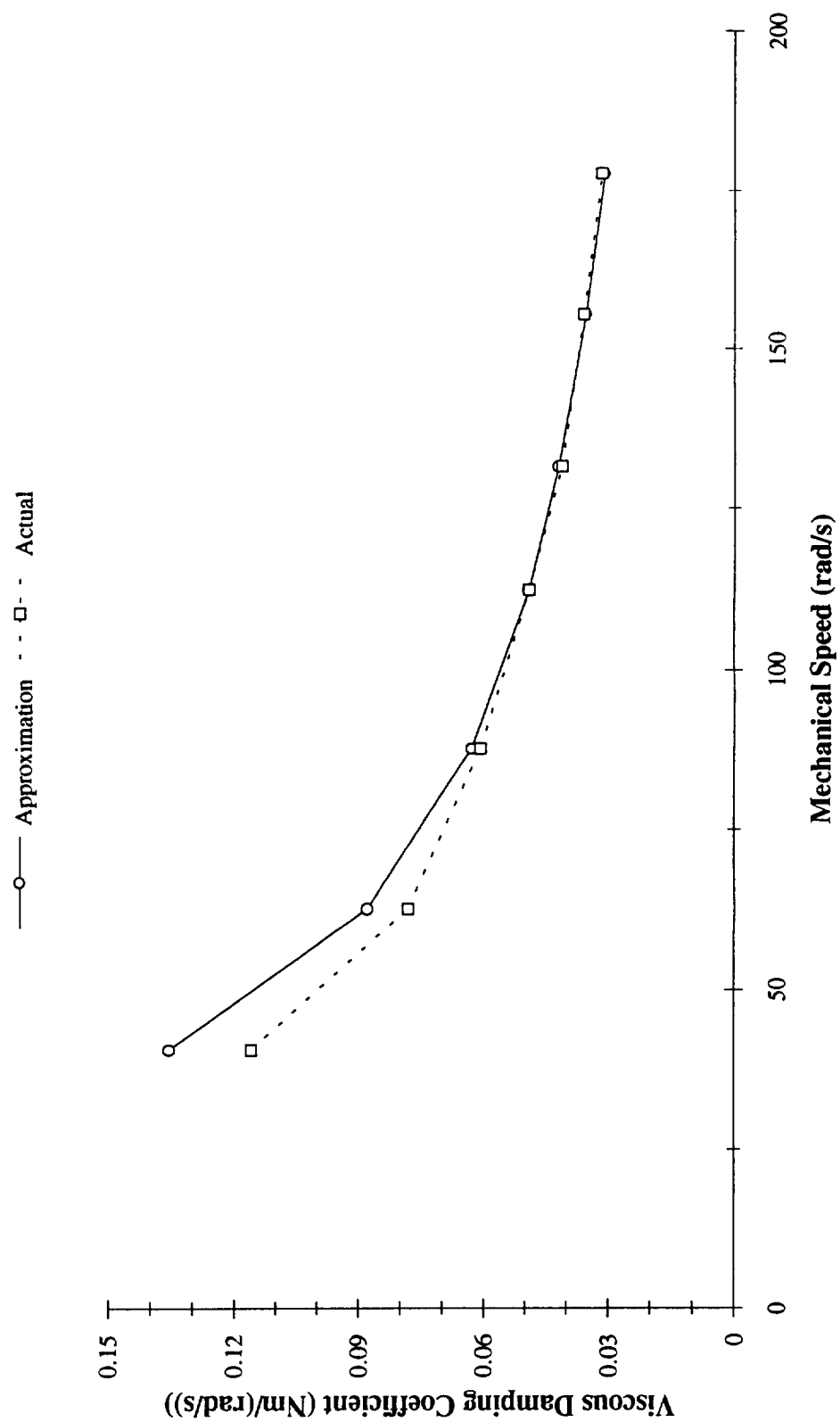


Figure 4.8 Test results used for evaluating the viscous damping coefficient

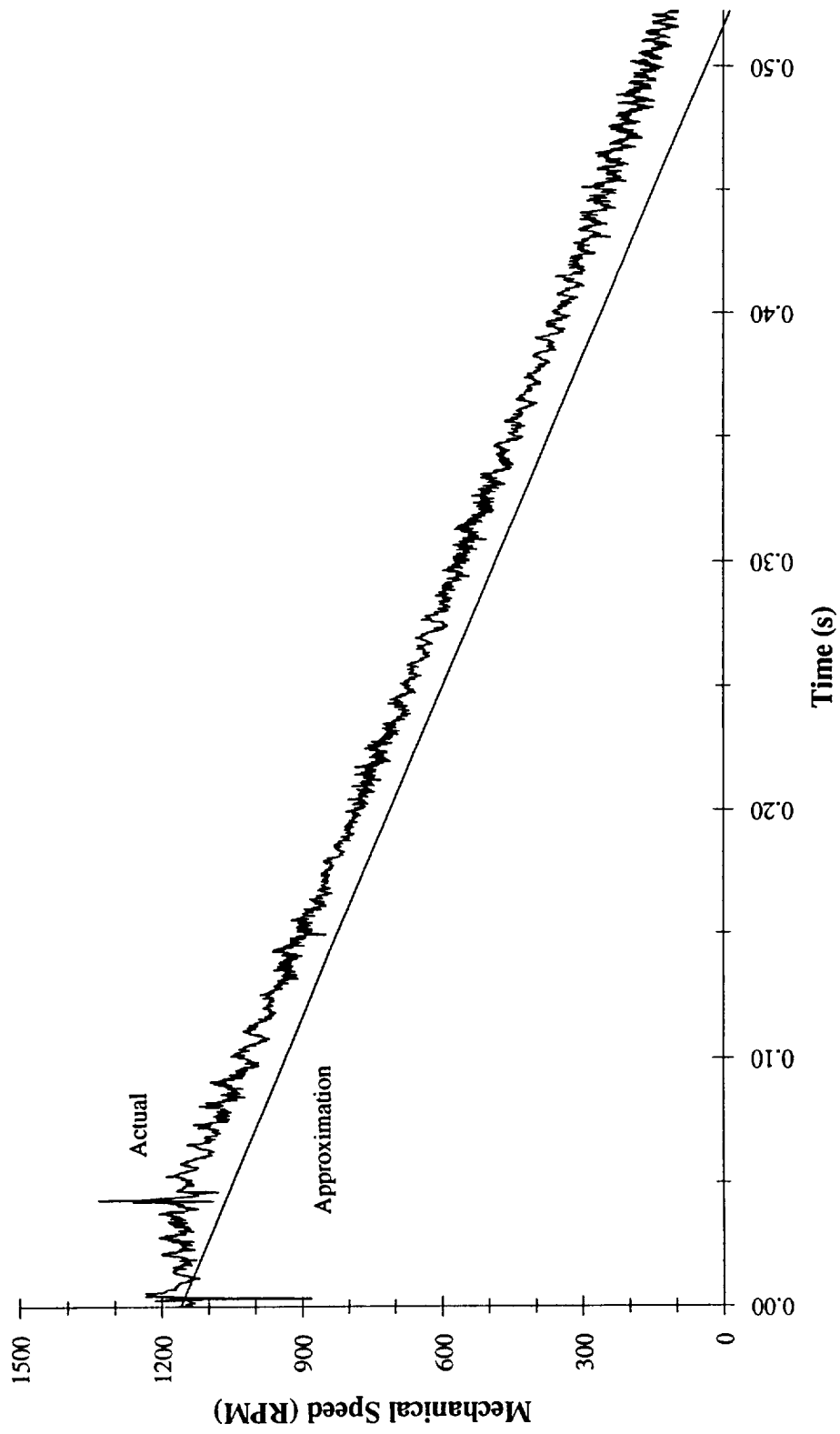


Figure 4.9 Test results used for evaluating the EMA system inertia

approximation for viscous damping by the slope of the best linear curve fit, which is shown in the figure.

4.2.4 Model Verification for Steady State Operation

After verifying all of the electrical and mechanical operating parameters for the machine model, simulation and experimental data was obtained for steady-state operation at various applied bus voltages. Figures 4.10 to 4.12 show the simulation and actual phase 'A' currents, line 'AB' voltages, and mechanical speeds for an applied bus voltage of 75.0 volts. Figures 4.13 to 4.15 show the simulation and actual phase 'A' currents, line 'AB' voltages, and mechanical speeds for an applied bus voltage of 150.0 volts. Figures 4.16 to 4.18 show the simulation and actual phase 'A' currents, line 'AB' voltages, and mechanical speeds for an applied bus voltage of 200.0 volts. Note that the simulation speed is slightly lower than the actual speed for the 75.0 volt bus data and is slightly higher than the actual speed for the 200.0 volt bus data. This observation is consistent with the slight inaccuracy contained in the approximation of the viscous damping term, as shown in Figure 4.8. From the results of these experiments, the simulation clearly models the operation of the motor in steady state.

4.2.5 Model Verification for Dynamic Operation

Establishing the accuracy of the model for simulating dynamic machine behavior is the last remaining step to complete the verification process. Therefore, both simulated and experimental data were obtained for transient motor operation, an increase of applied bus voltage. The simulation and actual phase 'A' currents of the motor for this experiment are

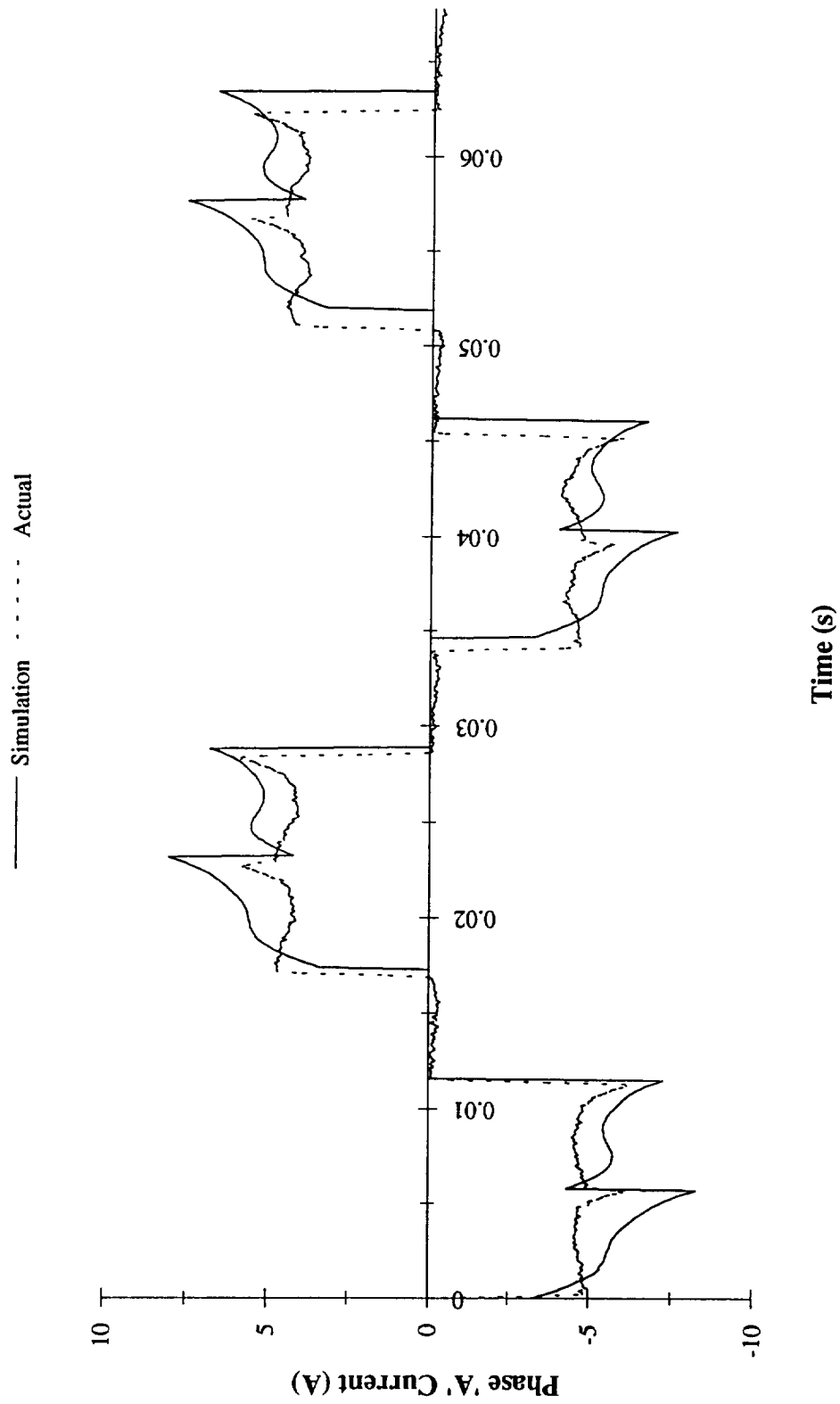


Figure 4.10 Steady state simulated and actual phase currents for a 75.0 volt bus

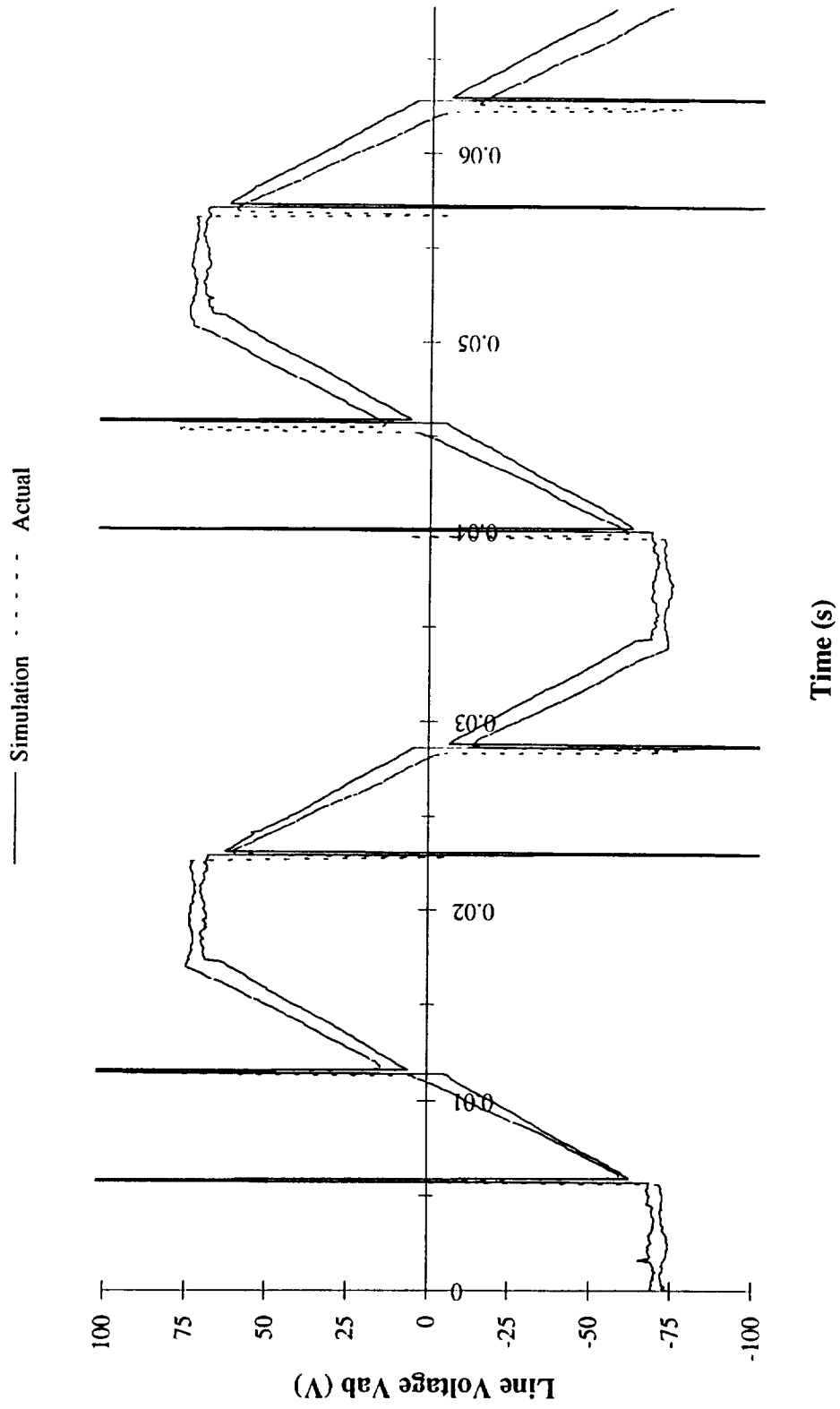


Figure 4.11 Steady state simulated and actual line voltages for a 75.0 volt bus

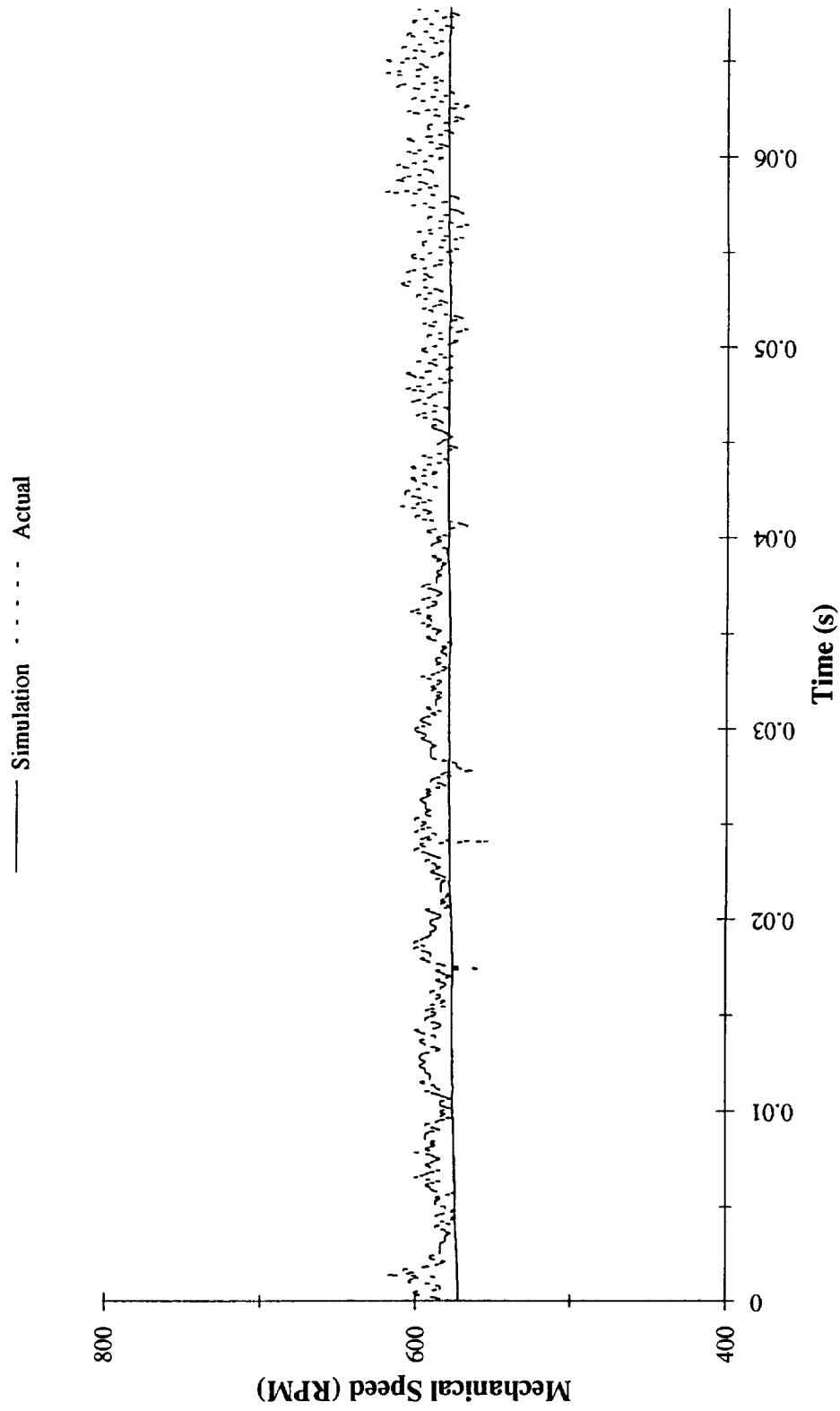


Figure 4.12 Steady state simulated and actual mechanical speeds for a 75.0 volt bus

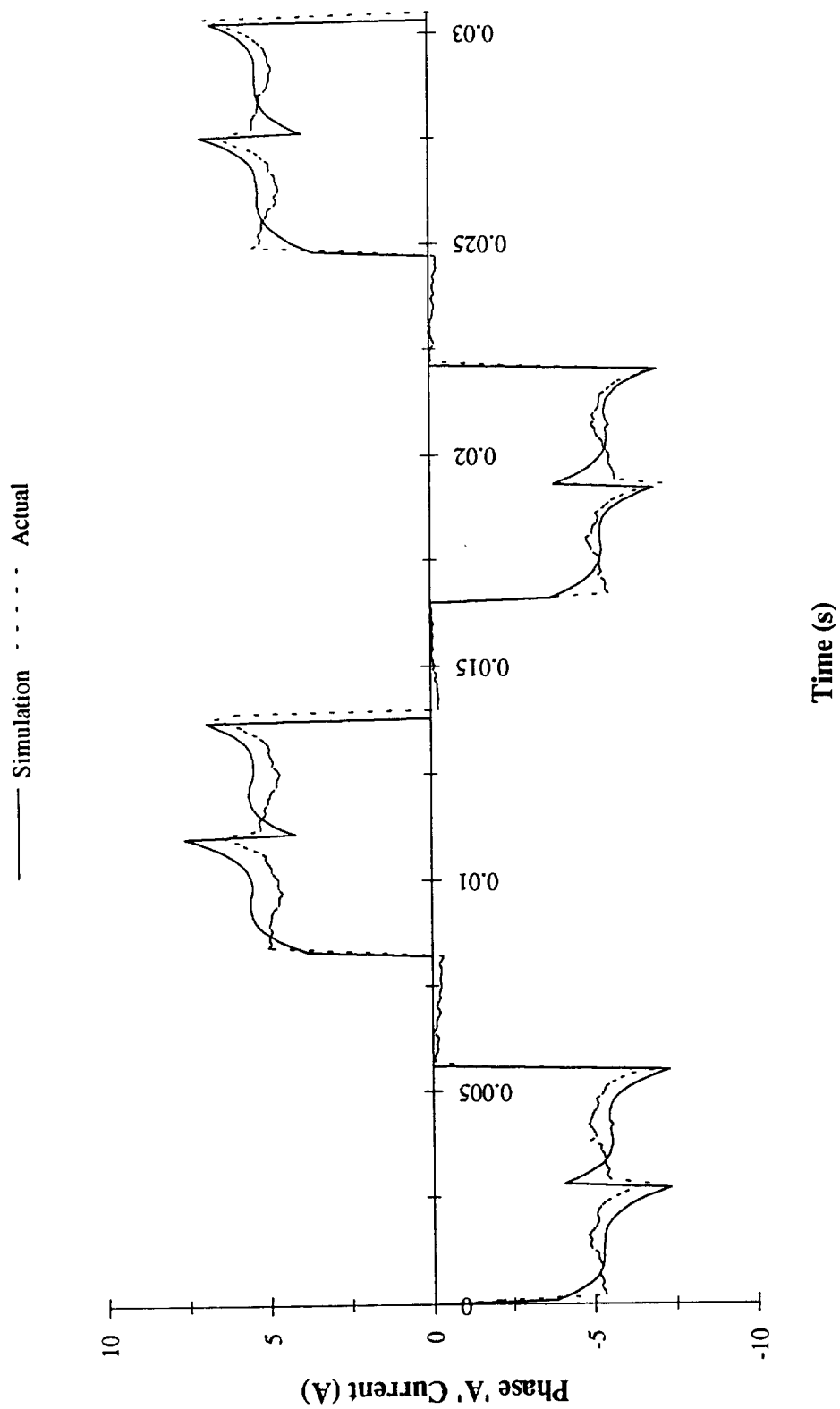


Figure 4.13 Steady state simulated and actual phase currents for a 150.0 volt bus

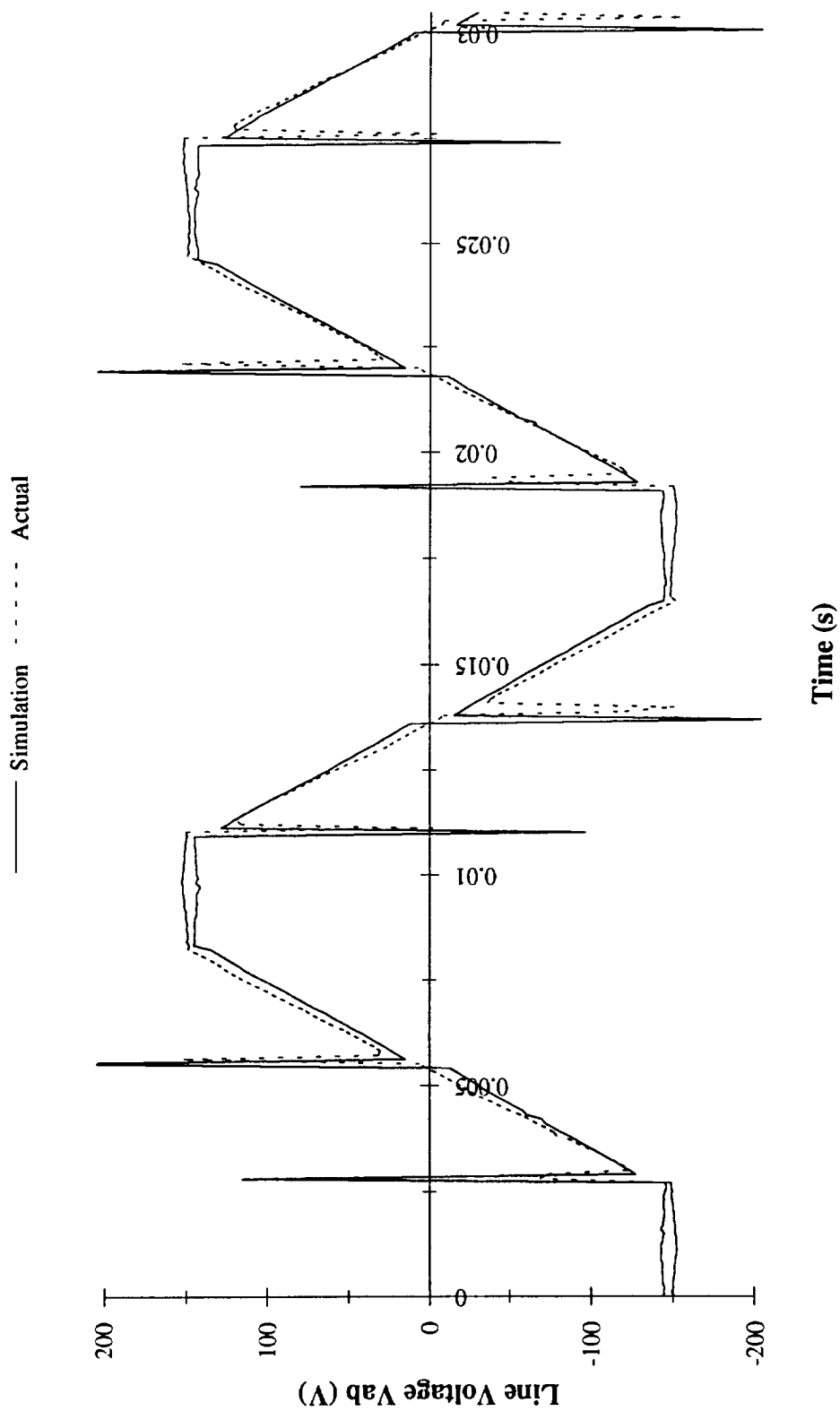


Figure 4.14 Steady state simulated and actual line voltages for a 150.0 volt bus

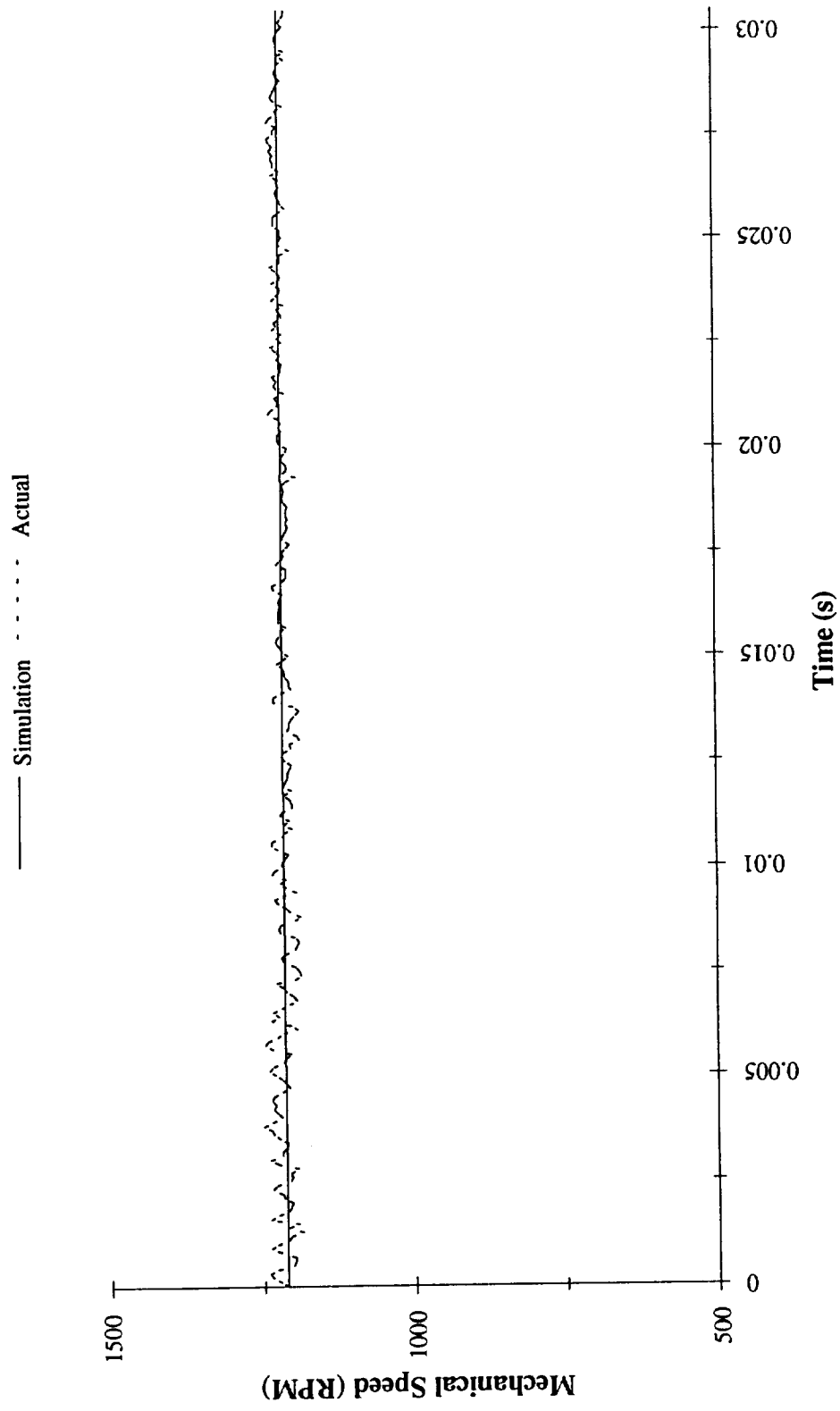


Figure 4.15 Steady state simulated and actual mechanical speeds for a 150.0 volt bus

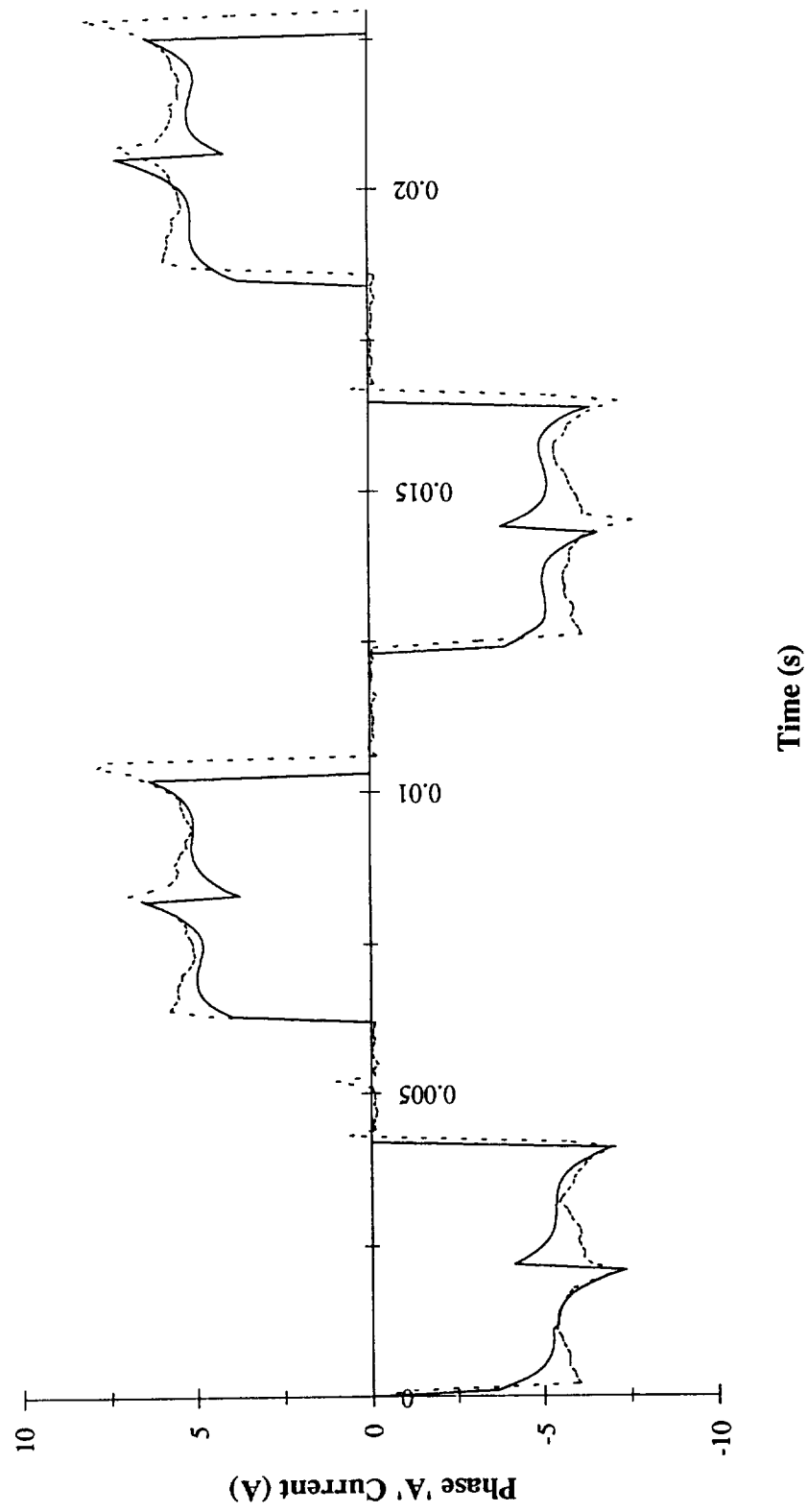


Figure 4.16 Steady state simulation and actual phase currents for a 200.0 volt bus

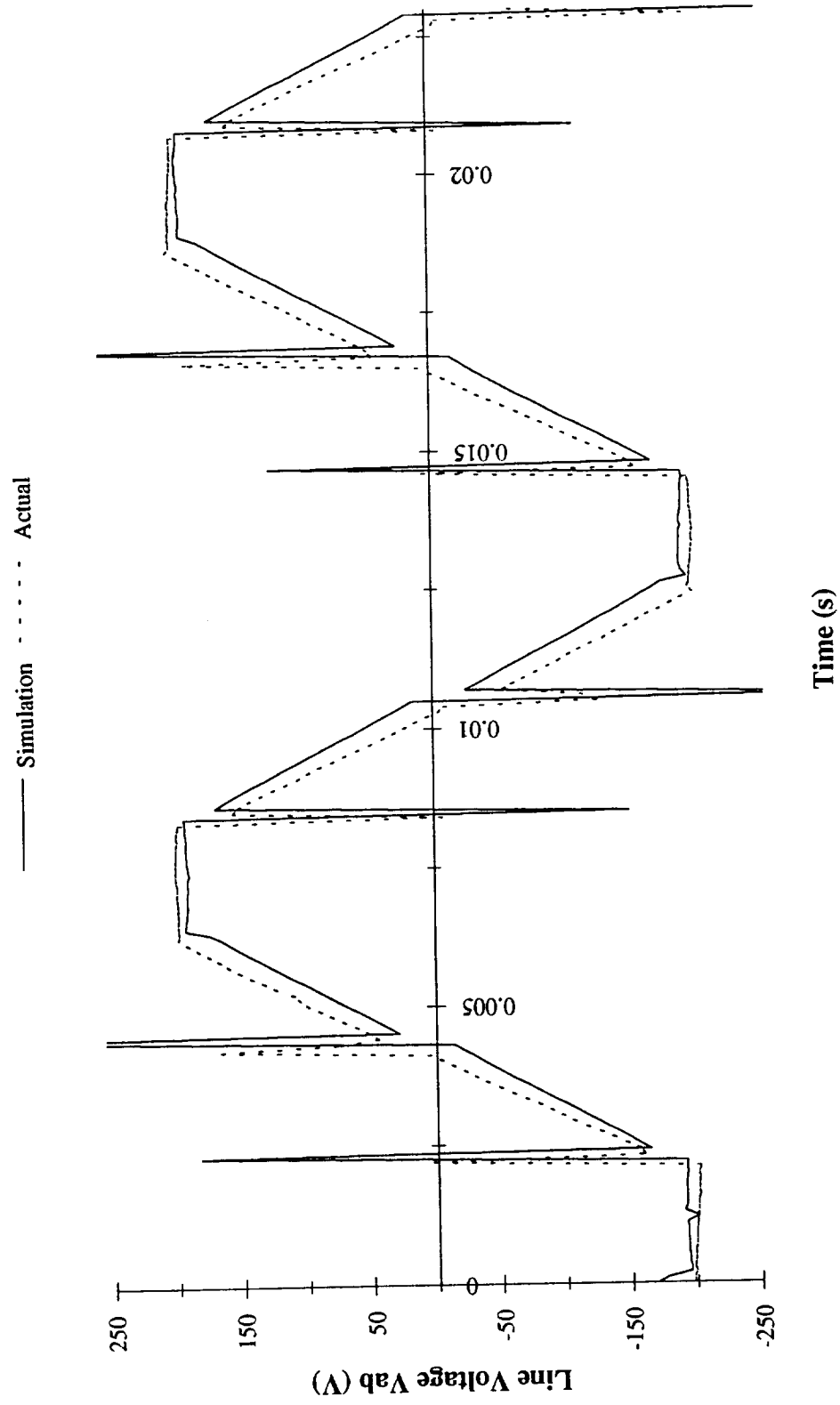


Figure 4.17 Steady state simulated and actual line voltages for a 200.0 volt bus

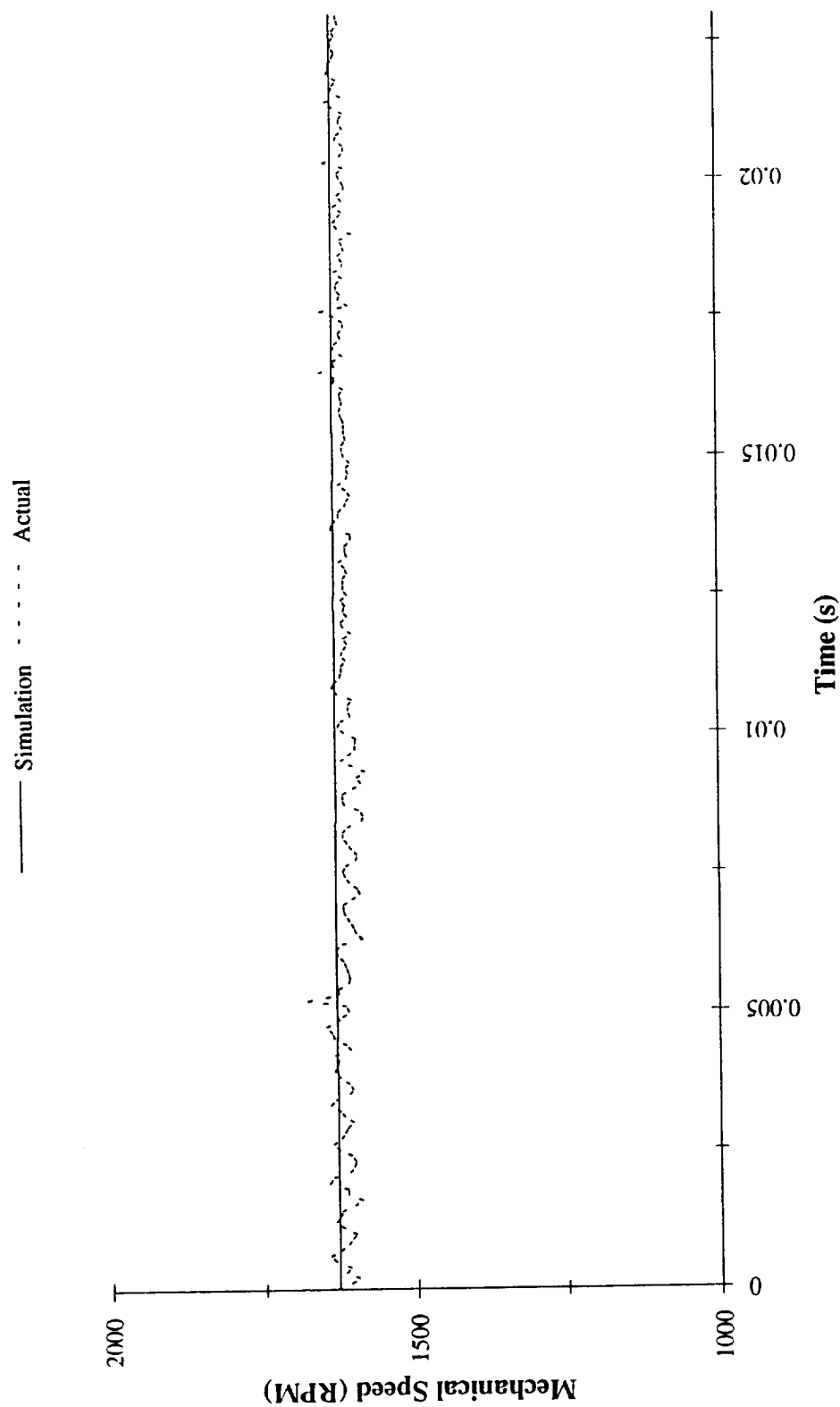


Figure 4.18 Steady state simulated and actual mechanical speeds for a 200.0 volt bus

shown beginning in Figure 4.19 and continuing on in Figure 4.20. The simulation and actual applied line 'AB' voltages are shown beginning in Figure 4.21 and continuing on in Figure 4.22. Finally, Figure 4.23 shows the simulation and actual mechanical speeds for the dynamic test. As a result of the alignment of simulated data with experimentally gathered data, it is evident that the machine simulation accurately portrays the dynamic operational characteristics of the brushless permanent magnet machine.

4.2.6 Model Verification for Failure Mode Operation

Since the machine failure mode experiments were designed to be non-destructive to the test equipment, the flux weakening failure mode was not implemented in the laboratory. However, simulation of this failure mode was performed with the machine model. Figure 4.24 shows the phase 'A' current, and Figure 4.25 shows the mechanical speed of the motor during a simulated flux weakening fault. As expected, the speed and current both increase to maintain motor torque production, which is decreasing with the loss of flux in the rotor.

The open circuit fault mode was experimentally implemented using the laboratory resistor bank as previously described (see Figures 3.5 and 4.1). Phase 'A' of the machine was arbitrarily selected for failure. Simulation results were also obtained to compare with the experimental data. However, the timed introduction of the fault resistance via the switch settings of the resistor bank was not sequenced between the simulation and laboratory experiments. Figures 4.26 and 4.27 show the simulation and actual phase currents for the machine, and Figure 4.28 shows the simulation and actual mechanical speed of the motor. Again, the agreement of simulated and actual data authenticates the

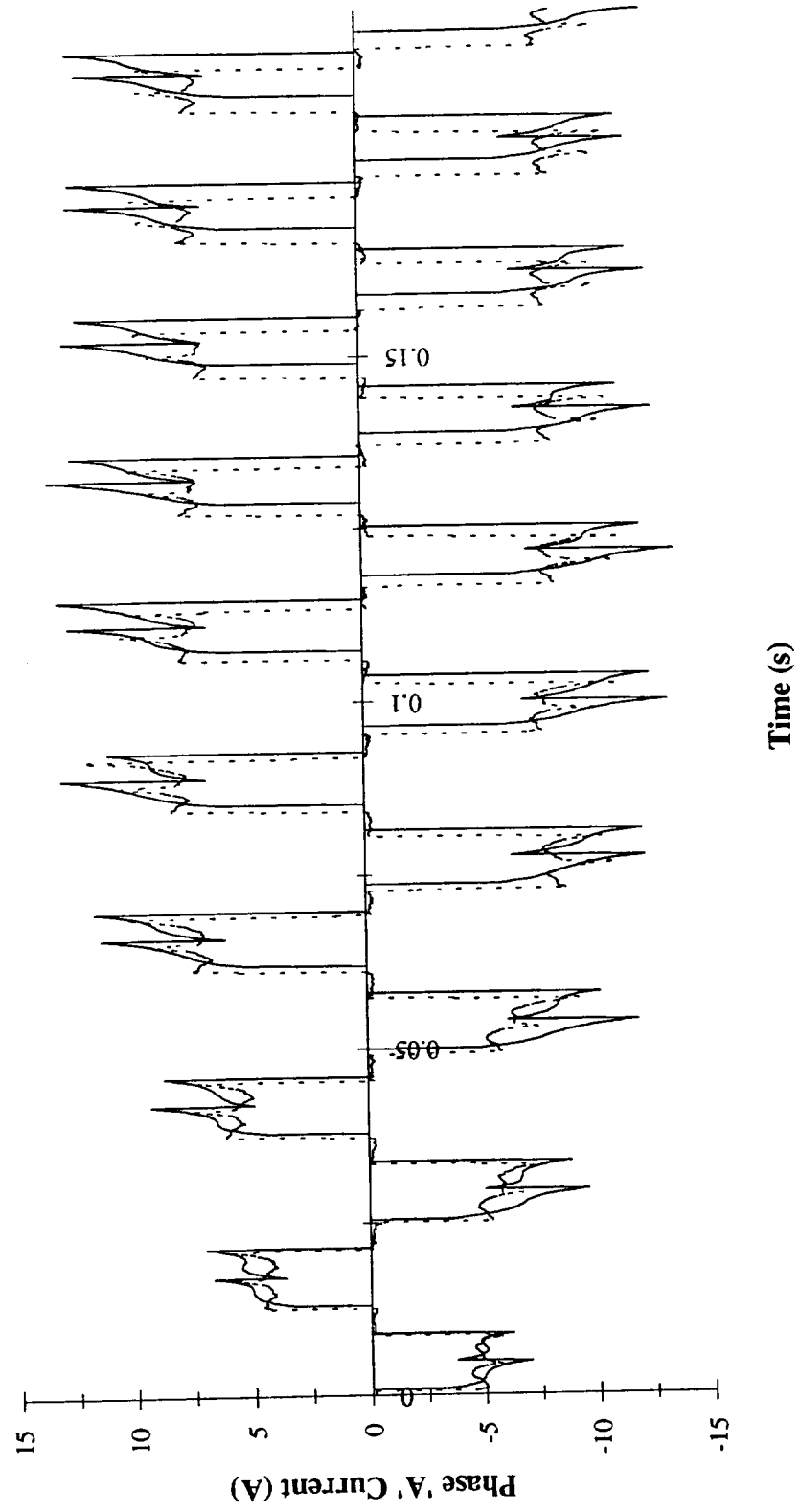


Figure 4.19 Simulated and actual phase currents for transient motor operation

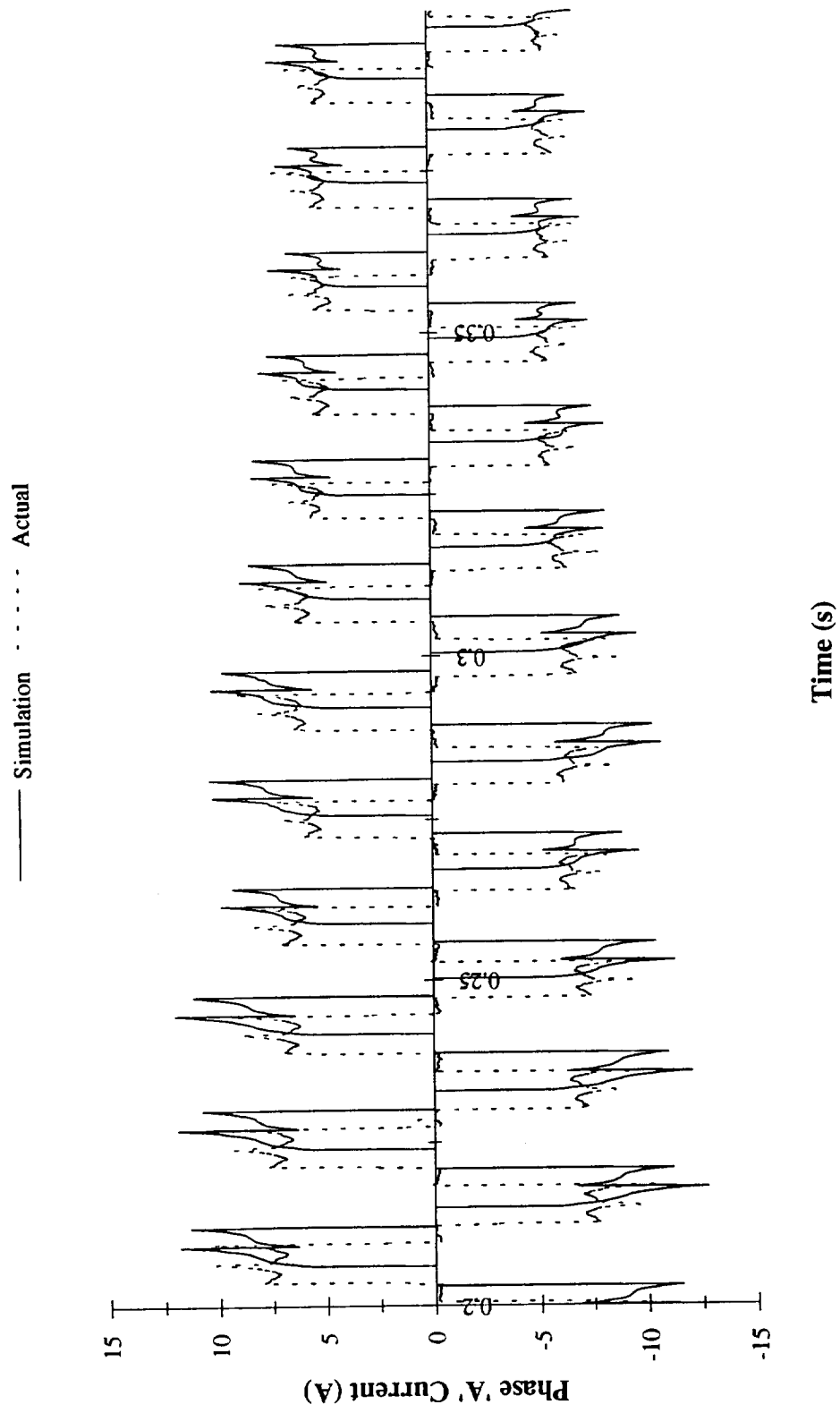


Figure 4.20 Simulated and actual phase currents for transient motor operation (continued)

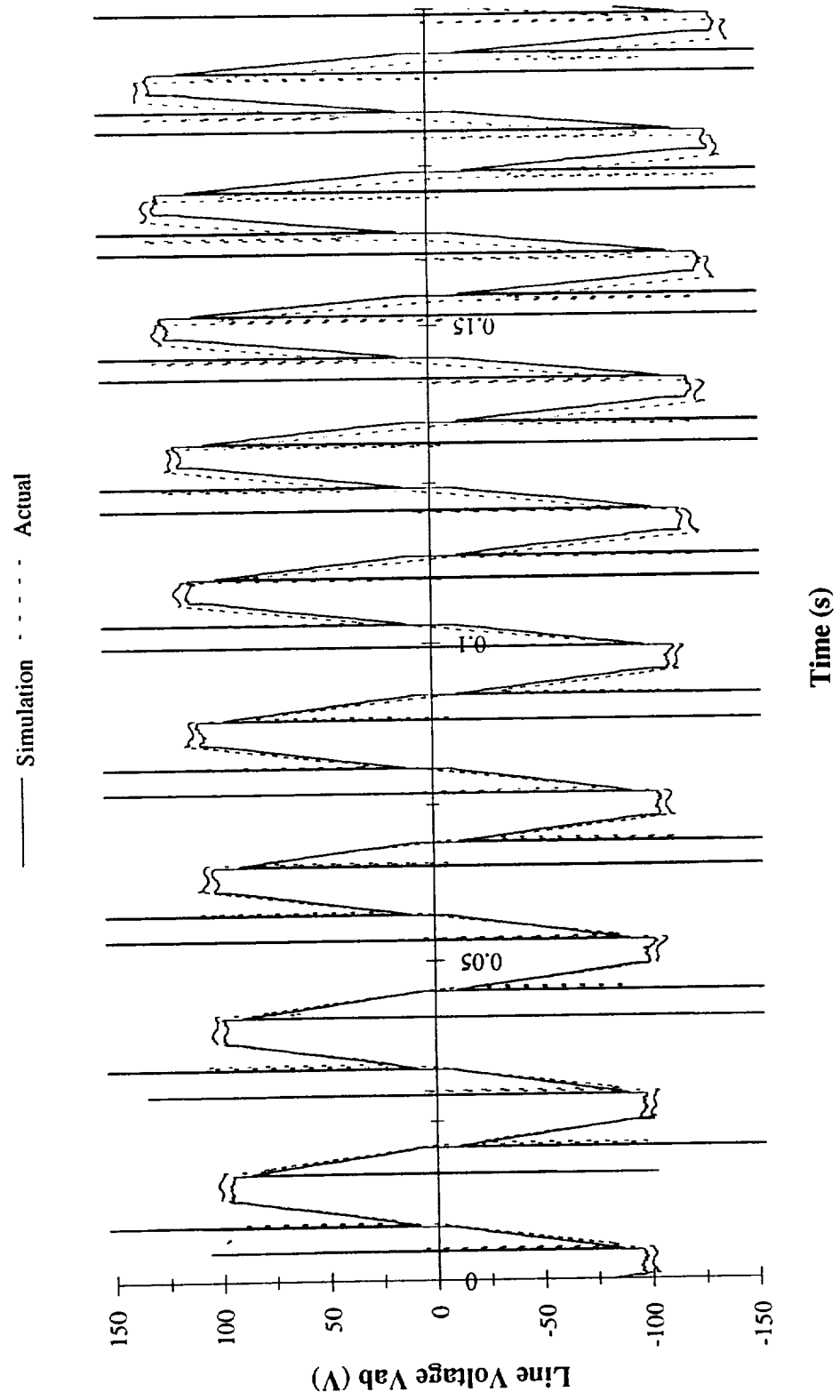


Figure 4.21 Simulated and actual line voltages for transient motor operation

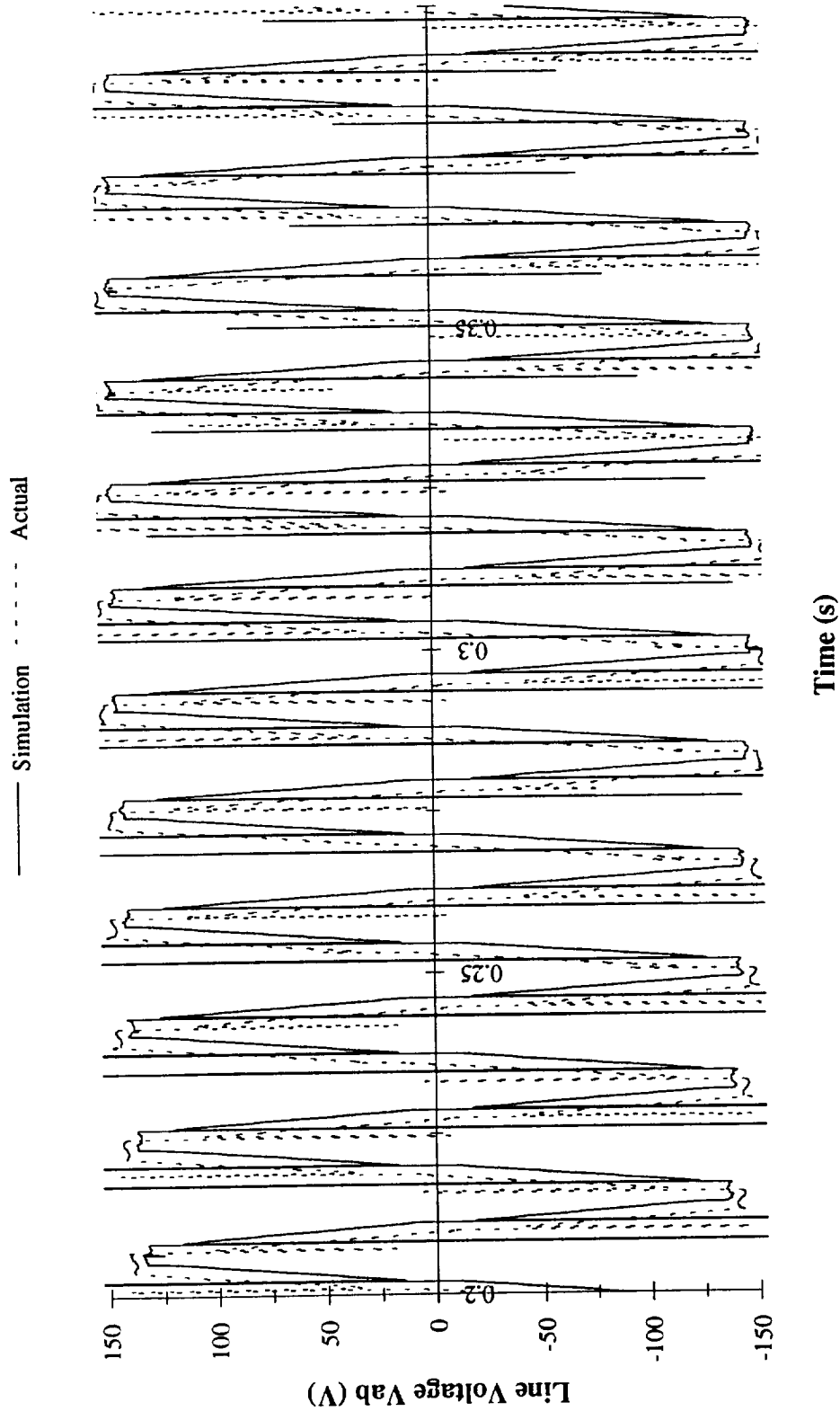


Figure 4.22 Simulated and actual line voltages for transient motor operation (continued)

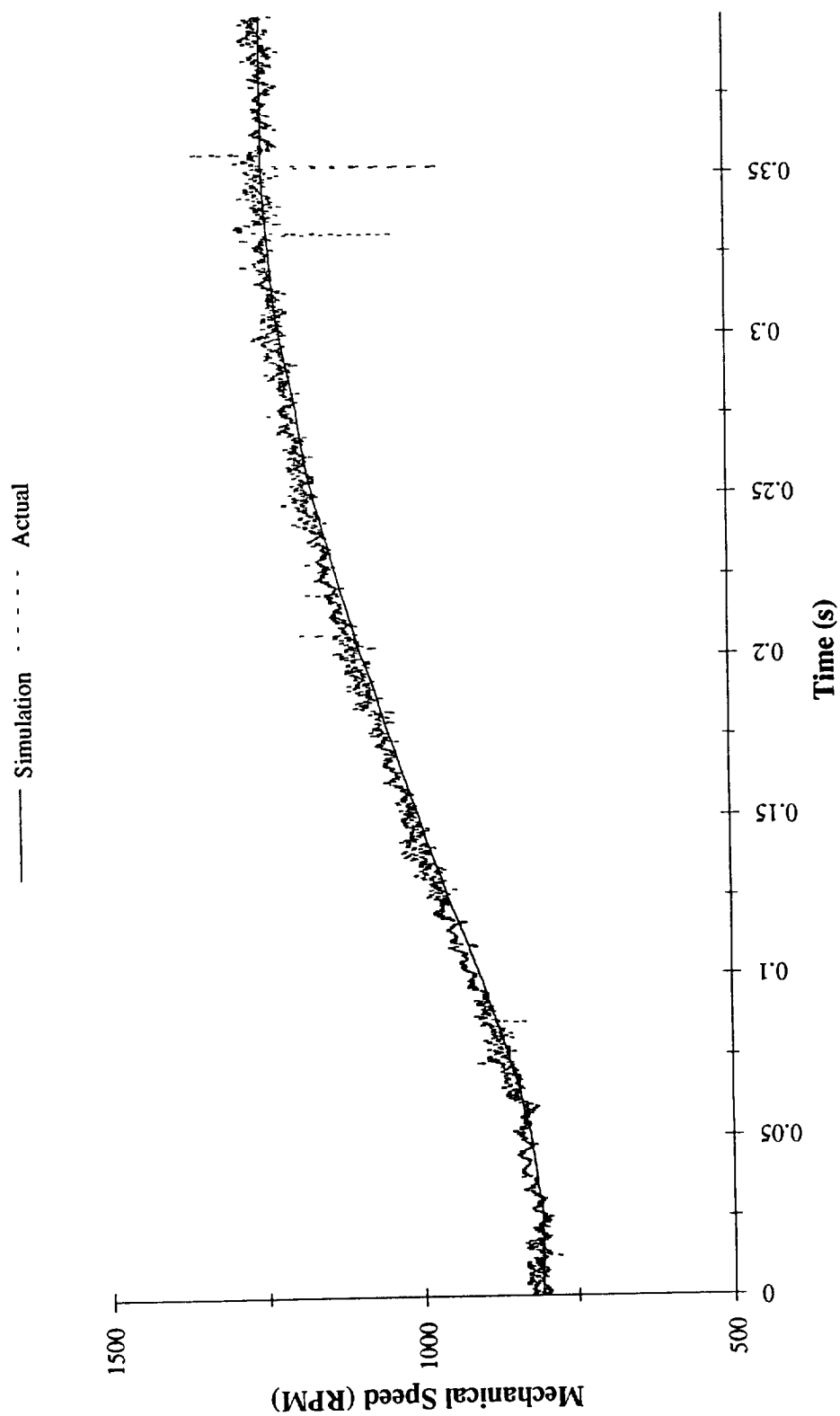


Figure 4.23 Simulated and actual mechanical speeds for transient motor operation

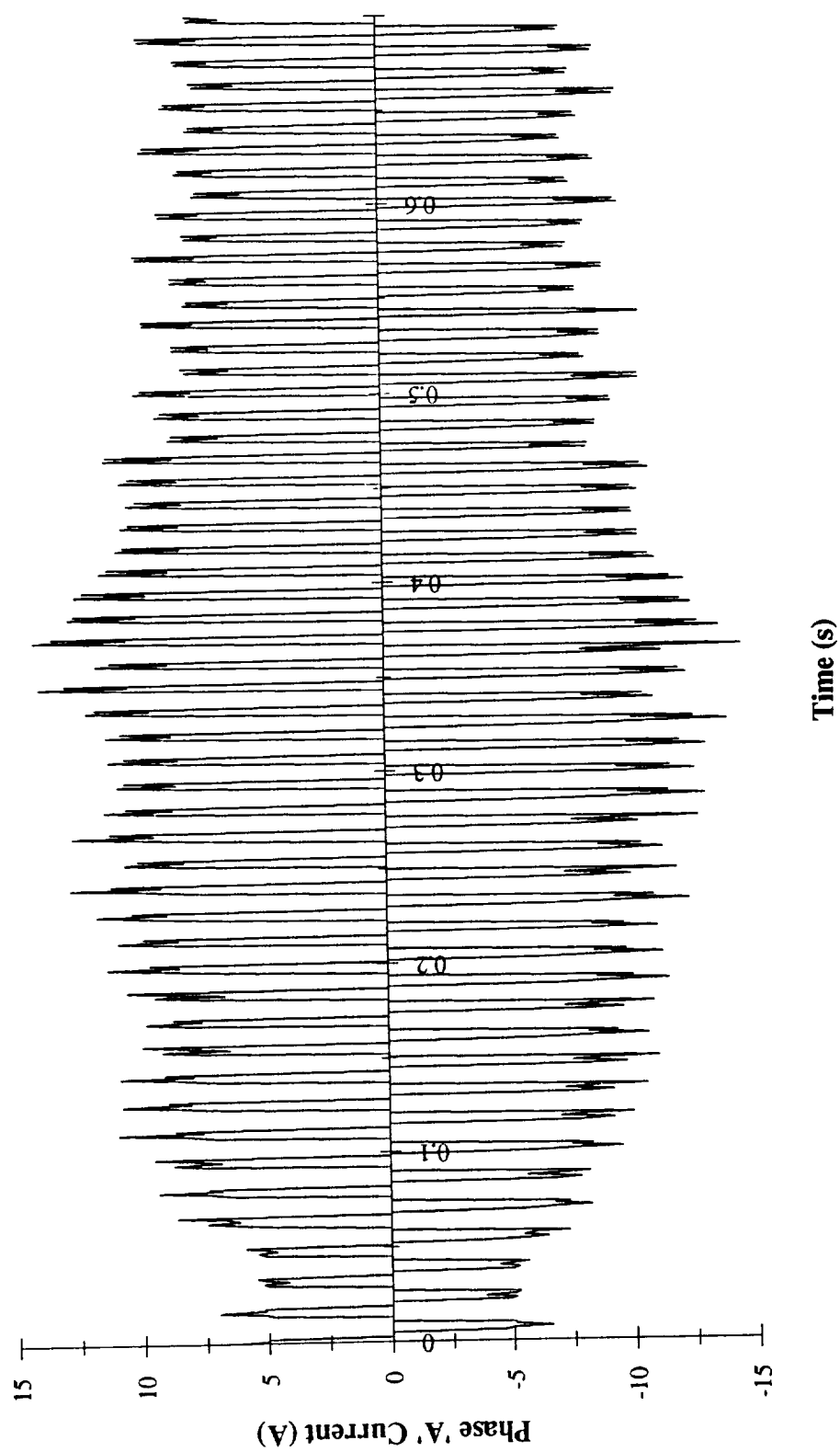


Figure 4.24 Simulated phase current for the flux weakening failure

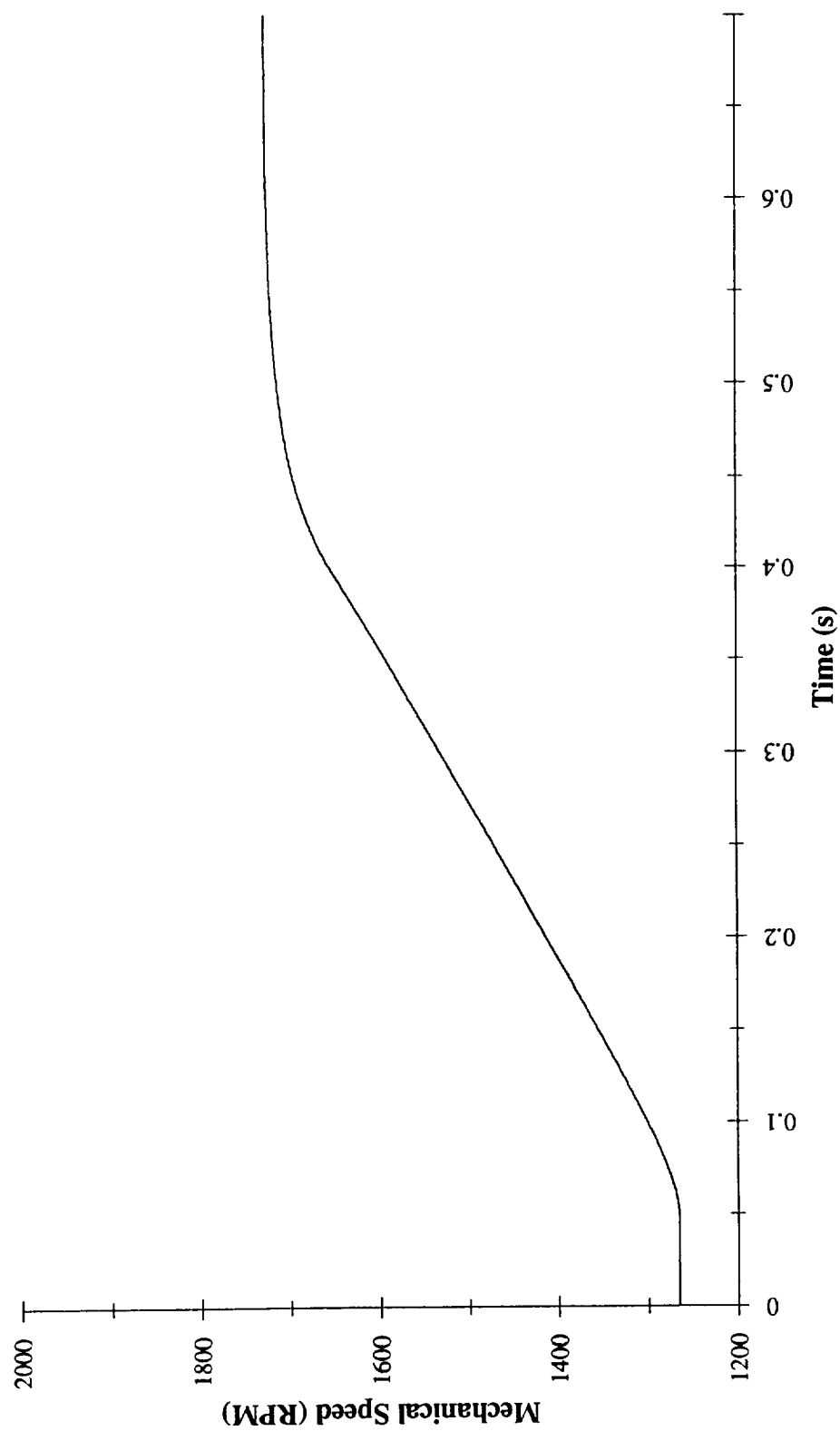


Figure 4.25 Simulated mechanical speed for the flux weakening failure

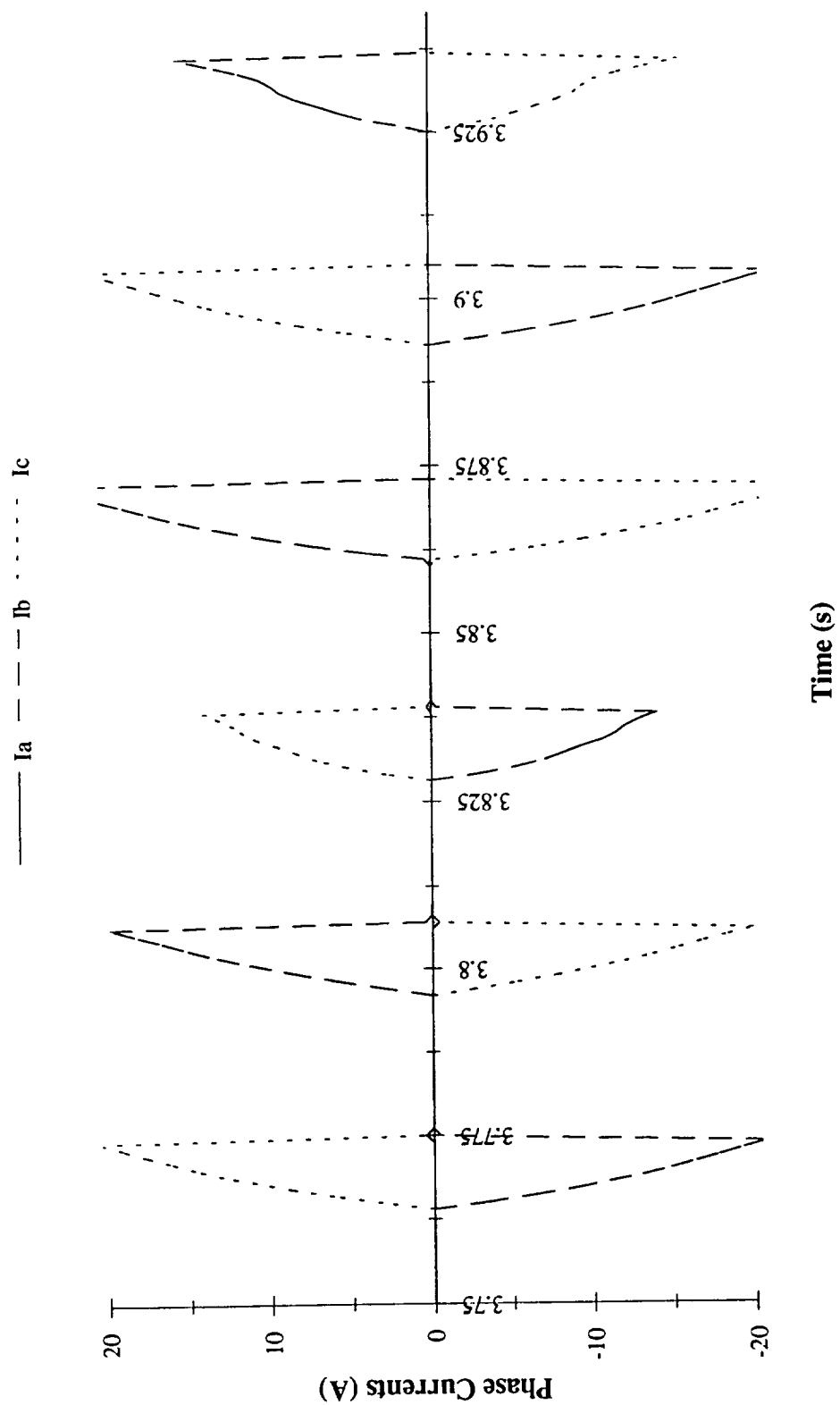


Figure 4.26 Simulated phase currents for the open circuit failure

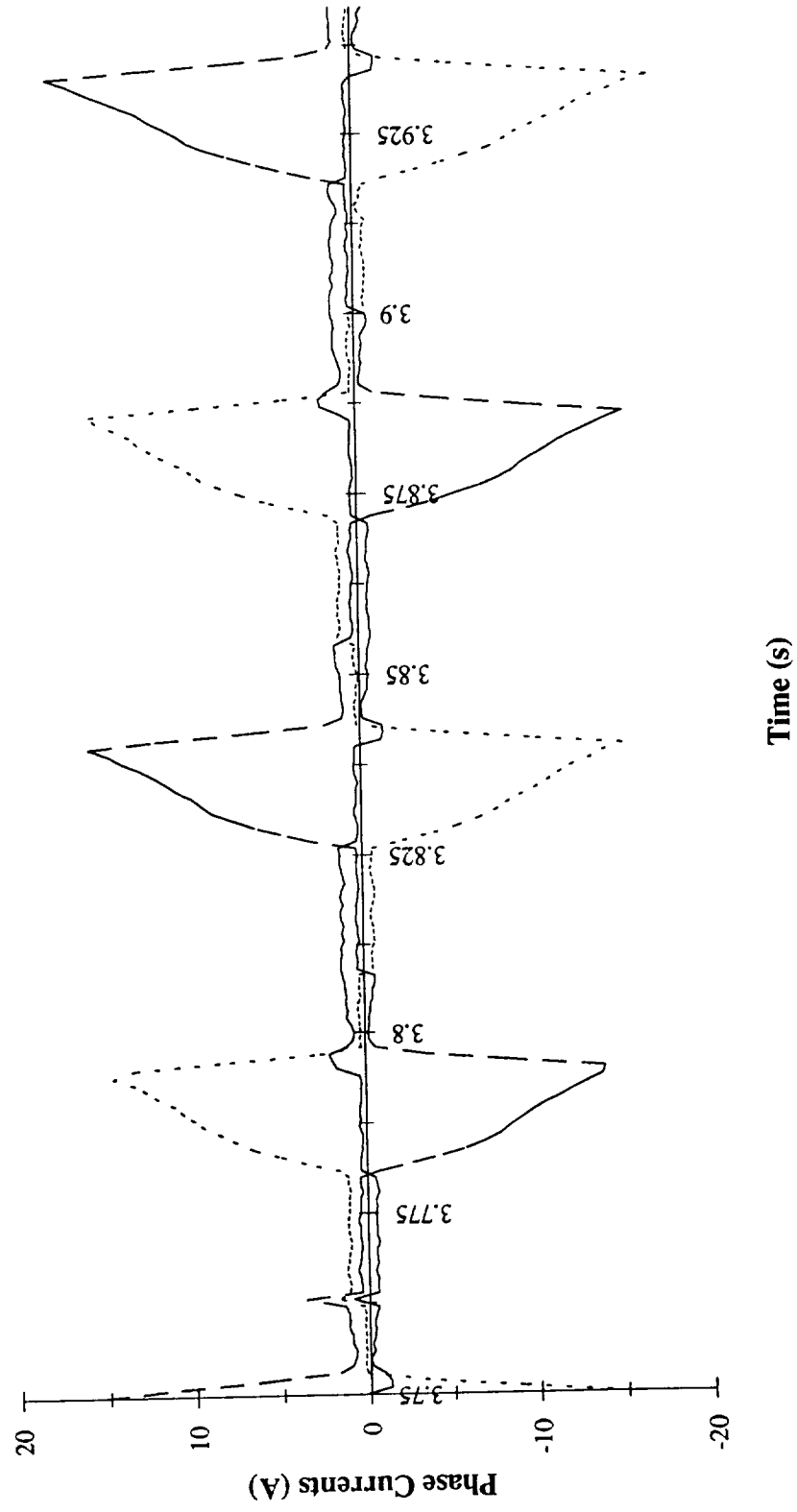


Figure 4.27 Actual phase currents for the open circuit failure

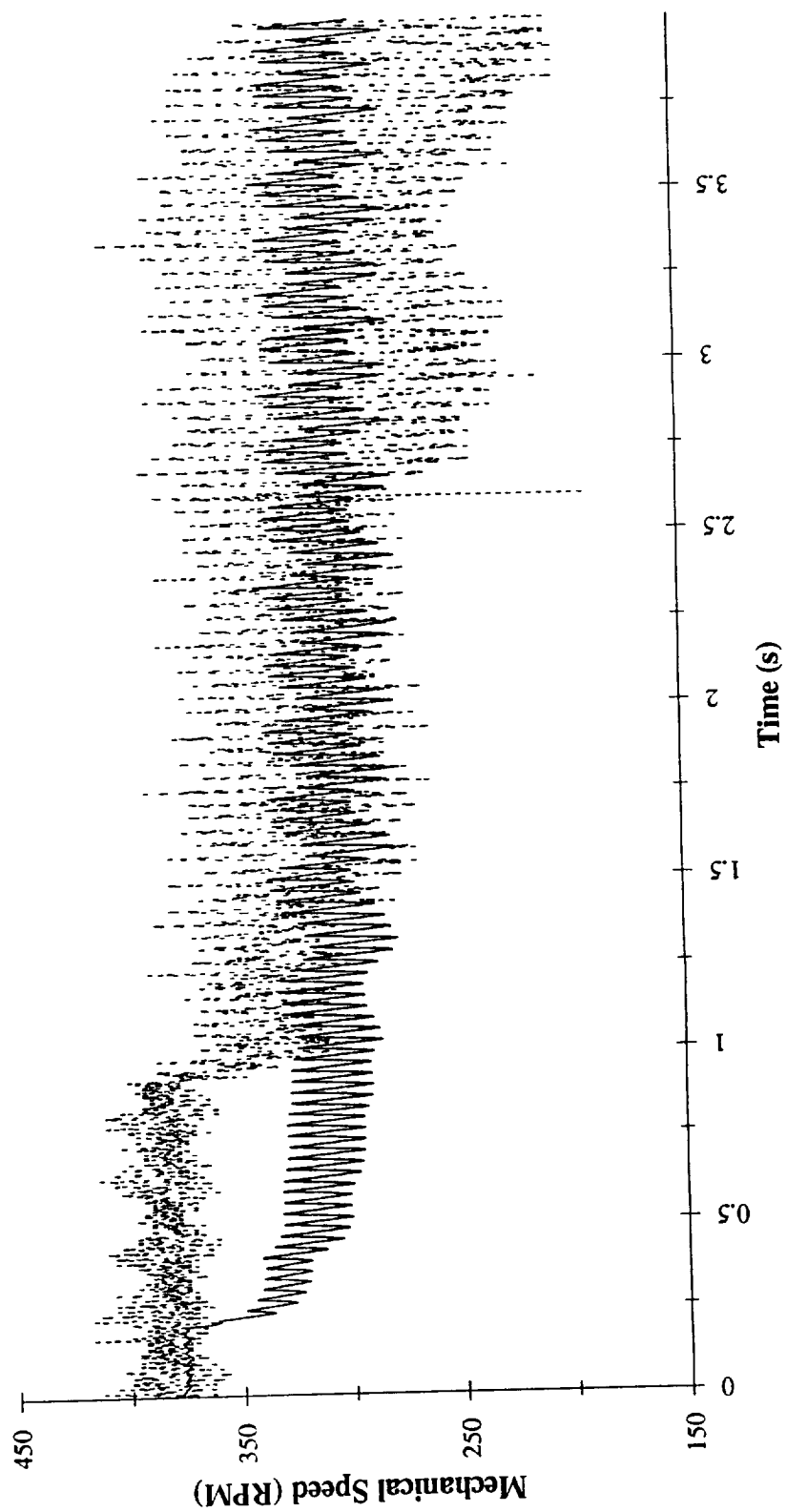


Figure 4.28 Simulated and actual mechanical speeds for the open circuit failure

model's ability to describe the open circuit fault mode for the brushless permanent magnet machine.

Finally, the short circuit fault mode was experimentally implemented using the laboratory resistor bank as previously described (see Figures 3.6 and 4.1). The fault location was arbitrarily chosen between the 'A' and 'B' phases of the motor. Simulation results were also obtained to compare with the experimental data. Again, the timed introduction of the fault resistance via the switch settings of the resistor bank was not sequenced between the simulation and laboratory experiments. Figures 4.29 and 4.30 show the simulation and actual phase currents for the machine, and Figure 4.31 shows the simulation and actual mechanical speed of the motor. Once again, the reasonable agreement of simulated and actual data authenticates the model's ability to describe this fault mode.

4.3 Discrete Kalman Filter Verification

Prior to implementing a health monitoring system using an adaptive Kalman filter with the BPMM, validation of the discrete Kalman filter as a signal processing technique for the motor was essential. Since the machine model was verified through both steady state and dynamic operation performance, the discrete Kalman filter was substantiated in a similar manner. Therefore, both the experimental and simulation data from the steady state and transient operation experiments were processed through a discrete Kalman filter. Before being utilized as a measurement signal by the Kalman filter, the machine simulation data was perturbed by simulated white noise with variance roughly equivalent to the noise contained on the actual laboratory signals. It should be noted that the discrete Kalman filter

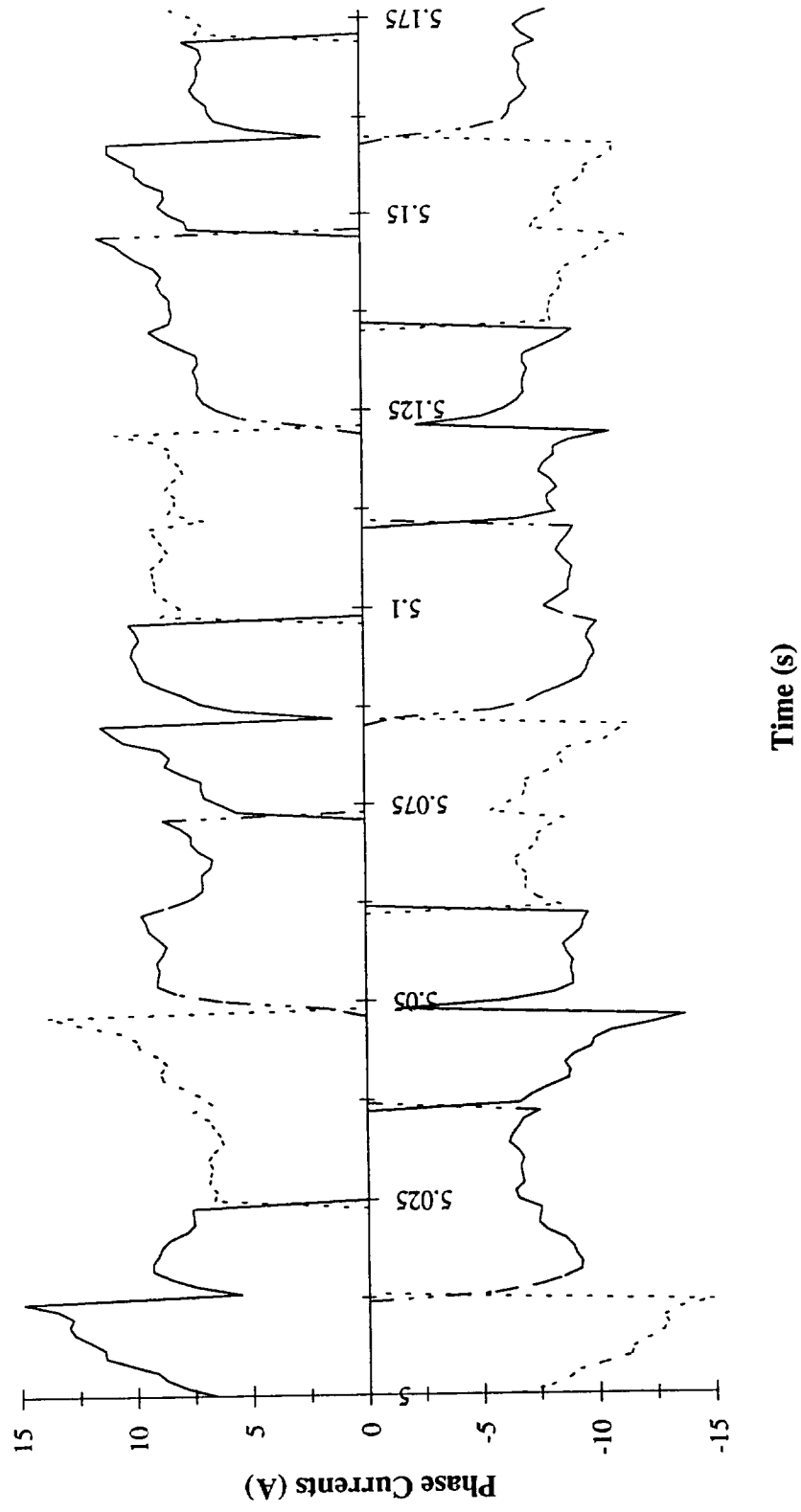


Figure 4.29 Simulated phase currents for the short circuit failure

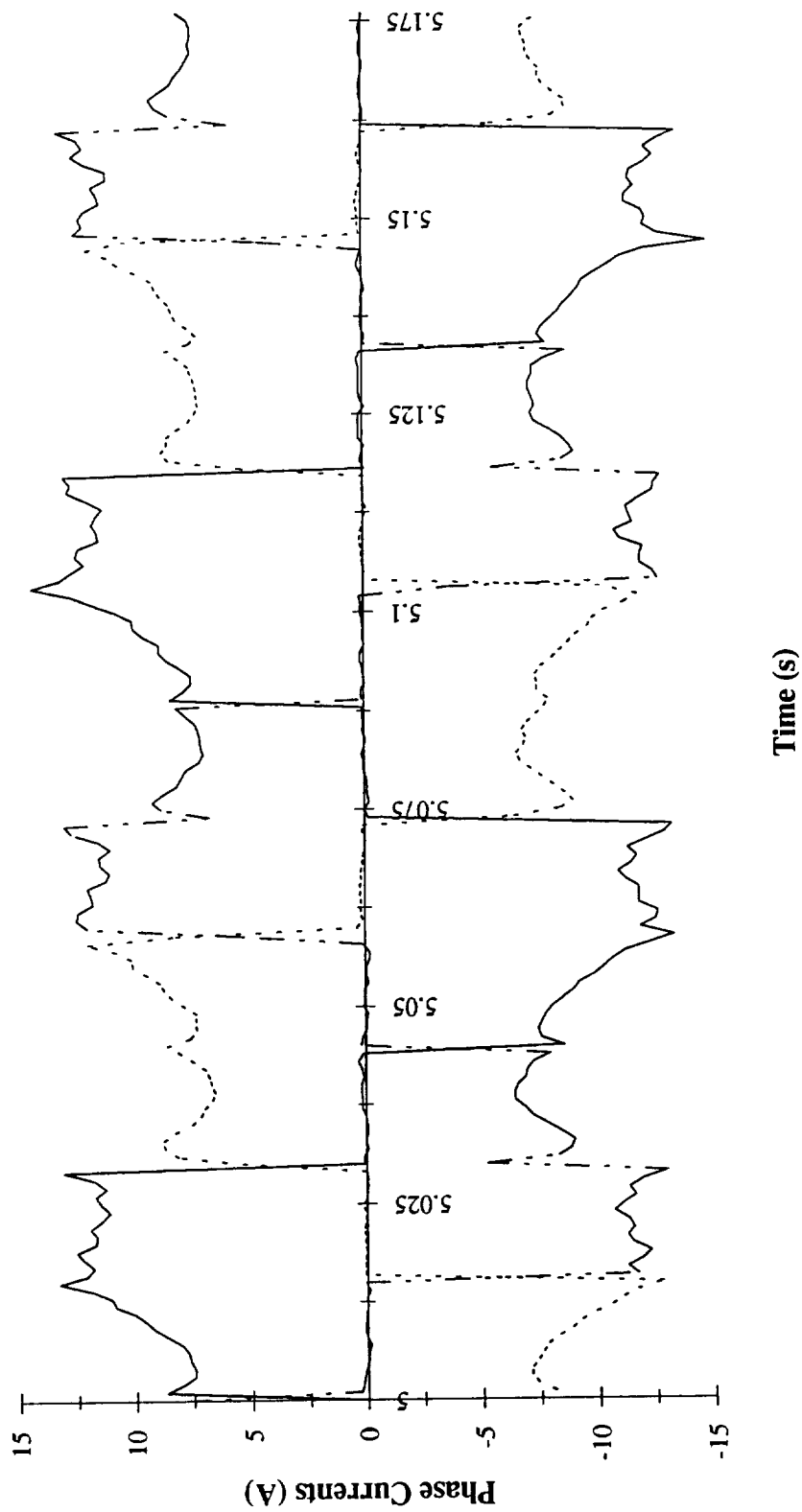


Figure 4.30 Actual phase currents for the short circuit failure

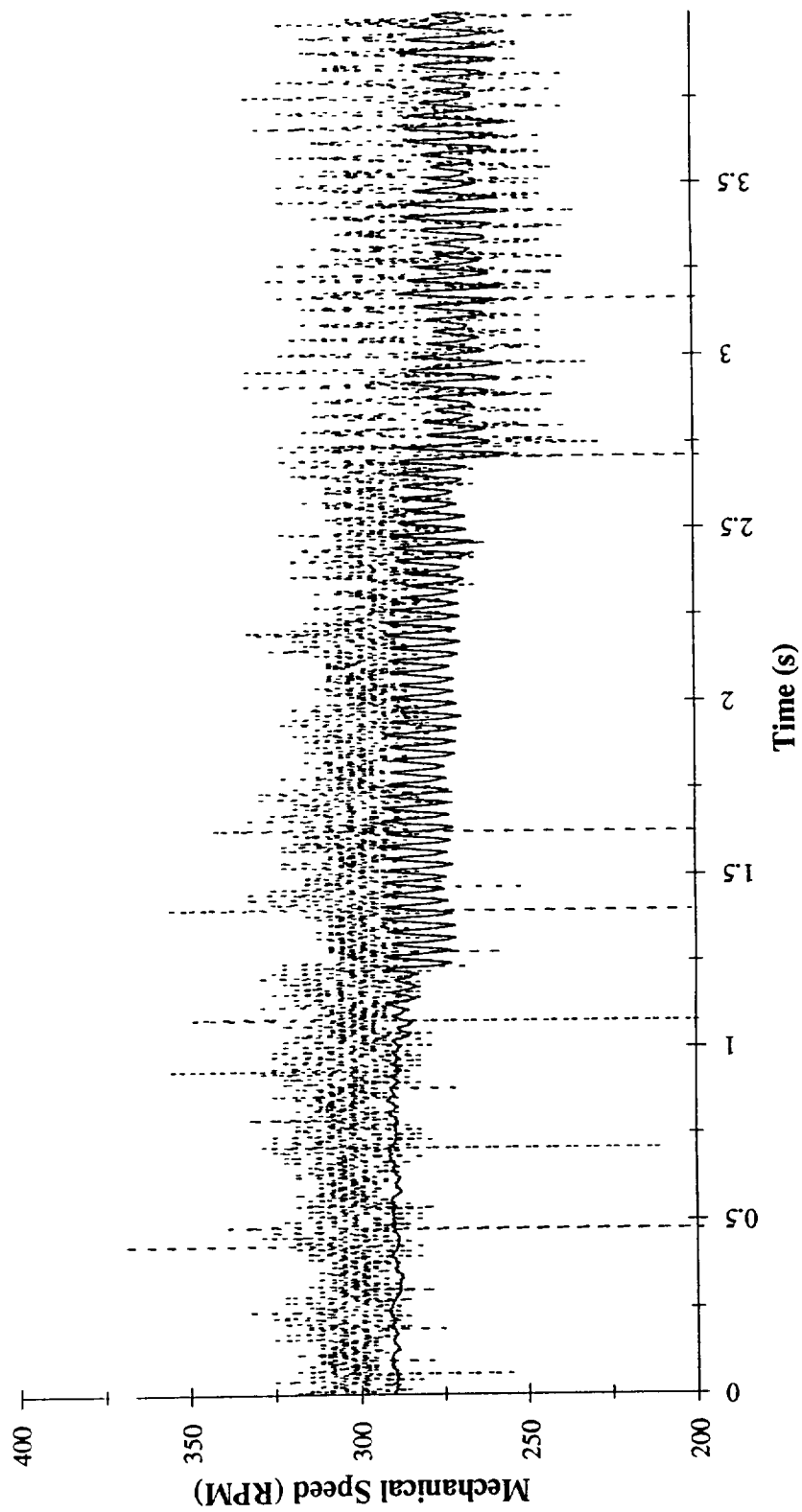


Figure 4.31 Simulated and actual mechanical speeds for the short circuit failure

program was not optimized for computational efficiency and was not operating at real-time data processing speeds during these tests.

4.3.1 Verification for Steady State Operation

Figures 4.32 and 4.33 show the noisy simulated phase 'A' current and mechanical speed signals with the Kalman filter estimates of the waveforms in steady state motor operation for a bus voltage of 75.0 volts. Figures 4.34 and 4.35 show the actual laboratory phase 'A' current and mechanical speed signals with the Kalman filter estimates of the waveforms in steady state motor operation for a bus voltage of 75.0 volts. Figures 4.36 and 4.37 show the noisy simulated phase 'A' current and mechanical speed signals with the Kalman filter estimates of the waveforms in steady state motor operation for a bus voltage of 150.0 volts. Figures 4.38 and 4.39 show the actual laboratory phase 'A' current and mechanical speed signals with the Kalman filter estimates of the waveforms in steady state motor operation for a bus voltage of 150.0 volts. Figures 4.40 and 4.41 show the noisy simulated phase 'A' current and mechanical speed signals with the Kalman filter estimates of the waveforms in steady state motor operation for a bus voltage of 200.0 volts. Figures 4.42 and 4.43 show the actual laboratory phase 'A' current and mechanical speed signals with the Kalman filter estimates of the waveforms in steady state motor operation for a bus voltage of 200.0 volts.

4.3.2 Verification for Dynamic Operation

Finally, the transient operation of the machine was processed by the discrete Kalman filter. Figures 4.44 to 4.46 show the noisy simulated phase 'A' current and

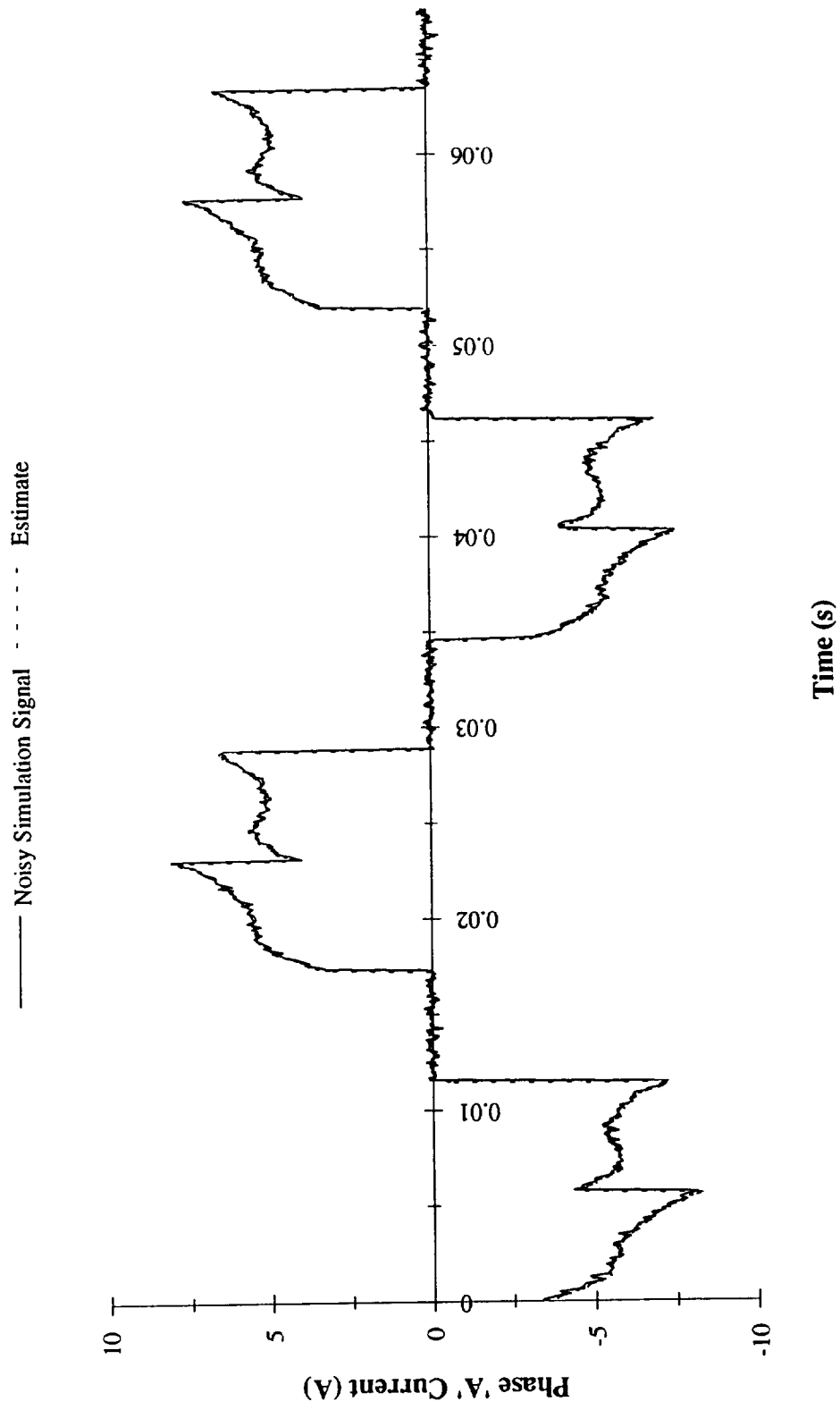


Figure 4.32 Steady state noisy simulated and estimated phase currents for a 75.0 volt bus

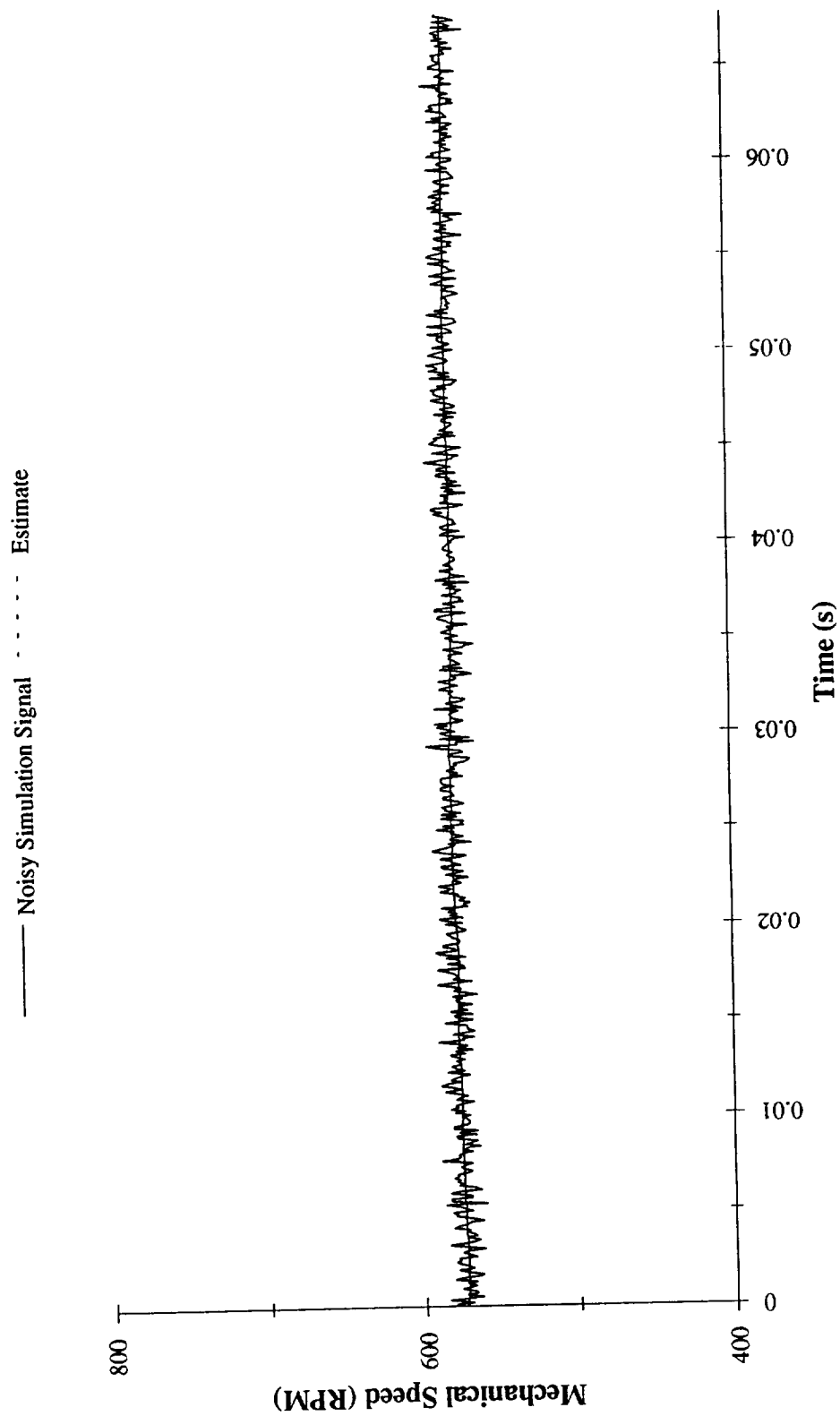


Figure 4.33 Steady state noisy simulated and estimated mechanical speeds for a 75.0 volt bus

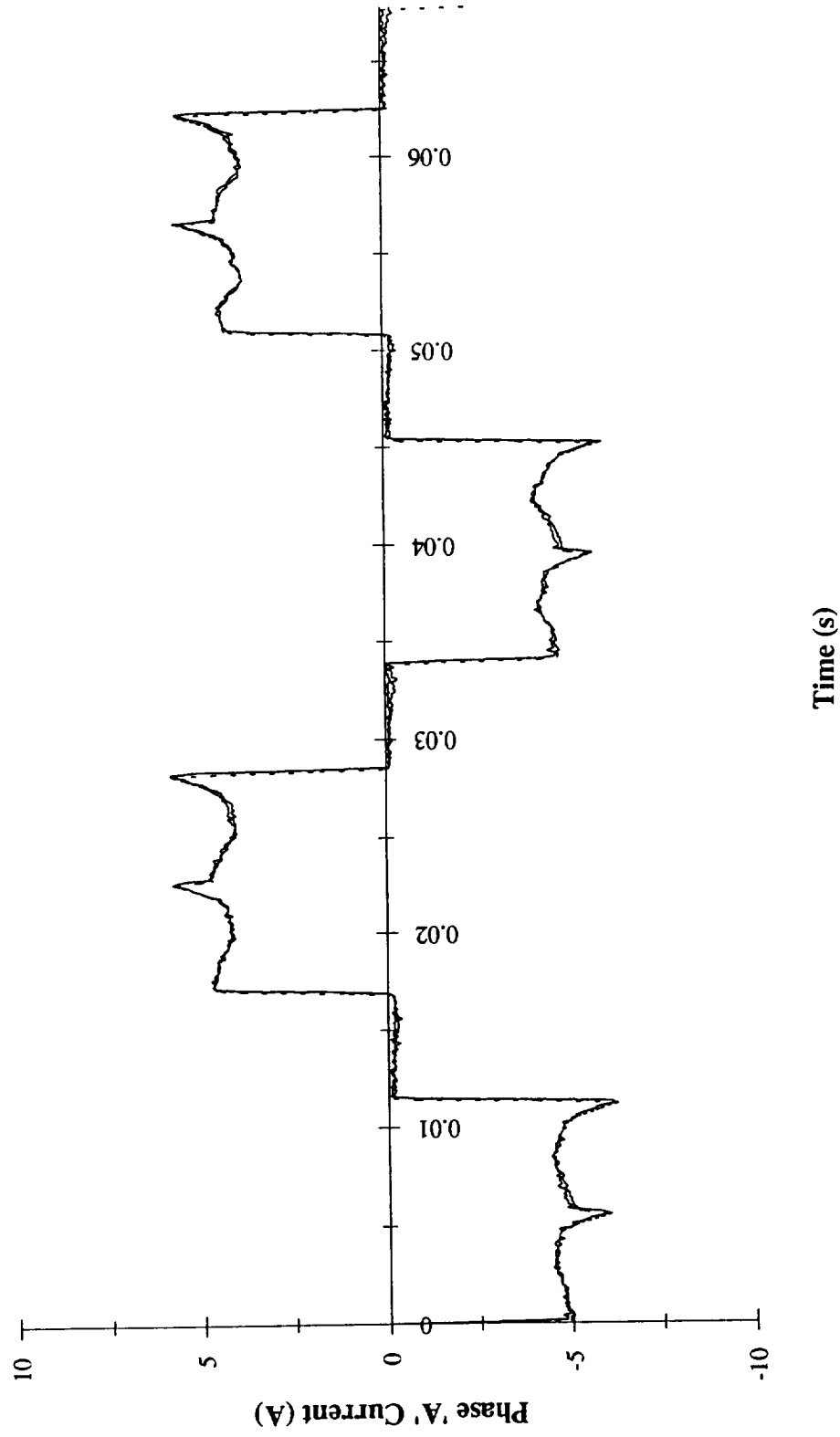


Figure 4.34 Steady state actual and estimated phase currents for a 75.0 volt bus

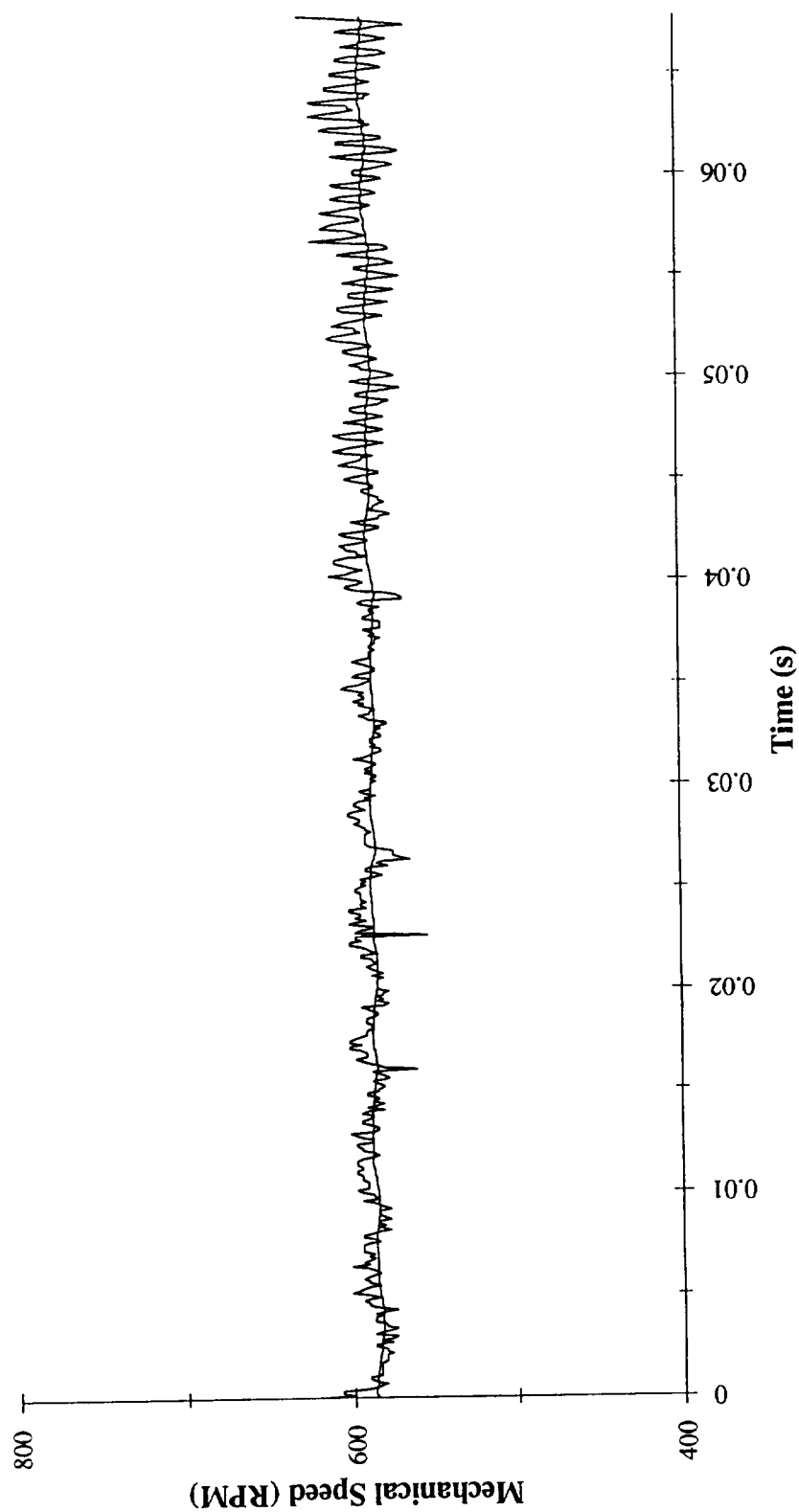


Figure 4.35 Steady state actual and estimated mechanical speeds for a 75.0 volt bus

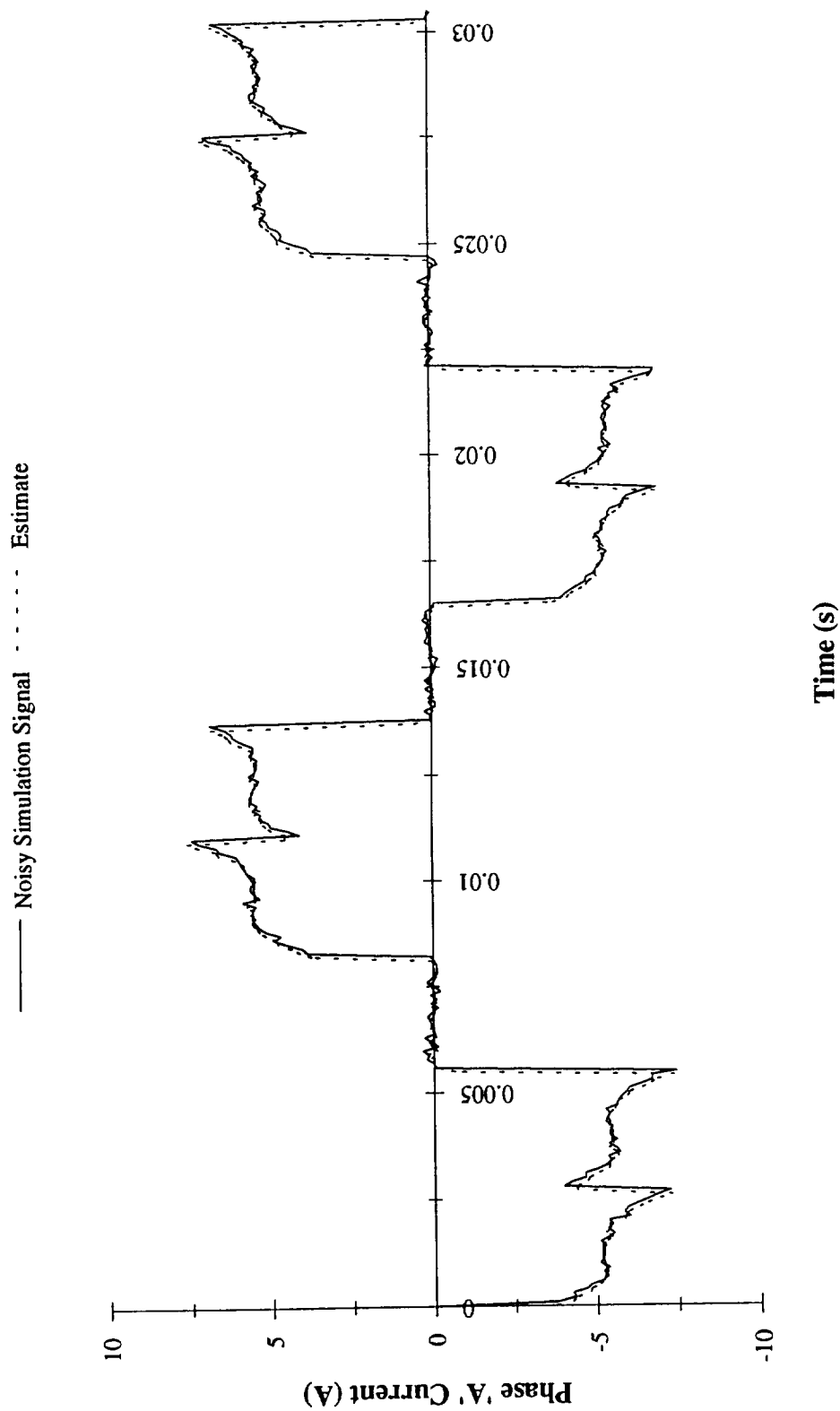


Figure 4.36 Steady state noisy simulated and estimated phase currents for a 150.0 volt bus

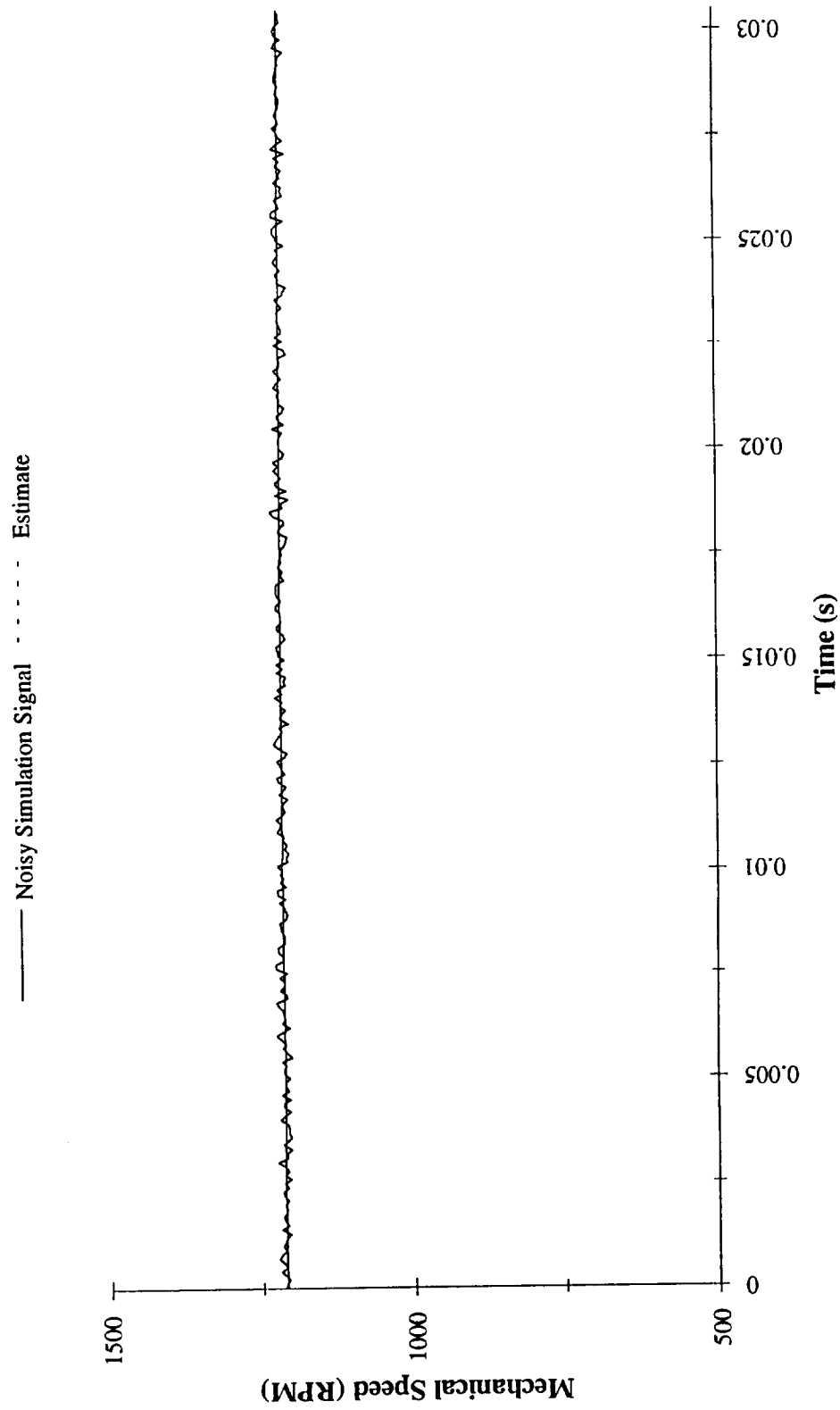


Figure 4.37 Steady state noisy simulated and estimated mechanical speeds for a 150.0 volt bus

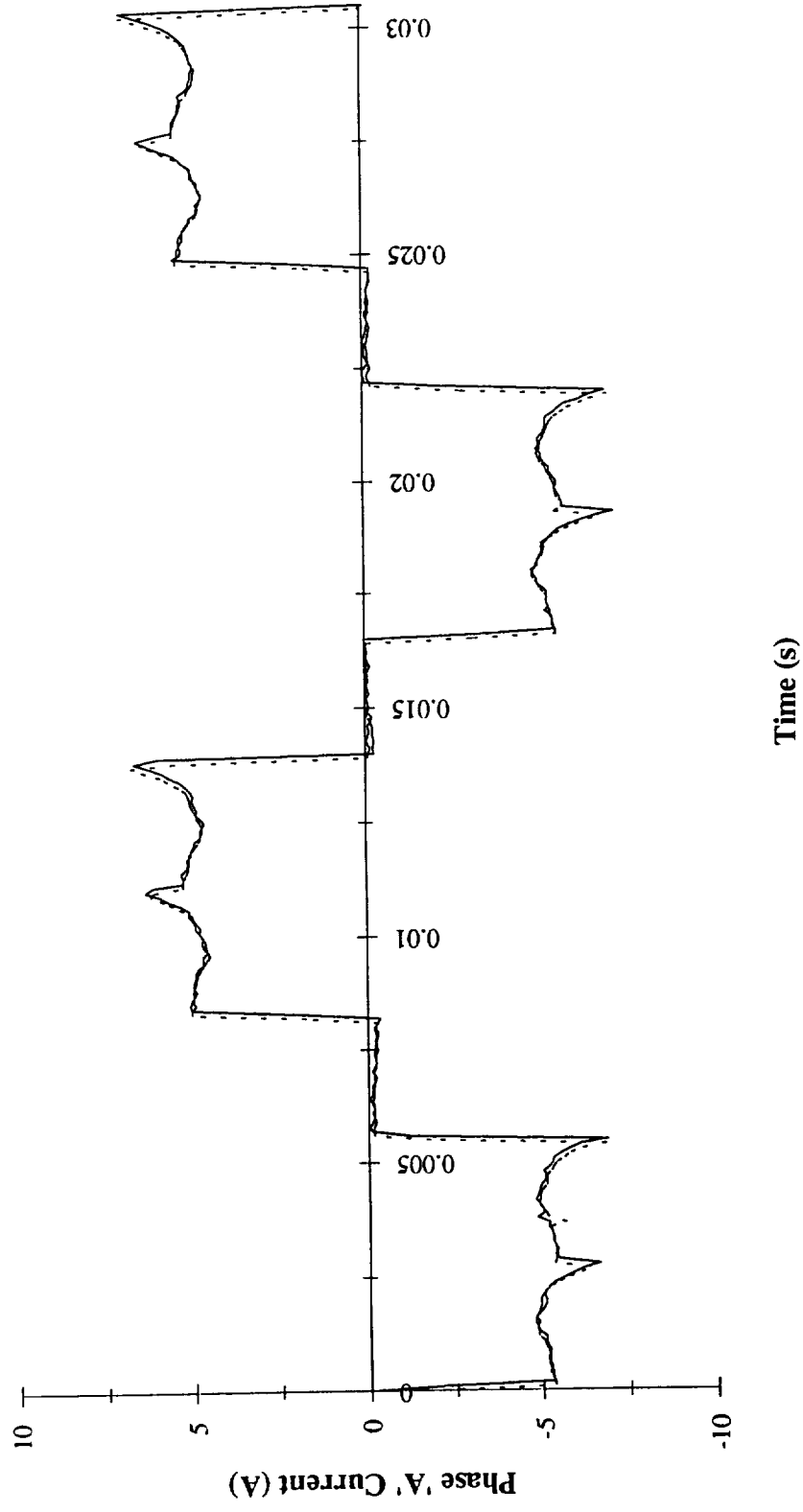


Figure 4.38 Steady state actual and estimated phase currents for a 150.0 volt bus

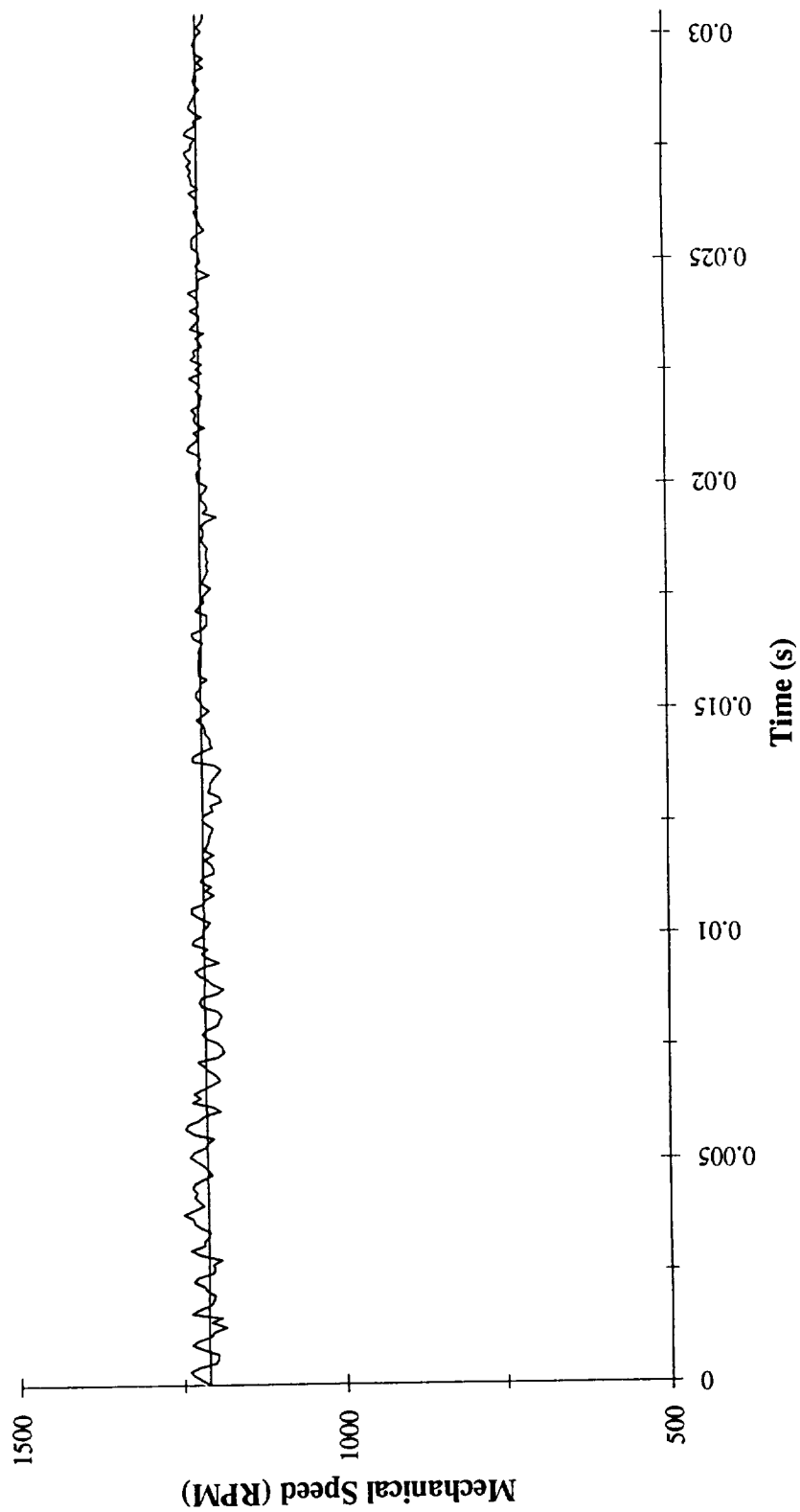


Figure 4.39 Steady state actual and estimated mechanical speeds for a 150.0 volt bus

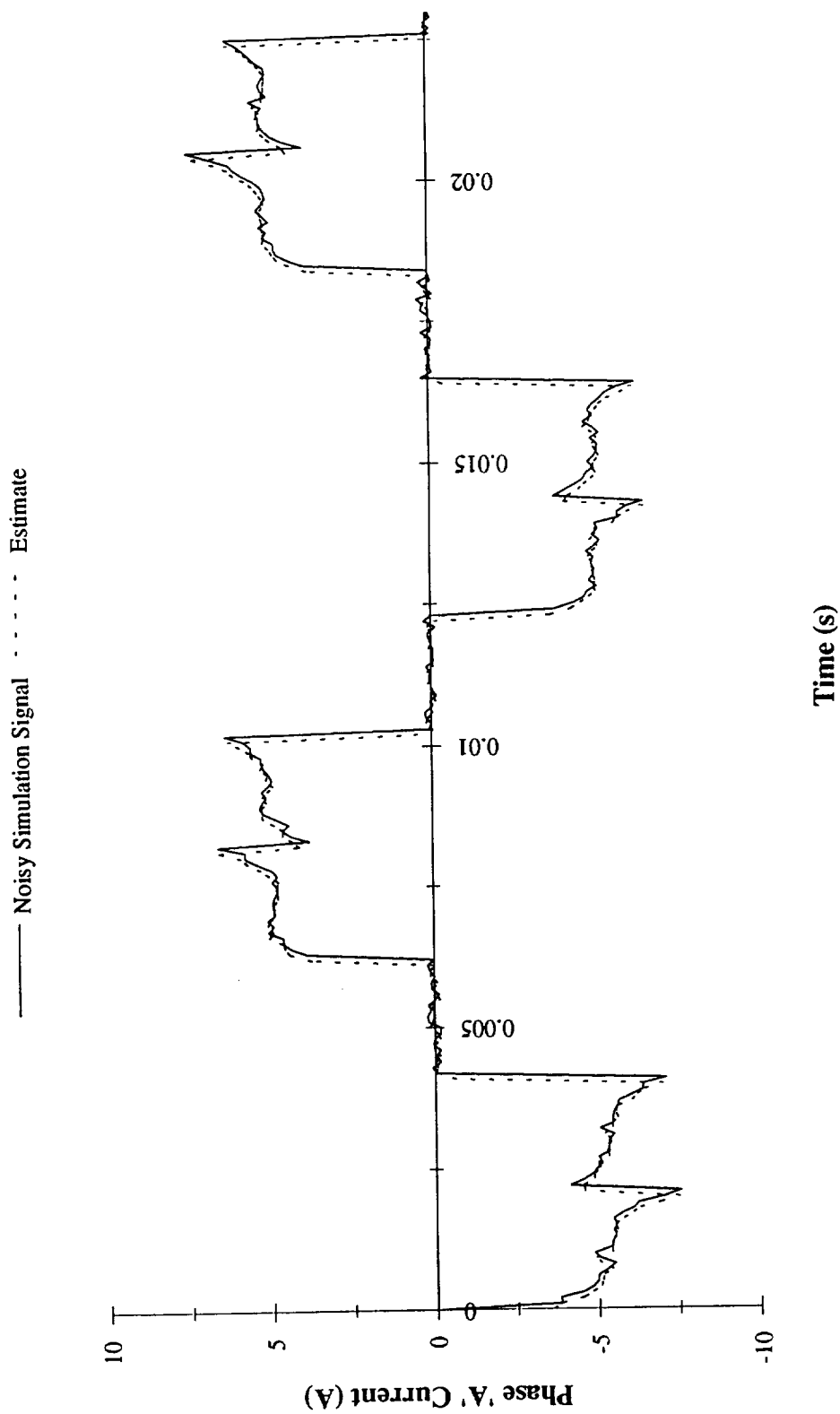


Figure 4.40 Steady state noisy simulated and estimated phase currents for a 200.0 volt bus

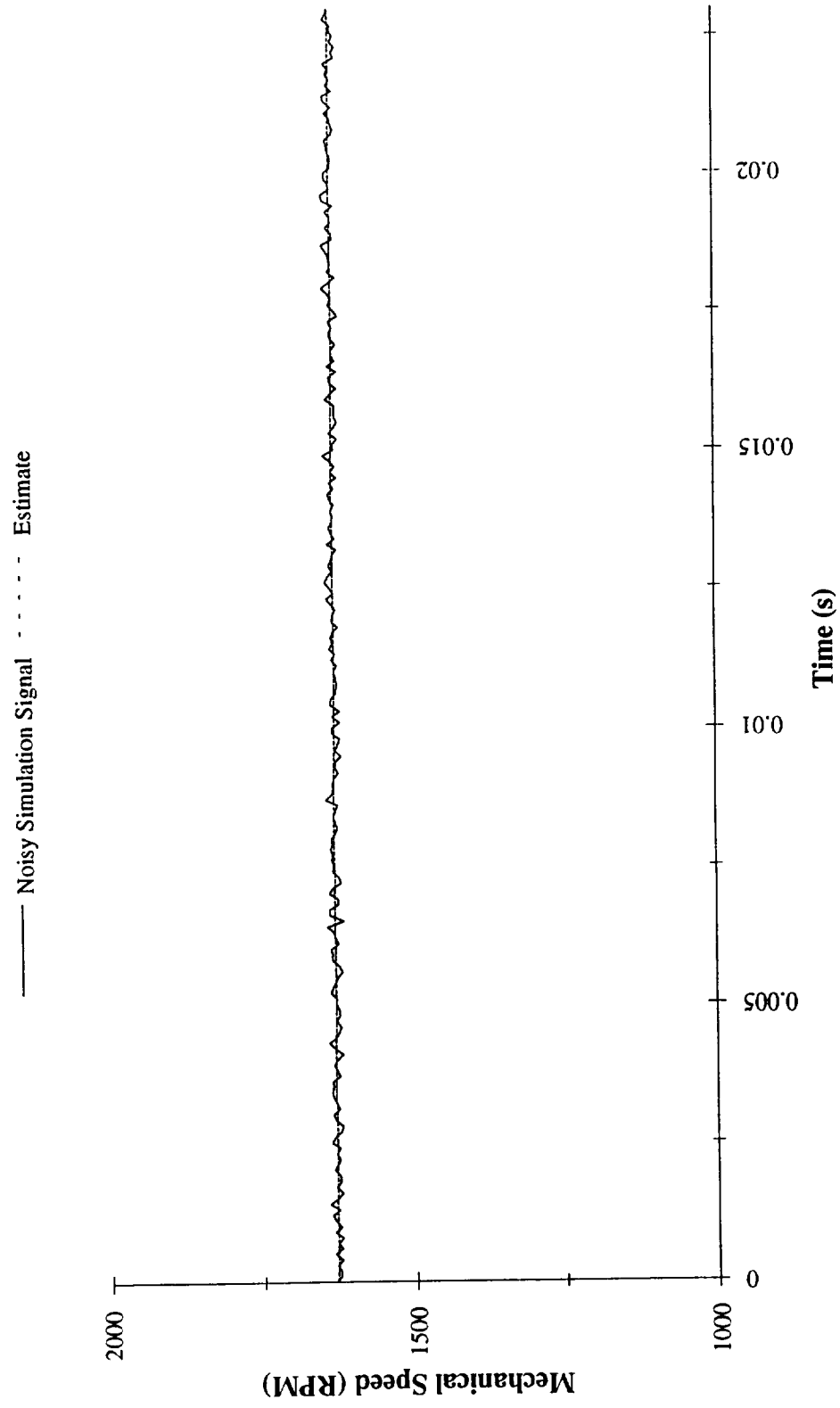


Figure 4.41 Steady state noisy simulated and estimated mechanical speeds for a 200.0 volt bus

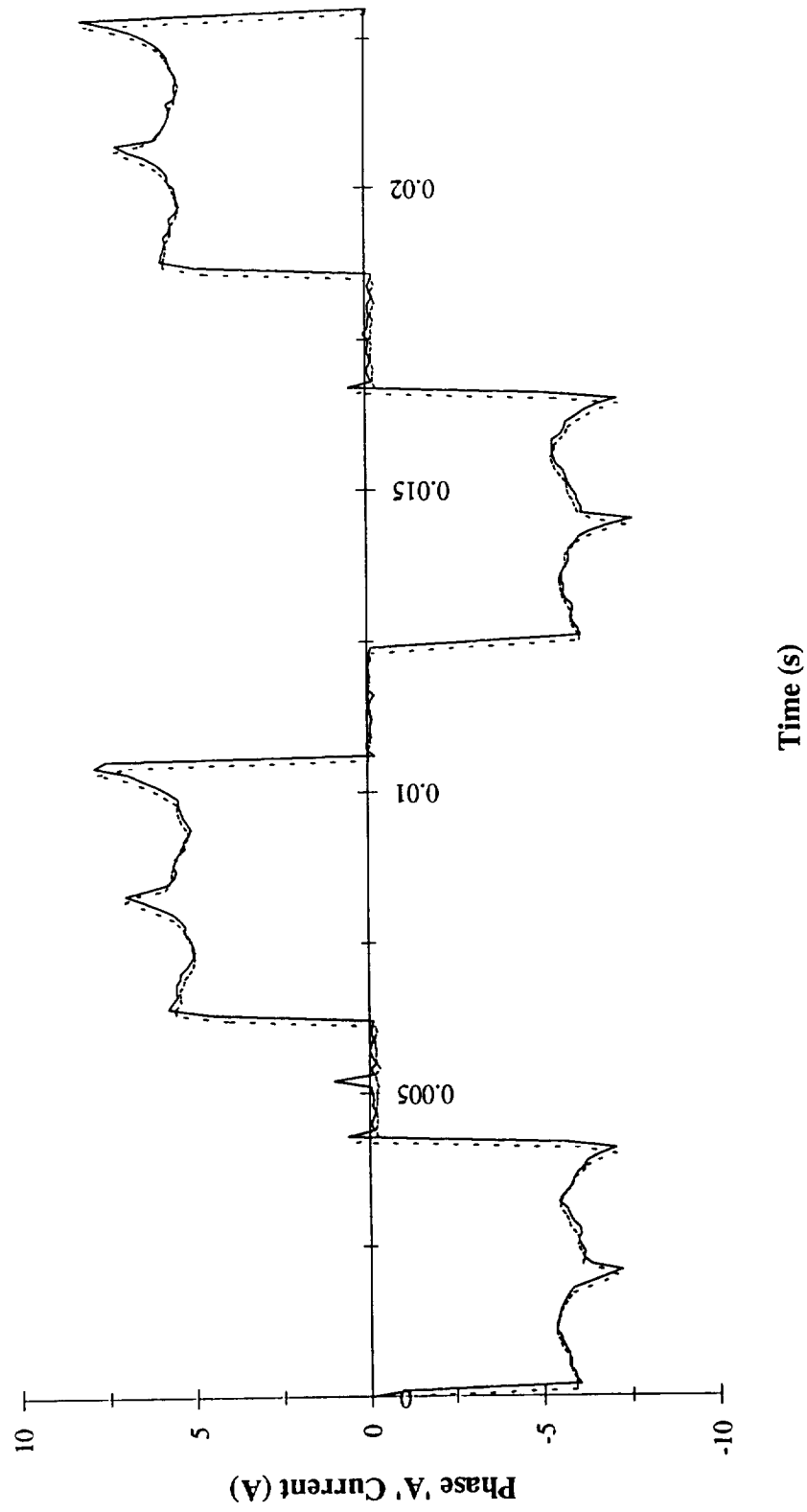


Figure 4.42 Steady state actual and estimated phase currents for a 200.0 volt bus

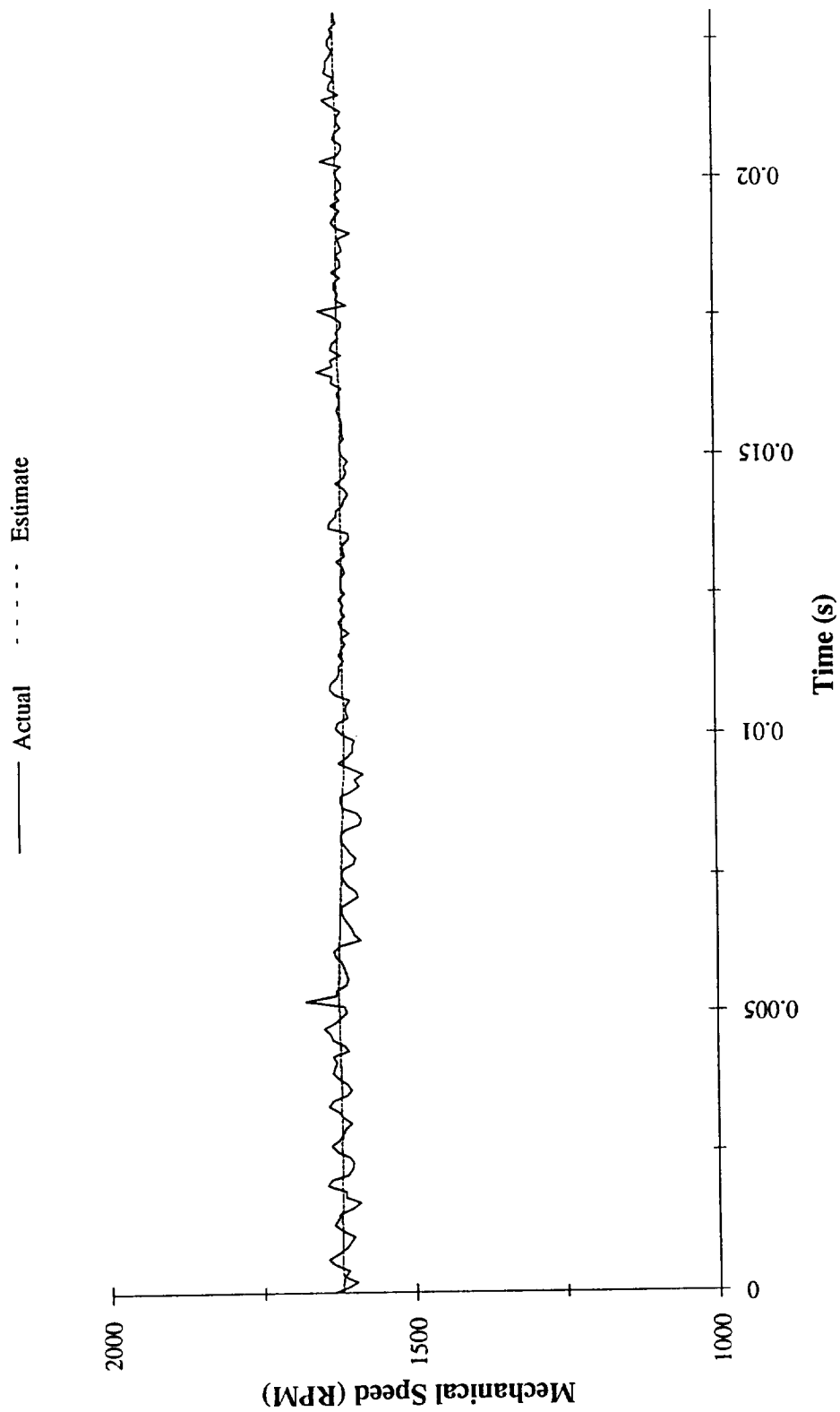


Figure 4.43 Steady state actual and estimated mechanical speeds for a 200.0 volt bus

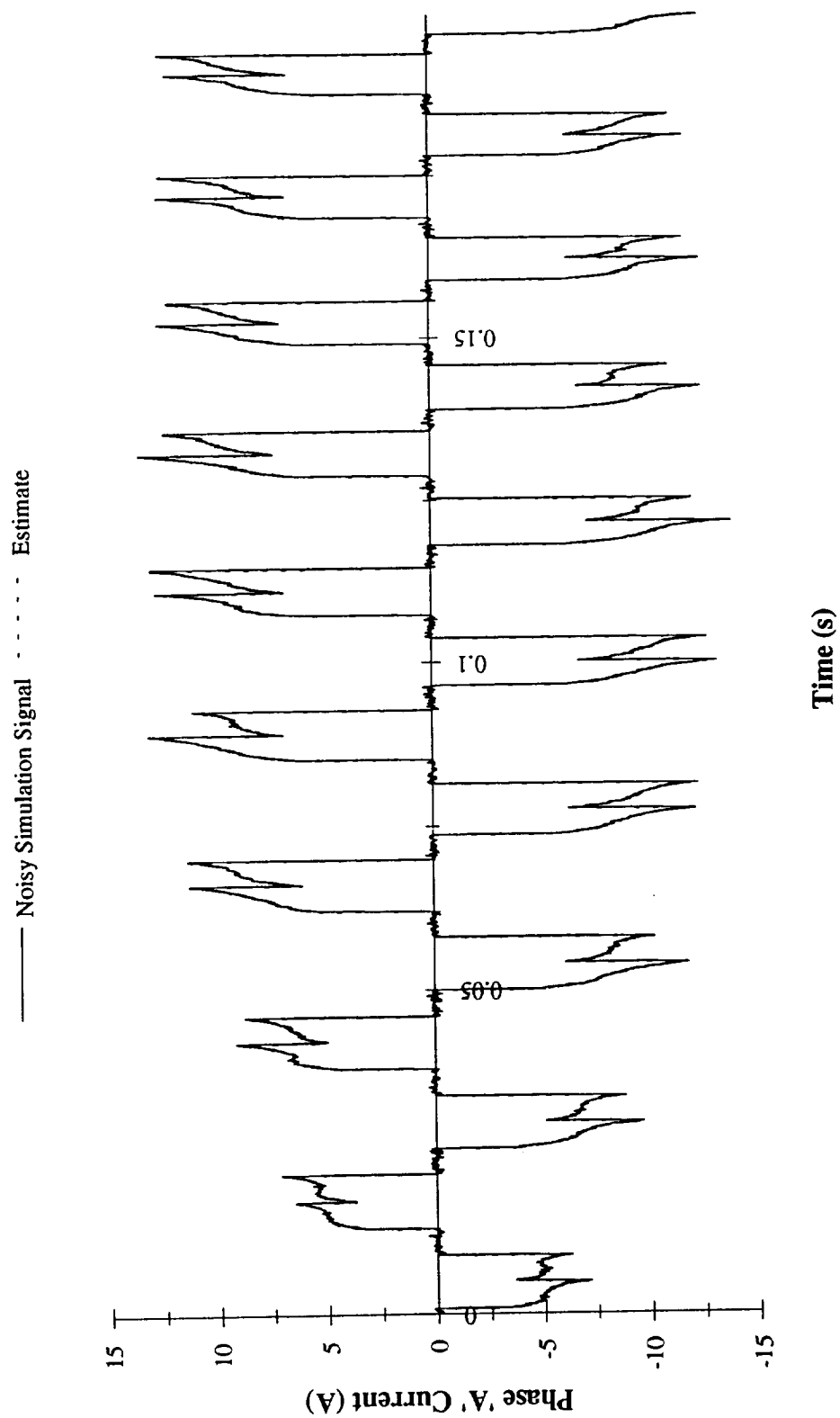


Figure 4.44 Noisy simulated and estimated phase currents for transient motor operation

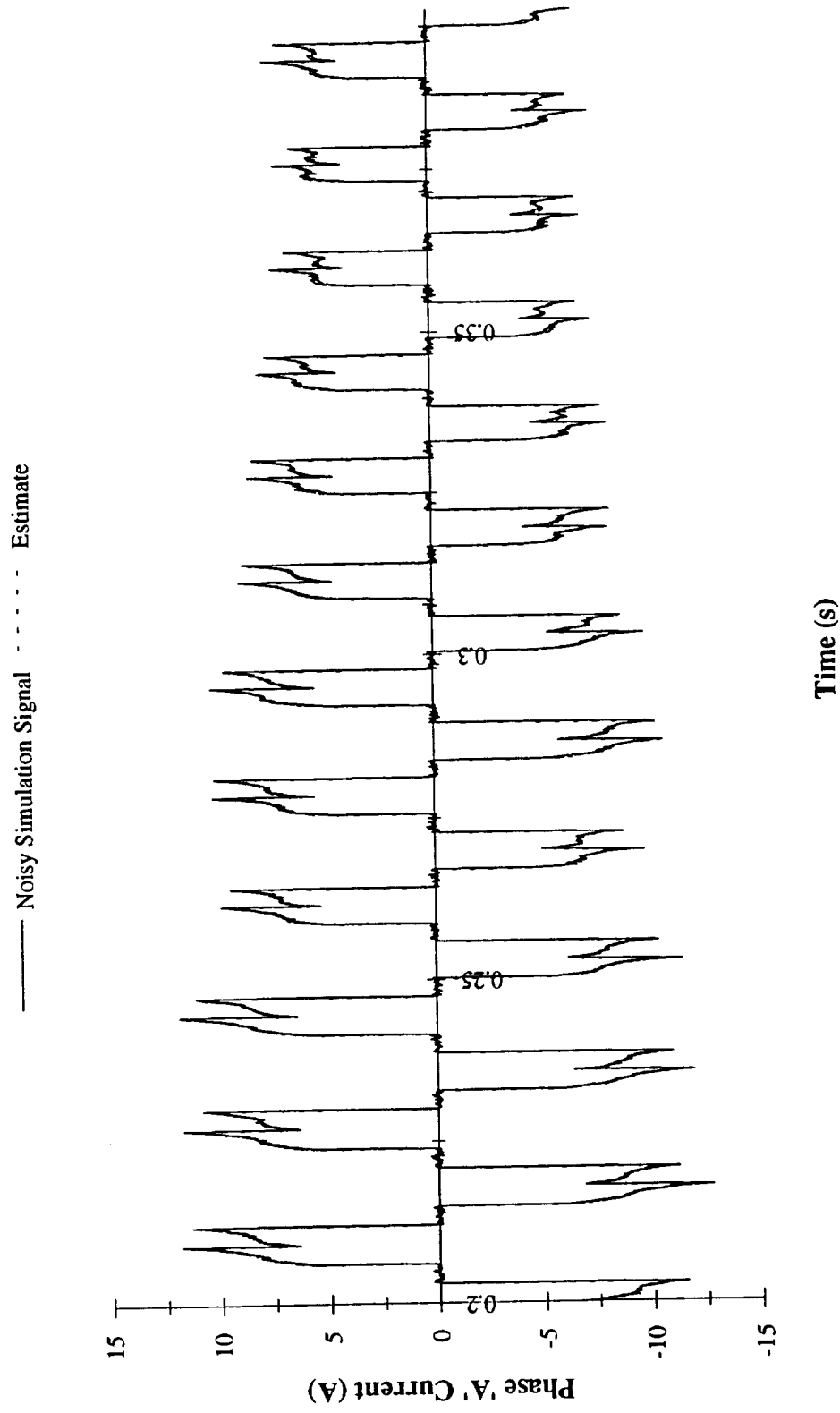


Figure 4.45 Noisy simulated and estimated phase currents for transient motor operation (continued)

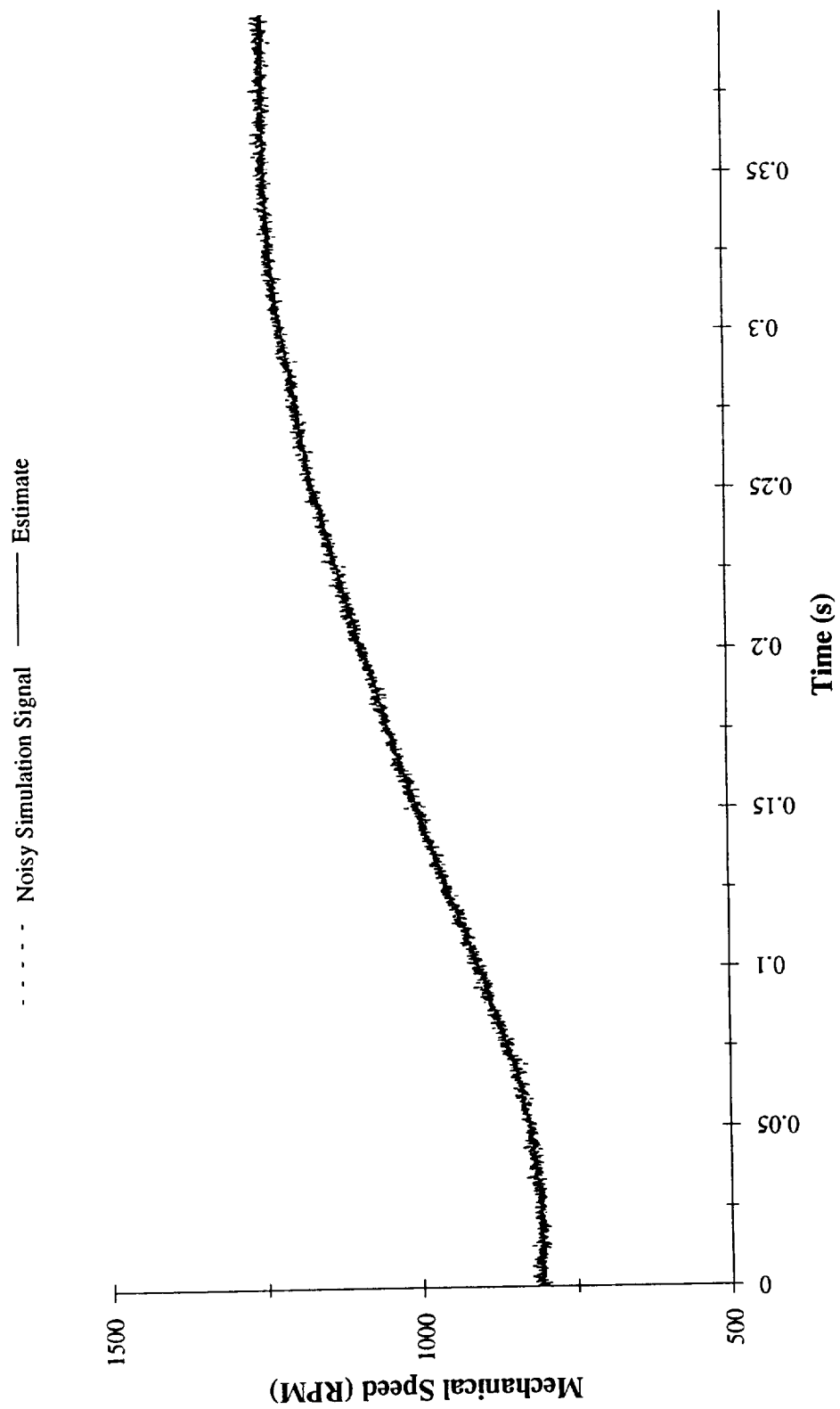


Figure 4.46 Noisy simulated and estimated mechanical speeds for transient motor operation

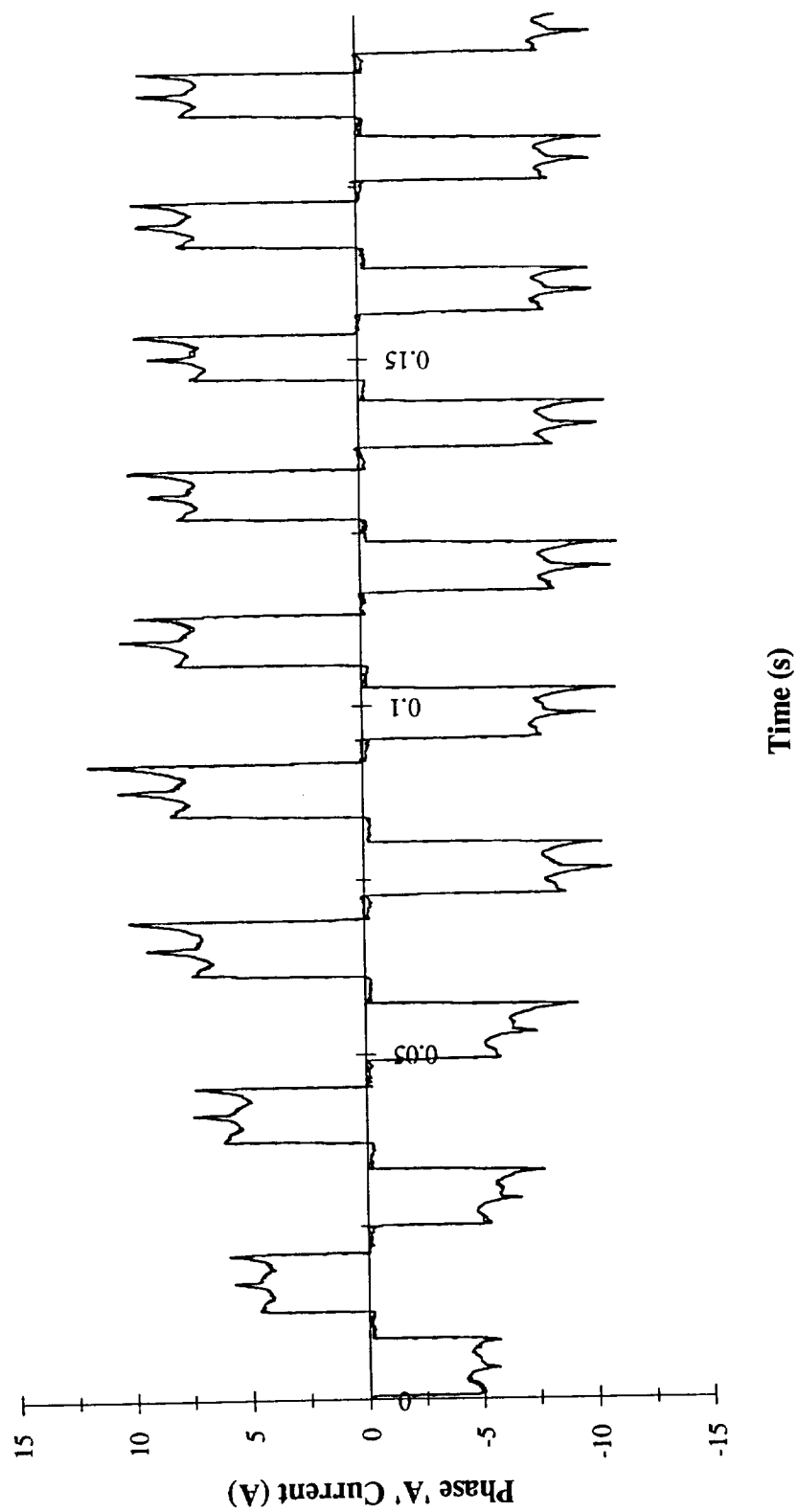


Figure 4.47 Actual and estimated phase currents for transient motor operation

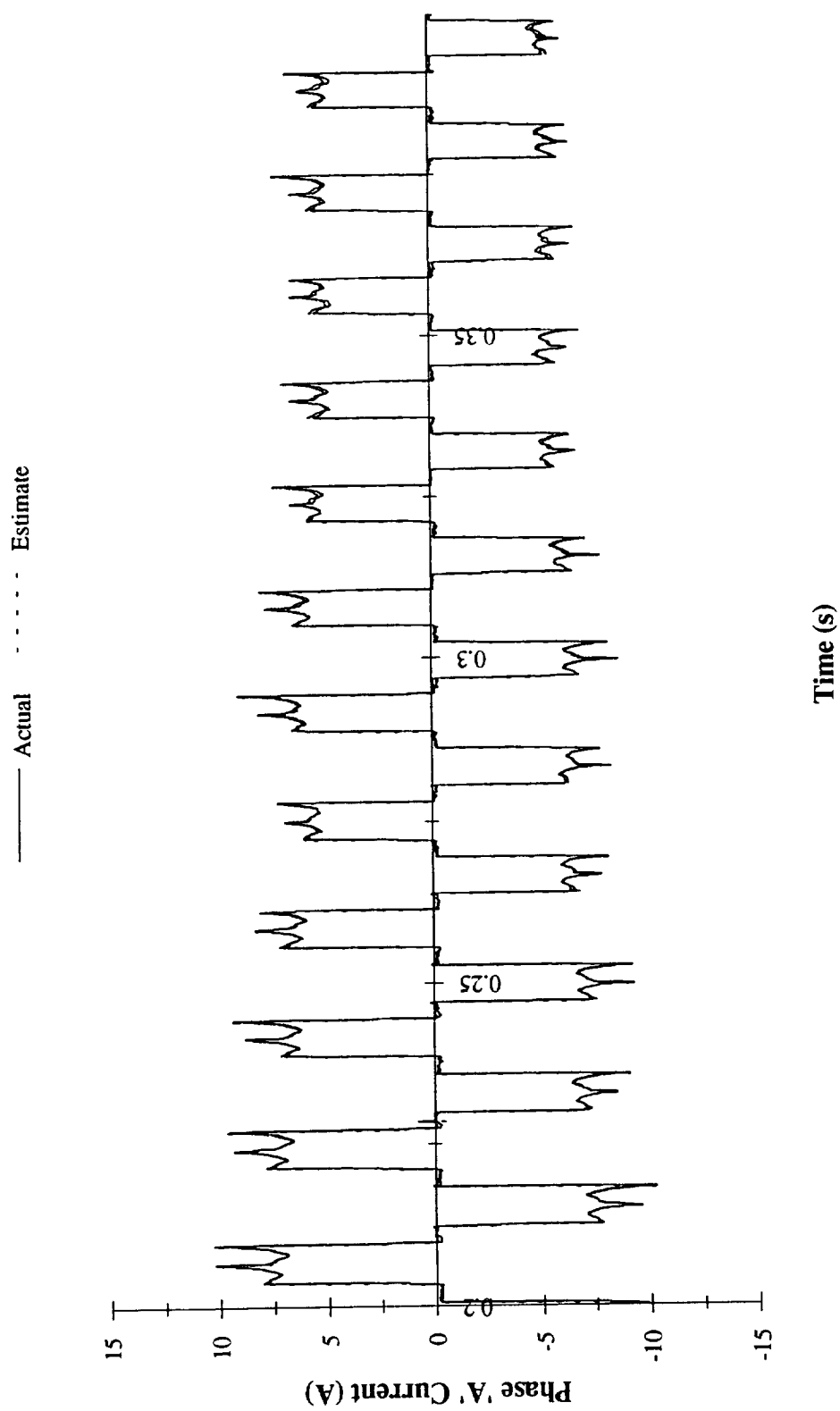


Figure 4.48 Actual and estimated phase currents for transient motor operation (continued)

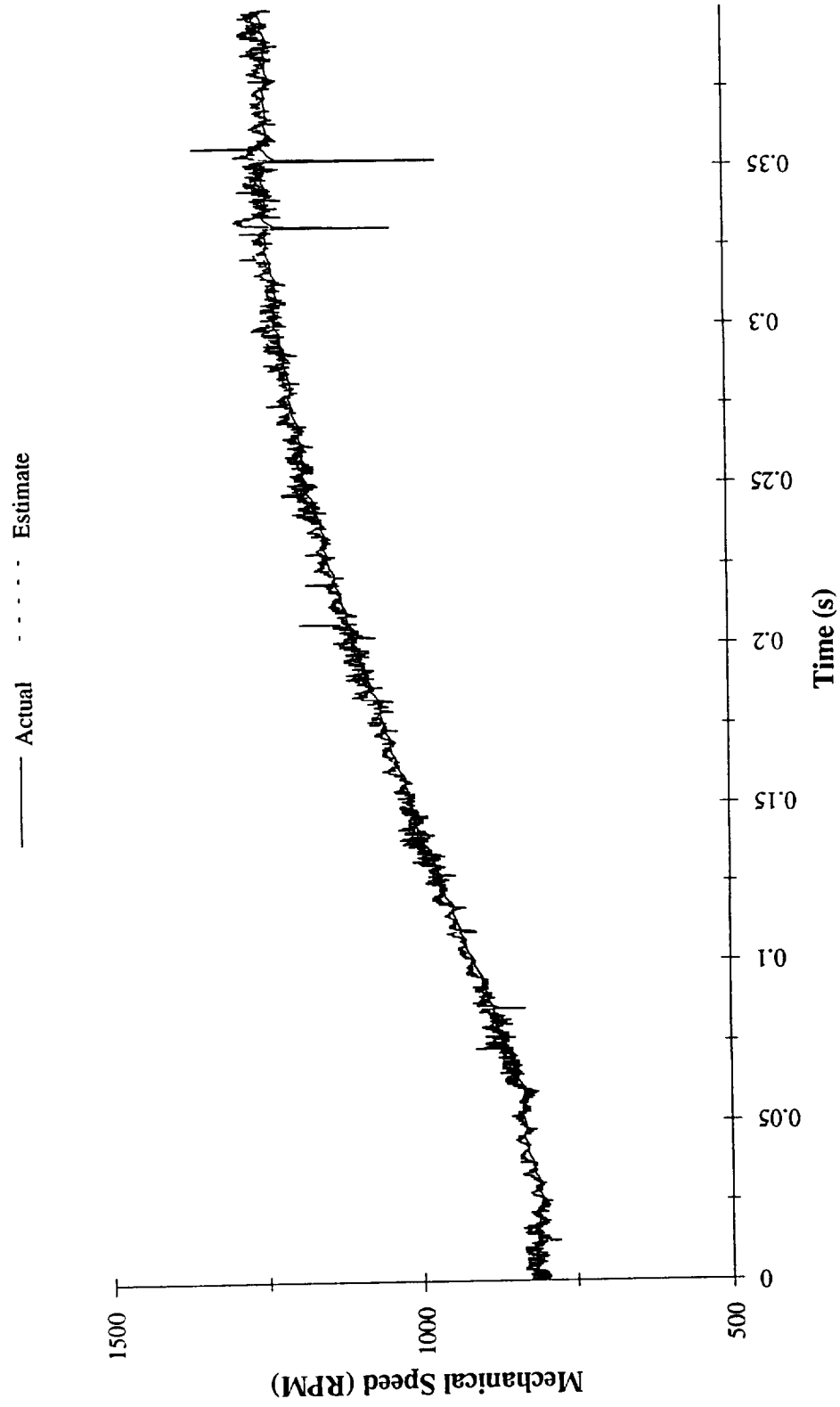


Figure 4.49 Actual and estimated mechanical speeds for transient motor operation

mechanical speed signals with the Kalman filter estimates of the waveforms. Figures 4.47 to 4.49 show the actual laboratory phase 'A' current and mechanical speed signals with the Kalman filter estimates of the waveforms. From the obvious agreement between the filter estimates and the signal waveforms for steady state and dynamic motor operation, using both simulated and actual data, the discrete Kalman filter is an accurate signal processing approach for the brushless permanent magnet machine.

4.4 Adaptive Kalman Filter Verification

Equipped with the knowledge that the discrete Kalman filter is an appropriate signal processing technique for the brushless permanent magnet machine, it is reasonable to hope that the adaptive filter will be adequate for the task of health monitoring the BPMM. This section describes the verification of the filter's performance with the nonlinear behavior associated with the flux weakening, open circuiting, and short circuiting failure modes. When possible, both simulated and actual laboratory fault data was evaluated with the adaptive filter strategy developed in section 3.4.

4.4.1 Flux Weakening Failure Mode

As previously stated, the flux weakening failure was conducted solely through simulation. Initial adaptive filtering results for processing this failure mode were surprisingly poor. Troubleshooting the filter's performance by allowing each filter estimate to become it's next state rather than blending the estimates of the two best filters led to the data shown in Figure 4.50. The plot depicts the simulated mechanical speed and two filter estimates for speed. The back EMF constant, which is the parameter used to describe this

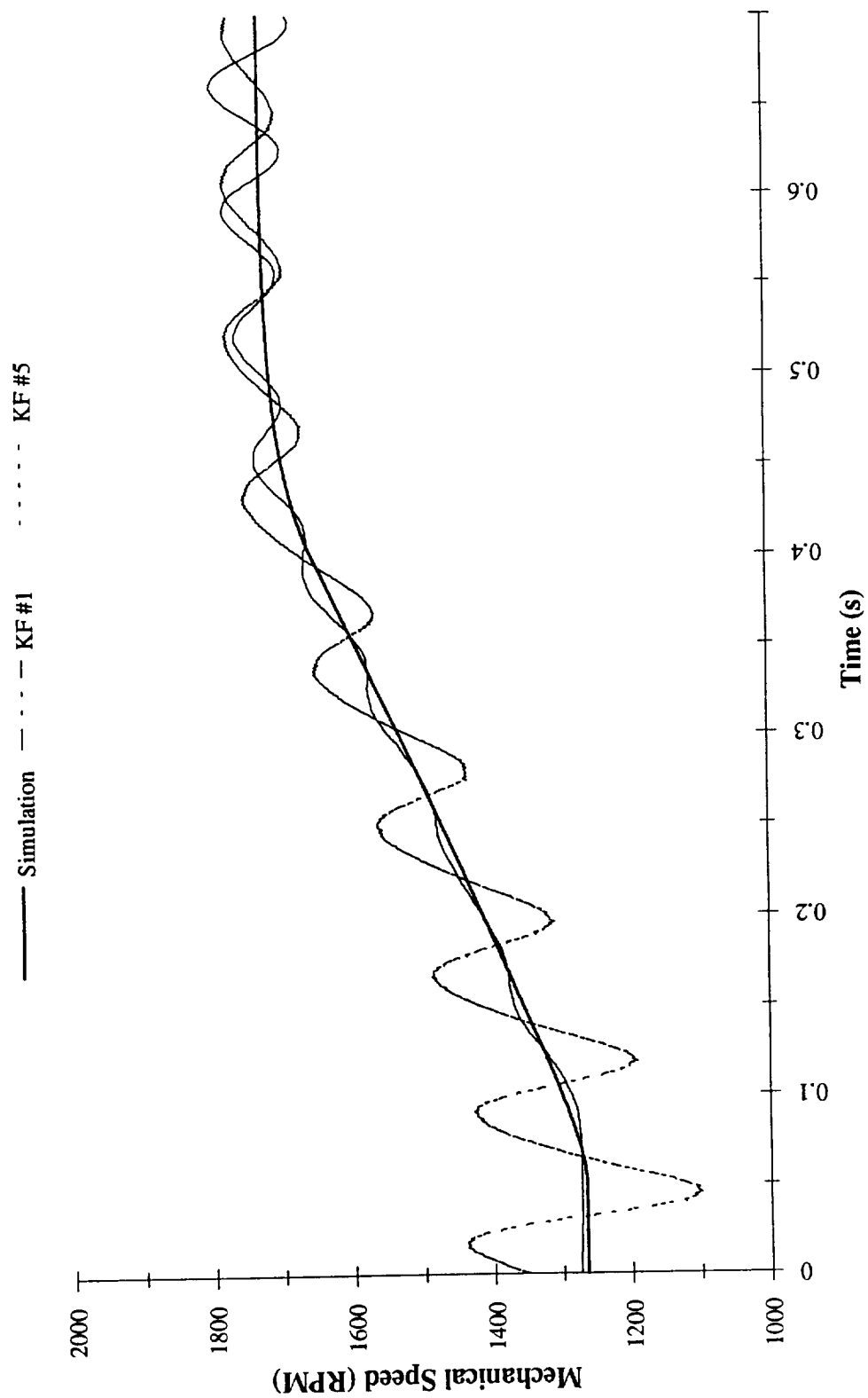


Figure 4.50 Simulated and estimated mechanical speeds for flux weakening failure

fault, is utilized by the model for calculating the generated back EMFs contained within the deterministic control input vector (\underline{u}_k). Therefore, rather than having the fault description expressed within the state transition matrix, the fault is currently being described within the control input vector. This is problematic since the control input vector also contains the rotor position signals which are strongly correlated to mechanical speed. Notice from Figure 4.50 that the fault reduces the oscillations of the estimate from the fifth filter, while the estimate from the first filter starts oscillating. For this test, the first filter depicted normal operation while the fifth filter exactly described the simulated fault, and the measurement data used was noiseless simulation signals.

4.4.2 Open Circuit Failure Mode

The adaptive Kalman filter was implemented for the open circuit failure mode and performed well with both simulation and actual data. Two strategies for filter selection were used. The first approach was designed to utilize the third filter of the five Kalman filters to describe the fault, thus the best estimate should emerge from the middle filter. The second approach was designed to utilize the fifth Kalman filter to describe the fault. Both strategies contained an averaging technique for expressing an estimate of the fault resistance. Figures 4.51 and 4.52 show the fault resistance estimate for both strategies of adaptive Kalman filtering using noisy simulation data as signal measurements. Figures 4.53 and 4.54 show the fault resistance estimate for both strategies of adaptive Kalman filtering using the actual laboratory data as signal measurements. The results from these tests indicate that the adaptive approach senses the presence of the open circuit failure as depicted by the increasing estimate for fault resistance. Therefore, the function of machine

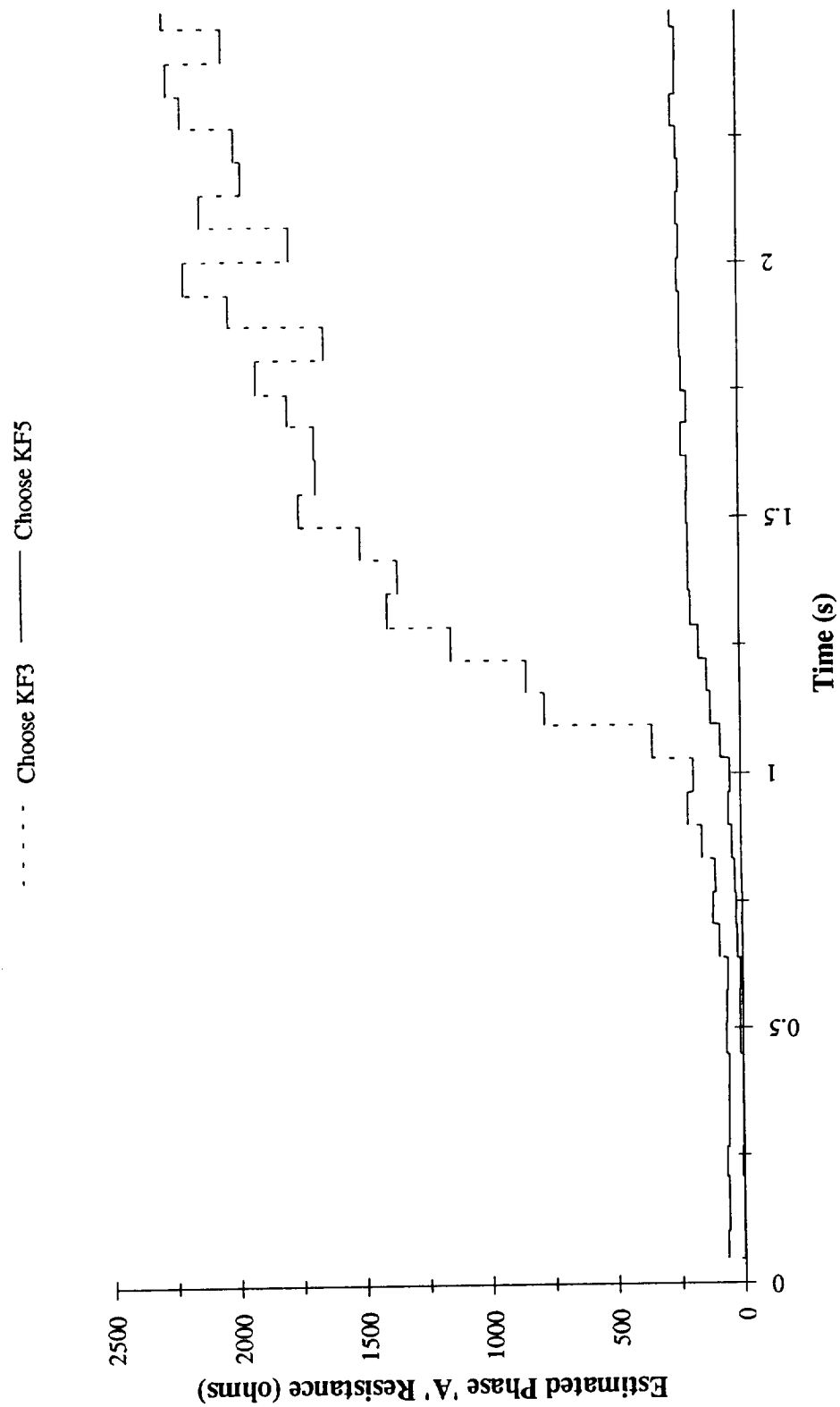


Figure 4.51 Estimated fault resistance for the simulated open circuit failure

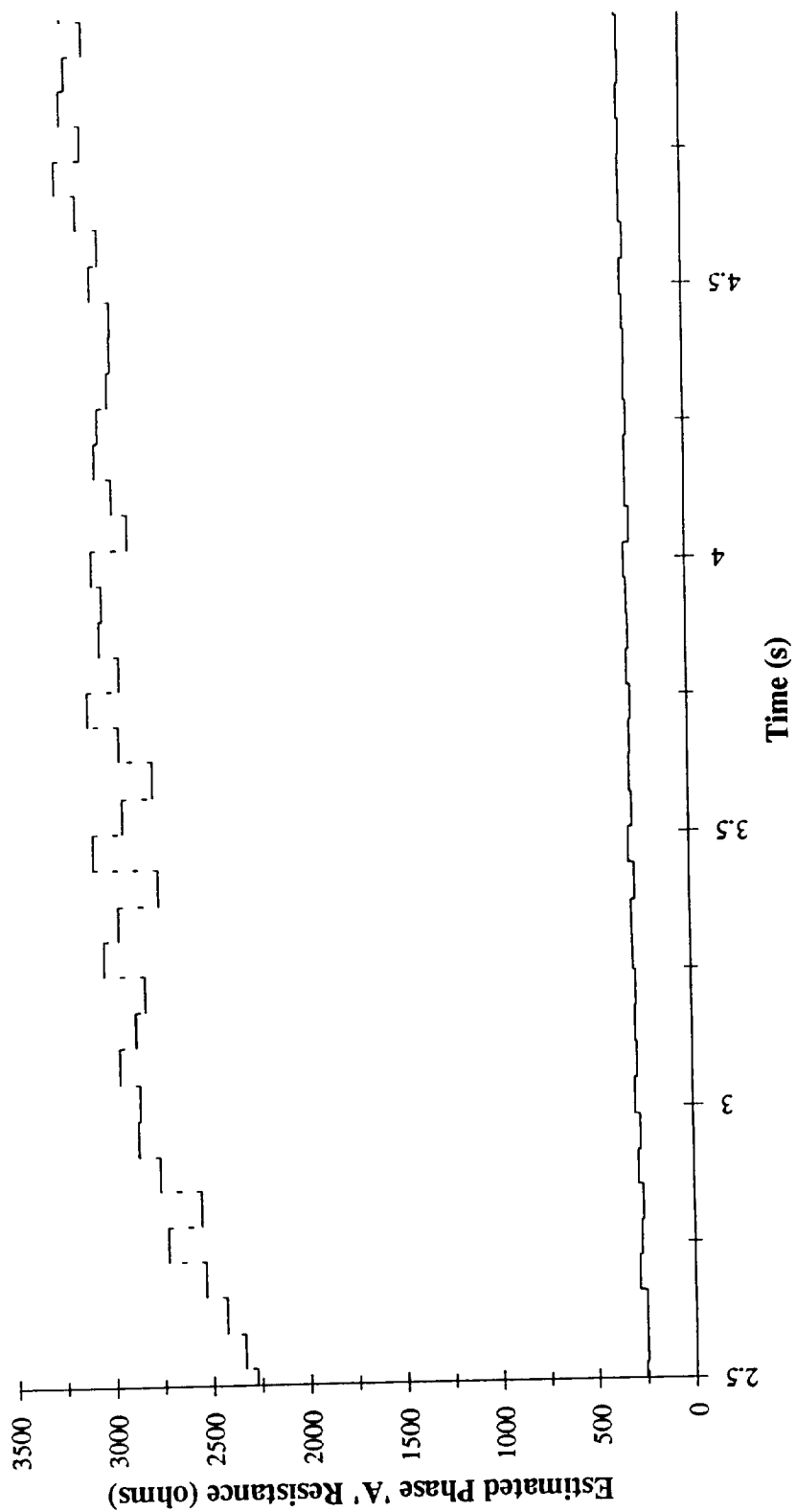


Figure 4.52 Estimated fault resistance for the simulated open circuit failure (continued)

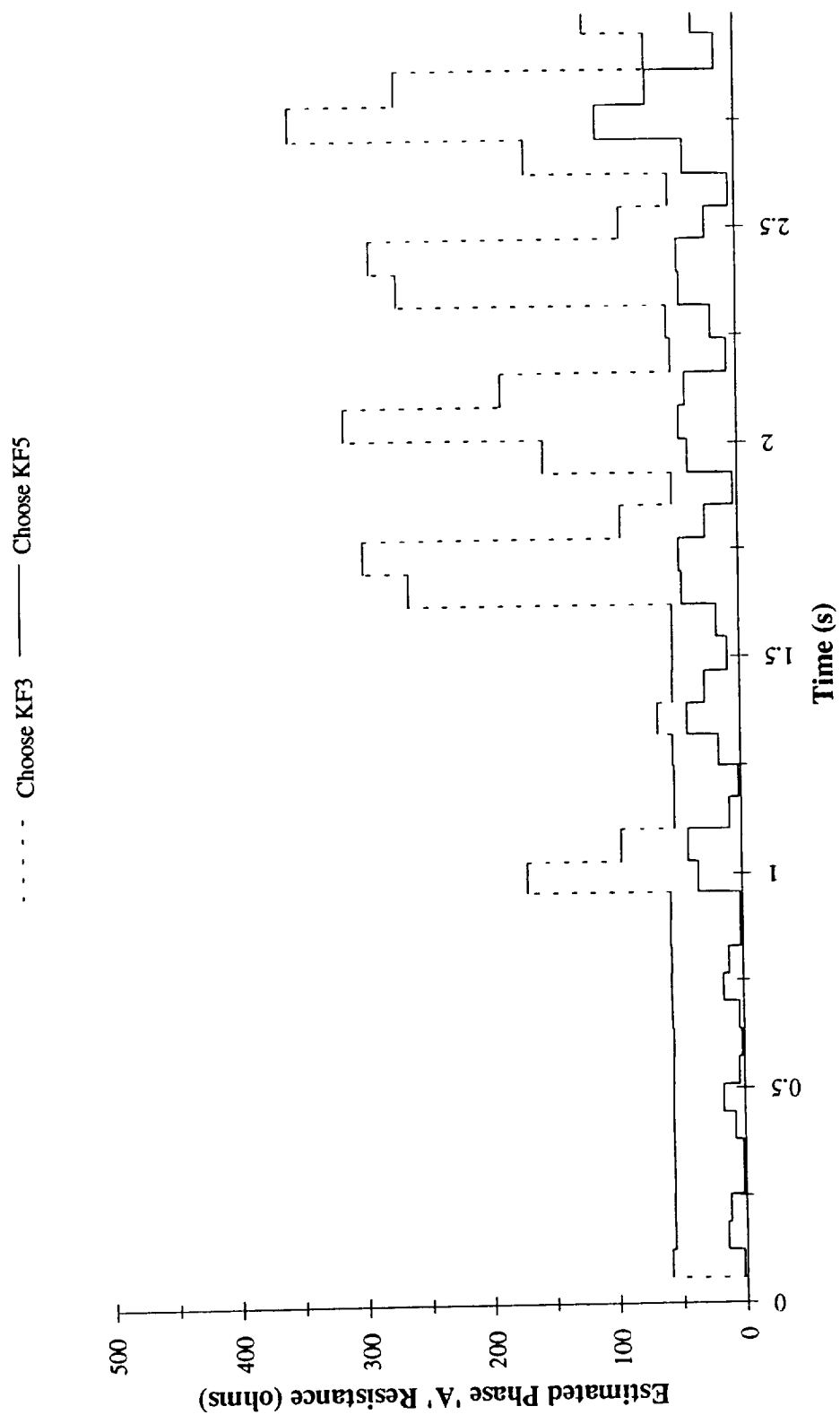


Figure 4.53 Estimated fault resistance for the actual open circuit failure

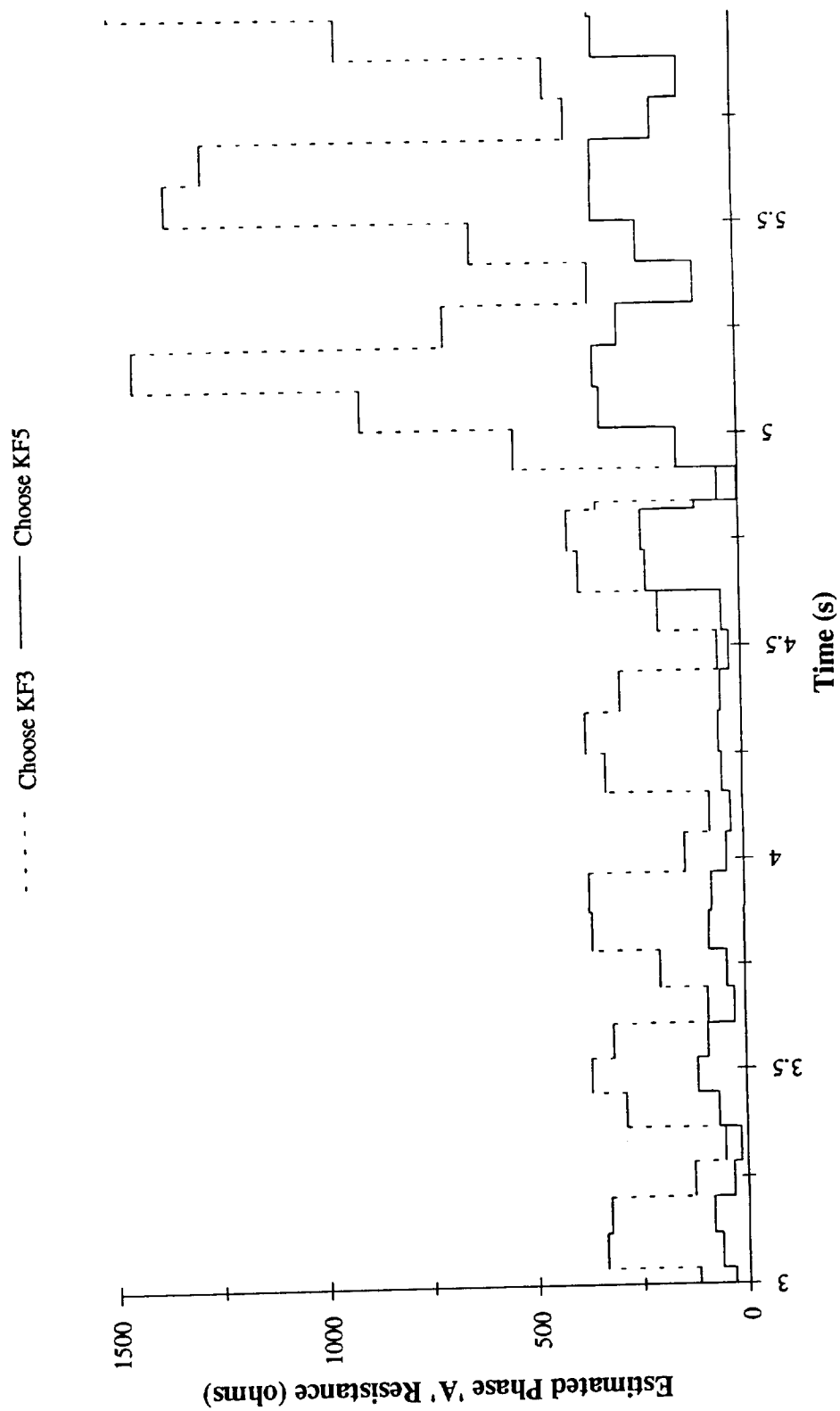


Figure 4.54 Estimated fault resistance for the actual open circuit failure (continued)

health monitoring for this failure mode can be accomplished via the adaptive Kalman filter strategy.

4.4.3 Short Circuit Failure Mode

Finally, the short circuit failure mode was evaluated with the adaptive Kalman filter. Again, an averaging scheme was used for estimating the fault resistance for the failure. Figure 4.55 shows estimated fault resistance from the adaptive Kalman filter with noisy simulated data as signal measurements. While the figure shows that the filter indeed senses the short circuit, the performance of the filter was determined to be marginal. When using actual laboratory data as signal measurements, the filter performance was inadequate. Troubleshooting the performance of the filter resulted in the discovery that the simplified motor drive model was not able to accurately depict all of the physical phenomena of the operation of the real motor drive. Specifically, when the motor speed decreases, the rotor produces a current due to the back EMF which circulates through the motor drive. The simplified model does not facilitate this current flow. Since the focus of this research is to accurately model the BPMM, resolution of the motor drive model deficiencies will become a topic for future study and development. However, once this modeling issue is resolved, the adaptive Kalman filter scheme ought to function adequately as a health monitor for this failure mode.

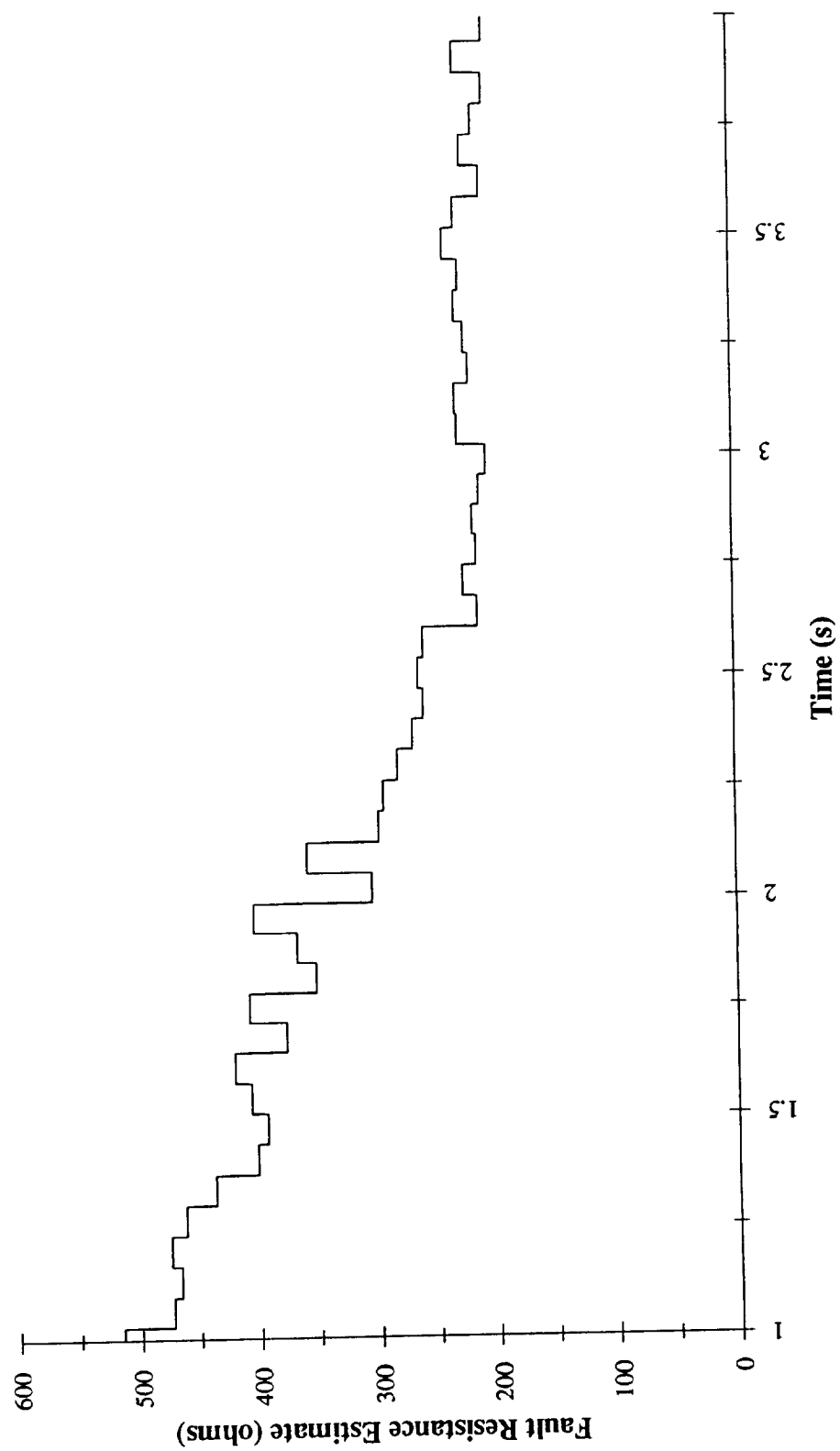


Figure 4.55 Estimated fault resistance for the simulated short circuit failure

CHAPTER 5

SUMMARY

The result of this research effort has yielded significant insight into the feasibility of using the adaptive Kalman filter as a health monitoring system for the brushless permanent magnet machine. This chapter begins with an application recommendation for utilizing this approach of health monitoring with the electromechanical actuator system. Included within the recommendation are specific concepts and tasks necessary for obtaining a practical implementation of this technology. Additionally, topics for future study and development have been defined and are presented in section 5.2.

5.1 Application Recommendation

The objective for a health monitoring system for the electromechanical actuator may be summarized as a non-intrusive, real-time fault prediction system requiring no additional sensors. To that end, the adaptive Kalman filter has been demonstrated to be a feasible approach towards a health monitoring system. While this research has not specifically addressed the issue of real-time processing, certainly it is reasonable to assert that the continued growth in computational processing capability would ensure the realization of this objective.

To obtain a practical implementation of this technology, several tasks need to be accomplished. First, the computer code which implements the adaptive Kalman filter needs to be optimized for computational performance. A twofold approach towards optimization should include enhancing the computer language structure of the code as well as reducing the computational burden of the adaptive filter. For example, the observability matrix ($[H_k]$) contains numerous zero entries which are currently being processed for each matrix multiplication involving $[H_k]$. Since $[H_k]$ does not change, the zero entry multiplication does not need to be computed during each time step. Secondly, the resulting optimized computer code should be transformed onto a digital signal processing platform. Studies should be conducted to determine the real-time processing capabilities for this architecture. The possibility exists that real-time processing is currently within reach or could be obtained with some additional code modification. Finally, the current system model used by the filter needs to be expanded to facilitate sensing the flux weakening failure as well as enhancing the capability to detect the short circuit failure. Once these tasks are accomplished, a practical implementation of the adaptive Kalman filter should be realized.

5.2 Future Development Topics

Several topics for future study and development have surfaced during the course of this research. Perhaps the most fertile opportunity for development resides in further understanding the performance of the adaptive filter as related to specific 'tuning' parameters. As previously discussed, the Kalman technique relies upon an understanding of the statistical nature of the process noise ($[Q_k]$), measurement noise ($[R_k]$), and prior state knowledge ($[P_k]$). Specifically, these covariance matrices reflect a quantification of

the confidence level for having an accurate process model, for having an accurate measurement, and for previously having an accurate state vector. Certain questions have yet to be thoroughly answered, such as, how do the covariance matrices interact with one another with respect to filter performance? Is there an optimal setting for the values of covariance which would enhance filter performance? Is the actual noise encountered statistically white, and if not, how does this impact the filter's performance?

Additional 'tuning' parameters used in the adaptive Kalman filter approach include the calculation of estimation error for each of the parallel filters and the error tolerance used for calculating the blending mixture. Currently, each filter's estimation error has been shown to be calculated as (3.26) as the statistical squared error between the measurement and state estimate. However, is this the best method for measuring the estimation error? Perhaps another method exists for quantifying the filter error that will yield better health monitoring performance. For example, one strategy for calculating the error may be,

$$\epsilon^{(j)} = \left(\underline{z}_{k+1} - [H]\hat{\underline{x}}_{k+1}^{(j)} \right)^2 [R]^{-1} \quad (5.1),$$

which would tend to minimize the estimation error due to states that have more uncertainty of measurement. Thus, the estimation error would be weighted toward the error between estimated and more accurately measured state variables. Furthermore, the current strategy chooses one filter's estimation to be accurate if the error of that filter comprises more than a defined percentage of total error for the two most accurate estimates. If the percentage of total error does not exceed the tolerance, then the two most accurate estimates are blended together. However, what is the optimal value for this tolerance setting? What is the interaction of this setting with other filter parameters? Is the current strategy for blending

the two estimates optimal? These are questions dealing with the 'tuning' of this adaptive strategy for optimal performance, and are worthy of future research.

As previously mentioned in section 5.1, the system model used by the Kalman filter needs to be expanded and refined. Clearly, the need exists for this system model to more accurately represent the operation of the motor drive and to facilitate sensing all fault modes. As long as the model is being revised, it would be valuable to clearly define the boundary conditions for the health monitoring system model. For example, should the roller screw, nut, gear box, and their associated sensors be included in the HM system? If the motor drive is included in the model, are additional sensors required? Are additional failure modes present with an expanded EMA system model?

The current strategy for parallel filter implementation utilizes five Kalman filters. Since the two most accurate estimates are utilized, is it optimal to calculate data for all five filters during each time step? Perhaps the structure could be revised and enhanced. For example, rather than using five filters, have three filters that dynamically adjust to include the most accurate state model and two additional models that allow the system to move towards differing state descriptions. Furthermore, rather than attempting to monitor each failure mode individually, would it be feasible to assess all system modes through a strategy of dynamic parameter modeling? How would these approaches differ with regard to normal parameter variance (such as the expected change in machine phase resistance due to thermal changes of the stator)?

Another topic that poses interesting questions yet to be considered is the impact of the control action of the machine with regard on the HM system. Pulse-width modulation (PWM) is one common technique for operating and controlling brushless permanent magnet machines. A machine operated with a PWM control strategy has the phase currents switched at high frequencies during normal operation. How would this switching

action affect the required sampling frequency of the HM system? How does a control action, like PWM, affect the fault detection strategy? Should the control system and HM system be interconnected in some manner?

Finally, the opportunity exists to develop further understanding of information usage with regard to the goal of health monitoring. For example, the three phase currents, pseudo Hall effect signals, and line voltages of the machine are all strongly correlated to the rotor speed of the machine. Is it possible to develop a redundant calculation of machine state variables due to this correlation? How may the state variable information be utilized to compensate for a loss of sensor failure? Currently, the machine speed signal is quite noisy, is it possible to reduce the measurement noise? If the HM system model is expanded to include the machine drive and mechanical system, will there be additional correlated signals that may be exploited for state variable calculation?

This research effort has been an initial probe into the concept of brushless permanent magnet machine health monitoring via the adaptive Kalman filter. While the study has demonstrated the feasibility of this concept, it seems as though numerous issues and items have been discovered which deserve future exploration. Hopefully, research work will continue to discover insight into these areas and a practical implementation of this technology will be fabricated.

REFERENCES

- [1] T.E. Salem, "Prime Mover Selection for Electromechanical Actuation in Thrust Vector Control Applications", *Thesis*, The University of Alabama, 1993.
- [2] R.E. Kalman, "A New Approach to Linear Filtering and Prediction Problems", *Transactions of the ASME - Journal of Basic Engineering*, March 1960, pp.35-45.
- [3] R.G. Brown and P.Y.C. Hwang, *Introduction to Random Signals and Applied Kalman Filtering*, John Wiley & Sons, Inc., 1992.
- [4] A.A. Girgis and D.G. Hart, "Implementation of Kalman and Adaptive Kalman Filtering Algorithms for Digital Distance Protection on a Vector Signal Processor", *IEEE Transactions on Power Delivery*, Vol. 4, No. 1, January 1989, pp.141-149.
- [5] J.M. Freeman, F.N. Hassan, and D. Morton, "Kalman Filter Estimation of Electrical Machine Parameters", *International Journal of Control*, Vol. 43, No. 1, 1986, pp. 305-312.
- [6] K.R. Cho, J.H. Lang, and S.D. Umans, "Detection of Broken Rotor Bars in Induction Motors Using State and Parameter Estimation", *IEEE Transactions on Industry Applications*, Vol. 28, No. 3, May / June 1992, pp. 702-708.
- [7] P. Pillay and R. Krishnan, "Application Characteristics of Permanent Magnet Synchronous and Brushless dc Motors for Servo Drives", *IEEE Transactions on Industry Applications*, Vol. 27, No. 5, September / October 1991, pp. 986-996.
- [8] N.A. Demerdash and T.W. Nehl, "Dynamic Modeling of Brushless dc Motors for Aerospace Actuation", *IEEE Transactions on Aerospace and Electronic Systems*, Vol. AES-16, No. 6, November 1980, pp. 811-821.
- [9] A. Rubbaai and R.C. Yalamanchili, "Dynamic study of an Electronically Brushless DC Machine Via Computer Simulations", *IEEE Transactions on Energy Conversion*, Vol. 7, No. 1, March 1992, pp. 132-138.
- [10] A. Consoli and A. Raciti, "Analysis of Permanent Magnet Synchronous Motors", *IEEE Transactions on Industry Applications*, Vol. 24, No. 2, March / April 1991, pp. 350-354.

- [11] S.D. Sudhoff and P.C. Krause, "Average-Value Model of the Brushless DC 120° Inverter System", *IEEE Transactions on Energy Conversion*, Vol. 5, No. 3, September 1990, pp. 553-557.
- [12] S.D. Sudhoff and P.C. Krause, "Operating Modes of the Brushless DC Motor with a 120° Inverter", *IEEE Transactions on Energy Conversion*, Vol. 5, No. 3, September 1990, pp. 558-564.
- [13] P. Pillay and R. Krishnan, "Modeling of Permanent Magnet Motor Drives", *IEEE Transactions on Industrial Electronics*, Vol. 35, No. 4, November 1988, pp. 537-541.
- [14] P. Pillay and R. Krishnan, "Modeling, Simulation, and Analysis of Permanent-Magnet Motor Drives, Part I: The Permanent-Magnet Synchronous Motor Drive", *IEEE Transactions on Industry Applications*, Vol. 25, No. 2, March / April 1989, pp. 265-273.
- [15] P. Pillay and R. Krishnan, "Modeling, Simulation, and Analysis of Permanent-Magnet Motor Drives, Part II: The Brushless DC Motor Drive", *IEEE Transactions on Industry Applications*, Vol. 25, No. 2, March / April 1989, pp. 273-279.
- [16] M. Chow, R.N. Sharpe, and J.C. Hung, "On the Application and Design of Artificial Neural Networks for Motor Fault Detection - Part I", *IEEE Transactions on Industrial Electronics*, Vol. 40, No. 2, April 1993, pp. 181-188.
- [17] M. Chow, P.M. Mangum, and S.O. Yee, "A Neural Network Approach to Real-Time Condition Monitoring of Induction Motors", *IEEE Transactions on Industrial Electronics*, Vol. 38, No. 6, December 1991, pp. 448-453.
- [18] P.V. Goode and M. Chow, "Using a Neural/Fuzzy System to Extract Heuristic Knowledge of Incipient Faults in Induction Motors: Part I - Methodology", *IEEE Transactions on Industrial Electronics*, Vol. 42, No. 2, April 1995, pp. 131-138.
- [19] W.T. Thomson, "On-Line Current Monitoring to Detect Electrical and Mechanical Faults in Three-Phase Induction Motor Drives", *Life Management of Power Plants*, Conference Publication No. 401, 1994, pp. 66-73.
- [20] J. Penman, H.G. Sedding, B.A. Lloyd, and W.T. Fink, "Detection and Location of Interturn Short Circuits in the Stator Windings of Operating Motors", *IEEE Transactions on Energy Conversion*, Vol. 9, No. 4, December 1994, pp. 652-658.
- [21] S.F. Farag, R.G. Bartheld, and T.G. Habetler, "An Integrated, On-Line, Motor Protection System", *IEEE Industry Applications Meeting*, Vol. 1, 1994, pp. 117-122.

- [22] F.C. Trutt, C.S. Cruz, J.L. Kohler, and J. Sottile, "Prediction of Electrical Behavior in Deteriorating Induction Motors", *IEEE Transactions on Industry Applications*, Vol. 29, No. 6, November / December 1993, pp. 1239-1243.
- [23] T. Kailath, "A View of Three Decades of Linear Filtering Theory", *IEEE Transactions on Information Theory*, Vol. IT-20, No. 2, March 1974, pp.146-181.
- [24] D.T. Magill, "Optimal Adaptive Estimation of Sampled Stochastic Processes", *IEEE Transactions on Automatic Control*, Vol. AC-10, No. 4, October 1965, pp.434-439.
- [25] R.G. Brown, "A New Look at the Magill Adaptive Filter as a Practical Means of Multiple Hypothesis Testing", *IEEE Transactions on Circuits and Systems*, Vol. CAS-30, No. 10, October 1983, pp. 765-768.
- [26] R. Dhaouadi, N. Mohan, and L. Norum, "Design and Implementation of an Extended Kalman Filter for the State Estimation of a Permanent Magnet Synchronous Motor", *IEEE Transaction on Power Electronics*, Vol. 6, No. 3, July 1991, pp. 491-497.
- [27] L.C. Zai, C.L. DeMarco, and T.A. Lipo, "An Extended Kalman Filter Approach to Rotor Time Constant Measurement in PWM Induction Motor Drives", *IEEE Transactions on Industry Applications*, Vol. 28, No. 1, January / February 1992, pp. 96-104.
- [28] L. Salvatore, S. Stasi, and L. Tarchioni, "A New EKF-Based Algorithm for Flux Estimation in Induction Machines", *IEEE Transactions on Industrial Electronics*, Vol. 40, No. 5, October 1993, pp. 496-504.
- [29] Y.R. Kim, S.K. Sul, and M.H. Park, "Speed Sensorless Vector Control of Induction Motor Using Extended Kalman Filter", *IEEE Transactions on Industry Applications*, Vol. 30, No. 5, September / October 1994, pp. 1225-1233.
- [30] F.N. Chowdhury, J.P. Christensen, and J.L. Aravena, "Power System Fault Detection and State Estimation Using Kalman Filter with Hypothesis Testing", *IEEE Transactions on Power Delivery*, Vol. 6, No. 3, July 1991, pp. 1025-1030.
- [31] T.E. Menke and P.S. Maybeck, "Sensor/Actuator Failure Detection in the Vista F-16 by Multiple Model Adaptive Estimation", *IEEE Transactions on Aerospace and Electronic Systems*, Vol. 31, No. 4, October 1995, pp. 1218-1228.
- [32] P.S. Maybeck and P.D. Hanlon, "Performance Enhancement of a Multiple Model Adaptive Estimator", *IEEE Transactions on Aerospace and Electronic Systems*, Vol. 31, No. 4, October 1995, pp. 1240-1253.
- [33] A.E. Fitzgerald, C.K. Kingsley, and S.D. Umans, *Electric Machinery*, McGraw-Hill Publishing Company, 1990.

- [34] J.F. Botha and G.F. Pinder, *Fundamental Concepts in the Numerical Solution of Differential Equations*, John Wiley & Sons Inc., 1983.
- [35] T.A. Harris, *Rolling Bearing Analysis*, John Wiley & Sons Inc., 1984.
- [36] D.F. Wilcock and E.R. Booser, *Bearing Design and Application*, McGraw-Hill Book Company, 1957.
- [37] K.S. Edwards and R.B. McKee, *Fundamentals of Mechanical Component Design*, McGraw-Hill Publishing Company, 1991.
- [38] D. Halliday and R. Resnick, *Fundamentals of Physics*, John Wiley & Sons Inc., 1981.
- [39] B.A. Wichmann and I.D. Hill, "Algorithm AS 183 An Efficient and Portable Pseudo-random Number Generator", *Applied Statistics*, Vol. 31, No.2, 1982, pp. 188-190.
- [40] W.W. Hines and D.C. Montgomery, *Probability and Statistics in Engineering and Management Science*, John Wiley & Sons Inc., 1990.
- [41] C.T. Leondes, *Theory and Applications of Kalman Filtering*, Technical Editing and Reproduction Ltd., Hartford House, 1970.
- [42] M.S. Grewal and A.P. Andrews, *Kalman Filtering Theory and Practice*, Prentice Hall, 1993.
- [43] T.A. Haskew and J. Wander, *Second Annual Progress Report: Design and Application of Electromechanical Actuators for Deep Space Missions*, Bureau of Engineering Research Report No. 612-163, The University of Alabama, August 1994.
- [44] W.L. Brogan, *Modern Control Theory*, Prentice Hall, 1991.
- [45] W.D. Stevenson, *Elements of Power System Analysis*, McGraw-Hill Publishing Company, 1975.

APPENDIX

Calibration program:

```
*****
*** This statement enables Qbasic to call functions configured
*** by the DAQ manufacturer. The CB.BI file must be in the
*** C:\MDRIVE directory. Also note that the CB.CFG file must
*** be in the C:\MDRIVE directory and it must be set for 16
*** channel analog input.

$INCLUDE: 'CB.BI'

*****
*** Declare and define variables

CONST BoardNum = 0           'AD board ID
CONST NUMPOINTS = 5000      'Total number of samples per channel
FirstPoint = 0              'Index used in streamer file access

SUM0 = 0!                   'Counter used for averaging Chan0
SUM1 = 0!                   'Counter used for averaging Chan1
SUM2 = 0!                   'Counter used for averaging Chan2
SUM3 = 0!                   'Counter used for averaging Chan3
SUM4 = 0!                   'Counter used for averaging Chan4
SUM5 = 0!                   'Counter used for averaging Chan5
SUM6 = 0!                   'Counter used for averaging Chan6
SUM7 = 0!                   'Counter used for averaging Chan7
SUM8 = 0!                   'Counter used for averaging Chan8
SUM9 = 0!                   'Counter used for averaging Chan9
SUM10 = 0!                  'Counter used for averaging Chan10
SUM11 = 0!                  'Counter used for averaging Chan11
SUM12 = 0!                  'Counter used for averaging Chan12
SUM13 = 0!                  'Counter used for averaging Chan13
SUM14 = 0!                  'Counter used for averaging Chan14
SUM15 = 0!                  'Counter used for averaging Chan15
```

```

LowChan% = 0                'Lowest channel sampled
HighChan% = 15              'Highest channel sampled
Channels& = HighChan% - LowChan% + 1    'Total number of channels sample
Count& = NUMPOINTS * (Channels&)        'Total number of data samples
Rate& = 10000                'Sampling rate for each channel (samples/second)
Options% = NODTCONNECT       'Variable for the cbFileAInScan statement
Gain% = BIP10VOLTS           'Variable for the cbFileInScan statement

```

```

*****

```

```

CLS

```

```

'*** The SHELL command launches DOS operation of the RAMDAT batch
'*** file, which creates the data streamer file.

```

```

SHELL "C:\MDRIVE\BATCH\RAMDAT"

```

```

'*** RAM.DAT is the filename for the data streamer file located on
'*** the D drive, which is a RAM disk. The data file has been
'*** configured to hold 500,000 data points.

```

```

RAMDRIVE$ = "D:\RAM.DAT"

```

```

Spreadsheet$ = "C:\MDRIVE\CALIB.DAT" 'Filespec for calibration results

```

```

*****

```

```

'$STATIC

```

```

    DIM AddData%(Channels&) 'dimension an array to hold the input values

```

```

    DIM ChanTags%(Channels&) 'dimension an array to hold the channel tags

```

```

*****

```

```

'*** Launch the error handling routine, this is a function call

```

```

UDStat% = cbErrHandling%(PRINTALL, STOPALL)

```

```

*****

```

```

CLS

```

```

X% = POS(0)

```

```

Y% = CSRLIN

```

```

PRINT "Collecting data.", TIME$

```

```

PRINT

```

```

*****

```

```

'*** cbFileAInScan is a function call to scan the DAQ an stream

```

```

'*** the data into a specified file.

```

```

UDStat% = cbFileAInScan%(BoardNum, LowChan%, HighChan%, Count&, Rate&,
Gain%, RAMDRIVE$, Options%)

```

```

PRINT "Data collection complete.", TIME$

```

```
PRINT
PRINT "Beginning data conversion."
PRINT
```

```
OPEN Spreadsheet$ FOR OUTPUT AS #1
```

```
*****
```

```
FOR j = 1 TO NUMPOINTS
```

```
UDStat% = cbFileRead%(RAMDRIVE$, FirstPoint, Channels&, ADDData%(0))
UDStat% = cbAConvertData%(Channels&, ADDData%(0), ChanTags%(0))
```

```
*****
```

```
'*** The CHAN# variables convert the binary channel information
'*** contained in the ADDData% array into actual values. The channel
'*** voltage range is assumed to be +/-10 volts; therefore,
'*** 20/4096 * ADDData% - 10 centers and converts the binary signal to
'*** the +/-10 volt scale.
```

```
CHAN0 = (20! / 4096!) * ADDData%(0) - 10!
CHAN1 = (20! / 4096!) * ADDData%(1) - 10!
CHAN2 = (20! / 4096!) * ADDData%(2) - 10!
CHAN3 = (20! / 4096!) * ADDData%(3) - 10!
CHAN4 = (20! / 4096!) * ADDData%(4) - 10!
CHAN5 = (20! / 4096!) * ADDData%(5) - 10!
CHAN6 = (20! / 4096!) * ADDData%(6) - 10!
CHAN7 = (20! / 4096!) * ADDData%(7) - 10!
CHAN8 = (20! / 4096!) * ADDData%(8) - 10!
CHAN9 = (20! / 4096!) * ADDData%(9) - 10!
CHAN10 = (20! / 4096!) * ADDData%(10) - 10!
CHAN11 = (20! / 4096!) * ADDData%(11) - 10!
CHAN12 = (20! / 4096!) * ADDData%(12) - 10!
CHAN13 = (20! / 4096!) * ADDData%(13) - 10!
CHAN14 = (20! / 4096!) * ADDData%(14) - 10!
CHAN15 = (20! / 4096!) * ADDData%(15) - 10!
```

```
*****
```

```
'*** Sum is used for calculating the average.
```

```
SUM0 = SUM0 + CHAN0
SUM1 = SUM1 + CHAN1
SUM2 = SUM2 + CHAN2
SUM3 = SUM3 + CHAN3
SUM4 = SUM4 + CHAN4
SUM5 = SUM5 + CHAN5
SUM6 = SUM6 + CHAN6
SUM7 = SUM7 + CHAN7
```



```
SUM8 = SUM8 + CHAN8
SUM9 = SUM9 + CHAN9
SUM10 = SUM10 + CHAN10
SUM11 = SUM11 + CHAN11
SUM12 = SUM12 + CHAN12
SUM13 = SUM13 + CHAN13
SUM14 = SUM14 + CHAN14
SUM15 = SUM15 + CHAN15
```

```
*****
***   Increment Firstpoint so that the next set of 16 data
***   samples can be accessed in the cbFileRead statement.
```

```
FirstPoint = FirstPoint + (Channels&)
```

```
*****
```

```
NEXT
```

```
PRINT
PRINT "Data conversion completed.", TIME$
```

```
*****
***   Compute the average values for each channel
```

```
SUM0 = SUM0 / NUMPOINTS
SUM1 = SUM1 / NUMPOINTS
SUM2 = SUM2 / NUMPOINTS
SUM3 = SUM3 / NUMPOINTS
SUM4 = SUM4 / NUMPOINTS
SUM5 = SUM5 / NUMPOINTS
SUM6 = SUM6 / NUMPOINTS
SUM7 = SUM7 / NUMPOINTS
SUM8 = SUM8 / NUMPOINTS
SUM9 = SUM9 / NUMPOINTS
SUM10 = SUM10 / NUMPOINTS
SUM11 = SUM11 / NUMPOINTS
SUM12 = SUM12 / NUMPOINTS
SUM13 = SUM13 / NUMPOINTS
SUM14 = SUM14 / NUMPOINTS
SUM15 = SUM15 / NUMPOINTS
```

```
*****
***   Output the results to #1 and the screen
```

```
PRINT #1, SUM0, SUM1, SUM2, SUM3, SUM4, SUM5, SUM6, SUM7, SUM8,
SUM9, SUM10, SUM11, SUM12, SUM13, SUM14, SUM15
```

```

PRINT
PRINT "Channel Calibrations:"
PRINT
PRINT "Chan 0 ... Vdc1", SUM0
PRINT "Chan 1 ... Vdc2", SUM1
PRINT "Chan 2 ... Idc ", SUM2
PRINT "Chan 3 ... Va  ", SUM3
PRINT "Chan 4 ... Ia  ", SUM4
PRINT "Chan 5 ... Vb  ", SUM5
PRINT "Chan 6 ... Ib  ", SUM6
PRINT "Chan 7 ... Vc  ", SUM7
PRINT "Chan 8 ... Ic  ", SUM8
PRINT "Chan 9 ... Hall A", SUM9
PRINT "Chan 10 ... Hall B", SUM10
PRINT "Chan 11 ... Hall C", SUM11
PRINT "Chan 12 ... Speed Act", SUM12
PRINT "Chan 13 ... Speed Des", SUM13
PRINT "Chan 14 ... Carrier", SUM14
PRINT "Chan 15 ... PWM", SUM15

```

```
CLOSE #1
```

```
END
```

Data acquisition program:

```

'*****
'*** This statement enables Qbasic to call functions configured
'*** by the DAQ manufacturer. The CB.BI file must be in the
'*** C:\MDRIVE directory. Also note that the CB.CFG file must
'*** be in the C:\MDRIVE directory and it must be set for 16
'*** channel analog input.

```

```
'$INCLUDE: 'CB.BI'
```

```

'*****
'*** Declare and define variables

```

```

CONST BoardNum = 0          'AD board ID
CONST NumPoints = 1000      'Total number of samples per channel
CONST Rate& = 5000          'Sampling rate for each channel (samples/second)

FirstPoint = 0              'Index used in streamer file access

```

```

LowChan% = 0                'Lowest channel sampled
HighChan% = 15              'Highest channel sampled
Channels& = HighChan% - LowChan% + 1    'Total number of channels sampled
Count& = NumPoints * (Channels&)        'Total number of data samples
Options% = NODTCONNECT      'Variable for the cbFileAInScan statement
Gain% = BIP10VOLTS          'Variable for the cbFileInScan statement

```

```

'*****

```

```

'$STATIC
  DIM ADDData%(Channels&) 'dimension an array to hold the input values
  DIM ChanTags%(Channels&) 'dimension an array to hold the channel tags
  DIM CalData%(4500)

```

```

'*****

```

```

'***  Get the Channel Calibration results

```

```

OPEN "C:\MDRIVE\CALIB.DAT" FOR INPUT AS #2

```

```

INPUT #2, BIAS0, BIAS1, BIAS2, BIAS3, BIAS4, BIAS5, BIAS6, BIAS7, BIAS8,
BIAS9, BIAS10, BIAS11, BIAS12, BIAS13, BIAS14, BIAS15

```

```

RANGE0 = 40! / BIAS2      'Variable used to convert Idc
RANGE1 = 40! / BIAS4      'Variable used to convert Ia
RANGE2 = 40! / BIAS6      'Variable used to convert Ib
RANGE3 = 40! / BIAS8      'Variable used to convert Ic
'*****

```

```

CLS

```

```

'***  The SHELL command launches DOS operation of the RAMDAT batch
'***  file, which creates the data streamer file.

```

```

SHELL "C:\MDRIVE\BATCH\RAMDAT"

```

```

'***  RAM.DAT is the filename for the data streamer file located on
'***  the D drive, which is a RAM disk. The data file has been
'***  configured to hold 500,000 data points.

```

```

RAMDRIVE$ = "D:\RAM.DAT"

```

```

PRINT
PRINT
INPUT "Filename (no extension) to store data"; File$

```

```

CLS

```

```

'***  C nverted data spread sheet file

```

```
Spreadsheet$ = "C:\MDRIVE\TOM" + File$ + ".wk1"
```

```
*****
```

```
*** Launch the error handling routine
```

```
UDStat% = cbErrHandling%(PRINTALL, STOPALL)
```

```
*****
```

```
X% = POS(0)
```

```
Y% = CSRLIN
```

```
PRINT "Collecting data.", TIMES$
```

```
PRINT
```

```
*****
```

```
UDStat% = cbFileAInScan%(BoardNum, LowChan%, HighChan%, Count&, Rate&, Gain%, RAMDRIVE$, Options%)
```

```
PRINT "Data collection complete.", TIMES$
```

```
PRINT
```

```
PRINT "Beginning data conversion."
```

```
PRINT
```

```
OPEN Spreadsheet$ FOR OUTPUT AS #1
```

```
*****
```

```
*** Tag variables provide column header information for the spreadsheet
```

```
Tag0$ = "V Dc1"
```

```
Tag1$ = "V Dc2"
```

```
Tag2$ = "I Bus"
```

```
Tag3$ = "Va"
```

```
Tag4$ = "Ia"
```

```
Tag5$ = "Vb"
```

```
Tag6$ = "Ib"
```

```
Tag7$ = "Vc"
```

```
Tag8$ = "Ic"
```

```
Tag9$ = "Hall A"
```

```
Tag10$ = "Hall B"
```

```
Tag11$ = "Hall C"
```

```
Tag12$ = "Speed Act"
```

```
Tag13$ = "Speed Des"
```

```
Tag14$ = "Carrier"
```

```
Tag15$ = "PWM"
```

```
Tag16$ = "Samp Rate"
```

```
PRINT #1, USING "&.&.&.&.&.&.&.&.&.&.&.&.&.&.#####"; Tag0$;  
Tag1$; Tag2$; Tag3$; Tag4$; Tag5$; Tag6$; Tag7$; Tag8$; Tag9$; Tag10$; Tag11$;  
Tag12$; Tag13$; Tag14$; Tag15$; DATE$; TIME$; Tag16$; Rate&  
'*****  
FOR j = 1 TO NumPoints
```

```
UDStat% = cbFileRead%(RAMDRIVE$, FirstPoint, Channels&, ADDData%(0))
UDStat% = cbAConvertData%(Channels&, ADDData%(0), ChanTags%(0))
```

```
*****
*** The CHAN# variables convert the binary channel information
*** contained in the ADDData% array into actual values. The channel
*** voltage range is assumed to be +/-10 volts; therefore,
*** 20/4096 * ADDData% - 10 - BIAS# centers and converts the
*** binary signal to the +/-10 volt scale.
```

CHAN0 = 25! * (((.0048828125#) * ADDData%(0) - 10!) - BIAS0)	'Vdc1
CHAN1 = 25! * (((.0048828125#) * ADDData%(1) - 10!) - BIAS1)	'Vdc2
CHAN2 = RANGE0 * (((.0048828125#) * ADDData%(2) - 10!) - BIAS2)	'Idc
CHAN3 = 25! * (((.0048828125#) * ADDData%(3) - 10!) - BIAS3)	'Va
CHAN4 = RANGE1 * (((.0048828125#) * ADDData%(4) - 10!) - BIAS4)	'Ia
CHAN5 = 25! * (((.0048828125#) * ADDData%(5) - 10!) - BIAS5)	'Vb
CHAN6 = RANGE2 * (((.0048828125#) * ADDData%(6) - 10!) - BIAS6)	'Ib
CHAN7 = 25! * (((.0048828125#) * ADDData%(7) - 10!) - BIAS7)	'Vc
CHAN8 = RANGE3 * (((.0048828125#) * ADDData%(8) - 10!) - BIAS8)	'Ic
CHAN9 = .0048828125# * ADDData%(9) - 10!	'Hall A
CHAN10 = .0048828125# * ADDData%(10) - 10!	'Hall B
CHAN11 = .0048828125# * ADDData%(11) - 10!	'Hall C
CHAN12 = 687.5 * (.0048828125# * ADDData%(12) - 10! - BIAS12)	'Speed Act
CHAN13 = 275 * (.0048828125# * ADDData%(13) - 10!)	'Speed Des
CHAN14 = .0048828125# * ADDData%(14) - 10!	'Carrier
CHAN15 = .0048828125# * ADDData%(15) - 10!	'PWM

```
'*****'
'***  Output the results
```

```
PRINT#1,USING"#####.#####.#####.#####.#####.#####.#####.#####.#####.#####.#####,##  
###.#####.#####.#####.#####.#####.#####.#####.#####.#####.#####.#####.#####.###  
###.#####.#####"; CHAN0; CHAN1; CHAN2; CHAN3; CHAN4; CHAN5; CHAN6;  
CHAN7; CHAN8; CHAN9;CHAN10; CHAN11; CHAN12; CHAN13; CHAN14;  
CHAN15
```

```

*** Increment Firstpoint so that the next set of 16 data
*** samples can be accessed in the cbFileRead statement.

```

$$\text{FirstPoint} = \text{FirstPoint} + (\text{Channels} \&)$$

NEXT

'*****'

PRINT

PRINT "Data conversion completed.", TIMES

CLOSE #1

END

